ION IMPRINTED POLYMER/METAL-ORGANIC FRAMEWORK COMPOSITES AS EFFICIENT ADSORBENTS FOR SELECTIVE RECOGNITION AND SEPARATION OF SELECTED PLATINUM GROUP METALS FROM WASTEWATER

By

THABISO CAROL MAPONYA

THESIS

Submitted in fulfilment of the requirements for the degree of

DOCTOR OF PHILOSOPHY

In

CHEMISTRY

In the

FACULTY OF SCIENCE AND AGRICULTURE

(School of Physical and Mineral Sciences)

At the

UNIVERSITY OF LIMPOPO

SUPERVISORS: PROF KD MODIBANE

CO-SUPERVISORS: PROF MJ HATO

DR K MAKGOPA (TUT)

2023

DEDICATION

***To my beloved late grandmother*.**

Hendrica Ramadimetja Maponya

And

My amazing beautiful daughter

Oratilwe Metja Maponya

DECLARATION BY CANDIDATE

I declare that the “Ion Imprinted Polymer/Metal-Organic Framework Composites As Efficient Adsorbents For Selective Recognition And Separation Of Selected Platinum Group Metals From Wastewater” thesis hereby submitted to the University of Limpopo, for the degree Doctor of Philosophy (Chemistry) has not previously been submitted by me for a degree at this or any other university; that it is my own work in design and in execution, and that all material contained herein has been duly acknowledged.

Maponya T.C (Ms) **Date: 05/04/2023**

ACKNOWLEDGEMENTS

I would like to express my deepest appreciation to my supervisor Prof KD Modibane for his unlimited and unconditional support throughout my postgraduate years. Your constant motivation, extraordinary encouragement and guidance has landed me where I am today. Prof Modibane, not only did he equip me with the necessary knowledge, problem solving and innovative skills to succeed in completely my studies, he has furnished me with good supervision and leadership skills. Working with Prof has greatly increased my interest in research and taught me to work hard, believe in myself and aim for greater heights. I truly appreciate all the time you patiently spent and priceless efforts you made to provide assistance and advice both academic and social, even during difficult times of the Covid-19 pandemic. Through your NRF Thuthuka research grant you provided the necessary laboratory facilities, which allowed me to complete my studies. I am forever indebted to you. Your personality and leadership is one of the kind.

To my co-supervisors; thank you for lending a helping hand, where you saw necessary throughout my academic studies. To Dr Katlego Makgopa, thank you very much for the tremendous academic support and assistance day in and out. Dr Makgopa made it a priority for me to get access to all the essential instruments I needed to complete my studies and continuously encouraged me to perserve. Your remarkable advices and support is much appreciated. Thank you many times.

To Prof Hato, thank you for your involvement and assistance in writing chapter two of this work. To my younger brother Mr TR Somo, without your support and involvement completing this work was going to be an unbearable struggle. I really appreciate your time, patience and significant contributions to this work. To Nanotechnology Research Group at University of Limpopo (NanoRG@UL), thank you for making lab a greatest place to be.

Special thanks to the University of Limpopo, Department of Chemistry under for giving me opportunity to study towards my postgraduate studies. The contribution done by various staff members and postgraduate students which I could not name individually is much appreciated and thanks for the support.

Without the support and encouragement of my family, I would not be where I am. Heartfelt appreciations to my mother, Mamma Constance Maponya, for the indefinite love, support and encouragement. Indeed ***Seswana se re: "Mmago ngwana o tshwara thipa ka bogaleng"***. My love for you can never be over emphasised. To my dearest siblings Itumeleng Maponya, Mmatsela Ramphele and Tebatso Matibidi thank you for the support and being there when you were needed. To all my friends who I cannot name individually thank you for the role you played. Lastly, I would like to thank God for life He enriched in me.

ABSTRACT

Platinum group metal (PGMs) are the most extracted non-renewable mineral resources in South African due to their high demand for various applications. During mineral processing some of these valuable metals are lost into the generated toxic which is excessively released into the environment. Adsorption technology offers advantages of ease operation, high effectiveness and opportunity to incorporate other techniques such as ion-imprinting method. Metal-organic frameworks have been explored as adsorbent due to their interesting properties such tuneable surface functionality and ability to host guest molecules. In this work, metal organic framework, MIL-101(Cr), (MIL= Matérial Institut Lavoisier) prepared from polyethylene-terephlalate waste was initially functionalised with ethylenediamine (ED) to form MIL-101(Cr)/ED for the adsorption of palladium (Pd) ions from aqueous solution. The successful incorporation of ED was confirmed by Fourier transform infrared spectroscopy with N-H vibrations at 3300 -3000 cm^{-1}. The MIL-101(Cr)/ED achieved a maximum adsorption capacity (qm) of 454.2 mg/g for the uptake of Pd(II) ions in a pH =3.0 and 0.03 g of the adsorbent dose. MIL-101(Cr)/ED adsorbent was selective and fast towards the adsorption of Pd(II) ions. However, the regeneration and reusability of the adsorbent was still a challenge. The MIL-101(Cr)/ED was further grafting with glutaraldehyde (GA) to enhance the regeneration and reusability. This functionalisation was noted by the appearance 1554 and 1052 cm^{-1} for N-H bend and C-N stretch in the MIL-101(Cr)/ED-GA due to the amide bond formation. The efficiency of MIL-101(Cr)/ED-GA was tested for Pd(II) and platinum (Pt(IV)) ions. The data showed a good fit to the Langmuir isotherm and pseudo-second order (PSO) kinetic models. The estimated qm values were 414.4 for Pt(IV) and 308.3 mg/g for Pd(II) ions. The adsorption rate of the MIL-101(Cr)/ED-GA adsorbent was very rapid towards Pd(II) ions intake than Pt(IV) ions and resulted in higher selectivity of Pd(II) ions over Pt(IV) ions. Adsorption-desorption cycles for the reusability of MIL-101(Cr)/ED-GA in removing both metal ions were stable for two successive cycles and started to decrease in the third cycle. The reusability of MIL-101(Cr)/ED-GA showed a significant

drop in removal efficiency (%R) towards Pd(II) ions from 84% in the first cycle to 73% in the fourth and fifth cycle. The regeneration and reusability of the MIL-101(Cr)/ED-GA was improved by ion-imprinting Pd(II) ions on a glycylglycine (glygly) functional monomer and formed an ion specific IPMIL-101(Cr) composite. The optimum adsorption conditions for the uptake of Pd(II) ions were achieved at 0.03 g of the IP-MIL-101(Cr) adsorbent and pH=2.0. This suggested electrostatic interaction between the protonated nitrogen (N) groups on the adsorbent surface and the Pd(II) ions complexes. The Langmuir isotherm was the well fitted model and estimated the qm of 195.3 mg/g for the adsorption of Pd(II) ions IPMIL-101(Cr) composite which was higher than 177.7 mg/g of the its non-imprinted counterpart (NIMIL-101(Cr). Kinetics data further confirmed the improved rapid adsorption rate of Pd(II) by the IPMIL-101(Cr) which obeyed the PSO kinetic model. The ion specific IPMIL-101(Cr) adsorbent was re-generable for five consecutive cycle without loss in the removal efficiency and adsorption capacity.

The Pt(IV) ion imprinted IIGlyMIL-101(Cr) composite, which was prepared using the same glygly functional monomer showed enhanced performance in the adsorption of targeted Pt(IV) ions from aqueous solution. In an initial solution pH of 3.0, 0.02 g of the IIGlyMIL-101(Cr) adsorbent was able to recover 85% of the Pt(IV) ions at 25 ^{o}C. The qm value were obtained from the Langmuir isotherm model to be 531.3 mg/g for the IIGlyMIL-101(Cr) adsorbent in the intake of Pt(IV) ions, which was higher than 296.4 mg/g of the non-imprinted counterpart (NIGlyMIL-101(Cr)) composite. Kinetics data revealed fast adsorption of Pt(IV) ions by IIGlyMIL-101(Cr) which equilibrated within 30 minutes and fitted well with PSO kinetic model. The selectivity towards Pt(IV) ions intake by the IIGlyMIL-101(Cr) composite was also improved with an efficiency of 80% in comparison to the non-imprinted adsorbent which was 50% in the presence of various anions. Moreover, the IIGlyMIL-101(Cr) composite was able to maintained 88% removal efficiency after five subsequent cycles, suggesting improved stability of the adsorption active sites. The results observed in this study proved the efficiency of ion-imprinted MOF composites and their potential application in the recovery of PGMs form industrial wastewater should be considered.

RESEARCH OUTPUTS

PUBLICATIONS

Maponya, T.C., Modibane, K.D., Makgopa, K and Somo, T.R., 2023. Selective adsorption of palladium ions from wastewater by ion-imprinted MIL-101(Cr) derived from waste polyethylene terephthalate: Isotherms and kinetics. Separation and Purification Technology, 307, p.122767.

Maponya, T.C., Makgopa, K., Somo, T.R., Tshwane, D.M. and Modibane, K.D., 2023. Highly adsorptive removal of palladium and platinum ions from wastewater using novel ethylenediamine-glutaraldehyde-grafted metal organic framework. Environmental Nanotechnology, Monitoring & Management, 20, p.100805.

Maponya, T.C., Makgopa, K., Somo, T.R. and Modibane, K.D., 2022. Highlighting the Importance of Characterization Techniques Employed in Adsorption Using Metal–Organic Frameworks for Water Treatment. *Polymers*, *14*(17), p.3613.

Maponya, T.C., Makgopa, K., Modibane, K.D. and Hato, M.J., 2020. Metal-Organic Frameworks for Heavy Metal Removal from Water. In *Metal-Organic Framework Nanocomposites* (pp. 13-52). CRC Press.

Maponya, T.C., Hato, M.J., Makhado, E., Makgopa, K., Khanuja, M. and Modibane, K.D., 2021. Photocatalytic Degradation of Dyes in Wastewater Using Metal Organic Frameworks. In *Metal, Metal-Oxides and Metal-Organic Frameworks for Environmental Remediation* (pp. 261-285). Springer, Cham.

Maponya, T.C., Ramohlola, K.E., Kera, N.H., Modibane, K.D., Maity, A., Katata-Seru, L.M. and Hato, M.J., 2020. Influence of magnetic nanoparticles on modified polypyrrole/m-phenylediamine for adsorption of Cr (VI) from aqueous solution. *Polymers*, *12*(3), p.679.

Maponya, T.C., Hato, M.J., Modibane, K.D. and Makgopa, K., 2020. Metal–Organic Frameworks as Possible Candidates for Photocatalytic Degradation of Dyes in

Wastewater. *Photocatalysts in Advanced Oxidation Processes for Wastewater Treatment*, pp.65-91.

Maponya, T.C., Hato, M.J., Somo, T.R., Ramohlola, K.E., Makhafola, M.D., Monama, G.R., Maity, A., Modibane, K.D. and Katata-Seru, L.M., 2019. Polyaniline-based nanocomposites for environmental remediation. In *Trace Metals in the Environment-New Approaches and Recent Advances*. IntechOpen.

Teffu, D.M., Ramoroka, M.E., Makhafola, M.D., Makgopa, K., **Maponya, T.C**., Seerane, O.A., Hato, M.J., Iwuoha, E.I. and Modibane, K.D., 2022. High-performance supercabattery based on reduced graphene oxide/metal organic framework nanocomposite decorated with palladium nanoparticles. *Electrochimica Acta*, *412*, p.140136.

Mabokela, T.E., Somo, T.R., **Maponya, T.C**., Hato, M.J., Makhado, E., Makgopa, K. and Modibane, K.D., 2022. Dynamic carbon dioxide uptake capacity of metal organic framework using thermogravimetrical evaluation at different CO2 pressure. *Materials Letters*, *317*, p.132086.

Modibane, K.D., Pesha, T., **Maponya, T.C**., Ramohlola, K.E., Monama, G.R., Makhatha, M.E., Makhado, E. and Hato, M.J., 2021. Electrochemical studies on the corrosion protection of aluminum metal in acid media by unsubstituted and 4-tetranitro substituted nickel (II) phthalocyanine inhibitors for hydrogen fuel cells. *International Journal of Corrosion and Scale Inhibition*, *10*(1), pp.314-330.

Makhafola, M.D., Hato, M.J., Ramohlola, K.E., Ramaripa, P.S., **Maponya, T.C**., Monama, G.R., Molapo, K.M., Iwuoha, E.I., Katata-Seru, L.M., Makgopa, K. and Modibane, K.D., 2021. Synergetic Effect of Graphene Oxide and Metal Organic Framework Nanocomposites as Electrocatalysts for Hydrogen Evolution Reaction. In *Carbon Related Materials* (pp. 23-54). Springer, Singapore.

Somo, T.R., **Maponya, T.C**., Davids, M.W., Hato, M.J., Lototskyy, M.V. and Modibane, K.D., 2020. A comprehensive review on hydrogen absorption behaviour of metal alloys prepared through mechanical alloying. *Metals*, *10*(5), p.562.

Malatji, N., Makhado, E., Modibane, K.D., Ramohlola, K.E., **Maponya, T.C**., Monama, G.R. and Hato, M.J., 2021. Removal of methylene blue from wastewater using hydrogel nanocomposites: a review. *Nanomaterials and Nanotechnology*, *11*, p.18479804211039425.

Makhafola, M.D., Modibane, K.D., Ramohlola, K.E., **Maponya, T.C**., Hato, M.J., Makgopa, K. and Iwuoha, E.I., 2021. Palladinized graphene oxide-MOF induced coupling of Volmer and Heyrovsky mechanisms, for the amplification of the electrocatalytic efficiency of hydrogen evolution reaction. *Scientific Reports*, *11*(1), pp.1-16.

Malatji, N., Makhado, E., Ramohlola, K.E., Modibane, K.D., **Maponya, T.C.,** Monama, G.R. and Hato, M.J., 2020. Synthesis and characterization of magnetic clay-based carboxymethyl cellulose-acrylic acid hydrogel nanocomposite for methylene blue dye removal from aqueous solution. *Environmental Science and Pollution Research*, *27*(35), pp.44089-44105.

Katata-Seru, L.M., **Maponya, T.C**., Makhado, E., Modibane, K.D., Hato, M.J., Matomea, S.M. and Bahadur, I., 2020. Green synthesis of polypyrrole/nanoscale zero valent iron nanocomposite and use as an adsorbent for hexavalent chromium from aqueous solution. *South African Journal of Chemical Engineering*, *34*(1), pp.1-10.

Hato, M.J., **Maponya, T.C**., Ramohlola, K.E., Modibane, K.D., Maity, A., Monama, G.R., Makgopa, K. and Bello, A., 2019. Polymer-Based magnetic nanocomposites for the removal of highly toxic hexavalent chromium from aqueous solutions. *Advanced Nanostructured Materials for Environmental Remediation*, pp.189-227.

Monama, G.R., Hato, M.J., Ramohlola, K.E., **Maponya, T.C**., Mdluli, S.B., Molapo, K.M., Modibane, K.D., Iwuoha, E.I., Makgopa, K. and Teffu, M.D., 2019. Hierarchiral 4-tetranitro copper (II) phthalocyanine based metal organic framework hybrid composite with improved electrocatalytic efficiency towards hydrogen evolution reaction. *Results in Physics*, *15*, p.102564.

PROVISIONAL PATENTS

Recovery of palladium ions from industrial wastewater by ion imprinted polymer system– Ref: ZA2022/10229.

PRESENTATIONS

Maponya T.C, Modibane K.D, Makgopa K and Hato M.J, Towards the synthesis and functionalisation of ion imprinted polyethylene terephthalate–derived MOF for selective adsorption of palladium ions from aqueous solutions: Isotherms and Kinetics. Oral Presentation. Faculty of Science and Agriculture Research Day, Bolivia Lodge, Polokwane, South Africa on the 23rd October 2022.

TABLE OF CONTENTS

LIST OF FIGURES

LIST OF TABLES

LIST OF ABBREVIATIONS

AAS	Atomic absorption spectroscopy
AC	Activated carbon
AHPP	4-amino-3-hydroxybenzoic acid and p-phthalaldehyde
AO	Amidoxime
AR1	Acid red I
BDC	1,4-benzenedicarboxylic acid
BET	Brunauer-Emmett-Teller
BTC	Benzene-1,3,5-tricarboxylate
CA	Cellulose aerogel
CA	Calcium alginate
CB	Carbon black
CB	Conduction band
Cs	Chitosan
Ch-DCMC	Chitosan-dialdehyde carboxymethyl cellulose
CIF	Crystallography information file
CSD	Cambridge structured database
DAMH	Diaminomaleonitrile
DI	Deionised
DSC	Differential scanning calorimetry
EC	Electrothermal
ED	Ethylenediamine

EDS	Energy dispersive spectroscopy
EDTA	Ethylenediamine tetra acetic acid
EDX	Energy dispersive X-ray
EG	Ethylene glycol
ET-AAS	Electro-thermal atomic absorption spectroscopy
FAAS	Flame atomic absorption spectroscopy
FE-SEM	Field emission electro microscopy
FIB-SEM	Focused ion beam electron microscopy
FTIR	Fourier transform infrared spectroscopy
GA	Glutaraldehyde
GCE	Glassy carbon electrode
glygly	Glycylglycine
GO	Graphene oxide
HOMO	Highest occupied molecular orbital
HP	Heterogeneous photocatalysis
ICP-AES	Inductively coupled plasma atomic emission spectroscopy
ICP-MS	Inductively coupled plasma mass spectroscopy
ICP-OES	Inductively coupled plasma optical emission spectroscopy
IIPs	Ion-imprinted polymers
ILAG	Ion and liquid assisted grinding
IP	Ion imprinting
IR	Infrared

LAG	Liquid-assisted grinding
LDH	Layered-double hydroxide
LOD	Limit of detection
LUMO	Lowest unoccupied molecular orbital
MB	Methylene blue
MCMSPE	Mechanochemical magnetic solid phase extraction
MIL	Material institut Lavoisier
MOFs	Metal-organic frameworks
MO	Methylene orange
MxMOFs	Mixed linker MOFs
NIP	Non imprinted polymer
NRF	National research foundation
OG	Orange G
OTC	Oxytetracycline
PAN	Polyacrylonitrile
PDE%	Photodegradation efficiency
PET	Polyethylene terephthalate
PFO	Pseudo first order
PGMs	Platinum group metals
PMT	Photoelectron multiplier tube
PPCPs	Pharmaceutical and personal care products
PSM	Post synthetic modification

PSO	Pseudo second order
Pyta	Pyridyltriazol
PZC	Point of zero change
RBB	Remazol black B
REE	Rare earth elements
ROS	Reactive oxygen species
SA	Sodium alginate
SBUs	Secondary building units
SEM	Scanning electron microscopy
STA	Simultaneous thermal analysis
TEM	Transmission electron microscopy
TEPA@CA	Tetraethylenepentamine@calcium alginate
TGA	Thermogravimetric analysis
UMC	Unsaturated metal centers
UV	Ultraviolet
UV-Vis	Ultraviolet-visible spectroscopy
VB	Valence band
XPS	X-ray photoelectron spectroscopy
XRD	X-ray diffraction
ZIF	Zeolitic imidazolate framework

LIST OF SYMBOLS

%T	Percentage transmittance
∆G°	Free Gibbs energy change
∆H°	Enthalpy change
∆S°	Entropy change
1D	One dimensional
2D	Two dimensional
3D	Three dimensional
A	Absorbance
a	Absorbility constant
As	Arsenic
Au	Gold
b	Path length of a cell
BE	Binding energy
C	BET constant
C	Molar concentration and Carbon
c	Speed of light and concentration of analyte
Cads	Adsorbed concentration
Cd	Cadmium
Ce	Equilibrium concentration
Cl	Chlorine
Co	Cobalt

Co	Initial concentration
Cr	Chromium
Ct	Concentration at specific time
Cu	Copper
d	Spacing of diffracting planes
D	Crystallite size
dT	change in temperature
dt	Change in time
Eg	Energy band gap
E	Energy
Ɛ	Molar absorptivity
Fe	Iron
h	Planck constant
He	Helium
Hg	Mercury
H	Hydrogen
Ir	Iridium
k_1	First order rate coefficient
k_2	Second order rate coefficient
KE	Kinetic energy
Keq	Equilibrium constant
KF	Freundlich adsorption constant

ki	Intra–particle diffusion rate constant
KL	Langmuir adsorption constant
La	Lanthanide
Li	Lithium
M	Molar
Mn	Manganese
Mo	Molybdenum
n	Specific amount of the gas absorbed
N	Nitrogen
Ni	Nickel
nm	Monolayer capacity of the gas absorbed
ɵ	Diffraction angles
Os	Osmium
P	Partial vapour pressure
Pb	Lead
Pd	Palladium
Po	Saturated pressure
Ppm	Parts per million
Pt	Platinum
qe	Equilibrium adsorption capacity
qm	Maximum adsorption capacity
qt	Adsorption capacity at a specific time

RBB	Remazol Black B
R6G	Rhodamine 6G
REE	Rare earth elements
Rh	Rhodium
RhB	Rhodamine blue
RL	Separation factor
Ru	Ruthenium
S	Sulphur
Se	Selenium
Sn	Tin
T	Temperature
Tg	Glass transition temperatures
Th	Thorium
U	Uranium
v	Frequency of the light
V	Volume of adsorbed gas
Vm	Monolayer volume
wt%	Weight percentage
Zn	Zinc
Zr	Zirconium
β	Constant heating rate and Scherrer constant
ϵ	Lattice strain

θ	Diffraction angle
λ	: wavelength
ρ	Dislocation density
φ_{spec}	Spectrometer work function

CHAPTER ONE

INTRODUCTION OF THE THESIS

1.1. BACKGROUND

Platinum group metals (PGMs) are naturally occurring mineral resources that have been widely used in various industries including electronics, catalysis, pharmaceuticals, mining, and others as depicted in Figure 1.1(a) [1][2]. Their growing demand and supply in order to meet the needs of the increasing global population have become a worldwide concern due to the limited availability of mineral ore reserves [2]. Furthermore, during mineral processing, some of the PGMs become highly concentrated in wastewater resulting in acid mine drainage , which has a negative impact on human health and the environment [3]–[5]. With South Africa being the number one producer of these mineral ores, there is a greater chance of increased disposal of industrial effluents into water bodies (see Figure 1.1(b)). As a result, this calls for the need to remove (reduce pollution) and recycle (increase supply) PGMs from wastewater in order to meet the increasing demand as well as protection of the environment. Different hydrometallurgical technologies that have been implemented for the recovery of PGMs include adsorption, solvent extraction, precipitation, membrane filtration, ion exchange, and cloud point extraction [5], [6]. Amongst these methods, adsorption has been identified as the beneficial technology owing to its easiness of operation at low capital cost, fast kinetics, less chemical intake, and flexibility in the merger with other methods [7], [8]. The effectiveness of the adsorption technology requires the selection of suitable adsorbent material.

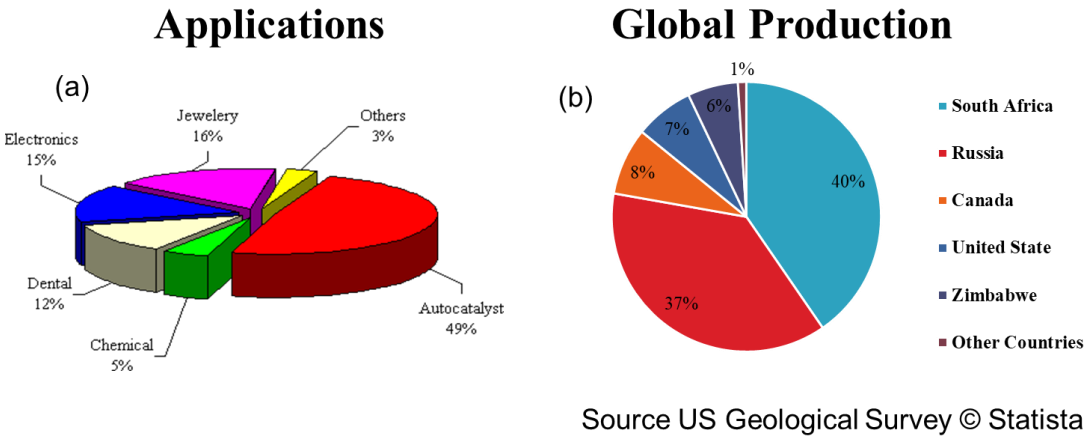

Figure 1.1: (a) Applications of PGMs, and (b) Global production of PGMs.

1.2. PROBLEM STATEMENT

Numerous adsorbent materials for PGMs ions removal such as zeolites, carbon nanotubes, polymers, biomass, and their composite have been explored [9]. For example, Fujiwara and colleagues [10] prepared a chitosan modified L-lysine for the recovery of divalent palladium (Pd(II)) and tetravalent platinum (Pt(IV)) metal ions from aqueous solutions. The composite was able to achieve a maximum adsorption capacity (qm) of 129.26 mg/g for Pt(IV) in acidic media of pH 1.0 and 109.47 mg/g for Pd(II) in pH of 2.0. In another study, Nikoloski *et al*. [11] used three different ion exchange resins (Lewatit M+MP 600, Purolite S985, and XUS 43600.00) to recover the PGMs from spent catalysts. The selectivity of these materials was more specific to palladium (Pd) and (Pt) ions in acidic conditions, however with limited capacities ranging from 0 - 12 g/L for Pt and 0 - 8 g/L for Pd. Another study from the literature reported by Snyders and co-workers [12] demonstrated the influence of temperature on the recovery of Pd, Pt, and gold (Au) by activated carbon (AC). The results revealed that the adsorption of PGMs was not specific in the presence of other metal ions such as nickel (Ni) and copper (Cu) as the temperatures of the systems were varied. Sharififard and co-authors [6] also investigated the adsorption capacity of acid-modified AC towards the uptake of selected PGMs. Their results indicated that 0.02 g

of bio-polymer-modified AC was able to adsorb 43.5 and 52.6 mg/g of Pd and Pt, respectively, in a pH of 2.0. Another example is on the synthesised chitosan cross-linked with dialdehyde carboxymethyl cellulose (Ch-DCMC) reported by Asere *et al.* [3]. The equilibrium data suggested electrostatic interaction between the PGMs with the nitrogen (N) groups on the adsorbent in acidic media and achieved qm values of 80.8 and 89.4 mg/g for Pt and Pd, respectively. In addition, the selectivity of PGMs uptake by the Ch-DCMC was affected by the presence of iron (Fe) metal ions, whereas the regeneration studies revealed the potential application of the Ch-DCMC in 5 subsequent cycles for both Pd and Pt. Nevertheless, most of the adsorbents have low adsorption capacity and poor selectivity of metal ions, low surface area as well as poor recovery of some of the materials [13]. Therefore, it is ideal to develop a material with high surface area, high PGMs uptake, and good selectivity.

1.3. RATIONALE

With the advancement in material science, a new class of crystalline coordination polymers named metal-organic frameworks (MOFs) have attained great attention for a wide range of applications [14]. These porous materials are composed of metal clusters or ions linked together by organic ligands through esterification forming a variety of dimensional structures ranging from 1D to 3D. MOFs offer extensive properties such as high porosity, large surface area, tuneable inner pore size, and vast functional groups for reactivity and have been used in gas sensing [12], hydrogen production and storage [13,14], catalysis [15] as well as in drug delivery [15,16]. In addition, MOFs can be easily prepared from polyethylene terephthalate (PET) plastic waste bottle, which is the source of the key ingredient that serves as the organic ligand called 1,4-benzenedicarboxylic acid (BDC) [16]. The development of a successful process for the use of PET from the waste bottle for the purpose of synthesising MOF materials would offer an economically attractive strategy for waste management [17].

For application in wastewater treatment, the unsaturated metal ions offer potential as an adsorption site [18]. Furthermore, tenability of MOFs by changing the central metal ion or organic linkers can also facilitate the chelation of metal ions and increase the uptake capacity of MOFs and their composites, which is a good prospect for the removal of metal ions from wastewater [18]. Luo *et al*. [19] reported on ethylenediamine-Material Institut Lavoisier (ED-MIL-101) composite for the removal of Pb(II), with the adsorption capacity of 87.64 mg/g. Yuan and co-workers [18] functionalised MIL-101 with glycine derivatives for the removal of Co(II). They obtained the maximum adsorption capacity to be 232.6 mg/g for the triglycine-MIL-101 adsorbent. Magnetite–pyridine/copper benzene-1,3,5-tricarboxylate $Cu_3(BTC)_2$ MOF composite for Pd(II) recovery was reported by Bhageri *et al*. [20] and obtained the maximum adsorption capacity of 105.1 mg/g. Lin *et al*. [21] prepared the University of Oslo UiO-66-NH_2 MOF with the qm of 1.58 and 0.67 mmol/g for Pd(II) and Pt(IV), respectively. Recently, Lim and co-authors reported on the preparation of MIL-101(Cr)-NH_2 by reduction of MIL- 101(Cr)-NO_2 which acquired qm values of 277.6 and 140.7 mg/g for Pd(II) and Pt(IV) ions through electrostatic interaction in acidic media. Although, MOFs have shown promising application for metal ions recovery, selectivity towards targeted metal ions is still a challenge [22]. Hence, ion imprinting (IP) technique offers great potential to improve the selectivity and thus increase the efficiency of MOFs for metal ions adsorption. The process of IP has many attractive features including the selective removal of metal ions over a broad range of pH and temperature, its rapid kinetics of sorption and desorption, low capital and operational costs [23]. The ion-imprinted polymers (IIPs) have been introduced by Nishide *et al*. [22] by cross-linking of poly(4-vinyl pyridine) with 1,4-dibromobutane in the presence of a metal ion. The selectivity of IIPs is governed by creation of metal ion memory or cavity on the surface of the cross-linked polymers using the template of the targeted metal ion. The generated binding sites match the coordination number and geometry, charge and size of the targeted metal ion [22],[23]. Yuan *et al*. [22] synthesised IIP

induced by glycine modified MOF for the removal of divalent cobalt Co(II) ions from aqueous solutions. However, there is no literature on the removal of PGMs by IIP/MOF composites. Hence, this study focussed on the preparation of modified MOF with ion imprinted polymer for the removal of PGMs from wastewater.

1.4. AIMS AND OBJECTIVES

1.4.1. Aim

The aim of the study was to develop an IIP/MOF composite for the recognition and separation of PGMs from wastewater.

1.4.2. Objectives

The objectives of the study were to:

i. synthesise MIL-101(Cr), MIL-101(Cr)/ED, and MIL-101(Cr)/ED-glutaraldehyde (GA).
ii. fabricate PdIPMIL-101(Cr), IPMIL-101(Cr) and NIMIL-101(Cr).
iii. prepare Pt@IIGlyMIL-101(Cr), IIGlyMIL-101(Cr) and NIGlyMIL-101(Cr).
iv. characterize the prepared materials using Fourier transform infrared spectroscopy (FTIR), X-ray diffraction (XRD), thermogravimetric analysis (TGA), Brunauer–Emmet–Teller (BET) and scanning electron microscopy (SEM) fitted with an energy dispersive X-ray spectroscopy (EDS) detector.
v. study the removal efficiencies of the synthesised MIL-101(Cr)/ED towards Pd(II) ions intake.
vi. examine the intake capacity of Pd(II) and Pt(IV) ions by the MIL-101(Cr)/ED-GA.

vii. investigate the adsorption behaviour of IPMIL-101(Cr) and NIMIL-101(Cr) towards the recovery of Pd(II) ions.

viii. compare the adsorption behaviour of the IIGlyMIL-101(Cr) and NIGlyMIL-101(Cr) towards the recovery of Pt(IV) ions.

ix. analyse the concentrations of PGM metal ions before and after adsorption using UV-Vis spectroscopy.

1.5. THESIS OUTLINE

This thesis is aimed at investigating the adsorption efficiencies of the of the prepared IPMIL-101(Cr) and IIGlyMIL-101(Cr) in the selective recovery of Pd(II) and Pt(IV) ions from aqueous solution by comparison with the NIMIL-101(Cr) and NIGlyMIL-101(Cr).

- Chapter one focused on the introduction of the study wherein the background on the PGMs is given based on their uses, production, and potential pollution associated with them. In addition, the chapter summarises the problem statement, motivation, aims, and objectives of the study.
- Chapter two provides a detailed literature review on the various synthetic routes for MOFs including composite formation and their application in various fields. Moreover, the application of MOF composite in the removal of pollutants is discussed with more emphasis on the adsorption of heavy metals including PGMs.
- Chapter three describes the numerous characterisation techniques used in this work for studying the structures of the prepared composites before and after adsorption of heavy metals as well as the analytical methods used in the determination of PGMs concentrations.
- Chapter four focuses on the preparation of MIL-101(Cr)/ED and its removal efficiencies towards the adsorption of Pd(II) ions.

- Chapter five deals with the synthesis and modification of MIL-101(Cr)/ED-GA and its investigations on the adsorption of Pd(II) and Pt(IV) ions from aqueous solutions.
- Chapter six reports on the preparation of the IPMIL-101(Cr) and NIMIL-101(Cr) and their adsorption behaviour towards Pd(II) ions recovery.
- Chapter seven provides details on the synthesis of IIGlyMIL-101(Cr) and NIGlyMIL-101(Cr) and their adsorption efficiencies in the recovery of Pt(IV) ions.
- Chapter eight provides a summary of the whole study and draws some conclusions based on the obtained results as well as suggestions on future recommendations.

1.6. REFERENCES

[1] M. H. Morcali, B. Zeytuncu, S. Akman, and O. Yucel, “Desalination and Water Treatment Preparation and sorption behaviour of DEAE-cellulose- thiourea-glutaraldehyde sorbent for Pt(IV) and Pd(II) from leaching solutions,” pp. 37–41, 2015, doi: 10.1080/19443994.2015.1010591.

[2] M. Chen, S. Li, C. Jin, M. Shao, Z. Huang, and X. Xie, “Removal of metal-cyanide complexes and recovery of Pt (II) and Pd (II) from wastewater using an alkali – tolerant metal-organic resin,” *J. Hazard. Mater.*, vol. 406, p. 124315, 2021, doi: 10.1016/j.jhazmat.2020.124315.

[3] T. G. Aserea, S. Mincke, K. Folens, F. V. Bussche, L. Lapeire, K. Verbeken, P. Van Der Voort, D. A. Tessema, G. Du Laing, C. V. Stevens, “Dialdehyde carboxymethyl cellulose cross-linked chitosan for the recovery of palladium and platinum from aqueous solution,” *React. Funct. Polym.*, vol. 572, pp. 428–441, 2019, doi: 10.1016/j.seppur.2015.01.023.

[4] J. Lee, H. Hong, K. Woo, and S. Kim, “Separation of platinum , palladium and rhodium from aqueous solutions using ion exchange resin : A review,” *Sep. Purif. Technol.*, vol. 246, p. 116896, 2020, doi: 10.1016/j.seppur.2020.116896.

[5] H. Zheng, Y. Ding, Q. Wen, B. Liu, and S. Zhang, “Separation and purification of platinum group metals from aqueous solution: Recent developments and industrial applications,” *Resour. Conserv. Recycl.*, vol. 167, p. 105417, 2021, doi: 10.1016/j.resconrec.2021.105417.

[6] H. Sharififard, M. Soleimani, and F. Z. Ashtiani, “Evaluation of activated carbon and bio-polymer modified activated carbon performance for palladium and platinum removal,” *J. Taiwan Inst. Chem. Eng.*, vol. 43, pp. 696–703, 2012, doi: 10.1016/j.jtice.2012.04.007.

[7] S. Lin, Y. Zhao, J. K. Bediako, C. Cho, and A. K. Sarkar, “Structure-controlled

recovery of palladium(II) from acidic aqueous solution using metal-organic frameworks of MOF-802 , UiO-66 and MOF-808," *Chem. Eng. J.*, vol. 362, pp. 280–286, 2019, doi: 10.1016/j.cej.2019.01.044.

[8] B. G.- Ż and J. Malejko, "Appraisal of Biosorption for Recovery , Separation and Determination of Platinum , Palladium and Rhodium in Environmental Samples," pp. 33–52, doi: 10.1007/978-3-662-44559-4.

[9] E. Aghaei, "Magnetic Adsorbents for the Recovery of Precious Metals from Leach Solutions and Wastewater," pp. 1–32, 2017, doi: 10.3390/met7120529.

[10] K. Fujiwara, A. Ramesh, T. Maki, H. Hasegawa, and K. Ueda, "Adsorption of platinum(IV), palladium(II) and gold(III) from aqueous solutions onto L-lysine modified crosslinked chitosan resin," vol. 146, pp. 39–50, 2007, doi: 10.1016/j.jhazmat.2006.11.049.

[11] A. N. Nikoloski, K. Ang, and D. Li, "Hydrometallurgy Recovery of platinum , palladium and rhodium from acidic chloride leach solution using ion exchange resins," *Hydrometallurgy*, vol. 152, pp. 20–32, 2015, doi: 10.1016/j.hydromet.2014.12.006.

[12] C. A. Snyders, S. M. Bradshaw, G. Akdogan, and J. J. Eksteen, "Hydrometallurgy The effect of temperature , cyanide and base metals on the adsorption of Pt , Pd and Au onto activated carbon," *Hydrometallurgy*, vol. 149, pp. 132–142, 2014, doi: 10.1016/j.hydromet.2014.07.012.

[13] M. Sha, M. Sheikh, A. Rashidi, and A. Samimi, "Synthesis and adsorption performance of a modi fi ed micro-mesoporous MIL-101(Cr) for VOCs removal at ambient conditions," vol. 341, pp. 164–174, 2018, doi: 10.1016/j.cej.2018.02.027.

[14] M. Salarian and A. Ghanbarpour, "A metal-organic framework sustained by a nanosized Ag12 cuboctahedral node for solid-phase extraction of ultra traces of

lead (II) ions," pp. 999–1007, 2014, doi: 10.1007/s00604-014-1200-2.

[15] C. M. Granadeiro, A. D. S. Barbosa, P. Silva, F. A. Almeida Paz, V. K. Saini, J. Pires, B. de Castro, S. S. Balula, L. Cunha-Silva "General Monovacant polyoxometalates incorporated into MIL-101(Cr): novel heterogeneous catalysts for liquid phase oxidation," *"Applied Catal. A, Gen.*, vol. 453, pp. 316–326, 2013, doi: 10.1016/j.apcata.2012.12.039.

[16] D. Senthil Raja, C. C. Pan, C. W. Chen, Y. H. Kang, J. J. Chen, and C. H. Lin, "Synthesis of mixed ligand and pillared paddlewheel MOFs using waste polyethylene terephthalate material as sustainable ligand source," *Microporous Mesoporous Mater.*, vol. 231, pp. 186–191, 2016, doi: 10.1016/j.micromeso.2016.05.035.

[17] X. Dyosiba, J. Ren, N. M. Musyoka, H. W. Langmi, M. Mathe, and M. S. Onyango, "Preparation of value-added metal-organic frameworks (MOFs) using waste PET bottles as source of acid linker," *SUSMAT*, vol. 10, pp. 10–13, 2016, doi: 10.1016/j.susmat.2016.10.001.

[18] G. Yuan, H. Tu, M. Li, J. Liu, C. Zhao, J. Liao, Jiali, Y. Yang, J. Yang, Jijun, N. Liu, Ning "Glycine derivative-functionalised metal-organic framework (MOF) materials for Co(II) removal from aqueous solution," *Appl. Surf. Sci.*, vol. 466, pp. 903–910, 2019, doi: 10.1016/j.apsusc.2018.10.129.

[19] X. Luo, L. Ding, and J. Luo, "Adsorptive Removal of Pb(II) Ions from Aqueous Samples with Amino-Functionalisation of Metal − Organic Frameworks MIL-101 (Cr)," vol. 101, 2015, doi: 10.1021/je501115m.

[20] A. Bagheri, M. Taghizadeh, M. Behbahani, and A. Akbar, "Synthesis and characterisation of magnetic metal-organic framework (MOF) as a novel sorbent , and its optimization by experimental design methodology for determination of palladium in environmental samples," *Talanta*, vol. 99, pp. 132–139, 2012, doi:

10.1016/j.talanta.2012.05.030.

[21] S. Lin, J. K. Bediako, C. Cho, M. Song, Yu. Zhao, J. Kim, J. C. Yun, “Selective adsorption of Pd(II) over interfering metal ions (Co(II), Ni(II), Pt(IV)) from acidic aqueous phase by metal-organic frameworks,” *Chem. Eng. J.*, vol. 345, pp. 337–344, 2018, doi: 10.1016/j.cej.2018.03.173.

[22] G. Yuan, H. Tu, M. Li, J. Liu, C. Zhao, J. Liao, Jiali, Y. Yang, J. Yang, Jijun, N. Liu, Ning “A novel ion-imprinted polymer induced by the glycylglycine modi fied metal- organic framework for the selective removal of Co(II) from aqueous solutions,” *Chem. Eng. J.*, vol. 333, pp. 280–288, 2018, doi: 10.1016/j.cej.2017.09.123.

[23] B. Le, B. G.- Ż, and A. Z. Wilczewska, “Separation and preconcentration of trace amounts of Cr(III) ions on ion imprinted polymer for atomic absorption determinations in surface water and sewage samples,” vol. 105, pp. 88–93, 2012, doi: 10.1016/j.microc.2012.08.014.

[24] M. Roushani, S. Abbasi, H. Khani, and R. Sahraei, “Synthesis and application of ion-imprinted polymer nanoparticles for the extraction and preconcentration of zinc ions,” *FOOD Chem.*, vol. 173, pp. 266–273, 2015, doi: 10.1016/j.foodchem.2014.10.028.

CHAPTER TWO

METAL–ORGANIC FRAMEWORKS FOR HEAVY METAL REMOVAL FROM WATER

2.1. INTRODUCTION

Members of the platinum group elements/metals (PGE/Ms) are economically valuable metals which are very popular for a variety of uses worldwide. This is due to various chemically and physically inherent properties that PGMs have such as very high melting points, chemical inertness to most compounds even at elevated temperatures, corrosion resistance and catalytic behaviour [1,2]. These PGMs including platinum (Pt), palladium (Pd), ruthenium (Ru), rhodium (Rh), osmium (Os) and iridium (Ir) occur together in nature (in combination with minor gold (Au)) [2]. Amongst them, the most widely used in industries such as automotive, electronics, hydrogen fuel cells, jewellery and oil refineries are Pt, Pd and Ru [3]. PGMs are dominantly produced in South Africa from the Bushveld complex, followed by other countries such as Russia, Canada, Zimbabwe and United States of America [1-3]. However, the increasing demand for PGMs as a result of increasing population has put a strain on the available scares reserves which poses concerns for future [4-6]. Moreover, the possibility of environmental issues such as water and land pollution, affecting the health of human beings and animal has been realisedd [4,7-9]. Hence, it is essential to recover PGMs from mining wastewater prior to being released into the environment. The recovery of PGMs has led to the development of many separation techniques such as solvent

extraction, chemical precipitation, ion-exchange, photocatalytic degradation and membrane technology (Figure 2.1) [8]. Nevertheless, some of the traditional technologies possess several drawbacks such as insufficient recovery, generation of harmful by-products, high capital cost and poor selectivity [10]. Adsorption technology has been identified as the beneficial technology owing to its easiness of operation at low capital cost, ability to regenerate spent adsorbent, generation of less secondary products, fast kinetics and flexibility to merger with other methods [6,11]. The success of the adsorption process requires the careful selection of a suitable adsorbent material.

Metal organic frameworks (MOFs) are coordination polymers which have emerged as nanomaterials with interesting physical and chemical properties including tuneable pore size and pore character, less density, higher surface area, elevated thermal stability, enormous porosity, and abundant active functional sites [12,13]. These properties have led to the application of MOFs in various fields as catalysts, gas sensors, nonlinear optics, gas storage and drug delivery materials [13-15]. Recently, MOFs have also found new application as adsorbent materials for the removal of pollutants such as metal ions, organics and pathogens from wastewater owing to their enormous surface area [11,13,16,17]. This can serve as adsorption active site and incredible porosity which allows dissemination of pollutants over the framework [18]. However, poor selectivity by MOFs towards PGMs in the presence of interfering ions is still a challenge [10]. Ion imprinting has appeared as a promising technique to

fabricate adsorbent materials which are highly selective towards targeted metal ions [19,20]. In this Chapter, MOFs as new materials are introduced and discussed in detail, from their various synthetic routes to the different composites and nanocomposites that can be formed. This is followed by the discussion of several applications of MOFs that have been studied including application in wastewater treatment, with more focus on adsorption of metal ions. Furthermore, we describe the challenges faced by MOF and the possibility of addressing the limitation through the employment of ion imprinting method. Finally, we summarise and give a future perspective for realisation of MOFs as ion imprinted adsorbents.

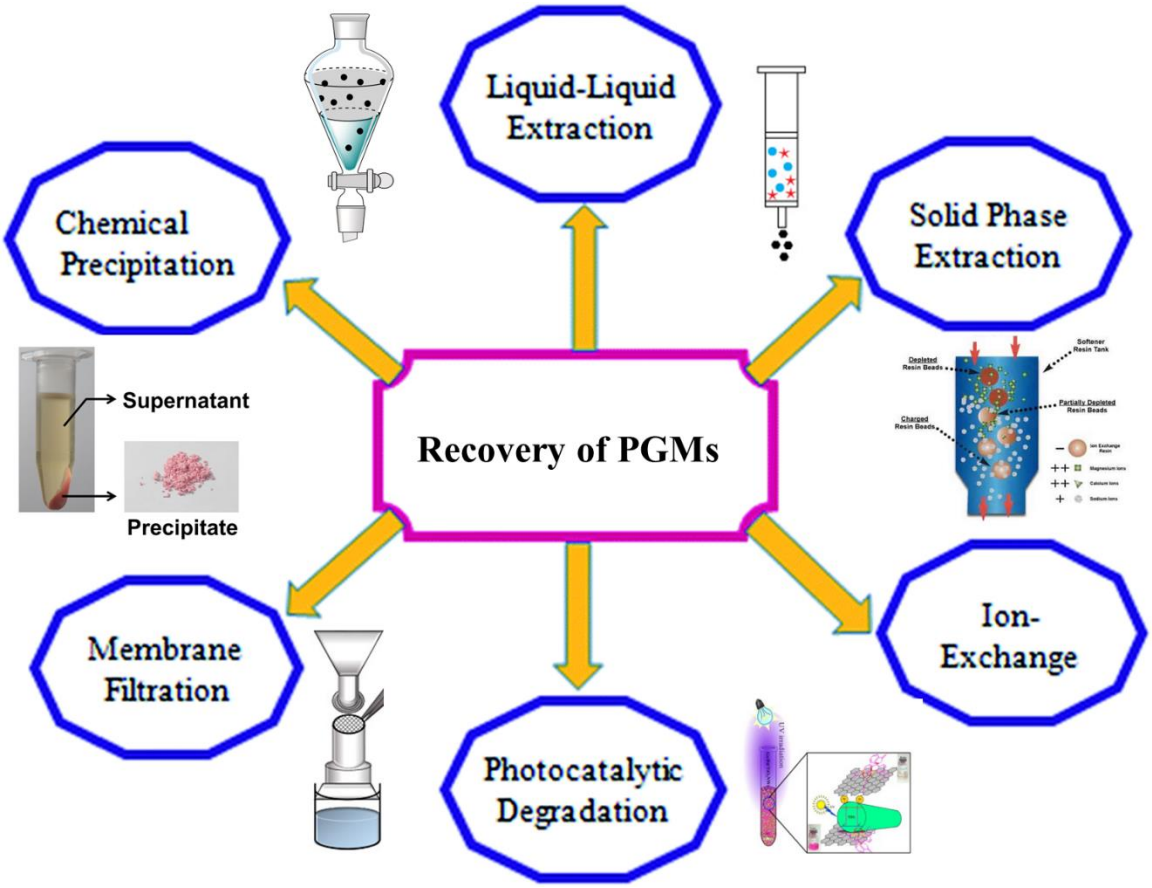

Figure 2.1: Methods used for platinum group metals recovery.

2.2. METAL ORGANIC FRAMEWORKS

2.2.1. Background

The metal organic framework first arose through the study of Zeolites [21]. The term metal organic framework was first introduced by Yaghi in 1995 for the newly synthesised copper-4,4'-bipryridal complex that exhibited extended metal-organic interactions [18,22]. Essentially, MOFs belong to the general family of coordination polymers. MOFs are more specific for one- ,two- or three-dimensional crystallized networks with porous property when compared to the general coordination polymers [23,24]. Since the beginning of millennium, there is exponential growth of interest in the preparation of MOFs and publications. As shown in Figure 2.2(a) represents Scopus database from 1998–2019 showing a significant increase in the number of publications on MOFs in general as well as articles of MOFs for heavy metal adsorption [16]. It was seen in Figure 2.2(b) that over 4500 MOF structures have been published in the Cambridge Structural Database (CSD) from 1970 to 2015 [25]. These MOFs as novel type of porous crystalline materials have attracted increasing attention in water treatment applications due to their high surface area, permanent porosity and controllable structures [12,18,26].

The structure of MOFs as shown in Figure 2.2(c), indicates that the metal nodes function as joining points and the organic linkers work as bridging ligands. The framework of the two components is detained together by covalent bonds to form

extended 3-D infinite network structures [24,27]. The defined crystallinity of MOFs allows for identification of the exact positions of all atoms in the framework. By definition, a porous solid is one in which permanent channels or pores permeate the structure and have dimensions large enough to allow solvent or other guest molecules to diffuse into the structure. The porosity and structure is maintained even when guest particles/compounds within the channels are removed by heating or vacuum [28]. Furthermore, the MOF structures are highly tuneable by varying the metal nodes or organic ligands which makes it possible to obtain a tailor-made MOF materials with the required structures and functionalities for specific application [29,30]. The porosity of known MOFs varies between 20 and 95 percent, where it is measured as the ratio of the accessible pore volume to the total volume of the solid [22]. This porosity relates to high internal surface areas, allowing for increased adsorption of guest molecules. As a result, MOFs have attracted considerable attention due to high surface area and porosity, tuneable structure, and functionality [21,31].

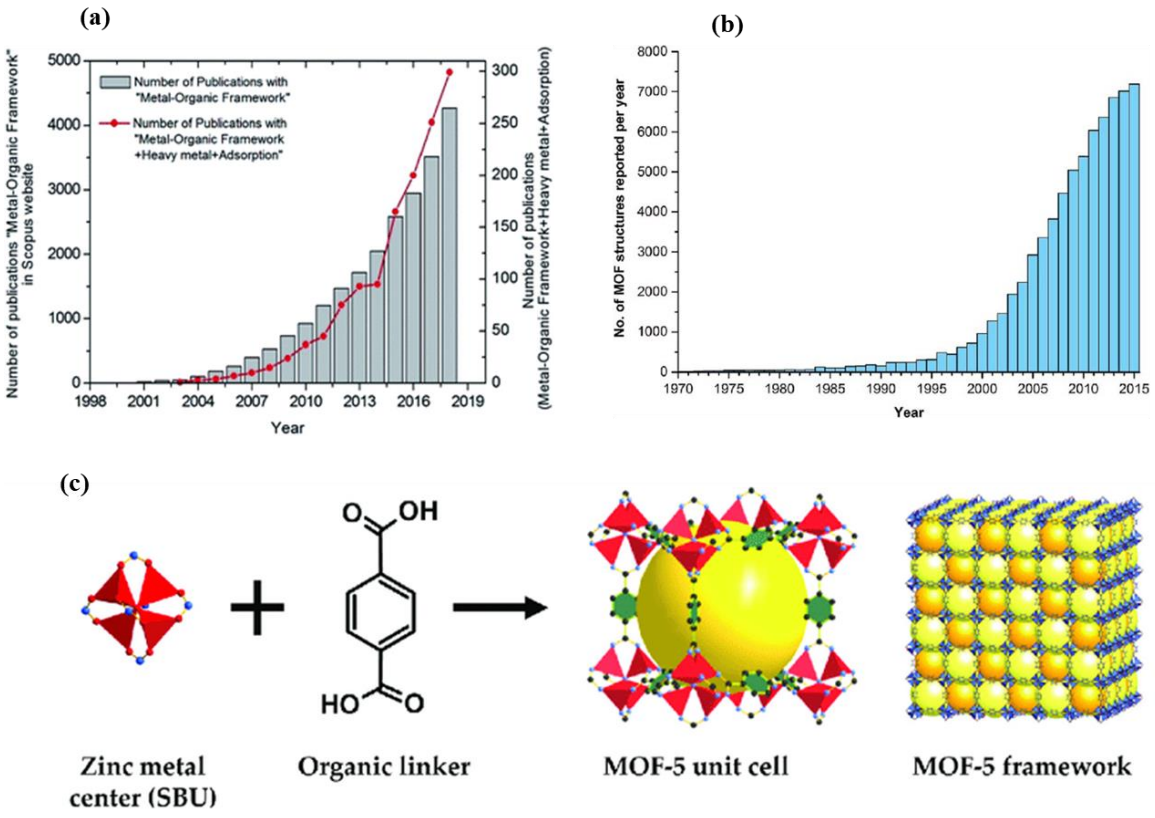

Figure 2.2: (a) graph of number of MOFs published per year since 1998 to 2019 [16]; (b) the change in percentage of the MOFs in the overall Cambridge Structural Database (CSD) since 1970 to 2015 [25]; and (c) Metal organic framework structure [27].

2.2.2. Different Structures of MOFs

The structural arrangement in MOFs extends from one- to two- and three- dimensional (1-D, 2-D and 3-D) networks, which are assembled from organic linkers and metal ion or cluster nodes [32]. For 1-D MOF geometries, the bonds between metal clusters and organic linkers form a one directional expansion throughout the polymer with the probable cavities being occupied by molecules of smaller size. 2-D MOF polymers are composed of single type layers superimposed from either preceding edges or

staggered type layers which are stacked by weak interactions existing between layers. Ligands modification constituting the layers are able to governor the way in which channel interiors stack and function [24]. The two possible ways in which 2-D MOF structures can accommodate guest species are; through the spaces found amongst the grids of layers and in between the layers. The structural frameworks of 3-D MOFs have high porosity and stability as a result of the spreading of coordination bonds in three directions and is common in many MOFs [33,34], as shown in Figure 2.3(a-l). The coordination that results into the above geometries (between metal ions and organic ligands) is facilitated by the non-covalent π-π stacking and hydrogen bonds. These interactions are responsible for converting the framework in MOFs to an infinitely dimensional network, as well as controlling their strength and direction. Moreover, the metal ion geometries have a great effect on the structures of MOF polymers [33].

Metal sites (referred as unsaturated metal sites or accessible metal sites) in MOFs have tremendous influence on their adsorption properties. The metal ions as the centre connectors are usually chosen from transition metals such as Cu, Zn, Mn, Co etc. The metals in the MOF structure often serve as Lewis acids which can activate the coordinated organic ligands for succeeding organic transformation [33-36]. The partially positive charges of metal sites in MOF structure have been proved to increase adsorption capacity [36,37]. The commonly used transition metals give different

geometries depending on their number of oxidation state [38,39]. Below are the commonly observed geometries of each metal and also in Figure 2.3(a-l):

a. Copper-electron configuration of zero-valent metal is $[Ar]3d^{10}4s_1$. Copper nodes are often in distorted octahedral and square-planar geometries. The distortion occurs mainly due to Jahn-Teller distortion commonly resulting in octahedral geometries having four short bonds and two longer bonds as the dz^2 orbital is filled whilst the dx^2-y^2 orbital is only partially filled.

b. Cobalt-electron configuration of the zero-valent metal is $[Ar]3d^74s^2$. There is a range of common coordination numbers for Co^{2+}. Geometries of cobalt(II) nodes are generally octahedral and tetrahedral.

c. Nickel-electron configuration of the zero-valent metal is $[Ar]3d^84s^1$. The most prevalent nickel geometries are octahedral and square-planar with consistent bond lengths.

d. Manganese-electron configuration of the zero-valent metal is $[Ar]3d^54s^2$. Manganese (II) compounds take on a range of coordination modes and geometries in metal-organic frameworks, the most common being octahedral.

e. Zinc-electron configuration of the zero-valent metal is $[Ar]3d^{10}4s^2$. Zinc(II) compounds often take up octahedral or tetrahedral geometries.

The organic linkers used to connect the metal nodes in coordination polymers are usually multidentate organic molecules [33]. The linkers contain aromatic rings in

frameworks, which help maintain the structural integrity of the complex and direct the geometry of the framework. The pore volume and surface area of MOFs can be organized by modifying organic ligands which act as spacers and create an open porous structure. The common organic linkers are shown in Figure 2.3 [40].

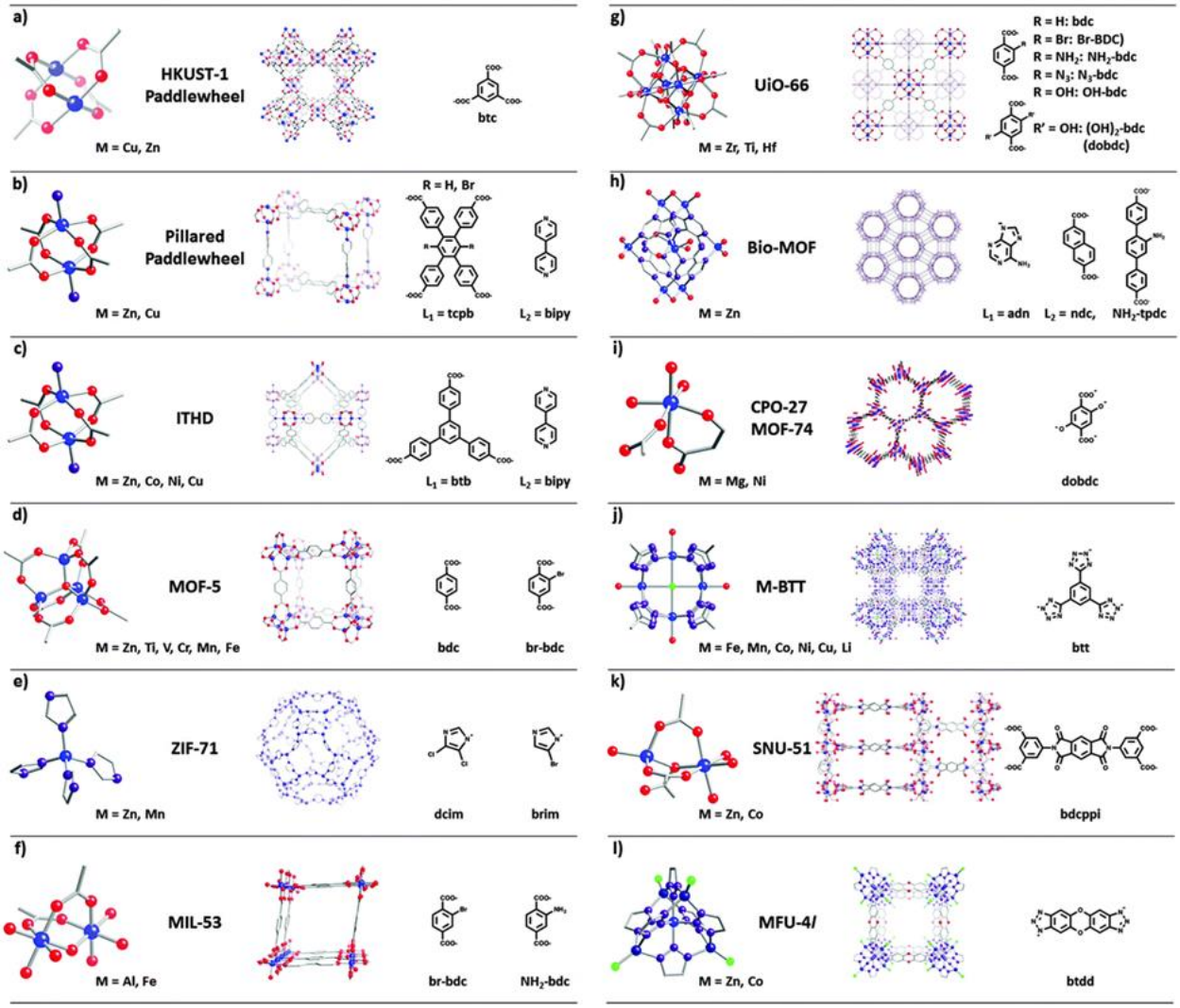

Figure 2.3: Lattice structures (middle) and corresponding SBUs (metal nodes (left), and organic linkers (right) of some of the MOFs discussed in this review. (Atom definition: blue-metal, red-oxygen, purple-nitrogen, grey-carbon, green-chlorine) [40].

Secondary Building Units (SBUs) play an important role as they dictate the final geometry of MOFs. The structure and chemical properties of the SBUs and organic ligands lead to the prediction of the schemes and preparations of MOFs [41]. Literature reports have shown that under careful selection of reaction preconditions, multidentate linkers can aggregate and thus locking metal ions at definite location to form SBUs [42]. The SBUs will subsequently join with rigid organic links to produce MOFs that exhibit high structural stability [24,41]. It was reported that the structure of the SBU is controlled by the metal-to-ligand ratio, solvent used as well as source of anions used in balancing metal ions charges [37,43]. Since the structure of MOF polymers are governed by SBUs geometries and organic linkers (shape and size), they are tuneable to a certain degree by careful selection of SBUs and organic ligands having appropriate pore size, structure, and functionality for the precise application.

MOFs have gained interest in studies having adsorption applications because they have easily modifiable surface pores which can lead to improved selectivity in adsorbing certain guest species with specific functional groups [11,44]. Hence, they have been extensively explored for the adsorption of numerous toxic materials which are organic and inorganic in nature. The ability of MOFs to remove pollutants from the environment is owed to their enormous porosity and incredible geometry of the pores. Furthermore, some of the MOF components that have been effectively employed to improve the adsorption interactions include coordinatively unsaturated metal sites, functionalised ligands and added active species. These properties make MOF

materials to have better adsorption performance than most porous materials towards toxic species [11].

2.2.3. Physical Properties of MOFs

MOFs are prominent due to their capability to convey various functionality through appropriate selection of the metal ions and organic ligands. Various studies available in literature have already demonstrated a number of synthesis methods for tuning the chemistry, stability, particle size, and flexibility of MOF structures [45]. Moreover, these coordination polymers can be further improved by “post-synthetic modification” for further tuning the properties by swapping, altering, or by removal of the ligand or metal ion from the structure. The mechanical properties of MOFs can be modified by introducing malleable ligands, modulating the strength of host-guest interactions, constructing multi-metallic framework and manipulating the size of crystals.

The most important property in designing MOFs is the stability. MOF polymers have to be stable in order for them to be characterized fully and be applied in various fields like adsorption, catalysis and sensing [46]. The stabilities in the MOFs include chemical, thermal, hydrothermal and mechanical. To improve the chemical stability of MOF polymers, metal clusters having higher valence such as Cr^{3+}, Fe^{3+}, and Zr^{4+} are used, together with soft ligands including triazolates, imidazolates and tetrazolates [34,36,47]. Furthermore, heterocyclic molecules containing nitrogen atoms can be

utilised in the preparation of MOFs together with soft divalent metal clusters like Zn^{2+}, or Co^{2+} to increase the stability. The thermal stability of MOFs shows degradation when metal-ligand bond breaks and the organic linkers get combusted [46]. This can however be improved by coordination of oxy-anions ligands to high valance metal ions [36]. On the other hand, the hydrothermal stability of MOF refers to the stableness of a materials in the existence of moisture at higher temperatures, and it was also shown that it can be improved by introduction of hydrophobic functional groups into the MOF framework [48,49]. The mechanical stabilities in MOF materials directly linked to their high porosity and they have an inversely proportional relationship. This type of stability is elevated in MOFs that have solvent-filled pores than in those that have vacant pores [36,46]. Figure 2.4 depicts various MOF materials with improved BET results. It was shown that MOF-177 possessed highest surface area in 2004 with BET surface area of 3780 m^2/g and porosity of 83% in 2007 [50]. Later in 2010, the surface area was doubled by MOF-200 and MOF-210 produced surface areas of 4530 and 6240 m^2/g; and porosities of 90 and 89%, respectively [51,52]. On the other hand, in 2007, MOF-5 material showed a surface area of 3800 m^2/g owing to active adsorption sites from zinc oxide SBU and the edges of the organic linker [52]. Furthermore, it has been reported that expanded tritopic linkers based on alkyne rather than phenylene units should increase the number of adsorption sites and lead to enhance the surface area [51]. NU-110 MOFs in 2012 have demonstrated a high surface area of 7140 [50]. Whereas UiO-66(Zr), MIL-100(Cr), MIL-101(Cr) and HKUST-1 showed a BET surface

of 1473, 1842, 3250 and 2642 m^2/g in 2013-2019, respectively [38,53,54]. For application in wastewater treatment a number of MOFs polymers which are water-stable such as chromium-based MIL-101 series [38,53,54], zeolitic imidazolate frameworks (ZIFs) [55], zirconium-based carboxylates [56], aluminum-based carboxylates and pyrazole-based MOFs have been reported [16,49]. These materials have improved stability which was achieved by increasing the coordination bonds strength of SBUs to organic ligands [49,37,57].

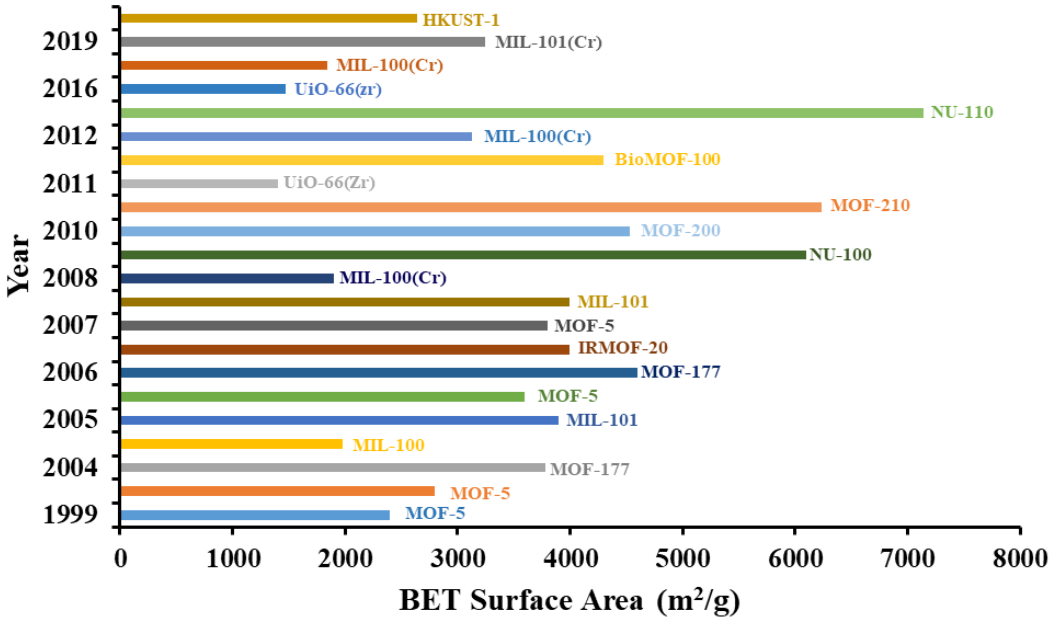

Figure 2.4: BET surface areas of MOFs and typical conventional materials were estimated from gas adsorption measurements.

2.2.4. Synthesis of MOFs

There are numerous methods that are available for the synthesising MOFs. Many of these methods takes place in liquid phase which involves the mixing of metal salt and ligand in a suitable solvent or preparing their solutions separately before mixing them. The important part in synthesising MOFs with good properties is choosing a proper solvent by looking at features such as redox potential, reactivity, stability constant and solubility [58]. Figure 2.5 illustrates a summary of several approaches for the preparation of MOFs. The main aspects purpose of investigating different methods of MOF preparations are to determine the synthetic routes which can result in a distinct inorganic building units without disintegration of the organic ligand. In this chapter, more focus is given to the selected preparation methods for synthesis of MOF structures and some are illustrated in Figures 2.5 and 2.6(a-c).

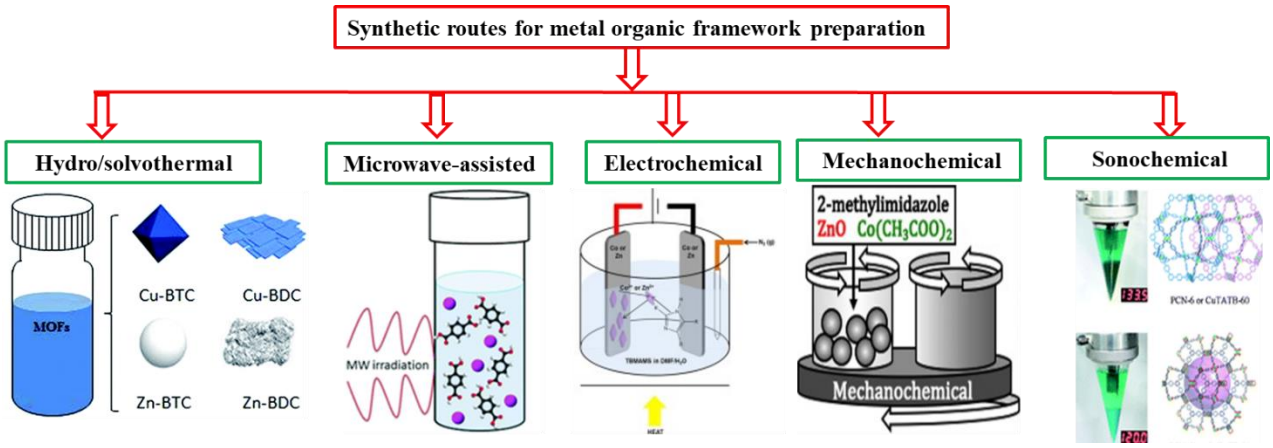

Figure 2.5: Overview of synthesis methods for preparation of MOFs.

2.2.4.1. Hydro/Solvothermal Method

The hydro/solvothermal process has been effectively implemented in preparing MOFs that exhibiting nanoscale structural morphologies which are unattainable by traditional

techniques [33,59]. The important parameters in the preparation of MOFs are temperature, the choice of metal and organic linker, concentration of metal salt, and the solubility of the reactants [39]. The metal ions in this case are coordinated via functional groups of organic linker to create a three-dimensional porous paddle-wheel-like unit with a cubic structure. In addition, the use of traditional preparation schemes has often resulted in powdered MOFs with low densities. However, the low density property is not suitable for hydrogen storage as MOFs require high volume for hydrogen storage density with improved stability in humid and reactive environments, which are unavailable in slack powdered materials [60,61]. Hydrothermal method is usually carried out in a stainless steel autoclave as shown in Figure 2.6(a). The method permits a precise regulation on the size and shape of the material to be synthesised, unlike conventional method [36,62]. For example, Figure 2.6(d) shows schematic representation for the synthesis of ZIFs prepared by solvothermal techniques. It was seen that crystals slowly developed after heated solution of a hydrated metal salt, imidazole organic linker, and solvent [63]. This process is ideal for generating monocrystalline MOF materials.

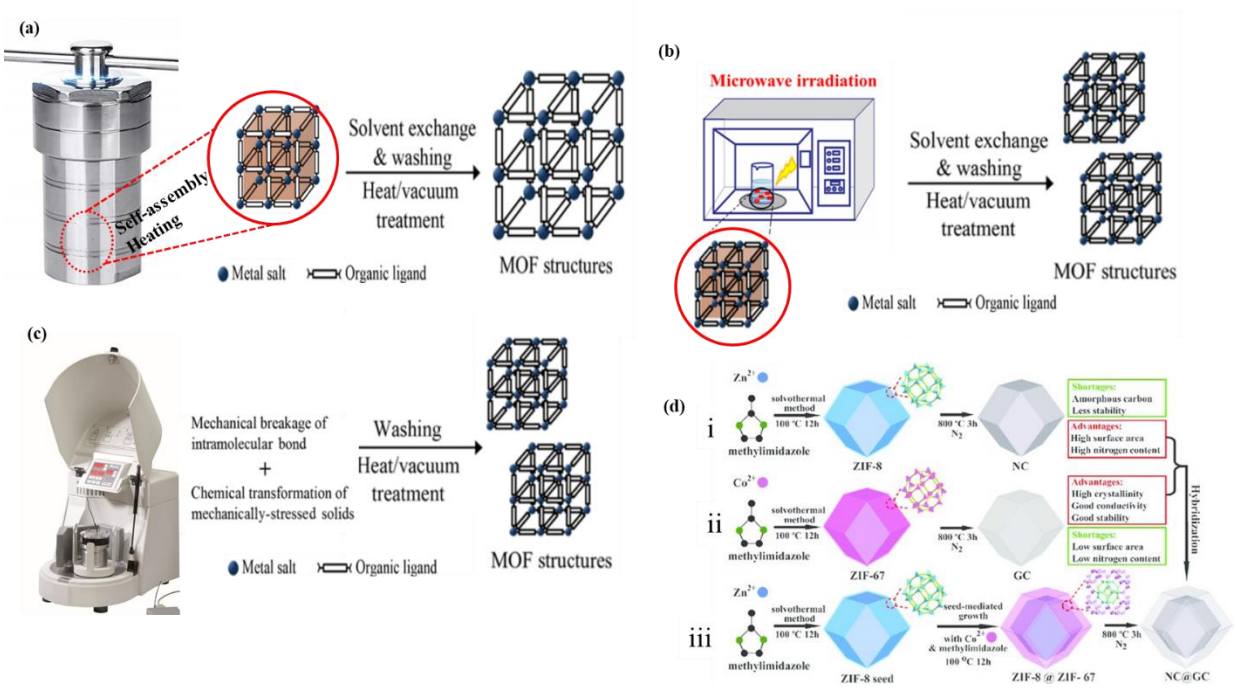

Figure 2.6: (a) Hydrothermal synthesis of MOFs structures, (b) microwave-assisted solvothermal preparation of MOF structures and (c) mechanochemical synthesis of MOF structures (d) Schematic representation for the preparation of (i) MOFs (ZIF-8) (ii) ZIF-67 crystals and NC@GC, and core-shell ZIF-8@ZIF-67 crystals and (iii) NC@GC via a conventional solvothermal method [61].

2.2.4.2. Microwave/Ultrasonic Method

Microwave-synthesis technique has demonstrated to be an appealing route for fast preparation of nanostructured porous materials through hydrothermal conditions [35,64]. In addition to the rapid crystallization and high efficiency, this method offers potential advantages such as phase selectivity, narrow particle size distribution, and facile morphology control [33]. The microwave-assisted synthesis, involves heating a substrate mixture in a suitable solvent with microwave for an hour in order to yield

nanosized crystals (Figure 2.6(b)). The quality of the crystals produced by microwave-assisted process matches that produced by the ordinary solvothermal methods, however it is much faster [64].

2.2.4.3. Electrochemical Synthesis

The method of synthesising MOFs electrochemically was initially described by BASF researchers in 2005 [33,36]. Electrochemical synthesis was developed in order to avoid the effects of anions from the metal salts such as nitrates, chlorides and perchlorates. As a result, this method offered simplicity, high purity of the produced materials and process controllability [33,36,65]. The process in electrochemical synthesis involves continuous introduction of metal ions instead of their salts into the anodic dissolution which them moves through the reaction medium to interact with the dissolved organic linkers at the cathode in the electrolyte [33,65,66]. To prevent metal from being deposited onto the cathode, protic solvents and compounds like acrylonitrile, acrylic, or maleic esters were used and H_2 gas was released during the process [23,61,65]. Furthermore, electrochemical synthesis offers an opportunity carry out a continuous process and attain a high solids content in industrial operation in comparison with normal batch reactions [65,67]. This method provides fast reaction rates and mild conditions which are essential in producing MOF materials in a large scale [36].

2.2.4.4. Mechanochemical Synthesis

Mechanochemical synthetic process is regarded as a solvent-free preparation procedure since it does not require any solvent for MOFs synthesis (Figure 2.6(c)). It proceeds through two steps, wherein the first step involves the mechanical disintegration of intramolecular bonds which is accompanied by chemical transformation [68]. The advantage of this solvent free process is that reactions can proceed at room temperature without the use of an organic solvent. Qualitative yield of small amount of product is obtainable in a short period of time ranging between 10-120 minutes. In several cases, preference of the starting material was metal oxides rather than metal salts as they resulted in water as the only side product [69,70]. In recent years, mechanochemical synthesis has been effectively implemented for the fast preparation of MOFs through the use of liquid-assisted grinding (LAG). This process involves the addition of small amount of solvent into a solid reaction mixture, where it acts as a structure-directing agent. Furthermore, the method was developed to ion and liquid assisted grinding (ILAG) which demonstrated high efficiency for the selective manufacturing of pillared-layered MOFs [65,71]. Nonetheless, the process is restricted to explicit MOF types which cannot produce large amount of product [72-74].

2.2.4.5. Sonochemical Synthesis

The sonochemical technique involves the use of high ultrasonic energy of about 20 kHz–10 MHz in a chemical reaction mixture. The ultrasound makes chemical/physical modifications through cavitation method, where smaller bubbles are created and grow in the liquid state [43]. The bubbles collapse to form local hot spots having a short lifespan with temperature and pressure, generating homogeneous nucleation centres and reducing the time for crystallization in comparison to traditional solvothermal process [43,75].

2.2.4.6. Diffusion Method

The diffusion method is normally used in the preparation of materials to avoid the creation of polycrystalline powdered compounds by generating crystals that are suitable for single X-ray diffraction analysis [33,67].The working principle behind this technique involves bringing slowly different species into contact and this can be done achieved in different phases including gas, liquid and gel diffusion [33,43]. The rate of reaction in all of these diffusions is influenced by one of the reactants. In solvent liquid diffusion, two layers having dissimilar densities form where one the solvent containing the product and other solvent is for the precipitant. The two layers are further separated from each other by another solvent layer and the precipitant solvent gradually penetrates into the separating layer and allow crystals formation at the interface [33,43]. Liquid phase diffusion involves the dissolution of the metal ions and

organic linkers in immiscible solvents, whereas gas phase diffusion uses an organic ligand solvent that is volatile. In gel diffusion method, MOF crystals form from mixing metal ion solution and organic ligand prior to dispersing them in a gel substance in order to prevent bulk material from precipitating. The gel substance help to slow down the diffusion rate and the preparation of MOFs by diffusion method which is usually carried out in mild conditions and it is time-consuming [43].

2.2.4.7. Solvent Evaporation Technique

Solvent evaporation is another available technique for the synthesis of MOF coordination polymers. This synthetic route involves the formation of crystals through a gradually increasing concentration of mother liquor [33]. In solvent evaporation method, the first step entails mixing precursors in a suitable solvent, followed by stirring of the mixture to obtain a clear solution. The mixture is then exposed to a specific temperature in an inert environment for the solvent to evaporate and allow the crystals to grow [33,36]. The main advantage of this traditional technique of synthesising MOFs is that it does not require any external energy supply and can be used at room temperature. However, it is time-consuming and poor solubility of reactants poses some drawbacks for the preparation of MOFs. The poor solubility of the reactants is then improved by mixing different solvents and the process is accelerated by using low-boiling point solvents which can evaporate quicker [36,43].

2.2.4.8. Post Synthesis Method

Amongst other advantages of MOFs, it is their capability to incorporate complex functionalities into their framework, therefore generating a series of MOFs with diverse functionality while maintaining the same topology [76]. However, it remains a challenge to introduce functional groups onto the structure of MOF during its synthesis. The above mentioned drawback can be addressed through the post-synthesis modification (PSM) method, which is the chemical modification or functionalisation of MOFs following their formation (Figure 2.7). The introduction of functional groups onto the structure of MOFs can be achieved by through noncovalent, coordinative or covalent interactions [39,40,77]. Some of the simplest approaches employed in carrying out PSM are protonation and doping.

Covalent interactions have been the successfully used in PSM for amino-functionalisation of MOFs owing to the high reactivity of amino functional groups. It must be noted that many PSM reaction methods make the functional groups to increase in size and more complex in the pores, but there is the possibility of making the groups smaller and instantaneously unmask the protected functional group [47,78]. For dative PSM processes, there are two types that exist. Firstly, the one in which metal nodes bond coordinatively to the neutral sites of the linker. The second one

occurs when metal ions coordinate to the organic linker by deprotonation like transformation of hydroxyl groups into alkoxides [47].

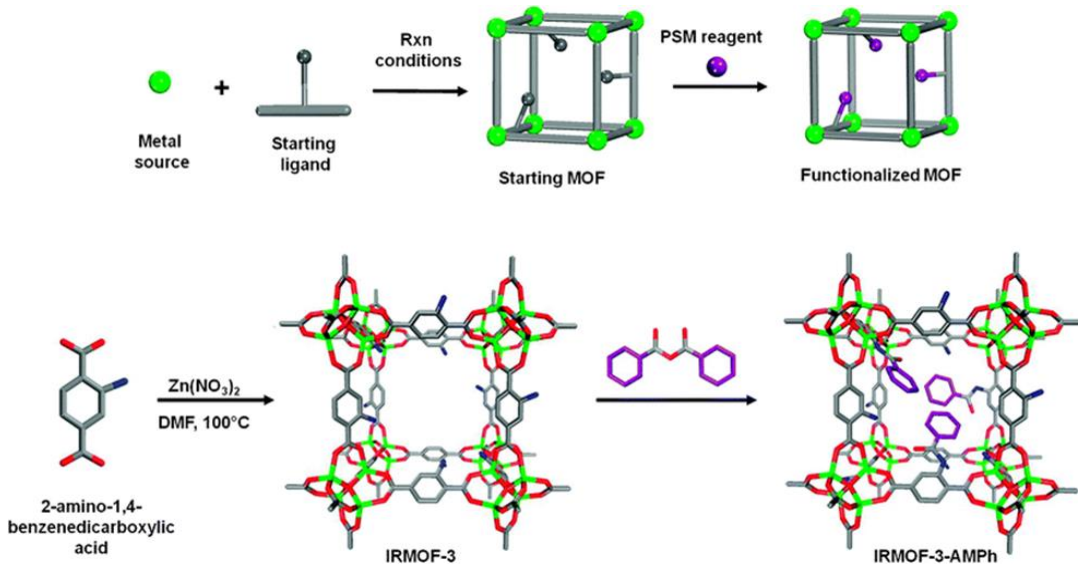

Figure 2.7: PSM of MOFs and functionalised ligands during MOFs synthesis [79].

2.3. MOF NANOMATERIALS

The application of MOFs in various fields has led to the development of MOF nanostructures and MOF composites. Nanostructures of MOFs are formed when the size of the materials are reduced to a nanoscale [80]. These type of materials have gained interest due to their properties which include luminescence, electrical and magnetic properties, enormous surface area, narrow pore volumes and unique size-dependent optical behaviour in comparison to compared traditional MOF polymers [65,80,81]. Furthermore, nanostructured MOFs are highly diverse in terms of composition, morphology, characteristics, and have shown to be greatly dispersible and biocompatible. When comparing nanostructured MOFs with other nanostructured materials, their diversity in the morphology includes nano-cavities, hollow spheres and

polyhedrons [41]. The synthesis of these type structures involve doping of inorganic nodes, which allows for modification of functional characteristics of MOF polymers while maintaining their coordination characteristics [65,81]. MOF materials are sometimes mixed with appropriate metals and graphene based nanomaterials to obtain highly effective composites structures Sometimes, graphene based nanomaterials are combined both with suitable metals and MOF structure. As a result, very effective composites were obtained. An examples is a study conducted by Asadian and co-workers [82]. They were able to prepare nickel copper (NiCo) layered double hydroxide (LDH) nanosheets/GNRs. They put the synthesised material on glassy carbon electrode (GCE) and utilised it for detecting non-enzymatic glucose (Figure 2.8).

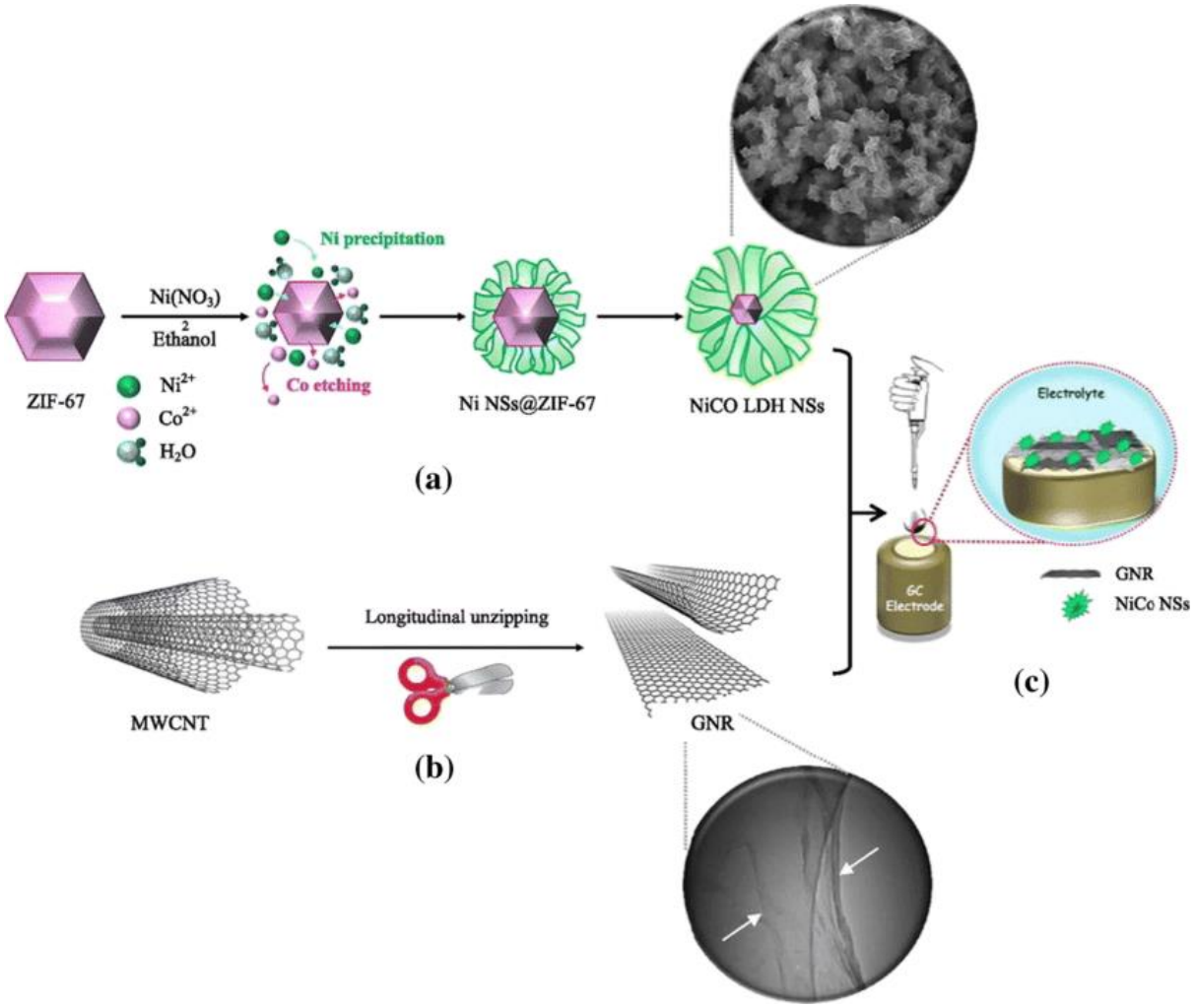

Figure 2.8: A carbon nanomaterial/MOF composite based sensor [82].

2.4. MOF COMPOSITES

A composite is a material that has multiple components with various phase domains, wherein one type of the domain is continuous [83]. Such materials are regularly employed in industrial systems, due to the combination of phase properties which are tuneable. Hence, there are some studies on composites which have been conducted such improving gas sorption/separation and heavy metals adsorption [65,83,84]. Additionally, composites can be easily handled when comparing them to crystalline MOF polymers. In catalysis, the interest in composites lie in the combination of the

catalytic activity of the dispersed phase and the stability of the continuous phase [65,83]. Formation of composites by modifying the surface of MOFs has been also investigated in biomedicine and found to improve the water dispersity and stability of MOFs. This results in the enhancement of drug loading, reduction in plasma protein binding, avoided uptake by the reticuloendothelial system, etc [85]. In addition to other applications, various MOF composites have been synthesised and studied, with many of them showing potential in enhancing efficiency for a specified application [84,86,87]. It was reported that incorporation of an ultrathin layer of MOF-derived nanocarbon on graphene oxide sheets resulted in the formation of a nanocarbon/graphene oxide/nanocarbon sandwich-like structure (Figure 2.9) with high specific surface area and excellent electronic conductivity [88].

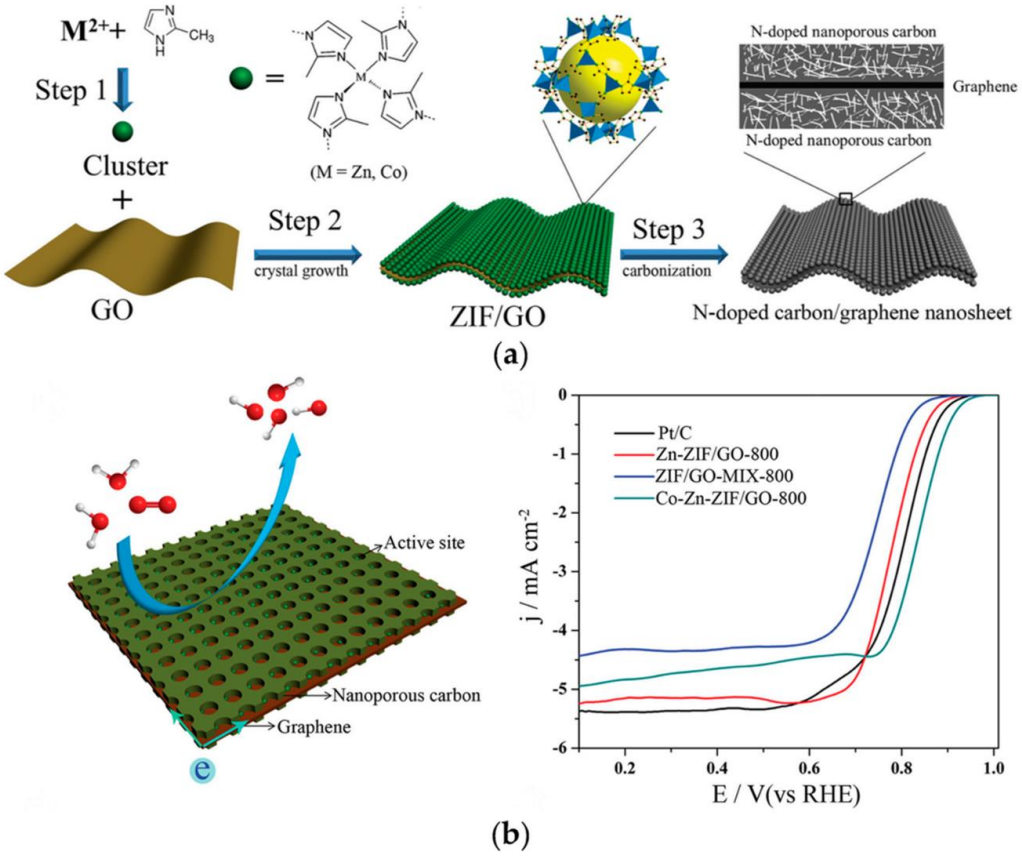

Figure 2.9: (a) MOF composite of ZIF/GO and N-doped nanoporous carbon/graphene/ nanoporous carbon sandwiches; and (b) Their linear sweep voltammetry curves and oxygen reduction process and conducted in alkaline conditions [88].

2.5. APPLICATIONS OF MOFS

The fascinating structural diversity of MOFs and their nanostructures and composites have earned these coordination polymers the unlimited possibilities for a wide range of application. MOFs can be tailored for a particular application through appropriate alteration of the structure. Literature reports have shown that properties of the system that have been measured correlates completely with chemical functions and matrix that have changes [85,89,90,91]. The surveys have shown that there are complete correlations between the measured properties of the systems and the changes occurring on their chemical functionality and matrix [92,93]. For this reason, a variety of design methodologies can be implemented in order to obtain the anticipated performances of the MOF materials. The following section provides an insight on some of the significant applications of MOF materials.

2.5.1. Biomedicine

The development of MOF composites and nanomaterials for drug delivery has been a growing research in the field of medicine, since, the emergence of using pristine MOFs

for drug delivery in the mid-2000 [94]. MOFs possess numerous ideal properties as drug carriers such as high surface area which offers high drug loading ability, large pore size and improved controlled release kinetics. Furthermore, the labile metal-ligand coordinated bonds and flexible functionality for post synthetic grafting of drug molecules offer potential of biodegradability of these materials [95]. MOFs application as drug carriers is hindered by their insolubility in water which is addressed by surface modification and composite formation with components that are hydrophilic or coordinating with water attracting ligands [94].

The utilisation of MOF materials as drug carries can improve the efficiency in drug delivery and reduce the side effects of the active pharmaceutical ingredient. The main objective in developing MOF drug carriers is to use metal ions and organic ligands that display insignificant toxicity in the human body system. Less toxic metals which are widely used include iron, calcium, copper, nickel, zinc, titanium, manganese and their oral lethal dose is below 50 (LD50) within different metabolic body systems. In terms of organic ligands, the chosen ones are those prepared from natural compounds which have no effect on the body systems [33,94]. As an example, Haydar *et al.* [96] synthesised four different MOFs namely Fe-100, Fe-MIL-101, Fe-MIL-53 and Ca-MOF using hydrothermal method for the delivery of flurbiprofen. The Fe-MIL-100 and Fe-MIL-101 MOFs showed the loading percentage of 46% and 37%, respectively.

2.5.2. Sensors

The diversity in the structural designs and tuneable surface chemistry of MOF properties have motivated their utilisation in various sensing application such as gas sensing, bio-sensing, electrochemical and chemical-sensing [81]. Generally, a sensor comprises two components;(i) a sensing unit which collects information, (ii) transduction unit that is used for translating the collected information into either an electrical or optical signal [97]. MOF materials having magnetic or luminescence characteristics, as well as size/shape-selective adsorption can offer potential for the application in sensing devices. The preparation of luminescent networks can be achieved by using organic linkers and metal ions which are luminescent organic, or by using the metal-to-ligand charge transfer [98]. Hence, the properties of MOFs that contribute significantly to their usage in developing a MOF luminescent sensing device include its structural characteristics, coordination environments, porosity, interactions with guest species and non-covalent interactions. Lanthanides are the promising candidates in preparing MOF based sensors owing to their large coordination sphere (coordination number up to 12) as well as lacking strong coordination geometry [33,67,97].

MOFs may be used in electrochemical sensor which operates based on the oxidation and reduction reactions of the analytes. The measurement in electrochemistry takes place in electrochemical system of two or three electrodes made of a working electrode, a counter electrode, or reference electrode. The quantitative measurement

of species involved in the reaction can be achieved by measuring the current, electric potential, or other electrical signals. MOF composites have shown to a good candidate for electrochemical gas sensing owing to their high surface area, pore volume, good absorbability, and high catalytic activity [97]. Mashao *et al.* [99] reported electrochemical hydrogen gas sensor based on polyaniline/ZIF (Figure 2.10). They showed that electrochemical gas sensors based on MOFs have the capability to sense low concentration (ppm level) of hydrogen gas without requirement of heating.

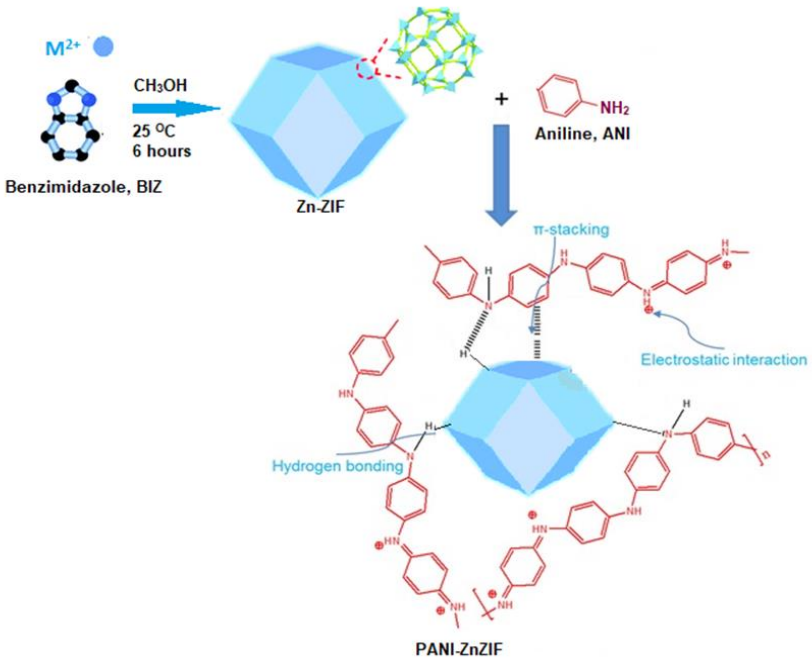

Figure 2.10: Schematic representation of polyaniline doped with ZIF for electrochemical hydrogen gas sensing [99].

2.5.3. Catalysis

In catalysis, the porosity and the thermal stability of MOF materials play a vital role. Moreover, the tuneable nature of the size of the pores in MOFs allow them to be easily designed for the exact application as catalysts. The preferred catalyst are usually homogeneous catalysts owing to their higher efficiency and selectivity, however, their study is limited by the instability and limited recovery and separation of the spent catalyst. MOFs as solid materials offer potential in addressing the above mentioned shortcomings since their framework can be altered to allow various catalytic reactions. MOF possesses a heterogeneous catalytic characteristic due to its porous nature and structural properties such as high surface area, permanent porosity and multifunctional ligands [100]. It was seen that the most vital characteristic responsible for its heterogeneous catalytic ability is lack of non-accessible volume. Literature shows that there are numerous of MOFs that have been used as heterogeneous catalysts for formation of organic oxidation, epoxidation, knovenagel condensation, aldol condensation, hydrogenation, Suzuki cross-coupling, or Friedel–Craft's alkylation reactions [101]. The advantage of employing a MOF catalyst in synthesis of organic compounds (Figure 2.11) is its ease separation from the target product by centrifugation and its reusability [102]. It was reported that rates of organic transformation depends on the surface area and pore size of MOF since the catalytic reaction takes place on the outer surfaces of the MOF particles under UV radiation [102].

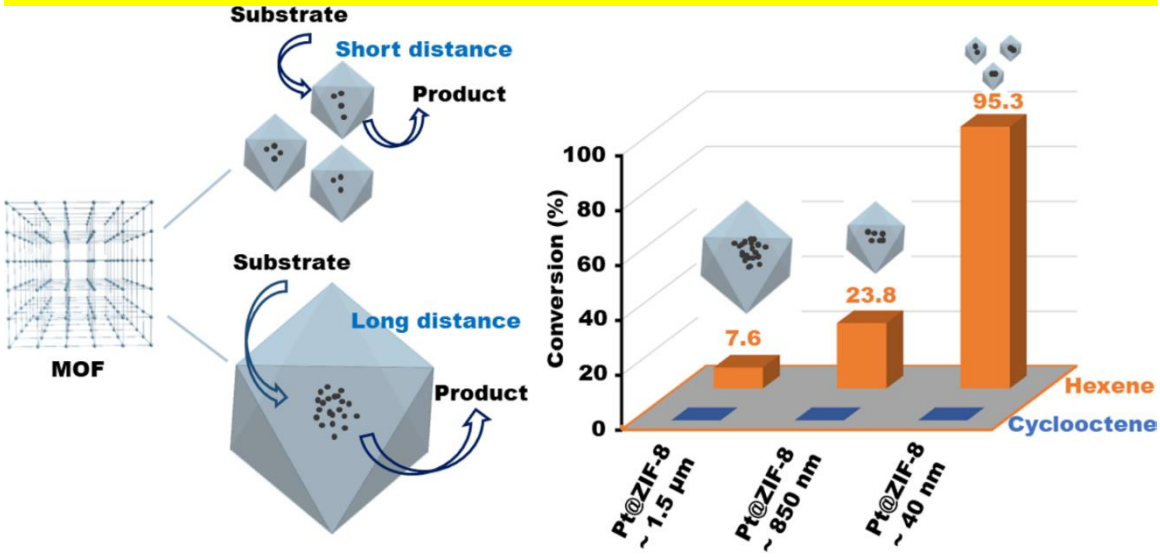

Figure 2.11: Formation of organic compounds using MOF catalyst and transport limitations in MOFs indicated by particle size effects on conversions [32].

Figure 2.12 presents four strategies for the important role that MOFs play in catalysis [103]. The firs approach is on the transition metal ions which can act as active sites, requirement being vacant coordination sites on the metal centres. The second approach is based on the metal nanoparticles which are saturated into the pores of MOF structure, however, they occupy the space in the pores that leads to a decrease in the surface area and pore volume which will reduce the catalytic activities. The third approach is on the organic linker which features the functional side-groups and possesses a possibility of post functionalisation to enhance its catalytic activity. The last approach is on the preparation of mixed organic linker MOFs which are made from two iso-reticular linkers that are disseminated in a mixed structure. It was seen that the challenges in the preparation of MOF catalyst are the introduction of unsaturated metal centres (UMC) and creation of void spaces into the framework structure. Current studies have shown that transition metal ions and multifunctional organic ligand are

used as the building blocks and specific structure to obtain microporous MOFs [95,104]. In addition, the introduction of N-heterocyclic carbenes (NHC) into MOF makes a powerful heterogeneous catalysts and allows multiple catalytic active sites [33,36].

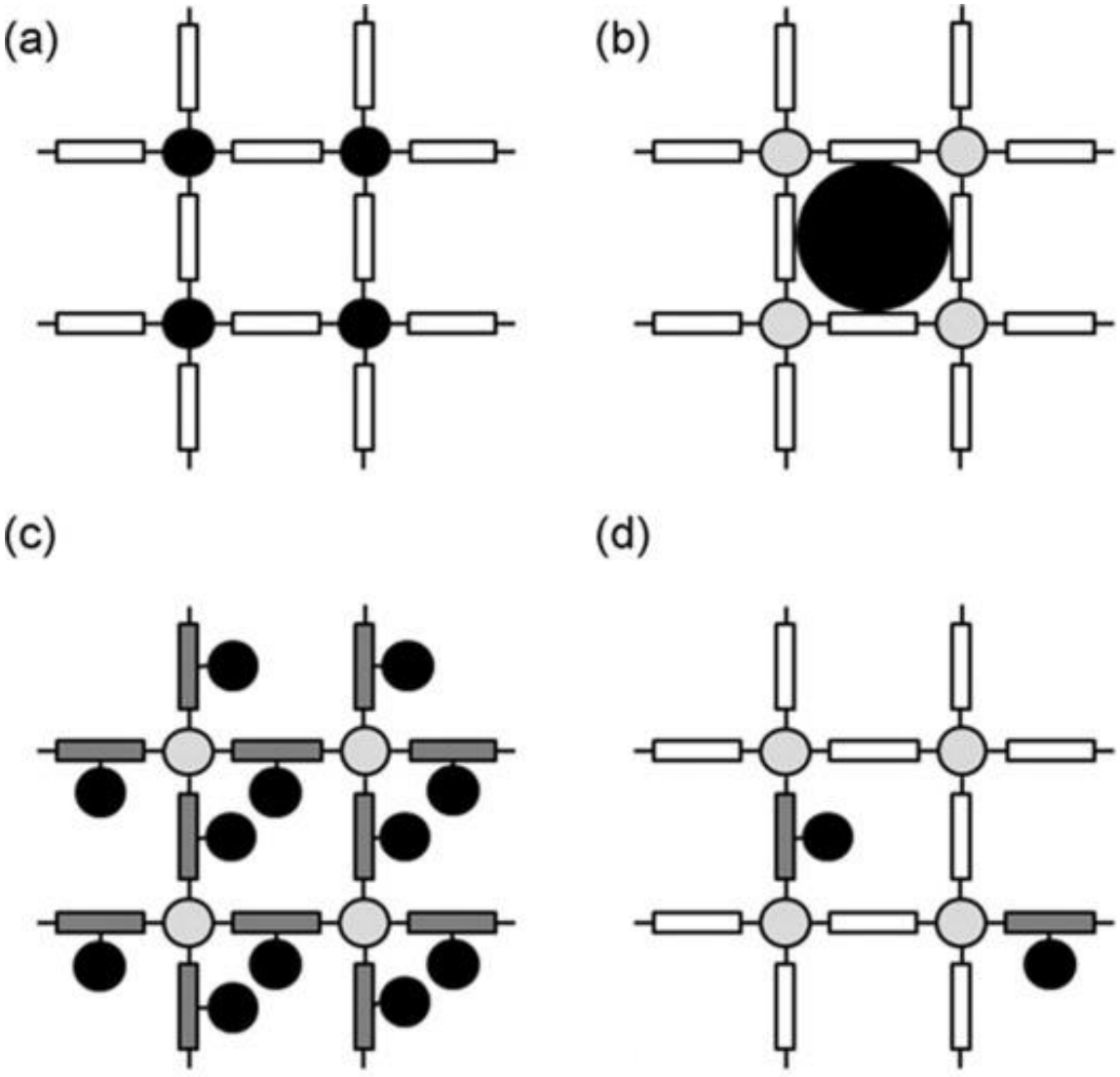

Figure 2.12: Different approaches for the use of MOFs in catalysis: (a) framework metals as active centres, (b) generation of metal nanoparticles inside the pores, (c) immobilization of active metal complexes via functional side-groups of the linker

molecule and (d) synthesis of mixed-linker MOFs (MIXMOFs) Black circles represent active metal centres and grey circles symbolise metal centres which are only used to build up the framework (no free coordination sites) [103].

2.5.4. Gas Storage and Separation

It was documented that a porous adsorbent material has the ability to safely and economically store gas at lower pressure due to high surface area [33]. These kind of porous materials are the candidates to replace the conventional storage methods of high pressure and multi-stage compressors. The literature survey shows that the reports on the utilisations of activated carbon, carbon nanotubes, zeolites for gas storage, interest on MOFs as gas storage materials is increasing owing to its tuneable structural properties. MOF materials have been applied in for hydrogen gas storage whereby hydrogen molecules are adsorbed on the surface of the pores of MOF structure through a physisorption process [39,45]. There are number of MOF materials that exhibit outstanding performance for hydrogen adsorption under cryogenic conditions and high pressure up to 100 bar [85,105], However, their hydrogen store efficiency was shown to be low at ambient conditions [39,51,106]. Recently, extensive studies have been reported for the fabrication of MOF materials having high interaction energies for hydrogen gas at ambient conditions [51,67,103]. It was shown that the hydrogen uptake relates to surface area of the material, therefore, the enhancement of hydrogen adsorption may be achieved increase in surface area [105]. So far more than 150 microporous MOFs have been investigated for H_2 adsorption at different

conditions. For instance, the hydrogen uptake was tested for the documented carboxylate based MOFs such as MOF-5 and MOF-177 prepared from [Zn_4O] cluster with di and tri carboxylate ligands, respectively [51]. It was seen that MOF-5 possessed a BET surface area of 3800 m^2/g with 7.1 wt% of H_2 uptake at 40 bar and 77 K [51]. On the other hand, MOF-177 material with BET surface area of 4750 m^2/g showed 7.5 wt% of H_2 adsorption at 70 bar and 77 K [107]. Jihoon *et al*.[108] reported the preparation of Pt and Carbon Black (CB) impregnated MOF-5 composite, CB/Pt/MOF-5, possessing high hydrogen storage potential up to 0.62 wt% over pristine MOF-5 (0.44 wt%) at moderate temperatures and pressures. They further showed that the CB/Pt/MOF-5 composite has moisture resistant capability as compared to pure MOF-5. Hu *et al*. [109] have synthesised Pt impregnated on MOF/graphene oxide (GO) composites to form Pt@HKUST-1/GO and Pt@ZIF-8/GO. They indicated that the composites possessed increment in hydrogen uptake with respect to their pure MOFs [28].

2.5.5. Water Purification

The selection of a water treatment method is based on the initial quality of water, parameters established by regulations and the intended usage of the water after purification. These methods are regarded as physical, chemical or biological treatment

based on the mechanism of removal of pollutants [59,110], as presented in Figure 2.13(a).

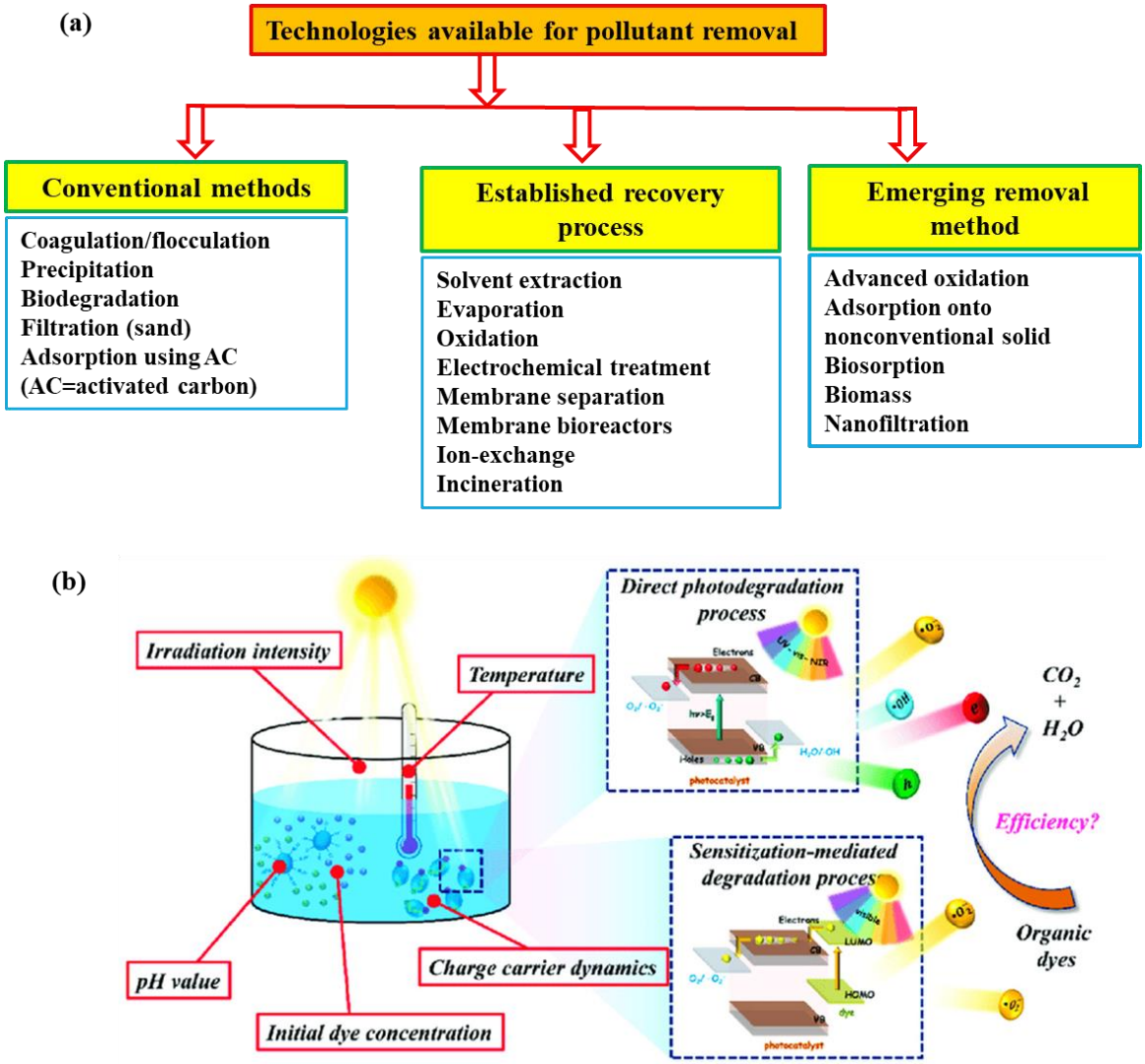

Figure 2.13: (a) Several technologies available for removing contaminants from wastewater. (b) Elimination of organic dyes from wastewater through photodegradation process [21].

The conventional treatment methods are inefficient for potable uses especially against raw water containing low concentrations of pollutants [49,111]. Treated water obtained from conventional methods can be reused for irrigation of crops or landscapes, refilling of aquifers and non-potable urban uses. Nevertheless, traditional remediation methods do not produce water that is sufficient enough for reusability in industrial applications (such as cooling and boiler feed) and also drinking [112]. Hence, there is a need to develop an improved wastewater treatment technology as demonstrated in Figure 2.13.

2.5.5.1. Adsorption of Organic Pollutants

MOFs are the promising porous adsorbent materials for the removal of organic contaminants from the environment due to their easy separation, high surface area, and highly selective towards removal of contaminants. MIL-101 material as one of the MOF materials have a zeotype crystal structure with high resistance to air, water and common solvents. It is a key property for an adsorbent for application in the pre-treatment of aqueous-containing samples. Zhou *et al*. [113] prepared novel magnetic Fe_3O_4@MIL-100(Fe) nanoparticles for removal of organochlorine pesticides from tea leaves in a mechanochemical magnetic solid phase extraction (MCMSPE). The Fe_3O_4@MIL-100(Fe) material was prepared employing the step-by-step method, showed to be effective towards organochlorine pesticide recovery and also be reused with no significant changes adsorption capacity after several cycles [113]. The findings

showed that MOF materials are ideal recyclable adsorbents for removal of organic contaminants. Furthermore, MOs have been used to adsorb organic dyes which has become a hazardous contaminant from industries in the environment [30]. Wang *et al*. [114] investigated the utilisation of magnetic Fe_3O_4/MIL-101(Cr) nanomaterial for removal of organic dyes such as acid red 1 (AR1) and orange G (OG). They reported that the prepared Fe_3O_4/MIL-101(Cr) nanomaterial possessed adsorption capacities of 142.9 and 200.0 mg/g for AR1 and OG, respectively. The results showed that MOF-based magnetic core-shell materials as good candidates as for dye removal from wastewater. Moreover, Yang *et al*. [115] reported a preparation of Fe_3O_4-PSS@ZIF-67 nanocomposite for selective adsorption of methyl orange (MO) from solution mixture of MO and methylene blue (MB) (Figure 2.14). They demonstrated that the adsorption capacity of the magnetic nanocomposites for MO was measured to be 738 mg/g with the separation rate of up to 92%.

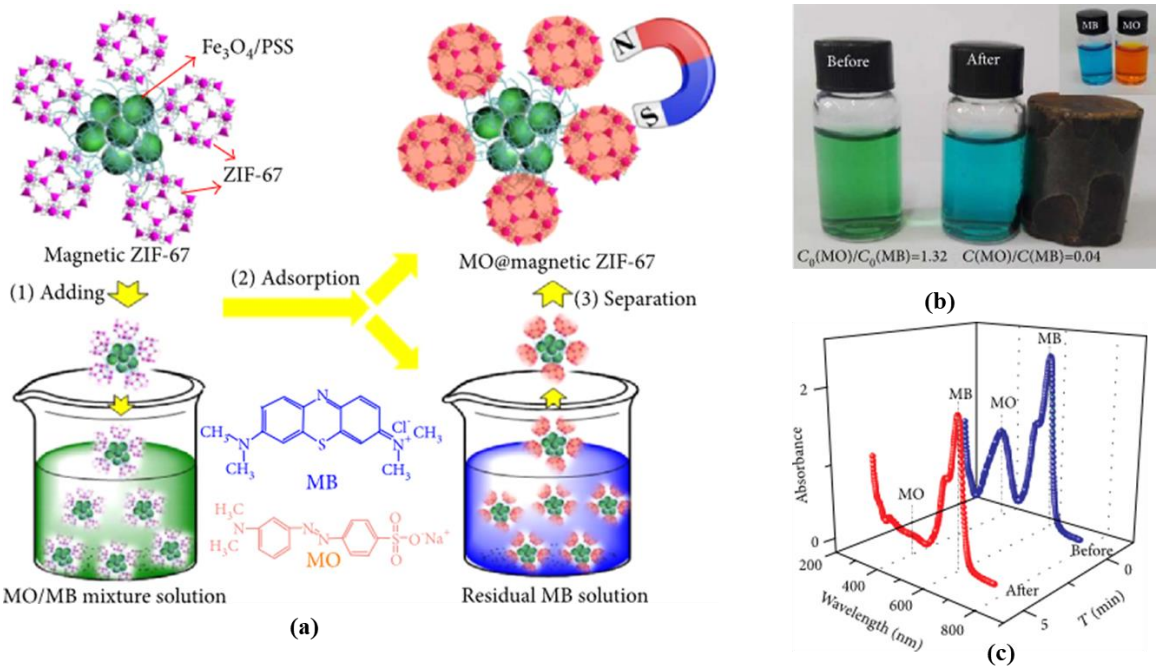

Figure 2.14: Scheme of selective adsorption of MO from the mixed MO/MB solution by Fe_3O_4-PSS@ZIF-67 magnetic composites; photographs (b) and UV-vis spectra (c) of the mixed MO/MB solution before and after magnetic separation [115].

2.5.5.2. Photodegradation of Organic Pollutants

It was well documented that heterogeneous photocatalysis (HP, Figure 2.13(b) is regarded as an emerging itinerary for water treatment for removal of organic dyes through photodegradation [21,116]. In HP, the photocatalyst is irradiated with UV light to separate charges followed by production of the reactive oxygen species (ROS) [70,117,118]. The material which is used in HP is known as a photocatalyst. It is a semiconductor, possessing the valence band (VB) and conduction band (CB). The VB is known as the highest occupied molecular orbital (HOMO) whereas the CB is the lowest unoccupied molecular orbital (LUMO) level. The distance amid of these levels is named band gap energy (E_g) [70]. For instance, the photocatalytic mechanism of pollutant removal is presented in Figure 2.13(b). Once a semiconductor is irradiated with UV light, it absorbs light with energy which is equivalent to its bandgap energy (≥ E_g) [119]. The electrons (e^{-s}) in the material are promoted from the VB to the CB for photogeneration of charges and leave an electron hole, h^+ behind [70]. At excited state, there are several pathways that photogenerated charges can take, such as recombination, releasing the excitation energy as heat, migration to the surface of the photocatalyst or production of the reactive oxygen species [117,119]. Lastly, OH is

produced through water oxidation process which is achieved by the h^+, whereas superoxide radical anions ($O_2\cdot^-$) is generated via adsorbed oxygen reduction mechanism. On the other hand, it was seen that the protonation process may take place to oxidize this $O_2\cdot^-$ to hydroperoxyl radicals ($HO_2\cdot^-$) [43,120]. It was observed that these oxidant species, together with direct oxidation by h^+, are capable to mineralize the organic dye to CO_2 and H_2O [116].

2.5.5.2.1. Photocatalysts for Wastewater Treatment

The fast growing interests in the area of photocatalysis for wastewater treatment has rose in the manufacture of different photocatalysts such as metal oxide [21,121] and metal sulfides [122]. Table 2.1 presents some of the most investigated photocatalysts in water purification. Several investigations have concentrated on the use of TiO_2 for water purification [123,124] owing to its high activity in photocatalysis. However, the application of TiO_2 powder has several setbacks such as poor porosity, low adsorption and its difficulty recovery [117]. In addition, it was seen that the photocatalytic activity of TiO_2 anatase, possesses a band gap energy of 3.2 eV ($\lambda \geq 387$ nm) which is high and needs to be activated by UV radiation [21,123,125]. As a result, surface modification of TiO_2 by addition of carbon, graphene or metal deposition, has been used in photocatalysis [123,125] . However, the preparation of a photocatalyst based on TiO_2 for practical wastewater treatment using visible and solar light is still a

challenging boundary. Consequently, it is imperative to explore competent, robust and cost-effective photocatalyst for replacement of the traditional ones. In the last two decades, a type of crystalline materials named metal organic organic frameworks (MOFs) have received consideration in photocatalysis. MOFs offer wide range of applications owing to their structural arrangement of coordination bonds between unsaturated metal core/node and multidentate organic linkers (catalytically active) [126]. Furthermore, their large surface area and well-ordered porous structures have significantly contributed towards their interest in numerous fields. In HP, the utilisation of MOFs as photocatalysts is mainly based on three aspects: (1) encapsulating chromophores in the internal structure of MOF; (2) promoting e^-/h^+ separation in the metal core; or (3) preparing MOFs using materials which have absorption bands at visible region [122,119]. Moreover, some MOFs can serve as semiconductors (e.g. MOF-5 [127], NTU-9 [128] and UiO-66 [129], in which the energy transfer takes place from the organic linker to the metal-oxo cluster [130]. Nonetheless, most MOF photocatalysts have a large band gap due to their poor conductivity caused by insulator characteristic of organic linker [21,124,131] that can simply harvest UV light, which immensely limits their further application [34]. There are several dissimilar approaches, including dye sensitization [132], decoration of linker or metal center [130,133] and combination with other semiconductors [134]. Hence, surface modification and functionalisation of MOFs are required for their application as suitable photocatalytic materials.

Table 2.1: Some of the Most Investigated Photocatalysts in Water Purification.

Photocatalyst	**Purpose**	**Refs.**
TiO_2	Photocatalytic degradation activity	[123]
	Photocatalysis for treating bacteria	[131]
	Photocatalyst in water treatment technology	[134]
ZnO	Photocatalytic degradation activity	[123]
	Photocatalyst in water treatment technology	[131]
WO_3	Photocatalytic degradation activity	[123]
CuS/ZnS	Exceptional visible-light driven photocatalytic activity	[124]
MoS_2/CdS	Enhanced visible-light photocatalytic activities	[130]
MOF	Photocatalytic degradation activity	[135]

2.5.5.2.2. Photocatalytic Degradation of Dyes using MOFs

The application of MOFs in water purification is subjected to their photochemical reaction and stability. This means that MOFs must retain their structural and textural properties during photocatalytic activity. Several organic dyes such as MB, MO, and

rhodamine blue (RhB) have been used as target pollutants and given in Table 2.2. The studies showed some of the approaches to establish photoactive materials which are founded from MOFs, as presented in Figure 2.15(a) [43,84,132]. Type I strategy uses the semiconductor dots characteristics of the metal cores in MOF that behaves like isolated nano-semiconductors which are sequestered by the organic ligands [122]. The type I MOFs are greatly effective compared to traditional semiconductors owing to their excessive porous nature. This favour the adsorption of contaminants that are near the semiconductor and photogenerated charges. Moreover, close to their high density of photoactive dots and the organic ligand which serves as antennae to absorb light, and accordingly enhancing the photoresponse of the MOF [56,136]. In type II MOFs, dye-based organic linkers with photoresponse are used for absorption of light as well as transfer of photogenerated charges to the metal cores [118,137]. Type III MOFs are regarded as the simplest route where MOFs act as porous matrix in which the photoactive species are compressed within its structure [138]. However, the main drawback of these MOF materials in photodegradation is their stability in water. In 2007, Alvaro *et al*. [139] described the photocatalytic degradation of phenol in water by MOF-5. In addition, Hausdorf *et al*. [138], observed that instability of MOF-5 depends on structural modification and water environment. The photodegradation of rhodamine 6G (R6G) by Fe-MOFs under visible light (550 nm) was studied by Laurier *et al.* [140]. They have observed that Fe-MOFs were better catalysts than the conventional TiO_2 and their structural properties were reasonably maintained after

photocatalytic activities. Other MOFs for photodegradation of MB organic dye have demonstrated high photodegradation efficiency (PDE%). Typical examples in this Chapter are presented in Figure 2.15(b) and (c) and Table 2.2. It was reported that Cd(II)-imidazole MOFs for photodegradation of the MB and methyl orange (MO) under UV light generates the photogenerated charges that are vital for photocatalytic degradation of organic dyes [111]. Furthermore, Zhang *et al.* [141] examined other types of Cd(II)-imidazole MOFs for photodegradation of MO and revealed that the bandgap energy, efficiency in the transference and separation of charges are the factors controlling the photogeneration of charges. On the other hand, Zn(II)-imidazolate MOF (ZIF-8) also showed a high photocatalytic efficiency for the removal of MB UV radiation [121]. Du *et al*. [121] reported a synthesis and application of MIL-101 in the photodegradation of Remazol Black B (RBB) dye. They have found that MIL-101 has high crystallinity, specific surface area (3360 m^2g^{-1}) and high stability in water and several organic solvents. The results showed that MIL-101 as a heterogeneous photocatalyst in the degradation reaction of RBB with 95% PDE after 4^{th} cycle and the photocatalytic mechanism was though electron transfer from photoexcited organic ligands to metallic clusters in MIL-101 [121].

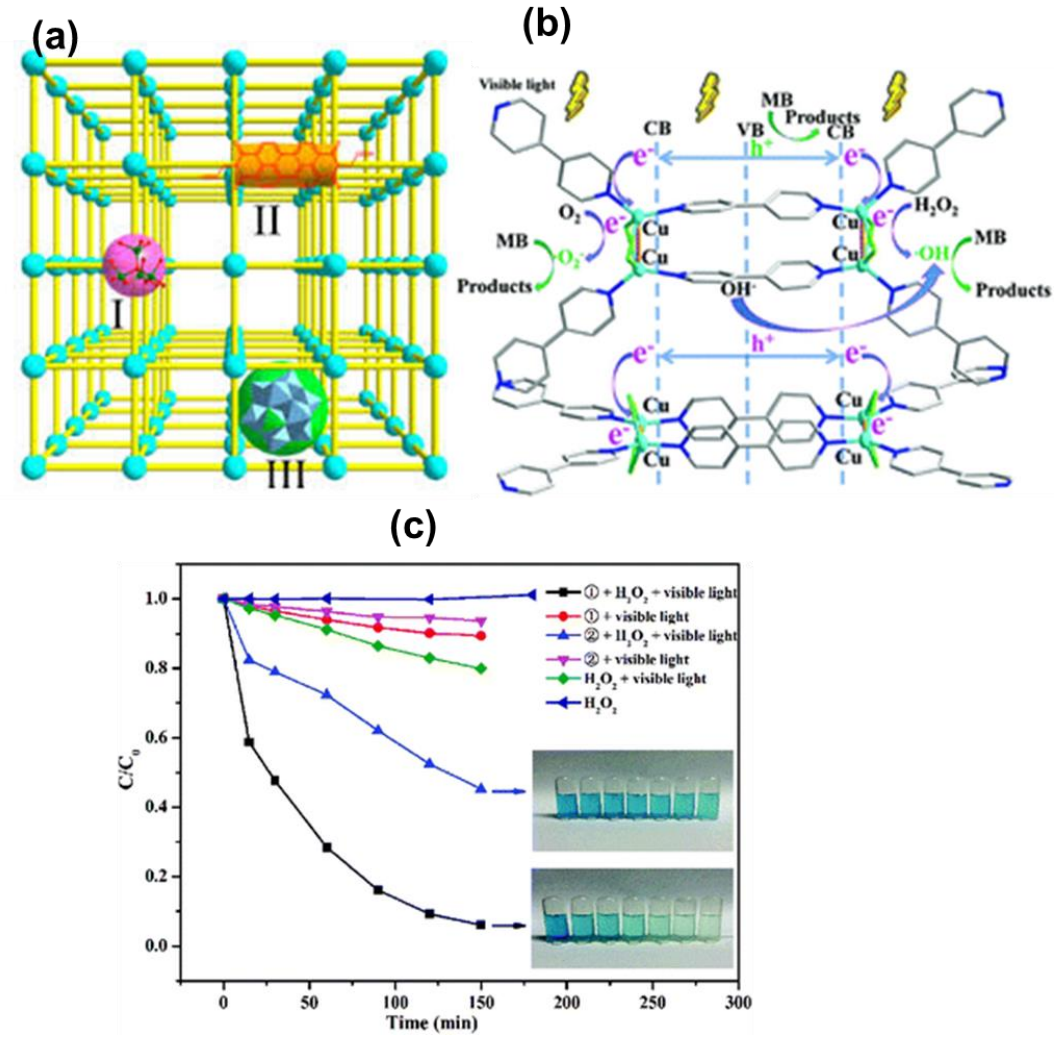

Figure 2.15: (a) Demonstration of the types of MOF developed for photocatalytic applications [70], (b) typical degradation mechanism of organic dyes using MOF as a photocatalyst and (c) effect of irradiation time on MB using MOF under UV radiation [142].

Table 2.2: Photocatalytic Degradation MOF Based Materials for Organic Dyes.

MOF based Photocatalysts	Organic Dye	Irradiation Time (min)	PDE%	Refs.
MOF, $[Cu(4,4'\text{-bipy})Cl]_n + H_2O_2$	MB	150	94	[119]
MOF, $[Co(4,4'\text{-bipy})(HCOO)_2]_n + H_2O_2$	MB	150	55	[119]
Fe_2O_3/MIL-53(Fe)	MB	240	70	[143]
BiOBr/NH_2-MIL-125	RhB	100	100	[144]
Bi_2MoO_6/MIL-100	RhB	90	90	[145]
Ag_3PO_4/MIL-53(Fe)	RhB	90	100	[129]
g-C_3N_4/MIL-125	RhB	60	100	[146]
g-C_3N_4/MIL-100	RhB	240	100	[133]
g-C_3N_4/MIL-53(Al)	RhB	75	100	[147]
rGO/NH_2-MIL-125	MB	30	100	[148]
rGO/MIL-88(Fe)	RhB, MB	20	100	[136]
GO/MIL-101(Cr)	MG	60	92	[149]
Au@MIL-100(Fe)	MO	150	100	[150]
Pd@MIL-100(Fe)	MO	150	100	[150]
Pt@MIL-100(Fe)	MO	150	100	[150]
MIL-53(Fe)	Phenol	180	99	[137]
NH_2-MIL-53(Fe)	Phenol	180	92	[137]
Fe(BDC)(DMF)	Phenol	180	99	[137]
MIL-53(Fe)	RhB	50	98	[151]

2.6. ADSORPTION OF HEAVY METAL IONS

Heavy metals are originally found in the natural environment from different types of rocks (i.e igneous, metamorphic and sedimentary). They interact with their surrounding environment through several processes including weathering, soil erosion and soil formation and results in the accumulation of these metal ions in higher toxic concentration [152]. The pollution of water by heavy metal ions such as copper (Cu), chromium (Cr), lead (Pb), cobalt (Co), nickel (Ni) PGMs, mercury (Hg) expelled from industrial activities is of major concern owing to their numerous toxicological effects to the human health and the environment [9,112]. The exposure to some of these heavy metal ions is accompanied by severe and irreversible effects even in lower concentrations [153]. The employment of adsorption technology as a feasible technique for wastewater treatment has been widely investigated owing to its simple designs and operation at a lower cost, production of less harmful secondary by-products and possible regeneration of the adsorbent. In the adsorption process, the adsorbent (usually porous solids) interact with the adsorbate of suitable size and shape through physical (adsorptive) or chemical (reactive) adsorption [11]. The physical/adsorptive adsorption mechanism involves the entrapment of adsorbate into the pores of the adsorbents via van der Waals forces. In chemical/ reactive adsorption, the mechanism of adsorbate-adsorbent interaction is through the formation of a chemical bond. The advantage of physical adsorption is the easy regeneration of the spent adsorbent using solvents exchange or by physical treatment like sonication, as compared to chemical adsorption which requires chemical treatments. Various

mechanisms of adsorption that are possible between the adsorbate and adsorbent are represented in Figure 2.16 [37]. The effectiveness of the adsorption process is evaluated based on the uptake capacity by the adsorbents, specific selectivity and of the rates mass transfer [112].

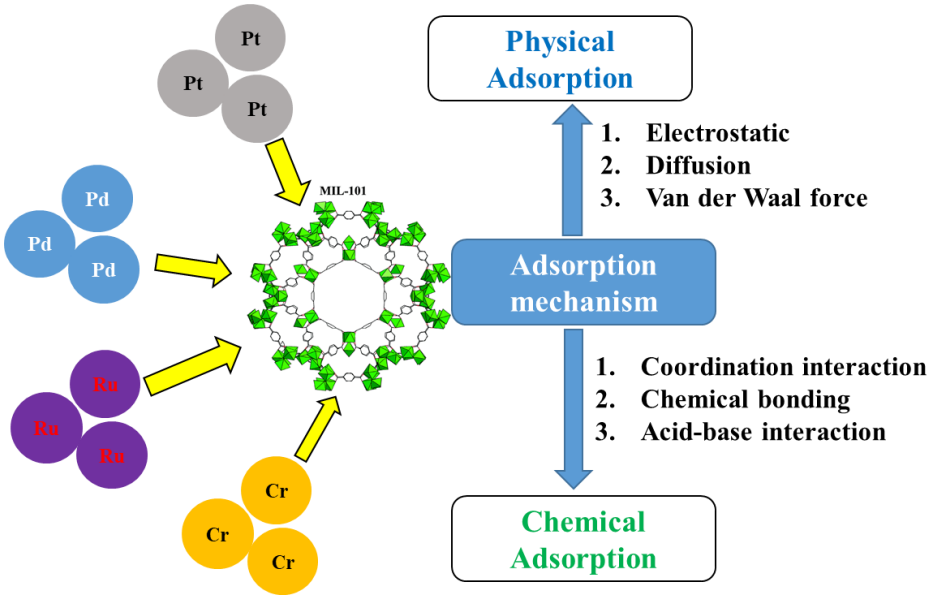

Figure 2.16: Various mechanisms of adsorption that are possible between the heavy metal and MIL-101.

MOFs offers offer good aspects in the removal of heavy metal pollutants from wastewater due to their structural diversity, higher surface area, tenability of their pore size, and enormous porosity. Furthermore, MOFs have shown to have significant partitioning coefficients that indicate higher adsorption capacity for heavy metals regardless of the initial conditions [59,154]. In some cases, MOFs capture inorganic pollutants on their nodes via pseudo-ion-exchange processes whereby less strongly coordinated organic linkers are removed by the inbound contaminant [56]. As an example, Wu *et al*. [155] synthesised thiol-functionalised copper terephthalate

Cu_4O(BDC) MOF via PSM for the removal of Hg^{2+} ions. They obtained the maximum adsorption capacity of 405.6 mg/g at and equilibrium time of 90 min. In another study, Lu and co-workers [156] prepared a sandwich structured metal–organic framework/graphene oxide (MIL-101(Fe)/GO) composite for the adsorption of Pb^{2+} ions from simulated wastewater. Though the composite showed the decrease in specific surface area from 1777 to 377 m^2/g, the Langmuir adsorption capacity was increased from 71.2 to 128.6 mg/g at equilibrium adsorption time of 15 min. Lin *et al.* [157] synthesised three zirconium based MOFs UiO-66, UiO-66-NH_2 and UiO-66-$NHCOCH_3$ through hydrothermal method. The MOF materials were tested for the selective removal of Pd(II) and Pt(VI) over Co(II) and Ni(II) competing ions. The functionalised MOFs showed an increase in the adsorption capacity towards Pd(II) and Pt(VI). However, the presence of competing ions showed to have an effect on the selectivity of PGMs uptake by the MOF based materials. Table 2.3 shows some of the reported MOFs based adsorbent for the removal of various heavy metal ions.

Table 2.3: Adsorption Capacity of MOFs for Heavy Metal Removal.

MOF Based Adsorbent	**Targeted Metal Ion**	**qm (mg/g)**	**Refs.**
UiO-66 and UiO-66-NH_2	U(VI)	109.9 and 114.9	[158]
ED-MIL-101	Pb(II)	87.64	[15]
Fe_3O_4@AMCA-MIL53(Al)	U(VI) and Th(IV)	227.3 and 285.7	[159]

Cu-MOFs/Fe_3O_4	Pb(II)	219	[154]
Azine-Decorated Zn(II) MOF (TMU-4, TMU-5, and TMU-6)	Pb(II)	237, 251 and 224	[160]
Fe_3O_4–Pyridine)/Cu_3(BTC)	Pd(II)	105.1	[161]
MOF-802, UiO-66 and MOF-808	Pd(II)	25.8, 105.1 and 163.9	[91]
MIL-101-triglycine	Co(II)	232.6	[162]
MIL-101(Cr)-NH_2	Pd(II) and Pt(IV)	277.6 and 119.5	[12]
MIL-101-TEPA@CA Beads	Pb(II)	273.59	[163]

* = Langmuir Adsorption Capacity

2.6.1. Photodegradation of Heavy Metals

The Mil-101, ZIF-8, UiO-66(Zr) and MIL-125(Ti) materials are the most studied MOFs in photocatalytic degradation [164]. Their photocatalytic mechanism relates to type II, and MIL-53 and MIL-88B (all Fe-based type I MOFs) where the light is absorbed by the Fe-O cluster to photogenerate electron and transferred from O^{2-} to Fe^{3+} [118,165]. In addition, the additional strategies were reported in literature showing the promotion of photocatalytic activity of MOFs by enlarging their visible light absorption, thus favouring their behaviour under solar light [118]. One methodology comprises in functionalising the organic linker or metal core to shift its photoresponse to lower

energy band gap. Shi *et al.* [165] prepared different amine-functionalised Fe-MOFs (NH_2-MIL-88B, NH_2-MIL-53 and NH_2-MIL-101) on the organic linker with high stability and activity for treatment of Cr(VI) via photoreduction mechanism under visible light. They established that the presence of an amine group in MOF structure increased the photodegradation efficiency (Figure 2.17(a)). Based on the observation, they projected a possible mechanism of photoreduction based on a dual excitation as presented in Figure 2.17(b). The figure shows the promotion of electron transfer and reduction of charge recombination. Based on the reported literature about adsorption and photodegradation, MOF based materials offer good potential as candidates for the removal of heavy metal ions from wastewater. However, selectivity for some of the reported composites is still a challenge.

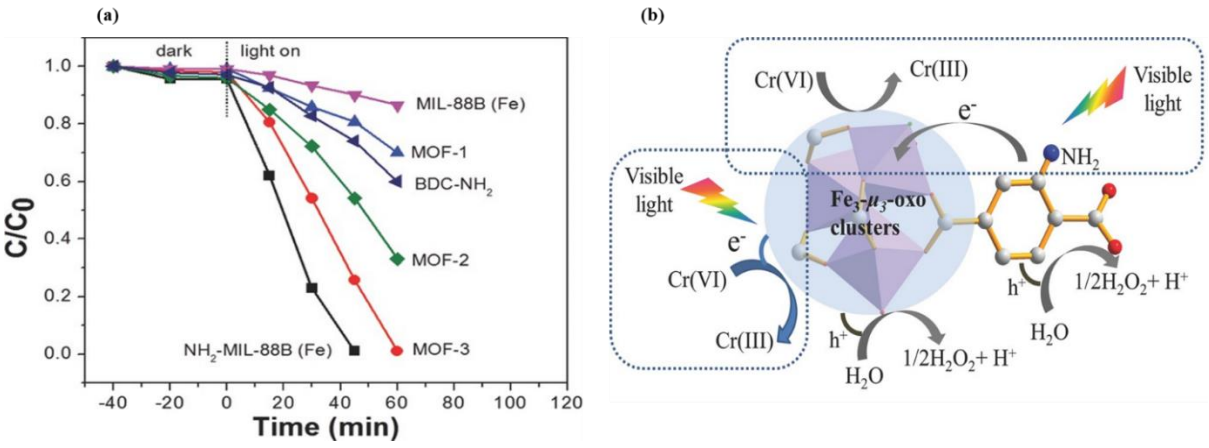

Figure 2.17: Photocatalytic reduction of Cr(VI) to Cr(III) using MOFs; (a) photocatalytic efficiency and (b) possible mechanism [165].

2.6.2. Ion-Imprinting Technique

Ion-imprinting technique is a promising technology that has been investigated for the removal targeted pollutants from wastewater [166]. This method involves the synthesis of polymer materials that can selectively interact with the specific targeted metal ions in the presence of competing ions. The first step of ion imprinting polymer (IIP) entails the interaction of the targeted metal template with an appropriate functional monomer to form a complex. This is followed by the polymerization of the formed complex in the presence of an appropriate linker to form a 3-D cross-linked structure [167,168]. Once the structure has formed, the metal ions template is removed out of the framework by leaching to allow the selective rebinding of the targeted metal ions into the remaining vacant sites even in the presence of competing ions [169]. Different composite materials have been reported for the selective removal of heavy metal ions [10,169,170]. MOFs offer great potential as adsorbent material due to their diverse structures which can be easily tuned by ion imprinting to improve their adsorption functionality and selectivity for the removal of heavy metal ions from wastewater. In a study conducted by Yuan and co-workers in 2018 [20], an ion-imprinted glycine UiO-66-NH_2 MOF was successfully synthesised for the selective adsorption of Co(II) ions from wastewater. The ion-imprinted composite (Co(II)-IIP) showed an improved maximum adsorption capacity of 175 mg/g as compared to the non-imprinted composite (NIP) which had a maximum adsorption capacity of 125 mg/g (Figure 2.18(a)) [20]. Furthermore, the ion-imprinted UiO-66-NH_2 MOF had a higher surface area of 482.46 m^2/g than the non-imprinted UiO-66-NH_2 MOF which was having a

surface area of 471.65 m^2/g [20]. They came with adsorption mechanisms of Co(II) on Co(II)-IIP which are shown in Figure 2.18(b). The cobalt ions in the figure act as a template agent in the preparation process of Co(II)-IIP. When the cobalt ions are removed by suitable solvent, the composite selectively adsorbs Co(II) from the aqueous solution because of the template recognition for cobalt ions. It was seen that the Schiff base nitrogen, carboxyl oxygen and carbonyl oxygen in the framework are the main coordination atoms in the Co(II)-IIP [20]. Their discovery of ion-imprinted polymers based on MOFs provides new opportunities to the functionalisation of MOFs in recovery of PGMs from wastewater.

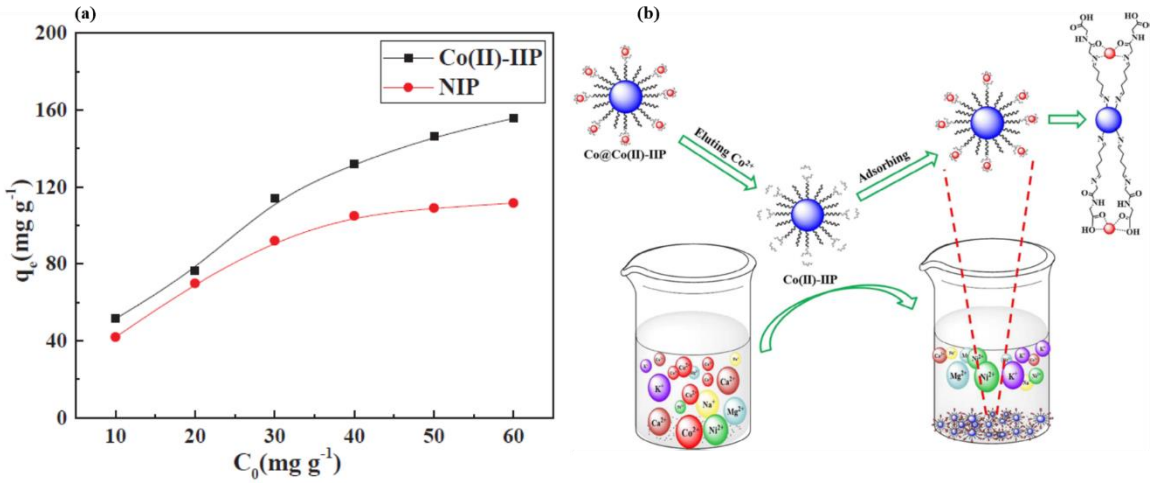

Figure 2.18: Effect of the cobalt(II) concentration on the sorption of cobalt (II) onto the Co(II)-IIP and NIP (t= 5 h; T= 298 K; V=50 mL; m = 0.01 g; pH = 8.4) [20].

2.7. SUMMARY AND FUTURE PERSPECTIVES

The presence of high concentrations of toxic heavy metal ions in the available water resources continues to be a global challenge. The priority on the removal and recovery

of some of the precious metals is a growing research in the field of wastewater treatment. Amongst the number of technologies that have been investigated, adsorption process has shown to be effective in removing various heavy metal ions from wastewater with the appropriate choice of the adsorbent material. Metal-organic framework materials have gained popularity for various applications including in heavy metal ions removal. In this review, MOF materials were briefly discussed starting from their interesting structural arrangement, followed by their various synthetic routes then finally to their various applications. MOFs have been exploited for various applications due to their highly porous nature, higher surface area and tuneable pore sizes which affects their functionality. Numerous data have been collected for comparison of MOF based materials with other porous materials for each specific application. For application in wastewater treatment, MOF based materials have demonstrated some significant improvement in both the adsorption and degradation of pollutants. This review summarised some of the work done on the adsorption of heavy metal ions (including PGMs) by MOFs which showed an increase in the adsorption capacity. However, there some MOF based composites which lacked selectivity towards the adsorption of heavy metals of targeted contaminants. To overcome this challenge, ion-imprinting technique was employed for the selective removal of specific pollutants from wastewater and the capacity improved further. In literature, there are only few reports on ion-imprinted MOFs for the adsorption of heavy metal. The process of ion-imprinting is implemented during the synthesis of the adsorbent materials to

generating foot prints of the targeted pollutants on the surface of the adsorbent. Considering the tuneable nature of MOFs and the ion-imprinting technique, there is a future perspective for the development of a highly porous MOF composite with higher removal uptake and high selectivity towards targeted pollutants.

2.8. REFERENCES

[1] Glaister BJ, Mudd GM, The environmental costs of platinum – PGM mining and sustainability : Is the glass half-full or half-empty ?, *Miner Eng* 2010;23:438–50.

[2] Mpinga CN, Eksteen JJ, Aldrich, C, Dyer L, Direct leach approaches to platinum group metal (PGM) ores and concentrates: A review, *Miner Eng* 2015;78, 93–13.

[3] Mudd GM, Jowitt SM, Werner TT, Science of the total environment global platinum group element resources, reserves and mining – A critical assessment, *Sci Total Environ* 2018;622–623:614–25.

[4] Maponya TC, Ramohlola KE, Kera NH, Modibane KD, Maity A, Katata-Seru LM, Hato MJ, Influence of magnetic nanoparticles on modified polypyrrole/m-phenylediamine for adsorption of Cr(VI) from aqueous solution, *Polymers* 2020;12: 679-95.

[5] Suoranta T, Zugazua O, Niemelä M, Perämäki P, Hydrometallurgy recovery of palladium, platinum, rhodium and ruthenium from catalyst materials using microwave-assisted leaching and cloud point extraction, *Hydrometallurgy* 2015;54:56–2.

[6] Can M, Bulut E, Özacar M, Reduction of palladium onto pyrogallol-derived nano-resin and its mechanism, *Chem Eng J* 2015;275:322–30.

[7] Sharma P, Bhardwaj D, Tomar R, Tomar R, Recovery of Pd (II) and Ru (III) from aqueous waste using inorganic ion-exchanger, *J Radioanal Nucl* 2007;274:281–86.

[8] Wei W, Lin S, Reddy DHK, Bediako JK, Yun Y, Poly(styrenesulfonic acid) - impregnated alginate capsule for the selective sorption of Pd(II) from a Pt(IV) - Pd (II) binary solution, *J Hazard Mater* 2016;18, 79–9.

[9] Utembe W, Matatiele P, Gulumian M, Hazards identified and the need for health risk assessment in the South African mining industry, *Hum Exp Toxicol* 2015;34: 1212-21.

[10] Mao J, Lin S, Juan X, Hui X, Zhou T, Yun Y, Ion-imprinted chitosan fi ber for recovery of Pd (II): Obtaining high selectivity through selective adsorption and two-step desorption, *Environ Res*, 2020;182: 108995.

[11] Khan NA, Hasan Z, Jhung SH, Adsorptive removal of hazardous materials using metal-organic frameworks (MOFs): A review, *J Hazard Mater* 2013;244–245: 444–56.

[12] Lim C, Lin S, Yun Y, Highly efficient and acid-resistant metal-organic frameworks of MIL-101(Cr)-NH_2 for Pd(II) and Pt(IV) recovery from acidic solutions: Adsorption experiments, spectroscopic analyses, and theoretical computations, *J Hazard Mater* 2020;387: 121689.

[13] Luo X, Shen T, Ding L, Zhong W, Luo J, Novel thymine-functionalised MIL-101

prepared by post-synthesis and enhanced removal of Hg^{2+} from water, *J Hazard Mater* 2016;306: 13–22.

[14] Qian K, Deng Q, Fang G, Wang J, Pan M, Wang S, Biosensors and bioelectronics metal–organic frameworks supported surface–imprinted nanoparticles for the sensitive detection of metolcarb, *Biosens Bioelectron* 2016;79: 359–63.

[15] Luo X, Ding L, Luo J, Adsorptive removal of Pb(II) ions from aqueous samples with amino-functionalisation of metal−organic frameworks MIL-101(Cr), *J Chem Eng* 2015;60: 1732-43.

[16] Ramanayaka S, Vithanage M, Sarmah A, An T, Kim KH, Ok YS, Performance of metal-organic frameworks for the adsorptive removal of potentially toxic elements in a water system: A critical review, *RSC Adv* 2019;9: 4359–76.

[17] Zhao G, Qin N, Pan A, Wu X, Peng C, Ke F, Iqbal M, Ramachandraiah K, Zhu J, Magnetic nanoparticles@metal-organic framework composites as sustainable environment adsorbents, *J Nanomater* 2019; 2019: 1-11.

[18] Kobielska PA, Howarth AJ, Farha OK, Nayak S, Metal–organic frameworks for heavy metal removal from water, *Coord Chem Rev* 2018;358: 92–7.

[19] Yu H, Shao P, Fang L, Pei J, Ding L, Pavlostathis SG, Palladium ion-imprinted polymers with PHEMA polymer brushes: Role of grafting polymerization degree in anti-interference, *Chem Eng J* 2019;359: 176–85.

[20] Yuan G, Tu H, Liu J, Zhao C, Liao J, Yang Y, Yang J, Liu N, A novel ion-imprinted polymer induced by the glycylglycine modi fi ed metal- organic framework for the selective removal of Co(II) from aqueous solutions, *Chem Eng J* 2018;333: 280–88.

[21] Chiu YH, Chang TFM, Chen CY, Sone M, Hsu YJ, Mechanistic insights into photodegradation of organic dyes using heterostructure photocatalysts, *Catalysts* 2019;9: 430-61.

[22] Meng Z, Lu R, Rao D, Kan E, Catenated metal-organic frameworks: Promising hydrogen purification materials and high hydrogen storage medium with further lithium doping, *Int. J. Hydrogen Energy* 2017;38; 9811–18.

[23] Farha OK, Hupp T, Activation of metal-organic framework materials, *Acc Chem Res* 2010;43: 1166-75.

[24] Jiang H, Makal TA, Zhou H, Interpenetration control in metal – organic frameworks for functional applications, *Coord Chem Rev* 2013;257: 2232–49.

[25] Rungtaweevoranit B, Diercks CS, Kalmutzki MJ, Yaghi OM, Spiers memorial lecture: Progress and prospects of reticular chemistry, *Faraday Discuss* 2017;201: 9–45.

[26] Petit C, Present and future of MOF research in the field of adsorption and molecular separation, *Curr Opin Chem Eng* 2018;20,: 132–42.

[27] Perez EV, Karunaweera C, Musselman IH, Balkus KJ, Ferraris JP, Origins and evolution of inorganic-based and MOF-based mixed-matrix membranes for gas separations, *Processes* 2016;4: 32-9.

[28] Yun W, Perera SP, Burrows AD, Microporous and mesoporous materials manufacturing of metal-organic framework monoliths and their application in CO_2 adsorption, *Microporous Mesoporous Mater* 2015;214: 149–55.

[29] Lee SJ, Yoon JW, Seo YK, Kim MB, Lee SK, Lee UH, Hwang YK, Bae YS, Chang JS, Microporous and mesoporous materials effect of purification conditions on gas storage and separations in a chromium-based metal–organic framework MIL-101, *Microporous Mesoporous Mater* 2014;93: 160–65.

[30] Huang Z, Kee H, Micro-solid-phase extraction of organochlorine pesticides using porous metal-organic framework MIL-101 as sorbent, *J Chromatogr A* 2015;1401: 9–6.

[31] Wu Z, Huang X, Zheng H, Wang P, Hai G, Dong W, Wang G, Environmental aromatic heterocycle-grafted NH_2-MIL-125(Ti) via conjugated linker with enhanced photocatalytic activity for selective oxidation of alcohols under visible light, *Appl Catal B Environ* 2018;224: 479–87.

[32] Yang D, Gates BC, Catalysis by metal organic frameworks: Perspective and suggestions for future research, *ACS Catal* 2019;9: 1779-98.

[33] Kumar K, Maddila S, Babu S, Jonnalagadda SB, A review on contemporary

metal–organic framework materials, *Inorganica Chim Acta* 2016;446: 61–4.

[34] Zhang S, Yang Q, Liu X, Qu X, Wei Q, Xie G, High-energy metal–organic frameworks (HE-MOFs): Synthesis, structure and energetic performance, *Coord Chem Rev* 2016;307: 292–12.

[35] Lee YR, Kim J, Ahn WS, Synthesis of metal-organic frameworks: A mini review, *Korean J ChemEng* 2013;30: 1667–80.

[36] Kurian VRRM, Synthesis and catalytic applications of metal–organic frameworks: a review on recent literature, *Int Nano Lett* 2019;9: 17–9.

[37] Elsaidi SK, Mohamed MH, Banerjee D, Thallapally PK, Flexibility in metal–organic frameworks: A fundamental understanding, *Coord Chem Rev* 2018;358: 125–52.

[38] Kim SI, Yoon TU, Kim MB, Lee SJ, Hwang YK, Chang JS, Kim HJ, Lee HN, Lee UH, Bae YS, Metal–organic frameworks with high working capacities and cyclic hydrothermal stabilities for fresh water production, *Chem Eng J* 2016;286: 467–75.

[39] Alhamami M, Doan H, Cheng C, A review on breathing behaviours of metal-organic-frameworks (MOFs) for gas adsorption, *Materials* 2014;7: 3198–50.

[40] Deria P, Mondloch JE, Karagiaridi O, Bury W, Hupp JT, Farha OK, Beyond post-synthesis modification: Evolution of metal-organic frameworks via building block

replacement, *Chem Soc Rev* 2014;43: 5896–12.

[41] Cook TR, Zheng Y, Stang PJ, Metal−organic frameworks and self-assembled supramolecular coordination complexes : Comparing and contrasting the design, synthesis, and functionality of metal−organic materials, *Chem Rev* 2020;113: 734-77.

[42] Langseth E, Swang O, Arstad B, Lind A, Cavka JH, Jensen TL, TKristensen TE, Moxnes J, Unneberg E, Heyn RH, Synthesis and characterisation of Al@MOF materials, *Mater Chem Phys* 2019;226: 220–25.

[43] Maponya TC, Hato MJ, Modibane KD, Makgopa K. Photocatalysts in advanced oxidation processes for wastewater Treatment. In: Fosso-Kankeu E, Pandey S, Sinha Ray S, editors. Metal-organic frameworks as possible candidates for photocatalytic degradation of dyes in wastewater. John Wiley & Sons Publishers; 2020. p. 65-92.

[44] Hashemi B, Zohrabi P, Raza N, Kim K, Metal-organic frameworks as advanced sorbents for the extraction and determination of pollutants from environmental, biological , and food media, *Trends Anal Chem* 2017;97: 65–2.

[45] Chen B, Xiang S, Qian G, Metal-organic frameworks with functional pores for recognition of small molecules, *Acc Chem Res* 2010;43: 1115–24.

[46] Ren J, Langmi HW, North BC, Mathe M, Review on processing of metal–organic framework (MOF) materials towards system integration for hydrogen storage,

Int J Energy Res 2014;39: 607-20.

[47] Kirchon A, Feng L, Drake HF, Joseph EA, Zhou HC, From fundamentals to applications: A toolbox for robust and multifunctional MOF Materials, *Chem Soc Rev* 2018;47: 8611-38.

[48] Bosch M, Zhang M, Zhou H, Increasing the stability of metal-organic frameworks, *Adv Chem* 2014;2014: 1-8.

[49] Dhaka S, Kumar R, Deep A, Kurade MB, Ji S, Jeon B, Metal–organic frameworks (MOFs) for the removal of emerging contaminants from aquatic environments, *Coord Chem Rev* 2019;380: 330–52.

[50] Li Y, Yang RT, Gas adsorption and storage in metal-organic framework MOF-177, *Langmuir* 2007;23: 12937–44.

[51] Thomas KM, Hydrogen adsorption and storage on porous materials, *Catal Today* 2007;120: 389–98.

[52] Furukawa H, Cordova KE, O'Keeffe M, Yaghi OM, The chemistry and applications of metal-organic frameworks, *Science* 2013;341: 1230444-55.

[53] Wang S, Bromberg L, Schreuder-gibson H, Hatton TA, Organophophorous ester degradation by chromium(III) terephthalate metal−organic framework (MIL-101) chelated to N,N-dimethylaminopyridine and related aminopyridines, *ACS Appl Mater* 2013;5: 1269-78.

[54] Wang Z, Ge L, Li M, Lin R, Wang H, Zhu Z, Orientated growth of copper-based MOF for acetylene storage, *Chem Eng J* 2019;357: 320-27.

[55] Zhang L, Wang J, Ren X, Zhang W, Zhang T, Liu X, et al., Internally extended growth of core-shell NH_2-MIL-101(Al)@ZIF-8 nanoflowers for the simultaneous detection and removal of Cu(II), *J Mater Chem A* 2018;6: 21029–38.

[56] Drout RJ, Robison L, Chen Z, Islamoglu T, Farha OK, Zirconium metal–organic frameworks for organic pollutant adsorption, *Trends Chem* 2019;3: 304-17.

[57] Jiao L, Yen J, Seow R, Skinner WS, Wang ZU, Jiang H, Metal–organic frameworks: Structures and functional applications, *Mater Today* 2018;27: 43-8.

[58] Rowsell JLC, Yaghi OM, Metal–organic frameworks: a new class of porous materials, *Microporous Mesoporous Mater* 2004;73: 3–14.

[59] Joseph L, Jun BM, Jang M, Park CM, Muñoz-Senmache JC, Hernández-Maldonado AJ, et al., Removal of contaminants of emerging concern by metal-organic framework nanoadsorbents: A review, *Chem Eng J* 2019;369: 928–46.

[60] Song Y, Yan B, Chen Z, Hydrothermal synthesis, crystal structure and luminescence of four novel metal–organic frameworks, *J Solid State Chem* 2006;179: 4037–46.

[61] Lee Y, Kim J, Ahn W, Synthesis of metal-organic frameworks: A mini review,

Korean J Chem Eng 2013;30: 1667–80.

[62] Monama GR, Hato MJ, Ramohlola KE, Maponya TC, Mdluli SB, Molapo KM, et al., Hierarchiral 4-tetranitro copper (II) phthalocyanine based metal organic framework hybrid composite with improved electrocatalytic efficiency towards hydrogen evolution reaction, *Res Phys* 2019;15: 102564-75.

[63] Zhao Y, Song Z, Li X, Sun Q, Cheng N, Lawes S, Metal organic frameworks for energy storage and conversion, *Energy Storage Mater* v2016;2: 35–2.

[64] Choi JY, Kim J, Jhung SH, Kim H, Chang J, Chae HK, Microwave synthesis of a porous metal-organic framework , zinc terephthalate MOF-5, *Bull Korean Chem Soc* 2006;27: 1523–24.

[65] Stock N, Biswas S, Synthesis of metal-organic frameworks (MOFs): routes to various MOF topologies, morphologies, and composites, *Chem Rev* 2012; 112, 933–69.

[66] Ren J, Dyosiba X, Musyoka NM, H. W. Langmi, Mathe M, Review on the current practices and efforts towards pilot-scale production of metal-organic frameworks (MOFs), *Coord Chem Rev* 2017;352: 187–19.

[67] Dey C, Kundu T, Biswal BP, Mallick A, Banerjee R, Crystalline metal-organic frameworks (MOFs): synthesis, structure and function, *Acta Crystallogr B* 2014;70: 3–10.

[68] Chen Y, Zhang R, Jiao L, Jiang H, Metal–organic framework-derived porous materials for catalysis, *Coord Chem Rev* 2018; 362: 1–23.

[69] Volkova EI, Vakhrushev AV, Suyetin M, Improved design of metal-organic frameworks for efficient hydrogen storage at ambient temperature: A multiscale theoretical investigation, *Int J Hydrogen Energy* 2014; 39: 8347–50.

[70] Zeng L, Guo X, He C, Duan C, Metal−organic frameworks: versatile materials for heterogeneous photocatalysis, *ACS Catal* 2016; 6: 7935-47.

[71] Tranchemontagne DJ, Hunt JR, Yaghi OM, Room temperature synthesis of metal-organic frameworks: MOF-5 , MOF-74 , *Tetrahedron* 2008;64: 8553–57.

[72] Ahmed I, Jhung SH, Composites of metal–organic frameworks: Preparation and application in adsorption, *Biochem Pharmacol* 2014;17:136–46.

[73] Burnett BJ, Barron PM, Hu C, Choe W, Stepwise synthesis of metal À organic frameworks: Replacement of structural organic linkers, *J Am Chem Soc* 2011;133: 9984–87.

[74] Azad FN, Ghaedi M, Dashtian K, Hajati S, Pezeshkpour V, Ultrasonically assisted hydrothermal synthesis of activated carbon-HKUST-1-MOF hybrid for efficient simultaneous ultrasound-assisted removal of ternary organic dyes and antibacterial investigation: Taguchi optimization, *Ultrason Sonochem* 2016;31: 383–93.

[75] Safaei M, Mehdi M, Ebrahimpoor N, A review on metal-organic frameworks: Synthesis and applications, *Trends Anal Chem* 2019;118: 401–25.

[76] Candu N, Tudorache M, Florea M, Ilyes E, Vasiliu F, Mercioniu I, et al., Postsynthetic modification of a metal-organic framework (MOF) structure for enantioselective catalytic epoxidation, *Chempluschem* 2013;78: 443–50.

[77] Burrows AD, Jiang D, Keenan LL, Burrows AD, Edler KJ, Synthesis and post-synthetic modification of MIL-101(Cr)-NH_2 via a tandem diazotisation process, *ChemComm* 2012;48: 99–02.

[78] Lei J, Qian R, Ling P, Cui L, Ju H, Design and sensing applications of metal–organic framework composites, *Trends Anal Chem* 2014;58: 71–8.

[79] Kim J, Kim DO, Kim DW, Sagong K, Synthesis of MOF having hydroxyl functional side groups and optimization of activation process for the maximization of its BET surface area, *J Solid State Chem* 2013;197: 261–65.

[80] Wang L, Zheng M, Xie Z, Nanoscale metal–organic frameworks for drug delivery: a conventional platform with new promise, *J Mater Chem B* 2018;6: 707-17.

[81] Hui M, Loon K, Zheng G, Synthesis and applications of MOF-derived porous nanostructures, *Green Energy Environ* 2017;2: 218–45.

[82] Asadian E, Shahrokhian S, Iraji A, Highly sensitive nonenzymetic glucose

sensing platform based on MOF-derived NiCo LDH nanosheets/graphene nanoribbons composite, *J Electroanal Chem* 2018;808: 114–23.

[83] Li S, Huo F, Metal–organic framework composites: from fundamentals to applications, *Nanoscale* 2015;7: 7482–01.

[84] Liu Y, Liu Z, Huang D, Cheng M, Zeng G, Lai C, Metal or metal-containing nanoparticle@MOF nanocomposites as a promising type of photocatalyst, *Coord Chem Rev* 2019;388: 63–8.

[85] Beg S, Rahman M, Jain A, Saini S, Midoux P, Pichon C, et al., Nanoporous metal organic frameworks as hybrid polymer–metal composites for drug delivery and biomedical applications, *Drug Discov Today* 2017;22: 625–37.

[86] Deria P, Mondloch JE, Karagiaridi O, Bury W, Hupp JT, Farha OK, Beyond post-synthesis modification: evolution of metal–organic frameworks via building block replacement, *Chem Soc Rev* 2014;43: 41–4.

[87] Yin Z, Wan S, Yang J, Kurmoo M, Zeng M, Recent advances in post-synthetic modification of metal–organic frameworks: New types and tandem reactions, *Coord Chem Rev* 2019;378: 500–12.

[88] Wei J, Hu Y, Liang Y, Kong B, Zhang J, Song J, et al., Nitrogen-doped nanoporous carbon/graphene nano- sandwiches : synthesis and application for efficient oxygen reduction, *Adv Funct Mater* 2015;25: 768–77.

[89] Chen Y, Mu X, Lester E, Wu T, High efficiency synthesis of HKUST-1 under mild conditions with high BET surface area and CO_2 uptake capacity, *Prog Nat Sci Mater Int* 2018;28: 584–89.

[90] Deng K, Hou Z, Li X, Li C, Zhang Y, Deng X, et al., Aptamer-mediated up-conversion core/MOF shell nanocomposites for targeted drug delivery and cell imaging, *Sci Rep* 2015;5: 7851–57.

[91] Lin S, Zhao Y, Bediako JK, Cho C, Sarkar AK, Structure-controlled recovery of palladium (II) from acidic aqueous solution using metal-organic frameworks of MOF-802 , UiO-66 and MOF-808, *Chem Eng J* 2019;362: 280–86.

[92] Ahmed I, Jhung SH, Remarkable adsorptive removal of nitrogen-containing compounds from a model fuel by a graphene oxide/MIL-101 composite through a combined effect of improved porosity and hydrogen bonding, *J Hazard Mater* 2016;314: 318–25.

[93] Kareem HM, Alrubaye RTA, Synthesis and Characterisation of Metal Organic Frameworks for Gas Storage, *IOP Conf Ser Mater Sci Eng* 2019;518: 062013-21.

[94] Chowdhury MA, Metal-Organic-Frameworks for biomedical applications in drug delivery, and as MRI contrast agents, *J Biomed Mater Res A* 2017;105: 1184-94.

[95] Katoch A, Goyal N, Gautam S, Applications and advances in coordination

cages : Metal-Organic Frameworks, *Vacuum* 2019;167: 287–00.

[96] Al MH, Abid HR, Sunderland B, Wang S, Metal organic frameworks as a drug delivery system for flurbiprofen, *Drug Des Dev Ther* 2017;11: 2685–95.

[97] Fang X, Zong B, Mao S, Metal–organic framework-based sensors for environmental contaminant sensing, *Nano-Micro Lett* 2018;10: 1–19.

[98] Qiu S, Zhu G, Molecular engineering for synthesising novel structures of metal – organic frameworks with multifunctional properties, *Coordin Chem Rev 2*009;253: 2891–11.

[99] Mashao G, Ramohlola KE, Mdluli SB, Monama GR, Hato MJ, Makgopa K, et al., Zinc-based zeolitic benzimidazolate framework/polyaniline nanocomposite for electrochemical sensing of hydrogen gas, *Mater Chem Phys* 2019;230: 287–98.

[100] Zhao M, Huang Y, Peng Y, Huang Z, Ma Q, Two-dimensional metal–organic framework nanosheets: synthesis and applications, *Chem Soc Rev* 2018;47: 6267-95.

[101] Xu W, Bahadur K, Ju Q, Fang Z, Huang W, Heterogeneous catalysts based on mesoporous metal – organic frameworks, *Coord Chem Rev* 2018;373: 199-32.

[102] Chughtai AH, Ahmad N, Younus HA, Laypkov A, F. Verpoort F, Metal-organic frameworks: Versatile heterogeneous catalysts for efficient catalytic organic transformations, *Chem Soc Rev* 2015;44: 6804-49.

[103] Kleist W, Maciejewski M, Baiker A, MOF-5 based mixed-linker metal–organic frameworks: Synthesis, thermal stability and catalytic application, *Thermochim Acta* 2010;499: 71–8.

[104] Wang B, Liu W, Zhang W, Liu J, Nanoparticles@nanoscale metal-organic framework composites as highly efficient heterogeneous catalysts for size- and shape-selective reactions, *Nano Res* 2017;10: 3826-35.

[105] Xue D, Wang Q, Bai J, Amide-functionalised metal – organic frameworks : Syntheses , structures and improved gas storage and separation properties, *Coord Chem Rev* 2019;378: 2–16.

[106] Li H, Li L, Lin R, Zhou W, Zhang Z, Xiang S, Porous metal-organic frameworks for gas storage and separation: Status and challenges, *Energy Chem* 2019;1: 100006-44.

[107] Zn O, Kaye SS, Dailly A, Yaghi OM, Long JR, Impact of preparation and handling on the hydrogen storage properties of Zn_4O(1,4-benzenedicarboxylate)$_3$ (MOF-5), *J Am Chem Soc* 2007;129: 14176-77.

[108] Kim J, Yeo S, Jeon JD, Kwak SY, Enhancement of hydrogen storage capacity and hydrostability of metal-organic frameworks (MOFs) with surface-loaded platinum nanoparticles and carbon black, *Microporous Mesoporous Mater* 2015;202: 8–15.

[109] Zhou H, Zhang J, Zhang J, Yan X, Shen X, High-capacity room-temperature

hydrogen storage of zeolitic imidazolate framework/graphene oxide promoted by platinum metal catalyst, *Int J Hydrogen Energy* 2015;40: 12275-85.

[110] Kumar P, Bansal V, Kim K, Kwon EE, Metal-organic frameworks (MOFs) as futuristic options for wastewater treatment, *J Ind Eng Chem* 2018;62: 130-45.

[111] Pi Y, Li X, Q. Xia Q, J. Wu J, Y. Li Y, J. Xiao J, et al., Adsorptive and photocatalytic removal of persistent organic pollutants (POPs) in water by metal-organic frameworks (MOFs), *Chem Eng J* 2018;337: 351–71.

[112] Peng Y, Huang H, Zhang Y, Kang C, Chen S, Song L, et al., A versatile MOF-based trap for heavy metal ion capture and dispersion, *Nat Commun* 2018;9: 1-9.

[113] Zhou Y, Zhu J, Yang J, Lv Y, Zhu Y, Bi W, et al., Magnetic nanoparticles speed up mechanochemical solid phase extraction with enhanced enrichment capability for organochlorines in plants, *Anal Chim Acta* 2019;1066: 49–7.

[114] Wang T, Zhao P, Lu N, Chen H, Zhang C, Hou X, Facile fabrication of Fe_3O_4/MIL-101(Cr) for effective removal of acid red 1 and orange G from aqueous solution, *Chem Eng J* 2016;295: 403-13.

[115] Yang Q, Ren S, Zhao Q, Lu R, Hang C, Chen Z, et al., Selective separation of methyl orange from water using magnetic ZIF-67 composites, *Chem Eng J* 2017;333: 49-7.

[116] Wang C, Zhang Y, Li J, Wang P, Photocatalytic CO_2 reduction in metal–organic frameworks: A mini review, *J Mol Struct* 2015;1083: 127–36.

[117] Ngoepe NM, Hato MJ, Modibane KD, Hintsho-Mbita NC, Photocatalysts in advanced oxidation processes for wastewater Treatment. In: Fosso-Kankeu E, Pandey S, Sinha Ray S, editors. Biogenic synthesis of metal oxide nanoparticle semiconductors for wastewater treatment. John Wiley & Sons Publishers; 2020. p. 3-31.

[118] Zhao H, Xia Q, Xing H, Chen D, Wang H, Construction of pillared-layer MOF as efficient visible-light photocatalysts for aqueous Cr(VI) reduction and dye degradation, *ACS Sustain Chem Eng* 2017;5: 4449-56.

[119] Zhao S, Wang G, Poelman D, Metal organic frameworks based materials for heterogeneous photocatalysis, *Molecules* 2018;23: 2947–69.

[120] Ahmed S, Rasul MG, Martens WN, Advances in heterogeneous photocatalytic degradation of phenols and dyes in wastewater: A review, *Water Air Soil Pollut* 2011; 215: 3–29.

[121] Du PD, Thanh HTM, To TC, Thang HS, Tinh MX, Tuyen TN, et al., Metal-organic framework MIL-101: Synthesis and photocatalytic degradation of remazol Black B dye, *J Nanomater* 2019;2019: 1-15.

[122] Yi X, Wang F, Du X, Fu H, Wang C, Highly efficient photocatalytic Cr(VI) reduction and organic pollutants degradation of two new bifunctional 2D Cd/Co-

based MOFs, *Polyhedron* 2018;152: 216–24.

[123] Kumar SG, Rao KSRK, Comparison of modification strategies towards enhanced charge carrier separation and photocatalytic degradation activity of metal oxide semiconductors (TiO_2 , WO_3 and ZnO), *Appl Surf Sci* 2017;391: 124–48.

[124] Mondal C, Singh A, Sahoo R, Sasmal AK, Negishi Y, Pal T, Preformed ZnS nanoflower prompted evolution of CuS/ZnS p-n heterojunctions for exceptional visible-light driven photocatalytic activity, *New J Chem* 2015;39: 5628–35.

[125] Islam MJ, Kim HK, Reddy DA, Kim Y, Ma R, Baek H, et al., Hierarchical BiOI nanostructures supported on a metal organic framework as efficient photocatalysts for degradation of organic pollutants in water, *Dalton Trans* 2017;46: 6013–23.

[126] Kojtari A, Ji H-F, Metal organic framework micro/nanopillars of Cu(BTC)3H_2O and Zn(ADC)DMSO, *Nanomaterials* 2015;5: 565–76.

[127] Rodríguez NA, Parra R, Grela MA, Structural characterisation, optical properties and photocatalytic activity of MOF-5 and its hydrolysis products: implications on their excitation mechanism, *RSC Adv* 2015;5: 73112-18.

[128] Kaur R, Rana A, Singh RK, Chhabra VA, Kim K, Deep A, Efficient photocatalytic and photovoltaic applications with nanocomposites between CdTe QDs and an NTU-9 MOF, *RSC Adv* 2017;7: 29015–24.

[129] Sha Z, Chan HSO, Wu J, Ag_2CO_3/UiO-66(Zr) composite with enhanced visible-light promoted photocatalytic activity for dye degradation, *J Hazard Mater* 2015;299: 132–40.

[130] Wang C, Lin H, Xu Z, Cheng H, Zhang C, One-step hydrothermal synthesis of flowerlike MoS_2/CdS heterostructures for enhanced visible-light photocatalytic activities, *RSC Adv* 2015;5: 15621–26.

[131] Lee KM, Lai CW, Ngai KS, Juan JC, Recent developments of zinc oxide based photocatalyst in water treatment technology: A review, *Water Res* 2016;88: 428–48.

[132] Wang CC, Li JR, Lv XL, Zhang YQ, Guo G, Photocatalytic organic pollutants degradation in metal–organic frameworks, *Energy Environ Sci* 2014;7: 2831-67.

[133] Hong J, Chen C, Bedoya FE, Kelsall GH, O'Hare D, Petit C, Carbon nitride nanosheet/metal-organic framework nanocomposites with synergistic photocatalytic activities, *Catal Sci Technol* 2016;6: 5042–51.

[134] Fagan R, McCormack DE, Dionysiou DD, Pillai SC, A review of solar and visible light active TiO_2 photocatalysis for treating bacteria, cyanotoxins and contaminants of emerging concern, *Mater Sci Semicond Process* 2016;42: 2–14.

[135] Gao Y, Li S, Li Y, Yao L, Zhang H, Accelerated photocatalytic degradation of organic pollutant over metal-organic framework MIL-53(Fe) under visible LED

light mediated by persulfate, *Appl Catal B, Environ* 2017;202: 165–74.

[136] Wu Y, Luo H, Wang H, Synthesis of iron(iii)-based metal-organic framework/graphene oxide composites with increased photocatalytic performance for dye degradation, *RSC Adv* 2014;4: 40435–38.

[137] Sun Q, Liu M, Li K, Zuo Y, Han Y, Wang J, et al., Facile synthesis of Fe-containing metal-organic frameworks as highly efficient catalysts for degradation of phenol at neutral pH and ambient temperature, *CrystEngComm* 2015;17: 7160-68.

[138] Hausdorf S, Mossig R, Mertens FORL, Proton and water activity-controlled structure formation in zinc carboxylate-based metal organic frameworks, *J Phys Chem A* 2008;112: 7567–76.

[139] Alvaro M, Carbonell E, Ferrer B, Llabrøs FX, Semiconductor behaviour of a metal-organic framework (MOF), *Chem. Eur. J.*, 2007;13: 5106–12.

[140] Laurier KGM, Vermoortele F, Ameloot R, De Vos DE, Hofkens J, Roe MBJ, Iron(III)-based metal−organic frameworks as visible light photocatalysts, *J Am Chem Soc* 2013;135: 14488-91.

[141] Zhang C, Ma D, Zhang X, Ma J, Liu L, Xu X, Preparation, structure and photocatalysis of metal-organic frameworks derived from aromatic carboxylate and imidazole-based ligands, *J Coord Chem* 2016;69: 985-95.

[142] Zhang M, Wang L, Zeng T, Shang Q, Zhou H, Pan Z, et al., Two pure MOF-photocatalysts readily prepared for the degradation of methylene blue dye under visible light, *Dalton Trans* 2018;47: 4251-58.

[143] Feng X, Chen H, Jiang F, In-situ ethylenediamine-assisted synthesis of a magnetic iron-based metal-organic framework MIL-53(Fe) for visible light photocatalysis, *J Colloid Interface Sci* 2017;494: 32–7.

[144] Zhu SR, Liu PF, Wu MK, Zhao WN, Li GC, Tao K, et al., Enhanced photocatalytic performance of BiOBr/NH_2-MIL-125(Ti) composite for dye degradation under visible light, *Dalt Trans* 2016;45: 17521–29.

[145] Yang J, Niu X, An S, Chen W, Wang J, Liu W, Facile synthesis of Bi_2MoO_6-MIL-100(Fe) metal-organic framework composites with enhanced photocatalytic performance, *RSC Adv* 2017;7: 2943–52.

[146] Wang H, Yuan X, Wu Y, Zeng G, Chen X, Leng L, et al., Synthesis and applications of novel graphitic carbon nitride/metal-organic frameworks mesoporous photocatalyst for dyes removal, *Appl Catal B Environ* 2015;174–175: 445–54.

[147] Guo D, Wen R, Liu M, Guo H, Chen J, Weng W, Facile fabrication of g-C_3N_4/MIL-53(Al) composite with enhanced photocatalytic activities under visible-light irradiation, *Appl Organomet Chem* 2015;29: 690–97.

[148] Huang L, Liu B, Synthesis of a novel and stable reduced graphene oxide/MOF

hybrid nanocomposite and photocatalytic performance for the degradation of dyes, *RSC Adv* 2016;6: 17873–79.

[149] Fazaeli R, Aliyan H, Banavandi RS, Sunlight assisted photodecolorization of malachite green catalysed by MIL-101/graphene oxide composites, *Russ J Appl Chem* 2015;88: 169–77.

[150] Liang R, Jing F, Shen L, Qin N, Wu L, M@MIL-100(Fe) (M = Au, Pd, Pt) nanocomposites fabricated by a facile photodeposition process: Efficient visible-light photocatalysts for redox reactions in water, *Nano Res* 2015;8: 3237–49.

[151] Ai L, Zhang C, Li L, Jiang J, Iron terephthalate metal–organic framework: Revealing the effective activation of hydrogen peroxide for the degradation of organic dye under visible light irradiation, *Appl Catal B Environ* 2014;148–149: 191–00.

[152] Abney CW, Gilhula JC, Lu K, Lin W, Metal-organic framework templated inorganic sorbents for rapid and efficient extraction of heavy metals, *Adv Mater* 2014;26: 7993-97.

[153] Salarian M, Ghanbarpour A, A metal-organic framework sustained by a nanosized Ag12 cuboctahedral node for solid-phase extraction of ultra traces of lead (II) ions, *Microchim Acta* 2014;181: 999–07.

[154] Shi Z, Xu C, Guan H, Li L, Fan L, Wang Y, et al., Magnetic metal organic frameworks (MOFs) composite for removal of lead and malachite green in

wastewater, *Colloids Surf A Physicochem Eng Asp* 2018;539: 382–90.

[155] Wu Y, Xu G, Liu W, Yang J, Wei F, Li L, et al., Postsynthetic modification of copper terephthalate metal-organic frameworks and their new application in preparation of samples containing heavy metal ions, *Microporous Mesoporous Mater* 2015;210: 110–15.

[156] Lu M, Li L, Shen S, Chen D, Han W, Highly efficient removal of Pb^{2+} by a sandwich structure of metal-organic framework/GO composite with enhanced stability, *New J Chem* 2019;43: 1032–37.

[157] Lin S, Bediako JK, Cho CW, Song MH, Zhao Y, Kim JA, et al., Selective adsorption of Pd(II) over interfering metal ions (Co(II), Ni(II), Pt(IV)) from acidic aqueous phase by metal-organic frameworks, *Chem Eng J* 2018;345: 337–44.

[158] Luo BC, Yuan LY, Chai ZF, Shi WQ, Tang Q, U(VI) capture from aqueous solution by highly porous and stable MOFs: UiO-66 and its amine derivative, *J Radioanal Nucl Chem* 2016;307: 269–76.

[159] Alqadami AA, Naushad M, Alothman ZA, Ghfar AA, Novel metal-organic framework (MOF) based composite material for the sequestration of U(VI) and Th(IV) metal ions from aqueous environment, *ACS Appl Mater Interfaces* 2017;9: 36026–37.

[160] Tahmasebi E, Masoomi MY, Yamini Y, Morsali A, Application of mechanosynthesised azine-decorated zinc(II) metal-organic frameworks for

highly efficient removal and extraction of some heavy-metal ions from aqueous samples: A comparative study, *Inorg Chem* 2015;54: 425–33.

[161] Bagheri A, Taghizadeh M, Behbahani M, Akbar A, Synthesis and characterisation of magnetic metal-organic framework (MOF) as a novel sorbent, and its optimization by experimental design methodology for determination of palladium in environmental samples, *Talanta* 2012;99: 132–39.

[162] Yuan G, Tu H, Li M, Liu J, Zhao C, Liao J, et al., Glycine derivative-functionalised metal-organic framework (MOF) materials for Co (II) removal from aqueous solution, *Appl Surf Sci* 2019;466: 903–10.

[163] Wang N, Yang LY, Wang YG, Ouyang XK, Fabrication of composite beads based on calcium alginate and tetraethylenepentamine-functionalised MIL-101 for adsorption of Pb(II) from aqueous solutions, *Polymers* 2018;10: 750-64..

[164] Wang C, Du X, Li J, Guo X, Wang P, Zhang J, Photocatalytic Cr(VI) reduction in metal-organic frameworks: A mini-review, *Applied Catal B, Environ* 2016;193: 198–16.

[165] Shi L, Wang T, Zhang H, Chang K, Meng X, Liu H, An amine-functionalised iron (III) metal–organic framework as efficient visible-light photocatalyst for Cr (VI) Reduction, *Adv Sci* 2015;2: 1500006-13.

[166] Yu H, Shao P, Fang L, Pei J, Ding L, Pavlostathis SG, Palladium ion-imprinted polymers with PHEMA polymer brushes: Role of grafting polymerization degree

in anti-interference, *Chem Eng J* 2019;359: 176–85.

[167] Guo Z, Florea A, Jiang M, Mei Y, Zhang W, Jaffrezic-renault N, Molecularly Imprinted polymer/metal organic framework based chemical sensors, *Coatings* 2016;6: 42–50.

[168] Lin S, Wei W, Wu X, Zhou T, Mao J, Yun Y, Selective recovery of Pd (II) from extremely acidic solution using ion-imprinted chitosan fiber: Adsorption performance and mechanisms, *J Hazard Mater* 2015;299: 10–7.

[169] Tao HC, Gu YH, Liu W, Huang SB, Cheng L, Zhang LJ, et al., Preparation of palladium (II) Ion-imprinted polymeric nanospheres and its removal of palladium (II) from aqueous solution, *Nanoscale Res Lett* 2017;12: 583-91.

[170] Mafu LD, Mamba BB, Msagati TAM, Synthesis and characterisation of ion imprinted polymeric adsorbents for the selective recognition and removal of arsenic and selenium in wastewater samples, *J Saudi Chem Soc* 2016;20: 594–05.

CHAPTER THREE

HIGHLIGHTING THE IMPORTANCE OF CHARACTERISATION TECHNIQUES EMPLOYED IN ADSORPTION USING METAL–ORGANIC FRAMEWORKS FOR WATER TREATMENT

3.1. INTRODUCTION

Fresh water is one of the vital needs that is required for life on earth. Unfortunately, due to the contamination of fresh water by several industrialised activities, water scarcity is a challenge across the globe [1,2]. Predictions have shown that there are possibilities that some areas will have serious water shortages by 2025 [3]. To overcome this challenge, the reusability of wastewater has become the ideal way to conserve and increase the availability of water in their reserves. The advantages of using recycled wastewater include irrigating agricultural soil, aquaculture, manufacturing consumption, recreational and environmental practices, as well as artificial groundwater recharge [1,2]. In general, recycled wastewater can be utilised in these processes and replace fresh water, provided a suitable purification procedure is implemented to acquire the desired water quality for the specified application [2]. Various water pollutants that are found in water bodies are classified according to their origin, with the main classifications being organic, biological, and inorganic [2,4,5]. Heavy metals (which form part of the inorganic pollutants) are the most investigated due to their persistence and non-biodegradable nature. Many of these types of contaminants are found to be toxic and carcinogenic, and can accumulate through food chains causing very serious health hazards to living organisms [6,7]. Furthermore, some heavy metals are of economic importance such as platinum group metals (PGMs), and therefore, their conservation and recycling have become important in order to meet future demands [8,9]. In an attempt to find solutions to these problems, scientists have investigated and developed several technologies including chemical precipitation, flocculation/coagulation, reverse osmosis, membrane filtration, and adsorption [6]. Due to the cost-effectiveness and simplicity of the adsorption method, in this review, we focus more on this method to narrate the instrumental techniques used to understand the structural effects of MOFs in wastewater treatment.

Adsorption is the process by which mass transfer occurs between substances at the interface of two phases. The phases in adsorption can either be liquid–solid, liquid–liquid, gas–liquid, or gas–solid. The solutes of gas or liquid (referred to as adsorbate) accumulate on the surface of an adsorbent (either solid or liquid) [10]. Depending on the properties and the constituents of the adsorbate and the adsorbent, there are two possibilities for the adsorption process that can take place. The first one is physisorption (adsorptive adsorption), which occurs when there is a physical adsorbate–adsorbent contact either through van der Waals, London, or dipole–dipole interactions [11,12]. These types of interactions are weak and can be reversed. Secondly, an interaction can occur between an adsorbent and an adsorbate which can result in the formation of a chemical bond referred to as chemisorption (reactive adsorption) [10,13,14]. Chemisorption takes place only on monolayers and the adsorbate–adsorbent interaction cannot be easily broken due to strong forces acting between them [10,11]. Factors that contribute to the type of adsorption process taking place are chemical structures such as functional groups and physical structures including specific surface area and pore size [15]. Generally, the adsorption process takes place naturally in many physical, biological, and chemical systems. Furthermore, this process is applicable in numerous industrial applications such as separation, purification of gases, [16,17], isolation of biological compounds [18], drug delivery [19] as well as in wastewater treatment [14,20].

The utilisation of adsorption technology in the remediation of polluted water is considered to be a feasible way to recycle wastewater by removing pollutants. The adsorption technique has enjoyed widespread attention in wastewater treatment due to the following advantages: cost-effectiveness, ease of implementation and operation, high efficiency, and the possibility to regenerate the adsorbent material since it is reversible [3,6]. Moreover, it allows for the use of a wide range of adsorbent materials and generates less harmful secondary products, which can be used for other applications. The process operates in the liquid phase where the dissolved pollutants (adsorbate) are transferred from the liquid state (wastewater) to the surface of an adsorbent, which, in many cases, is a solid material. The result of this mass transfer produces clean water which can be reused for other suitable applications [3]. For wastewater treatment through adsorption, the parameters that are taken into consideration include the properties (chemical and physical) of the characteristics of the adsorbent and adsorbate, effects of temperature, interaction time, solution pH,

amount of adsorbent, the initial concentration of adsorbate in liquid, as well as the effect of competing ions [21]. These parameters are the ones used when determining the adsorption capacities of adsorbent materials toward the targeted pollutant. In addition, the effectiveness of this method is deduced from the ability of the adsorbent to selectively target certain molecules, its reusability, and regeneration [3,15,22].

Metal–organic frameworks (MOFs) are currently in the spotlight of research due to their intrinsic properties that make them suitable for use in various applications. These materials are composed of metal ion centers that are connected to one another by organic linkers to achieve a variety of structural geometries [23,24]. Owing to the intriguing properties (i.e., high specific surface area, tuneable pore size, high porosity, and crystalline structure), MOFs have been explored in various applications such as gas sensors, energy storage, drug delivery, and water purification [25,26,27]. Furthermore, their surface functionality allows the incorporation of other functional materials to form composites. Recently, MOFs have attained great attention as suitable adsorbents for the recognition and elimination of heavy metal ions in wastewater treatment [23,28]. The presence of heavy metal ions in wastewater poses serious health threats to living organisms, even at low concentrations. One of the major steps in treating water that is contaminated with heavy metal ions is to determine and measure the initial concentrations of the pollutants that are present in the water. After the adsorption process has taken place, the efficiency/adsorption capacity of the adsorbent (i.e., MOFs) is obtained by measuring the remaining concentrations of heavy metal ions after separating the adsorbent from the adsorbate aqueous solution. The heavy metals that have been widely studied using MOFs and their composites as adsorbents include lead (Pb), chromium (Cr), rare earth elements (REE), mercury (Hg), arsenic (As), copper (Cu), cobalt (Co), nickel (Ni), and platinum group metals (PGMs). Analytical methods can be employed to determine the concentrations of heavy metals before and after adsorption. In addition, the adsorption mechanism can also be revealed by characterisation of the MOF adsorbent material before and after adsorption using spectroscopic, morphological and physical techniques. However, the poor solubility of MOFs in most organic solvents hinders the characterisation of MOF using some spectroscopic techniques. MOFs can easily be damaged by high energy electron irradiation using transmission electron microscopy. The most primitive MOFs have the inherent defects of poor electrical conductivity and low structural stability, which impact their practical performance.

In this review paper, we present some of the literature on the analytical techniques employed in studying and better understanding the adsorption behaviour of MOFs toward the removal of heavy metal ions in wastewater. Initially, a brief background on water pollution by heavy metal ions as well as MOFs as possible adsorbents is introduced in relation to the adsorption technology in wastewater treatment. This is followed by a discussion and comparison of different techniques such as UV-Vis, ICP-MS, ICP-OES, and FAAS used to analyse and to determine the remaining concentration of the heavy metals before and after adsorption. Furthermore, various methods of characterisation that assist in deducing the structures of MOF composites/nanocomposites and their possible interactions with heavy metals in the adsorption process are discussed.

3.2. ANALYTICAL METHODS FOR HEAVY METAL ANALYSIS

3.2.1. Inductively Coupled Plasma Mass Spectrometry

Inductively coupled plasma mass spectrometry (ICP-MS) is a powerful technique that combines both the advantages of ICP and a mass spectrometer to give elemental analysis data [29]. The incredible properties of this instrument include multiple elemental analysis ability, adequate precision, and lower detection limits. Furthermore, ICP-MS has a longer linear dynamic range, uncomplicated spectra, and the capability to rapidly analyse isotopes [29–31].

3.2.1.1. System Operation

The working principle of the ICP-MS is based on three main components:

Sample introduction and conversion to ions

In this step, the analyte (in liquid form) is introduced into the system through suction by a peristaltic pump which provides a constant uptake flow rate. In this case, an autosampler is used to optimize the analysis time and to reduce the consumption of reagents. The sample is pumped into the nebulization chamber, where it gets converted from a liquid solution to aerosol. The smallest droplets are carried to the plasma by the help of argon gas, whereas the larger droplets are drained out of the system.

ICP compartment

Initially, the analyte aerosol is filtered prior to being introduced into the plasma to prevent overloading the solvent which may result in plasma extinction. The argon plasma interacts with the electromagnetic field provided by the radiofrequency source

and it becomes generated on top of a torch. Once the aerosol is injected into the plasma, it instantaneously dissolves, vaporises, atomises, and subsequently ionizes depending on the ionisation potential of the individual elements. The argon plasma provides heat with high temperatures from 6000 to 10,000 K. Due to its chemical inertness and higher ionisation energy that emit a simple spectrum, argon gas is widely used in ICP. It is capable of ionising or exciting many elements of the periodic table without the formation of a stable compound with the analyte [32].

Mass spectrometer and detection system

The vaporized ions and atoms are then carried by argon gas from the ICP torch to the interface. The compartment of the interface is composed of two subsequent cones (skimmer and sampler) which permit the ions to focalize into a smaller volume. Followed by their introduction into the mass spectrometer, either a quadrupole or hexapole, they are separated based on their mass to charge ratio and then move to the detector. In ICP-MS, a detector is mostly an electron multiplier that works by converting ion signals to electric pulses [29,31–34]. The ICP-MS technique is adequate to quantitatively identify metal ions present in natural and drinking waters at trace levels, which are of particular relevance for toxicity control regions that may have been contaminated by toxic metals. ICP-MS has been recognised as a suitable method for adsorption/water treatment as it provides good sensitivity, requires minimal sample size, affords minimal elemental interferences, and readily provides a means to perform rapid and automated multi-elemental analyses. For example, an ICP-MS analytical instrument was employed in the work reported by Alqadami and colleagues [35]. The authors synthesised a nanocomposite of Fe_3O_4@AMCA-MIL-53(Al) for the adsorption of thorium Th(IV) and uranium U(IV) ions from simulated wastewater. Adsorption experiments were carried out by mixing 0.02 g of Fe_3O_4@AMCA-MIL-53(Al) with 25 mL of Th(IV) and U(VI) solutions containing 20 mg/L for 24 hours. For determining the maximum adsorption capacity, the initial concentrations of Th(IV) and U(VI) ranged between 20 and 400 mg/L with the optimum solution pH of 4.7 and 5.5 for Th(IV) and U(VI), respectively. Different temperatures of 25, 35, and 45 °C were investigated at a contact time of 300 min. The remaining concentrations of the analyte after adsorption were obtained from the ICP-MS analysis and the data are represented in Figure 3.1. For both Th(IV) and U(VI), the Fe_3O_4@AMCA-MIL53(Al) adsorbent showed increasing values of equilibrium adsorption capacities (q_e) as the temperatures and initial concentrations increased (see Figure 3.1 (a and b).

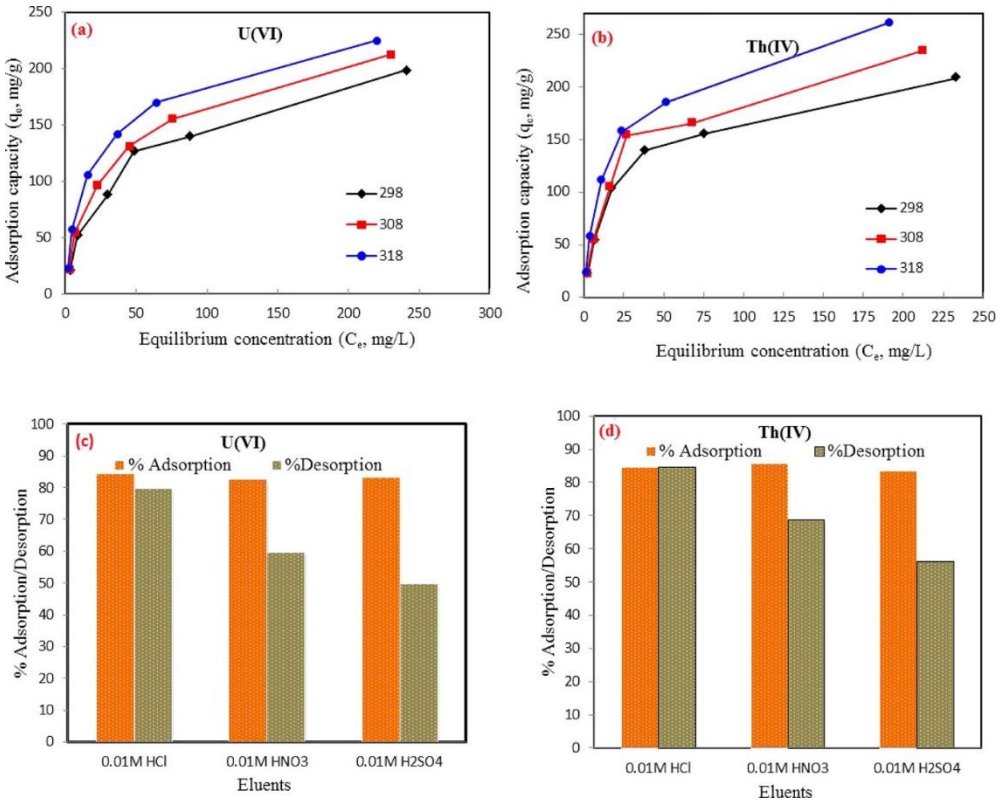

Figure 3.1: Temperature effect of the adsorption of (a) U(VI) and (b) Th(IV) ions by Fe_3O_4@AMCA-MIL53(Al) nanoadsorbent. Regeneration and reusability cycles towards (c) U(VI) and (d) Th(IV) metal ions [35].

Furthermore, the regeneration studies of the prepared Fe_3O_4@AMCA-MIL53(Al) were investigated by adsorption/desorption experiments and 25 mL of various acidic eluents of 0.01 M were used to regenerate the adsorbent material. The concentrations of Th(IV) and U(VI) were determined using ICP-MS and calculated from Equation (3.1):

$$\%adsorption = \frac{Co - Ce}{Co} \quad X \quad 100 \qquad (3.1)$$

The results obtained are represented in Figure 3.1 (c and d). On the basis of the data, the authors were able to conclude that 0.01 M HCl provided more desorption efficiency for Th(IV) and U(VI) as compared with HNO_3 and H_2SO_4 of the same concentration. The use of ICP-MS technique for adsorption studies provides the advantages of a smaller sample size, element-specific information, quantitation, rapid sample throughput, and significantly higher recovery of all elements of interest, especially the volatile elements. ICP-MS is characterised by the following advantages such as high sensitivity analysis, lower detection limits of most elements (ppt or ppb-range),

simultaneous multi-element analysis; wide dynamic range, and isotope composition. The disadvantages of ICP-MS are the high operational costs because of the high amount of argon used and the high susceptibility to high salt concentrations present in digest solutions or in sweat and saliva extraction solutions, resulting in interferences of the measurements.

3.2.2. Inductively Coupled Plasma Optical Emission Spectroscopy

Inductively coupled plasma optical emission spectroscopy (ICP-OES) was developed in the 1960s and first commercialized in the mid-1970s [33]. The sample introduction process in ICP-OES is analogous to one of the ICP-MS instruments. However, in ICP-OES, once the plasma has ionised, the analyte atoms move to the excited state and emit light energy upon their return to the ground state [33]. This light energy, which is emitted by metal atoms/ions, is transformed into an electrical signal followed by detection and quantitative measurements from a photoelectron multiplier tube (PMT). ICP-OES has advantages for the detection of heavy metals in water; however, this technique is limited by the need to transform a solid sample into a solution which is time consuming as it requires over 60% of the total time to complete the analysis. Thus, considerable improvement is required in this regard as there is a weak link in heavy metal analysis to ensure that the analytes are completely released and solubilised, i.e., total decomposition of the sample is achieved.

The recent work reported by Tang *et al*. [36] showed that pre-modification of Zr-based MOF with 4-amino-3-hydroxybenzoic acid and p-phthalaldehyde (AHPP) was effective in removing Pd(II) pollutants in simulated wastewater. They conducted their batch adsorption experiments by contacting 0.01 g of AHPP-MOF with 10 mL of 100 mg/L Pd(II) solution at a pH of 4.0. The samples were centrifuged for 24 hours at a speed of 280 rpm. The remaining concentrations of the Pd(II) ion were determined from the ICP-AES, Leeman Prodigy7, United States. The effects of initial concentration ranging from 100 to 600 mg/L and temperatures of 298, 308, and 318 K were used to determine the adsorption capacity. As shown in Figure 3.2(a), their results showed that the adsorption capacity increased as both the temperature and original concentration increased.

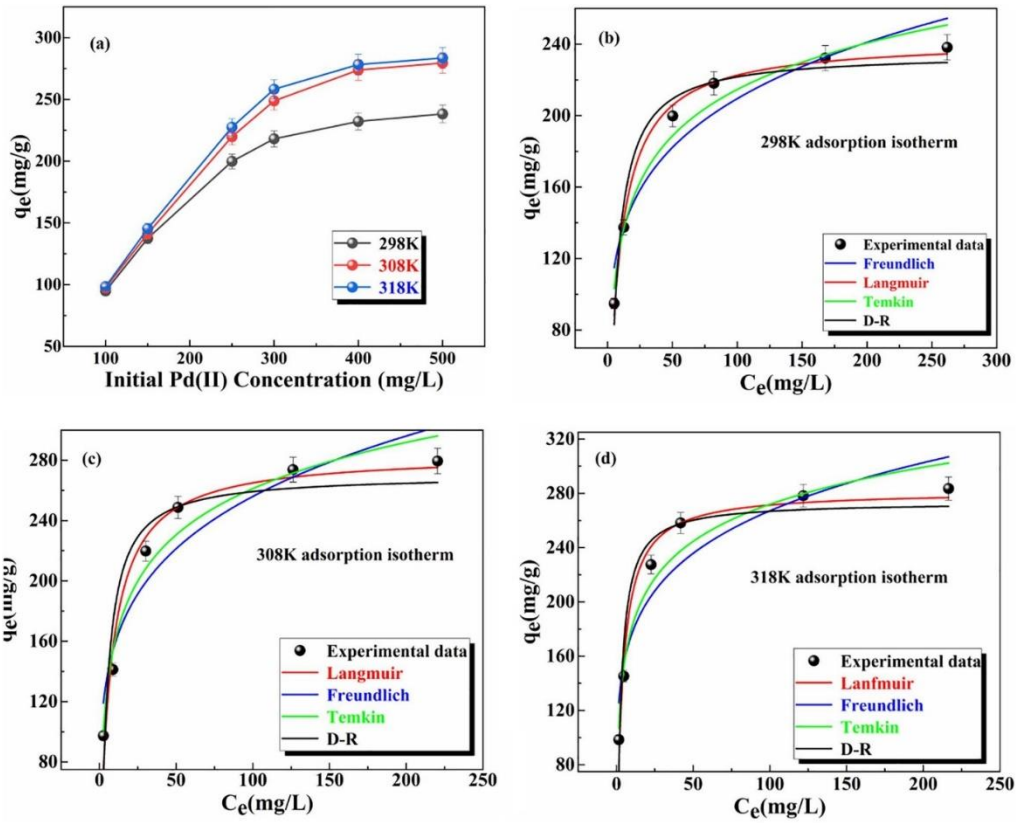

Figure 3.2: (a) Effect of Pd(II) initial concentration. Data fitting of adsorption isotherm models at: (b) 298 K; (c) 308 K; (d) 318 K [36].

Furthermore, the data obtained were fit to four different isotherm models (Langmuir, Freundlich, Temkin, and D-R), for the determination of maximum adsorption capacity (qm), as shown in Figure 3.2(b–d). The data fit the Langmuir more than others with qm values of 241.6, 288.48, and 293.65 mg g^{-1} at 298, 308, and 318 K, respectively. Therefore, the advantages of ICP-OES over an atomic absorption spectrometer and UV-VIS are that both simultaneous and sequential analyses of multiple elements is possible, the calibration function is spread over a wide dynamic range, and the number of measurable elements is high. However, one of the disadvantages of the ICP-OES method is the high argon consumption.

3.2.3. Flame Atomic Absorption Spectrometer

The spectroscopy of flame atomic absorption (FAAS) is one of the popular techniques that is utilised when determining the metal element concentrations present in particular analytes. The method was initially developed in 1952 and only became commercialized as an analytical technique in the 1960s [37] The FAAS technique was directly developed from atomic absorption spectroscopy (AAS) which is based on the

theory of atoms/ions having the ability to absorb light at a particular wavelength that is unique [38].

The main principle in FAAS involves the atomization of a solution containing the analyte using a flame. Firstly, the analyte (in solution form) is introduced into the system through an inlet tube into the nebulizer where the liquid is converted into small droplets (aerosol mist), followed by introduction into the flame [39,40]. Then, the flame atomizes the sample elements to their ground state atoms that are free and prone to excitation. A hollow cathode lamp provides pure light with a specific wavelength and energy which passes through the flame, and is absorbed by atoms/ions of the element of interest. Upon absorption of the light energy, the electrons in the atoms become excited and jump to higher energy levels. The radiation leaves the sample cell and goes to the monochromator where it is separated into wavelengths that are detected by a PMT. This is followed by intensification and conversion of the photon signals to electrons, which is quantified as electric current [41,42]. In AAS, these measurements assist in calculating the amount of the element present in an analyte in terms of absorbance and/or concentration [43]. The relationship between light absorption and the concentration of the element is described by the Beer–Lambert law, which assumes direct proportionality between them under certain conditions. To determine the unknown concentration of an analyte, a calibration curve is required which is obtained from the standard of a known concentration and more than 62 metal element concentrations can be obtained [39,44,45].

FAAS is preferred for determining trace levels of metal ions in environmental samples due to its simplicity and cost-effectiveness as compared with other instrumental techniques, such as ICP-OES and ICP-MS. However, analytes at lower levels than the detection limit of AAS and large amounts of salt in the real samples are the two primary limitations in determining metal ion levels though AAS. Such techniques are not sufficiently sensitive and selective for certain analyses. Thus, methods for separating or preconcentrating trace elements may be necessary before spectrometric analysis. In the work reported by Soltani and colleagues [46], a nanocomposite of layer-double hydroxide LDH/MOF was synthesised and employed in the adsorption of divalent mercury, Hg(II), and nickel, Ni(II) ions. For the adsorption experiments, they used a constant amount of 0.002 g mg of LDH/MOF nanocomposite, which was contacted with 20 mL of Hg(II) and Ni(II) at a temperature of 22 ± 3 °C and 200 rpm shaking speed. The main adsorption variables investigated were (see Figure 3.3): (a)

solution pH, (b) primary metal ions concentration, and (c) the interaction time. After the adsorption process took place, the LDH/MOF nanocomposite was separated from the Hg(II) and Ni(II) ions solutions by centrifuging at a speed of 5000 rpm. Then, the filtrates were analysed using a spectrometer (FAAS, PerkinElmer Model A300, Norwalk, USA) to determine the remaining concentrations of Hg(II) and Ni(II) in solution.

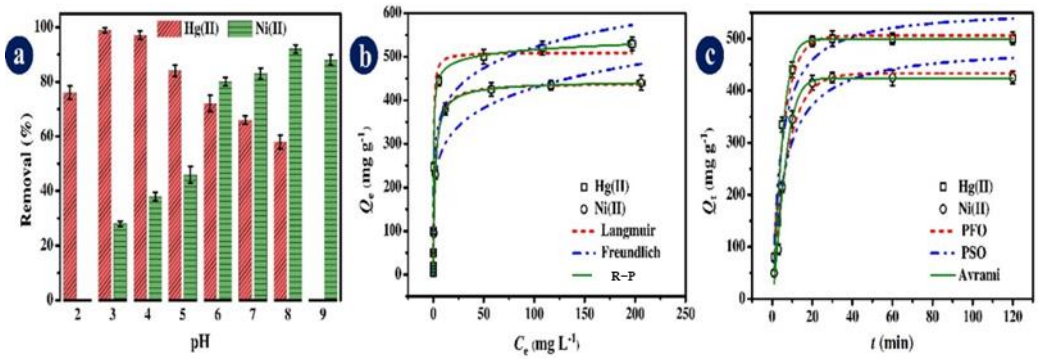

Figure 3.3: (a) Solution pH influence; (b) original Hg(II) and Ni(II) concentration with isotherm models fit; (c) interaction time with kinetic models fit [46].

From the pH studies, the authors observed an optimum removal percentage of 99% for Hg(II) at a pH of 3.0 and 96% for Ni(II) at a pH 8.0. As shown in Figure 3(b), there was an increase in the q_e with increases in the original concentration. The data was also used to calculate the qm value of LDH/MOF by fitting it to the nonlinear isotherm models of Langmuir, Freundlich, and Redlich–Peterson. From their conclusions, the data fitted the Langmuir more than the other models with qm values of 509.8 mg/g for Hg(II) and 441.0 mg/g for Ni(II). Furthermore, the kinetic data, as presented in Figure 3.3(c), showed that the LDH/MOF nanocomposite had fast kinetics for Hg(II) and Ni(II) and obeyed the Avrami kinetic model. Hence, AAS is appropriate for monitoring studies of a certain element. It is a fully automated procedure, and thus, a less labour-intensive method. The advantage is that this analytical method allows the determination of elements in very low mass concentrations (µg/L range), however, its disadvantage is the long analysis time per sample due to three or four replicates.

3.2.4. Ultraviolet-Visible Spectroscopy

The ultraviolet-visible (UV-Vis) spectroscopy is employed in studying the properties of samples by analysing the amount of light they can absorb or reflect [47]. The light that is used in the instrument is in the wavelengths of UV and the visible region of the

electromagnetic spectrum [47,48]. In principle, the light of a suitable wavelength is irradiated onto the molecule and absorbed by the π-electrons or non-bonding electrons within the molecule, and then detected and displayed as an absorbance peak. The absorbed wavelengths have energy associated with them and are responsible for the transition of electrons from the ground state to the excited state [49-58]. Depending on the composition of the sample that is being analysed, quantitative and qualitative measurements can both be obtained by comparing the analyte with a reference sample. The absorbed energy provides information about the components that are present in the sample, and therefore, their concentrations can be determined. This energy is determined from Equation (3.2) using the energy difference between the lower and higher energy levels:

$$E = hv \tag{3.2}$$

where *E*, *h,* and *v* represent the amount of energy absorbed, Planck constant, and the frequency, respectively. Then, Equation (3.2) is expanded into Equation (3.3), due to the wavelength associated with the light that is absorbed by molecules in spectroscopic studies [51,52]:

$$E = \frac{hc}{\lambda} \tag{3.3}$$

where the speed of light is denoted by *c* and *λ* is the maximum wavelength of light absorbed by the analyte sample. The UV-Vis instrument estimates the intensity of absorbed light as a function of absorbance (*A*) or transmittance (*T*), which are related by Equation (3.4):

$$A = -\log T \tag{3.4}$$

The interaction between electromagnetic radiation and molecules can be defined using Beer's law, which describes proportionality between the incident radiation and the concentration of the absorbing molecule with the rate of the monochromatic beam. Mathematically, Beer's law is expressed as Equation (3.5) [51]:

$$A = abc \tag{3.5}$$

Where *A, c, a,* and *b* representing the absorbance, concentration of the analyte, absorptivity constant, and path length of a cell, respectively. Due to the unit of concentration being molar (M), Beer's law is expressed as Equation (3.6):

$$A = \varepsilon bc \tag{3.6}$$

where ε denotes the molar absorptivity of the sample [47–54].

Daliran *et al*. [59] functionalised Zr-MOF with pyridyltriazol (Pyta) to selectively adsorb Pd(II) ions from an aqueous environment. For batch adsorption experiments, a 25 mL solution having 1 mg/L of Pd (II) at a pH of 4.5 was contacted with 0.01 g of UiO-66-Pyta for approximately 2−30 min. After adsorption, the authors separated the UiO-66-Pyta adsorbent from the Pd(II) ion solution by centrifuging at a speed of 5000 rpm and analysed the supernatant with a UV−Vis instrument at a wavelength of 410 nm. Figure 3.4(a) presents the results obtained after studying the influence of the original concentration of Pd(II) ions on the q_e value of UiO-66-Pyta. The data showed that q_e increased as the original concentration increased, and the qm value was deduced from the Langmuir isotherm as 294.1 mg/g.

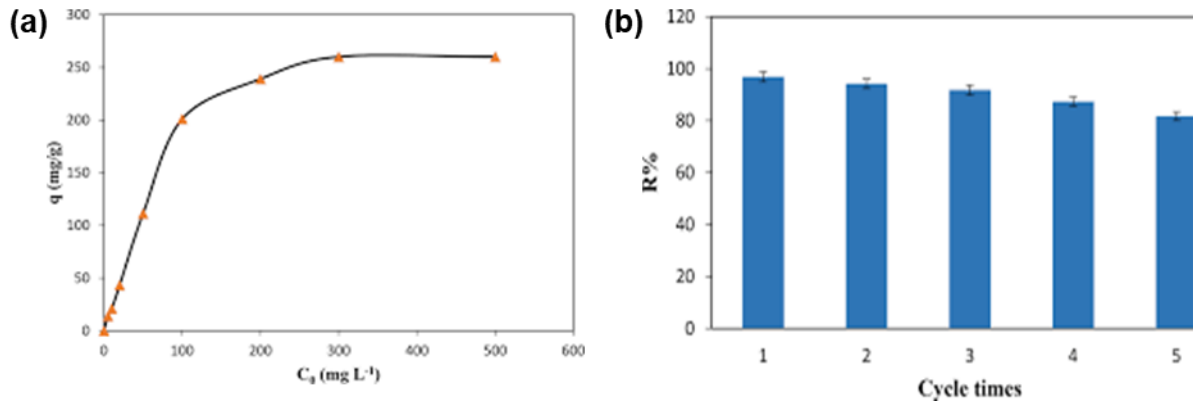

Figure 3.4: (a) The effect of initial Pd(II) ion concentration; (b) the reusability of UiO−66−Pyta for Pd(II) ions adsorption [59].

The authors further conducted adsorption/desorption trials to explore the potential reusability of the UiO−66−Pyta composite for the adsorption of Pd(II) ions, and the results are shown in Figure 3.4(b). The plotted data depicted that 96.9% was reduced to 81.7% after 5 consecutive cycles. The analysis conducted to determine the remaining concentrations of various metal ion pollutants in wastewater was shown to be effective using various detection techniques. Although some techniques have limited detection of other metal ion species, the obtained results display some potential utilisation of the prepared MOF-based adsorbent material. Table 3.1 presents some of the studies wherein different metal ions have been analysed by the chosen technique following adsorption with MOF composites. Therefore, there are several

advantages of UV-Vis such as a broad area of applicability, high sensitivity with a limit of detection (LOD) in the mg/L range, high selectivity, and a simple and rapid automatic method. However, there are some disadvantages including time-intensive sample preparation and measuring procedure (binding to complexes, adjusting of the pH value, special extraction procedures) to obtain coloured metal complexes which can be determined using UV-Vis interferences of other coloured substances in the sample.

Table 3.1: Different heavy metal detection techniques after the adsorption of heavy metal ions using MOF composites.

Prepared Adsorbent Material	**Targeted Metal Ion Pollutant**	**Analytical Technique Used**	**Adsorption Capacity Determined from the Isotherm Model (mg g^{-1})**	**Ref**
Diaminomaleonitrile (DAMN)/MIL-101(Cr)	U(IV)	ICP-AES and ICP-MS	601	[60]
MIL-125-HQ	Pb(II), Cd(II), Cu(II), and Cr(III)	AAS	262.1, 102.8, 66.9, and 53.9	[61]
MIL-101(Cr)/Fe_3O_4@ADTC	Se(IV) and Se(VI)	Electrothermal (ET)-AAS	197	[62]
NH_2-mSiO_2@MIL-101(Cr)	Cr(VI) and Pb(II)	UV-Vis and ICP-OES	73.2 and 161.3	[63]
MIL-101-PMIDA	Yttrium (Y) and lutetium (Lu)	ICP-MS	25.3 and 63.4	[64]
ED-MIL-101(Cr)	U(VI)	Trace uranium analyser	200	[65]
ED-MIL-101(Cr)	Cu(II) and Cd(II)	Optical emission spectrometer	69.9 and 63.15	[66]
$Ni_{0.6}Fe_{2.4}O_4$-UiO-66-PEI	Pb(II) and Cr(VI)	ICP-AES	273.2 and 428.6	[67]

SH@Cu-MOF	Hg(II)	FAAS	173	[68]

3.3. CHARACTERISATION OF MOF COMPOSITES FOR HEAVY METAL IONS ADSORPTION

3.3.1. Physical Characterisation

Physical methods are analytical techniques used to study and deduce information about the physical properties of compounds. These techniques assist in obtaining information about some of the phases that form part of the material structure, the potential surface reactivity looking at the area on the surface, as well as the functionality and possible geometry and atomic arrangements. They combine the fundamentals of both spectroscopic and microscopic techniques. Adsorption technology reveals information about the adsorption behaviour of MOF composites.

3.3.1.1. X-ray Diffraction

An X-ray diffraction (XRD) analytical instrument is mostly employed for determining the different phases of crystalline materials and obtaining data about the dimensions of the unit cell. The three major components of the XRD instrument are an X-ray tube, a sample holder, and an X-ray detector. The idea of this method is mainly grounded on the diffraction of light that is scattered by a periodic array of long-range order and results in the production of constructive interference at certain angles [69]. A beam of X-ray photons from the cathode ray tube passes through a slit where it is filtered to form monochromatic radiation that collimates to directly focus on the sample. Then, atomic or molecular crystals of powdered samples diffract the beam of X-ray photons, resulting in the scattering of photons in all directions [69–71]. When incident rays interact with an analyte, they result in a constructive interference obeying Bragg's law which is presented by Equation (3.7) [72]:

$$n\lambda = 2d\sin\theta \tag{3.7}$$

where λ and *d* denote the incident light wavelength and spacing of diffracting planes, respectively. The angle associated with diffraction is represented by θ and *n* = 1 is an integer.

XRD is commonly employed for identifying unknown compounds and measuring sample purity and crystallinity [69–71,73]. This technique is non-destructive to the sample and can be used for quantitative analysis, in which the data presentation includes two theta

angles, peak intensity, and the amount of lattice constant. The data that are obtained for qualitative analysis include phase analysis, whereby the type of phase can be identified; phase composition; crystallite size; and orientation [70,74]. The XRD technique has been used by many researchers for the physical characterisation of MOFs and MOF composites used in the adsorption of heavy metal ions. Moreover, after the adsorption process, the effects of the adsorbed metal ions on the phases and the crystallite size of MOF adsorbents have also been studied. From the obtained results, the crystallinity of the prepared materials has been deduced and, in some cases, the incorporation and modification with other functional components has been confirmed using this technique. For example, Yin and co-workers [75] synthesised UiO-66 MOF which they modified with melamine for the removal of Pb(II) ions. The diffraction patterns of UiO-66 and melamine-UiO-66 were obtained using an X-ray diffractometer (BRUKER AXS, D8 Advance), and the results are shown in Figure 3.5(a). The patterns of the prepared UiO-66 and melamine-modified UiO-66 show some similarity with those of simulated UiO-66 from CCDC 837796. The authors concluded that post-modification with melamine did not disrupt the crystal structure of melamine-UiO-66. Moreover, the melamine-UiO-66 displayed higher peak intensities at two theta values of 7.4° and 8.5°, suggesting an increased degree of crystalline on the MOF structure. The melamine peaks were also observed at 2θ = 26° and 30° to further support the chemical interaction between melamine and the UiO-66. Quan *et al*. reported on NH_2-$mSiO_2$@MIL-101(Cr) composite for adsorbing Pb(II) and Cr(VI) ions which were characterized using a PANalytical Empyrean X-ray diffractometer operating at a scan rate of 5° min^{-1}. As presented in Figure 3.5(b), MIL-101(Cr) was prepared and modified with $mSiO_2$ due to the appearance of a peak at 2θ = 2.5° on both the patterns of $mSiO_2$@MIL-101(Cr) and NH_2-$mSiO_2$@ MIL-101(Cr). The diffraction patterns for MIL-101(Cr) are also visible in both composites indicating that the crystal phases are still intact, however, are less intense on NH_2-$mSiO_2$@ MIL-101(Cr) nanoadsorbent, confirming the effective grafting of amino groups.

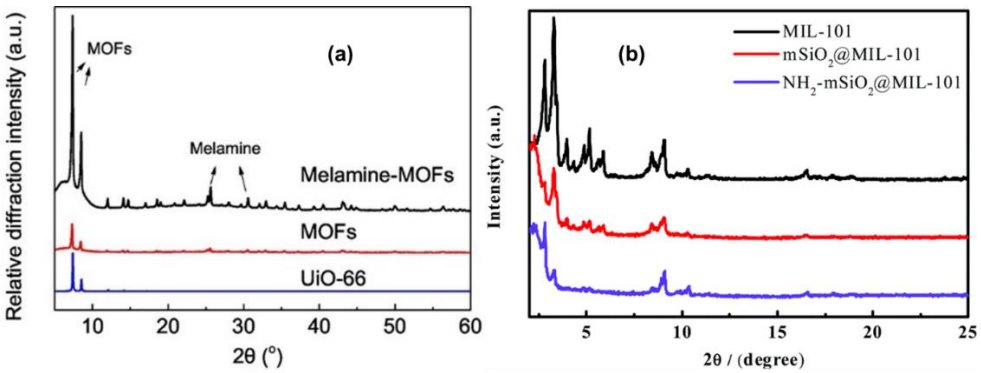

Figure 3.5: Diffractograms of: (a) MOFs and melamine-modified MOFs [75]; (b) pristine MIL-101(Cr), $mSiO_2$@MIL-101(Cr), and NH_2-$mSiO_2$@MIL-101(Cr) [63].

Other researchers have used the XRD technique to partially understand the mechanism of adsorption taking place between MOFs and heavy metal ions. Lim and colleagues studied the removal of Pd(II) and Pt(IV) ions using MIL-101(Cr)-NH_2 which was prepared by reducing MIL-101(Cr)-NO_2 [76]. The patterns were measured between $3° < 2\theta < 90°$ using a higher performance XRD, having a Cu-sealed tube of $\lambda = 1.54178$ Å. The XRD patterns for the prepared materials were obtained before and after metal ion adsorption, and are presented in Figure 3.6(a). The authors concluded that the pristine MIL-101(Cr)-NH_2 and MIL-101(Cr)-NO_2 structures were stable in acidic media since they retained peaks that were identical to those of the simulated MIL-101(Cr) before and after the adsorption of Pd(II) and Pt(IV) ions.

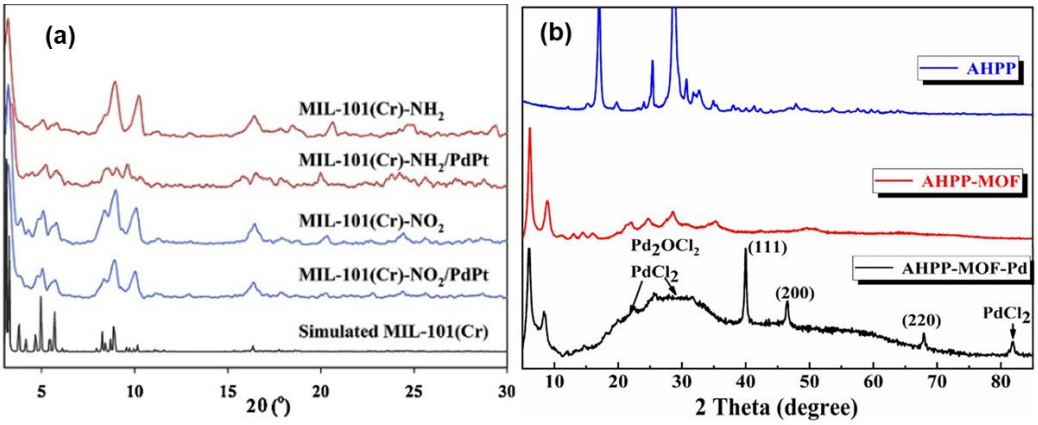

Figure 3.6: Diffractograms of: (a) MIL-101(Cr)-NH_2, and MIL-101(Cr)-NO_2, after the adsorption of Pd(II) and Pt(IV) ions [76]; (b) AHPP, AHPP-MOF, and AHPP-MOF-Pd [36].

Tang and his colleagues characterized AHPP-MOF-Pd after adsorbing Pd(II) ions and compared it with the diffraction peaks of AHPP and AHPP-MOF, as depicted in Figure 3.6b. According to their observations, the diffractograms of AHPP and AHPP-MOF were quite dissimilar. However, the peaks at 2θ = 6.0° and 8.09° for the AHPP-MOF corresponded to the conventional patterns of UiO-66 reported in the literature, indicating the successful combination of AHPP and $ZrCl_4$. Furthermore, the diffraction peaks at 2θ = 22.3°, 26.7°, and 82.8° for AHPP-MOF-Pd were attributed to $PdCl_2$ and Pd_2OCl_2. The authors also observed some peaks at 2θ = 40.061°, 46.506°, and 67.898° corresponding to the (111), (200), and (220) planes of palladium, respectively (JCPDS no. 65–2867). They observed that Pd(II) ions were interacting with some surface functional groups on the AHPP-MOF, which resulted in the formation of Pd compounds including metallic Pd. Although the XRD technique cannot provide information regarding the mechanism of interacting between MOFs and heavy metal ions, it is still of significant importance, since MOF structures have been shown to be very crystalline materials. Their successful composite formation with other compounds is most often confirmed by a reduction in crystallinity wherein some shift or broadening of diffraction peaks is observed as well as the appearance of new peaks. In addition, their interaction with heavy metal ions can also be confirmed by an increase or decrease in crystallinity. Hence, the XRD patterns of the MOFs composites after the adsorption of heavy metal ions should be obtained in order to confirm their interaction.

3.3.1.2. Thermal Gravimetric Analysis

A thermal analysis is a study conducted using a group of analytical techniques combined to give important information about the physicochemical properties of a material as a function of temperature. Thermogravimetry is one of the techniques of thermal analysis used to study variations in the quantity and frequency of the weight of a sample against temperature and time in a controlled atmosphere such as purged nitrogen gas [77–81]. The main components of a TGA instrument are the furnace, the microbalance, the temperature controller, and a data acquisition system [82,83]. In principle, a sample with a mass of 0.002–0.02 g is inserted into a pan (crucible) of suitable size, followed by setting the temperature variations according to an adapted temperature program. These may include isothermal ramp steps having various heating rates while measuring the

temperature with thermocouples that are in contact with the crucible. In a TGA instrument, the sample holder for putting the crucible is connected to the microbalance (mass sensitive element) which is used for detecting the weight changes associated with the sample. Then, the sample holder system is heated with an electric furnace that can reach maximum temperatures of about 2000 °C. However, the quantity of heat needed depends on the specifications of material, the design of the furnace, as well as other components [78,80].

The weight change recorded as a function of time is in isothermal mode, whereas weight change captured as a function of temperature is in scanning mode. The non-isothermal mode is usually associated with a constant heating rate (β) which is caused by the linear change in temperature with time and is expressed by Equation (3.8):

$$\beta = \frac{dT}{dt} \tag{3.8}$$

where *dT* and *dt* represent the change in temperature and change in time, respectively. The data obtained from TGA assist in deducing the type of reaction that can take place including decomposition, sublimation, vaporisation, etc. Furthermore, gaseous products that escape during the chemical reaction, thermal stability of composites, and associated degradation mechanisms can be studied by this technique. Generally, a compound is regarded as being thermally stable if the TGA curve shows no change in sample weight. However, its disadvantage is the destruction of the sample as well as the restricted number of elements to be analysed [80,83–86].

For the removal of heavy metal ions by MOF composites, authors have employed the TGA technique to examine the thermal stability of the synthesised materials. Depending on the MOF that one is working with and the type of modification taking place, the thermal stability of the resulting MOF composites (including nanocomposites) can either improve or degrade. The composite of MIL-101(Cr)/TEPA@CA (tetraethylenepentamine@calcium alginate) used in the adsorption of Pb(II) ions was synthesised by Wang *et al*. [87]. The obtained TGA curves for the composite and its precursors (MIL-101(Cr) and MIL-101(Cr)-TEPA) are shown in Figure 3.7(a). The prepared materials demonstrated weight loss due to moisture at less than 130 °C with weight losses of 4.95%, 8.35%, and 10.10% for the MIL-101, MIL-101(Cr)-TEPA, and

MIL-101(Cr)/TEPA@CA, respectively. The degradations occurring between 240–470 °C for MIL-101(Cr) and MIL-101(Cr)-TEPA corresponding to 45.21% and 39.96% weight loss were due to decomposition of the MIL-101 structure while converting to Cr_2O_3. For MIL-101(Cr)/TEPA@CA, the loss in weight increased by 49.64% at 240–520 °C and it included the conversion of cellulose aerogel (CA) into CaO. In another report, the thermal properties of the synthesised UiO-66-NH_2@cellulose aerogel composite were studied by Lei *et al*. [88] through a comparison with the thermal stabilities of UiO-66, UiO-66-NH_2, and CA materials. The thermograms were obtained from a TGA, TG 209 F1, Germany instrument that operated at 20 °C min^{-1} heating rate and 30 –700 °C under N_2 atmosphere. As presented in Figure 3.7(b), the CA was less thermally stable than MOF and showed maximum decomposition at 332.2 °C, whereas the value increased by 26.2 °C for UiO-66@CA and 26.7 °C for the UiO-66-NH_2@CA composite. The prepared UiO-66- NH_2@CA composite with improved thermal stability was utilised in the adsorption of Pb(II) ions from simulated wastewater. It was observed in TGA that the processes occurring during heating of the samples directly coincided with temperature. This suggested that the adsorption of heavy metals occurred on the surface of the MOF structure. TGA can reveal the chemical stability of MOFs after adsorption which strongly depends on the possibility of preserving their initial structure. The exchange of heavy metals and guest anions from the aqueous solution to the MOF surfaces can be observed by changes in thermal stability. The weight loss from TGA can be used to estimate the amount of heavy metals on the surface of MOF materials by determining changes in the mass of the MOF composites before and after adsorption.

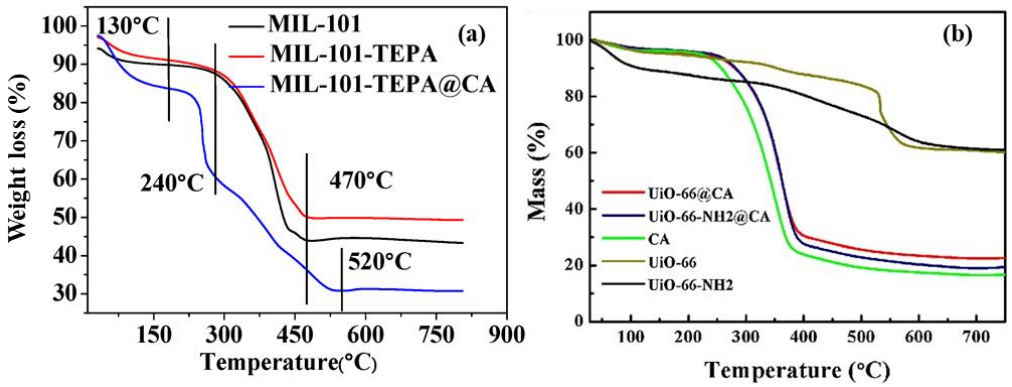

Figure 3.7: TGA curves of: (a) MIL-101(Cr), MIL-101(Cr)/TEPA, and MIL-101(Cr)/TEPA@CA [87]; (b) UiO-66, UiO-66-NH_2, CA, UiO- 66@CA, and UiO-66-NH_2@CA [88].

3.3.1.3. Differential Scanning Calorimetry

Differential scanning calorimetry (DSC) is another thermal analytical technique which was developed in 1962 by Watson and O'Neill and commercialised in 1963 [89]. This thermal analytical technique uses the same operating conditions as TGA and is sometimes coupled together in a system referred to as simultaneous thermal analysis (STA) [80]. DSC is based on the measurements of heat flow between a sample and inert reference materials as a function of temperature, wherein the changes in heat capacity and endothermic and exothermic activities occurring on a sample can be determined. It is a powerful and rapid method for providing qualitative and quantitative data concerning the physicochemical phase transitions experienced by materials when exposed to elevated temperatures (from 100 to 1800 K) [82,83,90–95]. The three basic phases that can occur when an amorphous substance is being exposed to heat are as follows: (a) glass transition, in this phase change, the structure of an amorphous substance changes from a moderately hard state to a rubbery state and it is reversible, and the glass transition temperature provides information concerned with the stability of the glassy or amorphous state; (b) crystallisation, this irreversible (two-steps) phase change entails assembling the disordered structures through nucleation and growth processes to form crystalline structures through an exothermic process; (c) melting, in this transition, a single step endothermic process occurs when the crystalline lattice becomes broken down into a disordered state from solid to liquid in a single step [89].

Efome *et al.* [96] synthesised polyacrylonitrile (PAN) nanofiber-supported Zr-based MOF-808 via co-electrospinning for the adsorption of Cd(II) and Zn(II) from an aqueous environment. The glass transition temperatures (Tg) of the PAN and PAN@MOF, as obtained from a TA Instruments DSC Q2000 V24.11 Build 124, are presented in Figure 3.8. The results were obtained by annealing approximately 0.05 g of the nanomaterials for 10 min at 150 °C, followed by quenching to 25 °C for another 10 min, and then the heating rate for Tg measurements was 5 °C min^{-1}. The DSC thermogram shows that the Tg of PAN@MOF-808 increases slightly by 3 °C, to 82 °C as compared with the initial Tg

value of 79 °C for PAN. The shift is attributed to the restricted chain movement on the PAN polymer brought about by its interaction with MOF-808. DSC is similar to TGA; it can also be used to monitor the adsorption mechanism of heavy metals by looking at the change in heat flow as a function of the sample temperature. The transition of heavy metal ions or guest anions from aqueous solution to the surface MOF composites can be observed by changes in heat flow corresponding to the endothermic and exothermic peaks.

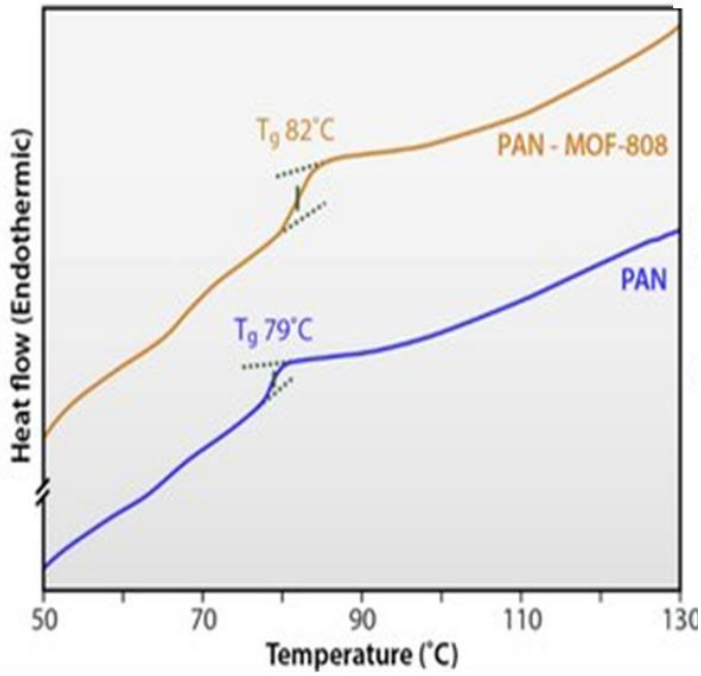

Figure 3.8: DSC thermogram of PAN and PAN@MOF-808 nanomembranes [96].

3.3.1.4. Brunauer, Emmett, and Teller Method

The measurement of the surface areas of materials is one of the studies that is conducted to deduce some of the properties of materials. The most commonly used method, developed by Brunauer, Emmett, and Teller in 1938, is the BET theory [97]. The main working principle of the BET analytical technique is associated with the amount of gas adsorbed onto the surface of materials. The types of interactions that can occur between an adsorbate and the adsorbent are physisorption (via van der Waals) and chemisorption (via chemical reaction) [97,98]. After the adsorbate–adsorbent interaction, the reaction ultimately reaches equilibrium at a particular constant temperature and relative vapour

pressures denoted as P/P_o. The quantity of the adsorbed gas is determined and the result is used to produce an adsorption isotherm. The total gas captured has a proportional relationship with the external and internal surfaces of the adsorbent material [98,99]. The BET theory can be derived similarly to the Langmuir theory (assumes monolayer adsorption between gaseous atoms and the adsorbent surface). However, multilayer adsorption can occur if the surface temperature of the adsorbent is less than the critical temperature of the adsorbate (gas molecules). In this process, many layers of adsorbed gas molecules form; however, some of them are not in contact with the adsorbent surface layers. The BET theory assumes multilayer adsorption where all layers are in equilibrium and atoms on the lower layers serve as adsorption sites for atoms on the above layers and the BET equation is expressed by the following Equation (3.9):

$$\frac{P/Po}{n(1-\frac{P}{Po})} = \frac{1}{n_m C} + \frac{C-1}{n_m C}(\frac{P}{Po}) \qquad (3.9)$$

where n and n_m denote the specific amount and monolayer capacity of the gas adsorbed, respectively. C represents the BET constant relating to the monolayer adsorption energy and it can be used to determine the shape of the isotherm [97,98,100–105].

The BET isotherms can form six different curves. Type I isotherms, which are reversible, have two patterns and are obtained from microporous solids having micropore widths that are below ≈1 nm. Type II isotherms are common for compounds that are nonporous or macroporous and are also reversible. Type III isotherms are achieved when the adsorbent−adsorbate interactions are weak and the monolayer surface coverage data are not given. Type IV isotherms have two patterns that are related to the width of the pores. However, type IV isotherms are reduced to type VI isotherms if the size of the width is higher than the critical width. Type V isotherms are observed at low P/P_o ranges and result from weak interactions between the adsorbent and adsorbate. Type VI isotherms are usually obtained over multilayer adsorption on substances having extremely uniform nonporous surfaces. The stepwise-shaped curves depend on the material, gas, and temperature [97,103,105,106].

The BET technique has been used to deduce the surface area, pore volume, and pore diameter of MOFs and MOF composites. From the reported literature, MOFs have been

described as highly porous materials with very high surface areas that can reach over 3000 m^2 g^{-1}. Furthermore, the pore volume and pore diameter that correspond to the specific surface areas of MOFs can be determined. The surface areas and pore volumes of MOFs both enable MOFs to be good host that can accommodate a variety of guest molecules. Since the adsorption of heavy metal ions by MOF composites is a surface phenomenon, the BET technique has been used to confirm the interactions of MOF materials with the heavy metal ions. During adsorption, these heavy metal ions penetrate into the pores of MOF composites resulting in a reduction in the surface area and subsequently the pore volume decreases indicating that there are some molecules occupying their space. Such information can be obtained by an analysis of an MOF composite after the adsorption. In a study reported by Luo and his colleagues [107], MIL−101(Cr) was prepared and functionalised with ethylenediamine (ED) for the adsorption of Pb(II) ions from an aqueous solution. The BET surface areas of MIL−101(Cr) and ED−MIL−101(Cr) are shown in Figure 3.9(a). The isotherm curves demonstrate a type I behaviour and the obtained BET surface area of 2290 m^2 g^{-1} for MIL−101(Cr) decreases significantly after grafting with 2 and 5 mmol of ED to 1270 and 347 m^2 g^{-1}, respectively. Furthermore, the corresponding pore volume of 1.4 cm^3 g^{-1} for MIL−101(Cr) shows the same trend of decreasing to 0.74 cm^3 g^{-1} for 2 mmol ED and 0.28 cm^3 g^{-1} for 5 mmol. The reduction in the porosity is attributed to the occupation of some pores on the MIL−101(Cr) by the ED moieties after surface modification, and thereby, preventing the adsorption of N_2 molecules. In another study, the porous nature of the prepared AHPP-MOF composite was deduced from ASAP-2020 plus, Micromeritics, USA.

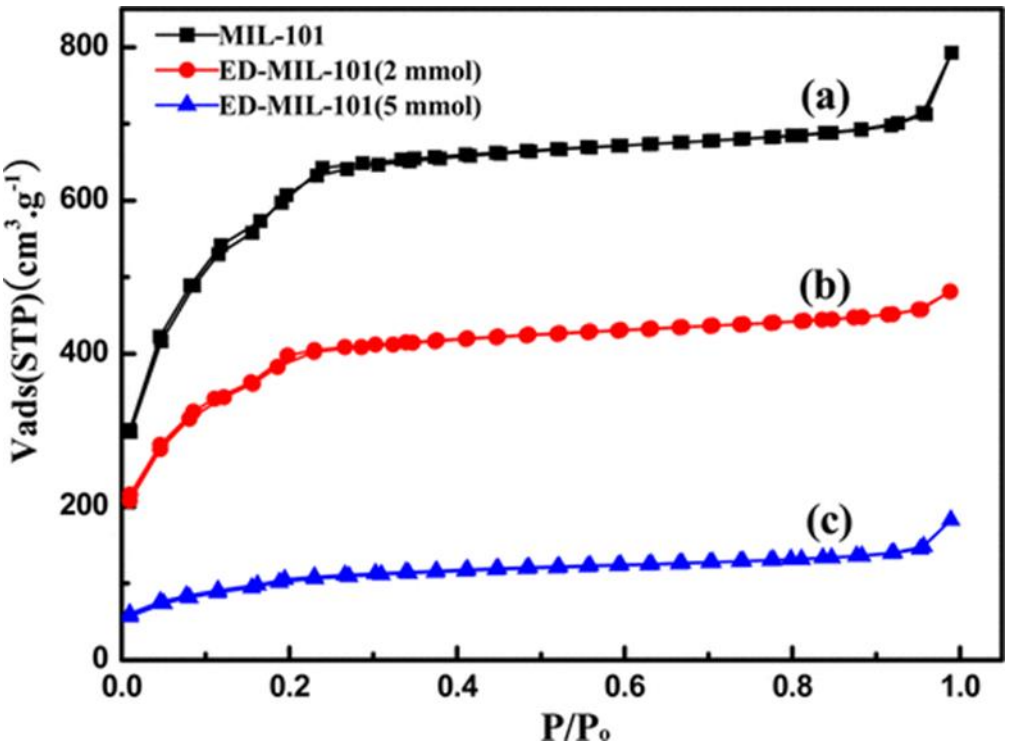

Figure 3.9: BET isotherms of: (a) MIL−101(Cr); (b) ED−MIL−101(Cr) 2 mmol; (c) ED−MIL−101(Cr) 5 mmol [107].

The N_2 adsorption-desorption isotherm curves before and after Pd(II) adsorption are represented in Figure 3.10(a) and the corresponding pore volumes are shown in Figure 3.10(b). From the BET isotherms of AHPP-MOF, it can be noted that the type IV behaviour is the prevailing curve. This characteristic hysteresis loop describes the porous nature of the AHPP-MOF with the calculated specific surface area and pore volume of 180.29 m^2 g^{-1} and 0.09 cm^3 g^{-1} [36]. After the adsorption of Pd(II) ions, both the specific BET surface area and pore volume decreased, confirming the occupation of the surface pores by the Pd(II). Yin and co-workers [75] reported that the functionalisation of MOF materials with melamine increased the BET surface area of the final composite of melamine-modified MOFs. As shown in Figure 3.10(c), the obtained type I shape of the N_2 adsorption-desorption isotherm curve confirmed the microporous surfaces. However, the melamine-modified MOFs curve demonstrated a type IV isotherm shape which suggested the mesoporous natures of the functionalised MOF surfaces. Furthermore, the specific BET surface areas of the MOFs increased from 302.9 to 371.0 m^2 g^{-1} for the melamine-modified MOF composites and the behaviour was supported by pore size distribution, as

presented in Figure 3.10(d). The results showed that MOFs had a narrow pore size distribution of about 20 Å, whereas the melamine-modified MOFs displayed a fairly larger pore size distribution with mesoporous architectures [75].

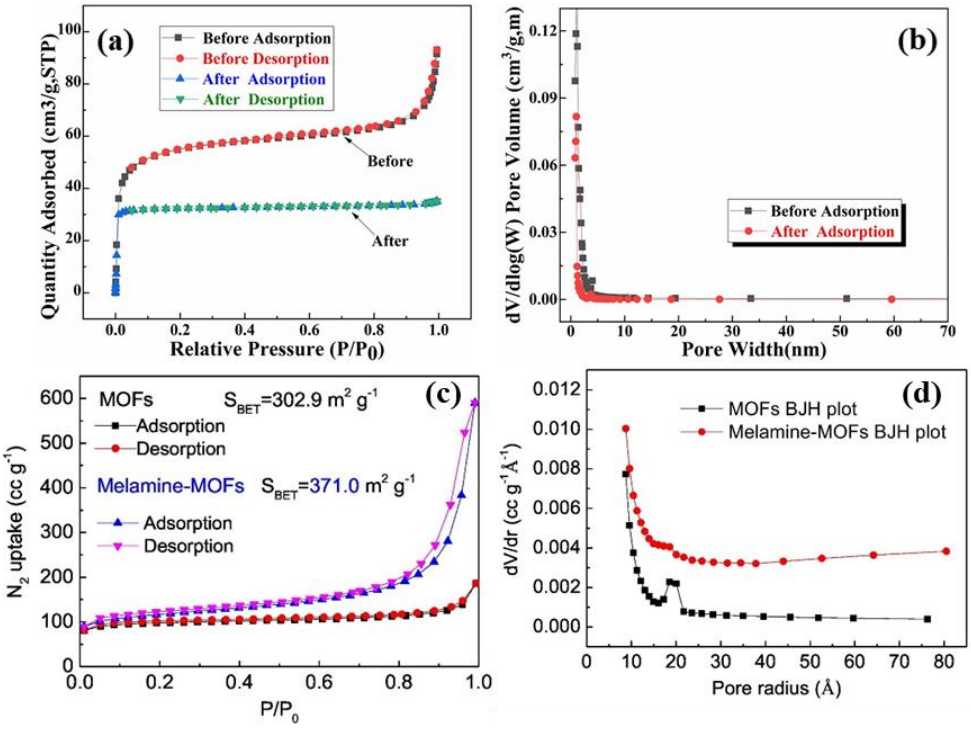

Figure 3.10: BET curves of: (a) AHPP−MOF and Pd@AHPP−MOF; (b) pore width distribution curve (before and after) adsorption [36]; (c) the MOFs and melamine−modified MOFs; (d) pore size distribution BJH plot [75].

3.3.2. Microscopic Characterisation

Microscopy is another powerful technique that is employed to study the morphological structures of prepared materials. The technique acquires information about the material at a microscopic level wherein different images relating to the structures of materials before and after functionalisation are obtained. Furthermore, these techniques can be coupled with various detectors to reveal the elements that are present in the structures as well as their distribution on the surface of the composites.

3.3.2.1. Scanning Electron Microscopy—Energy Dispersive Spectroscopy

The most powerful and versatile analytical technique used for studying and analysing the morphological micro-, nanostructure, and chemical composition of materials is scanning

electron microscopy (SEM) [108]. This technique involves generating a beam of electrons that have an energy of approximately 40 keV and is bombarded on the sample of interest. This beam interacts with the surface of the analyte by scanning it using scan coils [109–111]. This phenomenon results in excitation of the electrons on the surface and subsequently causes elastic and inelastic collisions until the electrons possess enough energy to escape. This interaction is followed by scanning of electrons along parallel lines, which emits various signals due to Auger electrons, secondary electrons, backscattered electrons, X-rays, and photons. Then, the particles that originate from the sample are collected by various detectors and produce an image or information about the surface of the analyte [83,108,112–116]. The SEM instrument is mostly coupled with the energy-dispersive X-ray spectroscopy (EDS) to attain qualitative data about the composition of the sample of interest. EDS works by detecting and “counting” the X-rays generated by the emitted electron beam. When an incident beam of electrons strikes the surface of an analyte, it causes the excitation of inner shell electrons which leaves vacant sites that are filled by electrons in the outer shell. This transition is accompanied by the release of X-ray energy that is signified by the differences in energy amongst the inner and outer shell electrons. The X-ray photons characterize all the elements in the periodic table except H, He, and Li. The elements that are present as major constituents can be identified and quantified [116–120].

The SEM-EDS technique has been employed for the morphological and elemental studies of MOFs and MOF composites/nanocomposites. This instrument provides two-dimensional images of higher resolution that reveal the geometry of a sample as well as spatial variations. Furthermore, the data can be used to acquire evidence regarding the external morphology, dispersion, and various phases of a sample [121]. Thanh *et al*. [122] synthesised and compared two different MOFs (i.e., MIL−101(Cr) and Fe–MIL−101) for the adsorption of Pb(II) from an aqueous solution. The obtained SEM images and EDS analysis, as shown in Figure 3.11(a), indicated an octahedral geometry with smooth facets for MIL−101(Cr) and the elemental analysis (see Figure 3.11(d)) confirmed the presence of Cr, O, and C which were the major constituents of MIL-101. The image of Fe–MIL−101, as represented in Figure 3.11(b), displayed irregular shapes mixed with octahedral structures. Further support from an elemental analysis, as shown in Figure

3.11(c), confirmed the elemental composition of the prepared MOF with the major constituents being Fe, Cr, O, and C.

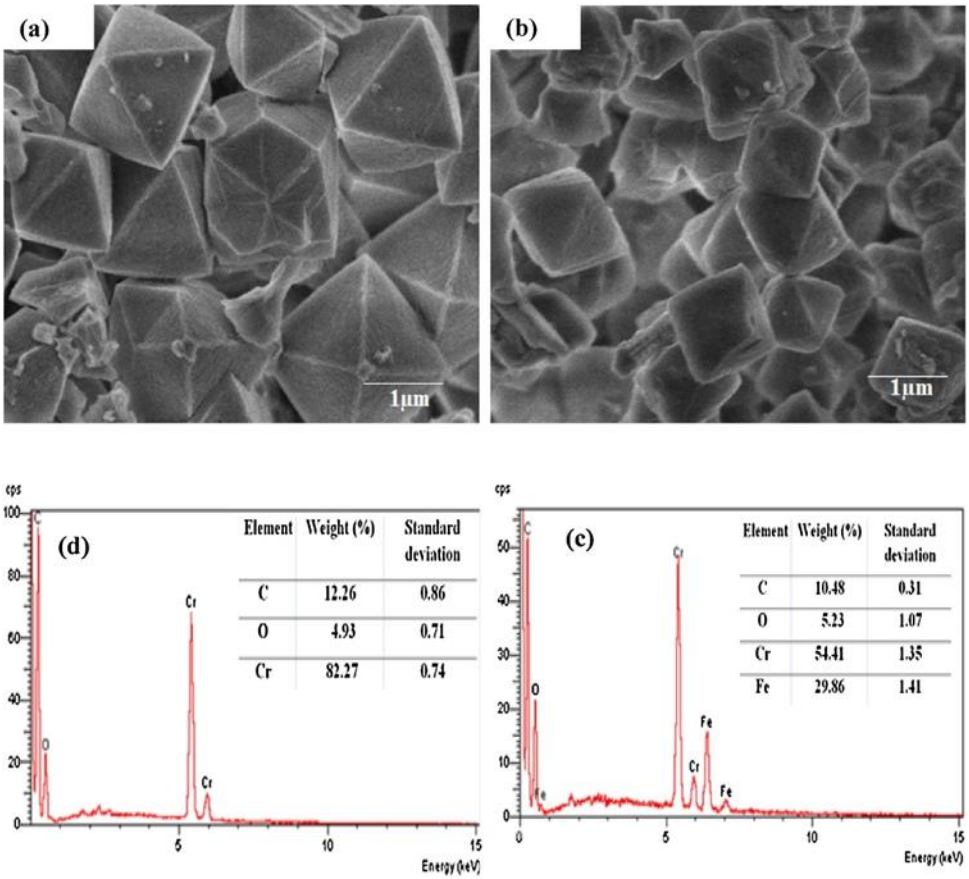

Figure 3.11: SEM images of: (a,b) of MIL−101(Cr); (b) Fe–MIL−101. EDS analysis of: (c) MIL−101(Cr); (d) Fe–MIL−101 [122].

In another study, Lim *et al*. [76] described the synthesis of MIL-101(Cr)-NO_2 using $CrCl_3$ as a source of Cr and reduced it to MIL-101(Cr)-NH_2 using $SnCl_2$ for removing Pd(II) and platinum Pt(IV) in acidic solutions. The SEM images, as shown in Figure 3.12, revealed prismatic crystals with a diameter and length of approximately 150 nm and 1000 nm, respectively, for both the MIL-101(Cr)-NH_2 and MIL−101(Cr)-NO_2. Furthermore, the inset elemental mapping images showed the even distribution of Cr on the surface of the MIL-101(Cr)-NH_2 and MIL-101(Cr)-NO_2 [76]. For example, the images obtained after the adsorption of both the Pd(II) and Pt(IV) which were supported by elemental mapping (see insets) are shown in Figure 3.13(i-iv). For the PGM-loaded MIL-101(Cr)-NH_2 (Figure 3.13(I and ii)), an even distribution of the prismatic crystals particles of the composite was

observed. This was attributed to the high adsorption capacity of MIL-101(Cr)-NH_2 towards Pd(II) and Pt(IV). Conversely, the low adsorption capacity of MIL-101(Cr)-NO_2 showed the inconspicuous distribution of Pd(II) and Pt(IV) on the elemental mapping images (Figure 3.13(iii and iv)).

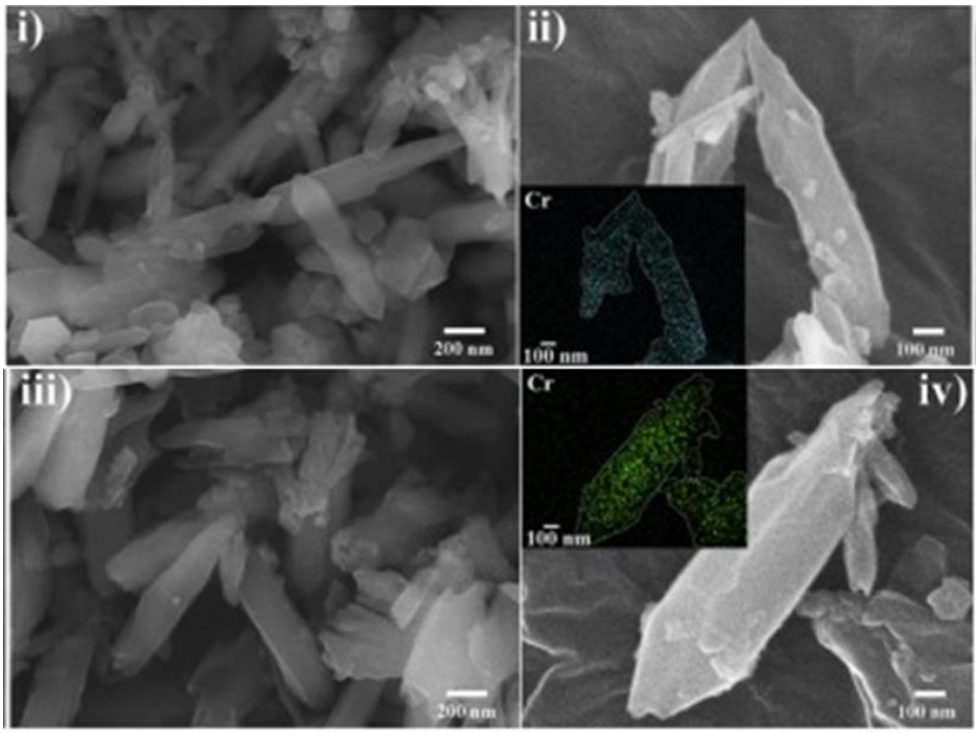

Figure 3.12: FE-SEM images of: (I and ii) MIL−101(Cr)−NH_2; (iii and iv) MIL−101(Cr) −NO_2 (insets show chromium elemental mapping images) [76].

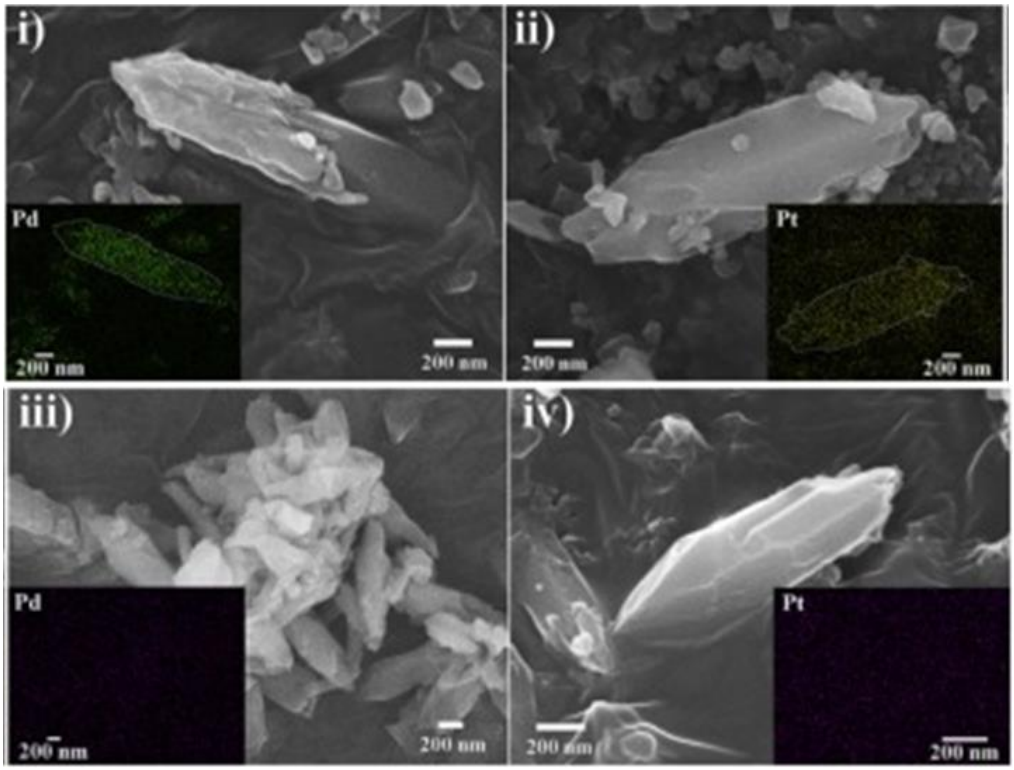

Figure 3.13: SEM and elemental mapping images of MIL-101(Cr)-NH_2 after: (i) Pd loading; (ii) Pt loading. MIL-101(Cr)-NO_2 after: (iii) Pd loading; (iv) Pt loading [76].

3.3.2.2. Transmission electron microscopy-energy dispersive X-ray spectroscopy.

Transmission electron microscopy (TEM) is a highly effective analytical technique used to study the internal surface morphologies of various materials. Its working principle is similar to that of a SEM instrument and can also be coupled with various detectors to attain data associated with the structure of the analytes. The difference with the TEM instrument is that the energies of the incident beam of electrons are much higher as compared with the SEM instrument [114,123,124]. This beam of primary/incident electrons, with energies between 80 and 300 keV, passes through lenses where it is filtered and focussed on the sample of interest. The beam of electrons penetrates into the sample and inelastically collides with the inner atoms, resulting in the emission of secondary electrons and X-rays. The emitted electrons that are scattered through smaller angles in all directions are limited and focussed onto the projector lens by the objective aperture. Subsequently, the image is collected onto the detector screen and its contrast is enhanced by altering the voltage from the gun [125–127]. High-quality images with

more information about a sample are formed due to the fact that the fast-moving electrons having shorter wavelengths. Many researchers have used TEM coupled with an energy dispersive X-ray spectroscopy (EDX) detector to study and obtain evidence relating to the structure, texture, shape, and size of MOFs and their composites [126,128]. For example, Lv and his colleagues [129] compared the internal morphologies of prepared MIL-101(Cr) and MIL-101(Cr)−NH_2 which were synthesised via the solvothermal method with the use of dimethylformamide (DMF). The MIL-101(Cr) was functionalised with amino functional groups to form MIL-101(Cr)-NH_2 which was employed for removing Pb, Cu, and Fe metal ions. As shown in Figure 3.14(a), the synthesised MIL-101 exhibited a hexagonal prismatic structure which remained intact after the introduction of amino groups, as depicted by Figure 3.14(b). Abedidni *et al*. [130] hydrothermally synthesised MIL-101 followed by post-modification with cuprous oxide nanoparticles (Cu_2O) for the adsorptive equilibria and kinetics separation of propylene. The obtained TEM images of the MIL-101(Cr) and 12%Cu@MIL-101(Cr) are presented in Figure 3.14(c and d), respectively. The evidence revealed that Cu_2O nanoparticles with sizes ranging between 1 and 3 nm were homogenously dispersed within the MIL-101(Cr) pores, and confirmed the successful reduction of the metal precursor into nanoparticles. In another study conducted by Luo and co-workers, MIL-101(Cr) with improved adsorption capacity for Pb(II) ions was prepared by PSM using ethylenediamine (ED) in anhydrous toluene. The authors compared the TEM images of MIL-101(Cr) before and after modification, as represented in Figure 3.15(a and b). The MIL-101(Cr) showed octahedral structures with smooth surface, however, after the incorporation of ED, the surface became rougher [107].

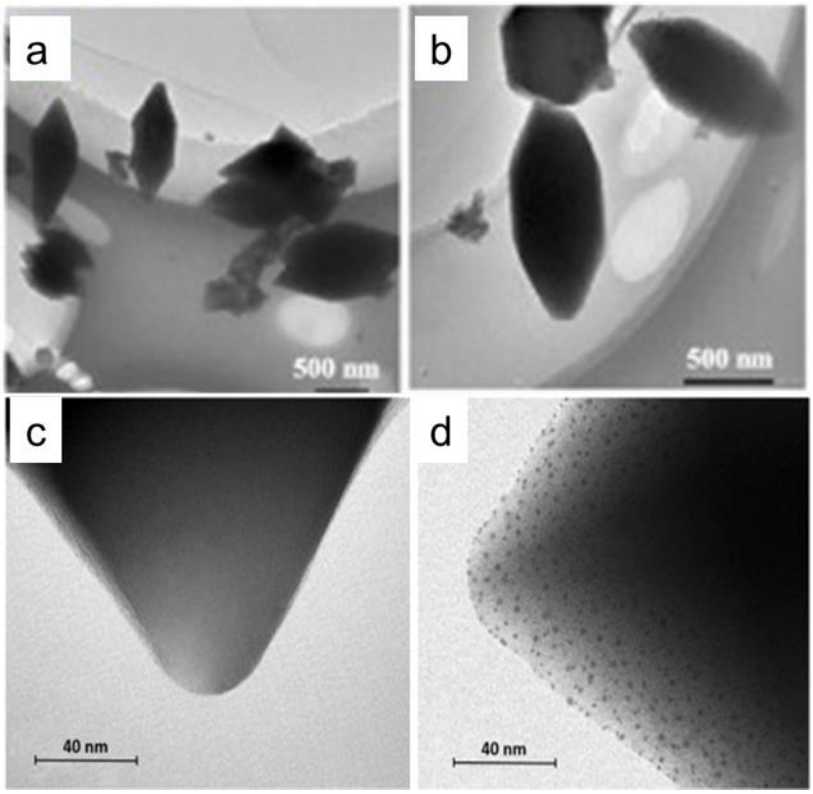

Figure 3.14: TEM images of: (a) MIL-101(Cr) NH_2; (b) MIL-101(Cr) [129]; (c) MIL−101(Cr); (d) 12% Cu@MIL-101(Cr) crystal [130].

In contrast, a study on the post-synthetic modification (PSM) of MIL-101 with amidoxime (AO) for removing uranium ions from seawater, which was conducted by Liu *et al*. [131], demonstrated a significant effect on the structure of MIL-101. The authors initially cholоromethylated MIL-101 and obtained an octahedral structure with a uniform dispersion of the Cl element, as shown by TEM-EDX images of MIL-101-CM in Figure 3.15(c and e). This was followed by grafting with diaminomaleonitrile before introducing amidoxime which resulted in an almost spherical morphology (Figure 3.15(d)). The significant change in the structure indicated the successful incorporation of AO and was further supported by the TEM-EDX mapping image which depicted a uniformly dense dispersion of N element from the AO on the MIL-101-AO (Figure 3.15(f)).

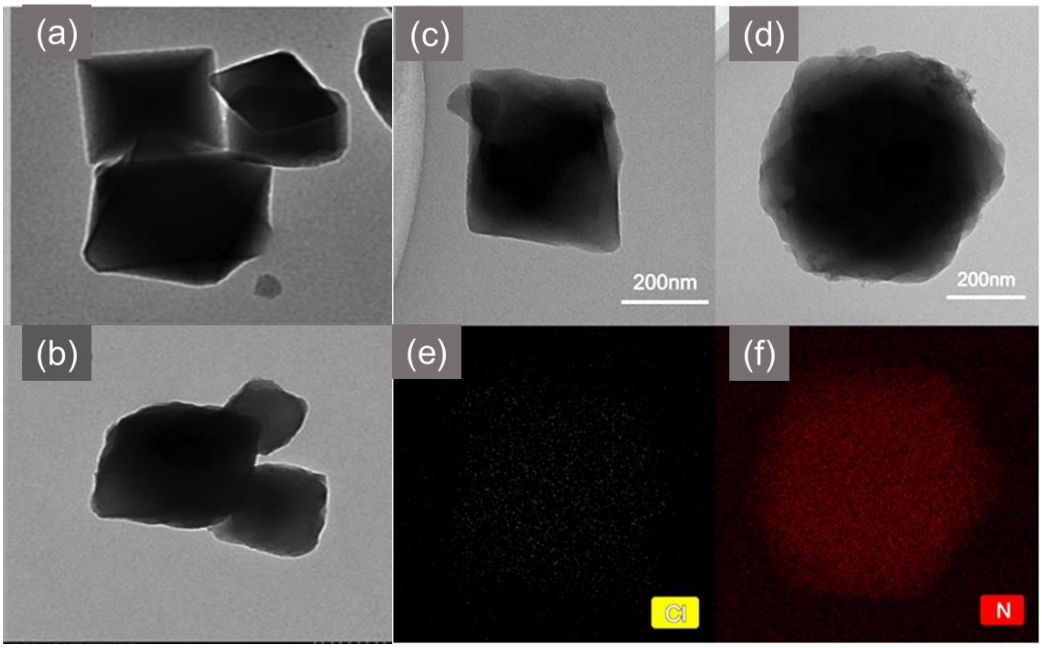

Figure 3.15: TEM images of: (a) MIL-101 and (b) ED-MIL-101 (5 mmol) [107]; (c) MIL-101-CM, (d) MIL-101-AO and EDS mapping images of: (e) MIL-101-CM and (f) MIL-101-AO [131].

3.3.3. Spectroscopic Characterisation

3.3.3.1. Fourier Transform Infrared Spectroscopy

The main working principle of Fourier transform infrared spectroscopy (FTIR) is based on the interactions of molecules/compounds with light in the infrared region of the electromagnetic spectrum. This analytical technique offers the opportunity to obtain information about the functional groups that are present in a sample (solid, liquid, or gas), as well as the possibility of understanding the molecular bonds that exist between matter [83,132]. In IR spectrophotometry, a beam of infrared radiation emitted from the source is passed through an interferometer and is spectrally encoded, creating an interferogram (i.e., constructive and destructive interferences). This is followed by the light interacting with the sample where specific frequencies are absorbed by the sample. The resulting vibrational frequencies due to the bonds that are present in molecules are detected and calculated in terms of wavenumbers ranging from 4000 to 400 cm^{-1} [83,113,132–137]. On the FTIR spectra, there are four regions where the different types of bonds can be clearly analysed. The first region, from 2500 to 4000 cm^{-1}, corresponds to single O-H, C-

H, and N-H bonds. It is followed by triple bonds which are found in the range between 2000-2500 cm^{-1}. The middle region, with the wavenumber range from 1500 to 2000 cm^{-1}, corresponds to detection of double bonds; the last area, below 1500 cm^{-1}, is the fingerprint region where the vibrations of carbon single bonds between the atoms produce overlapping bands [132]. The FTIR technique has been widely used to deduce the functional groups that form as part of the MOF structure as well as to understand its interaction with other materials after composite and nanocomposite formation for the removal of heavy metal ions from wastewater [4,61,64,138,139].

For example, Luo *et al*. [107] synthesised MIL-101(Cr) which was functionalised with ED for the adsorption of Pb(II) ions from wastewater. The amount of ED was varied to achieve the optimum removal of Pb(II), and the results are shown in Figure 3.16. The IR spectra for the functionalised ED-MIL-101 demonstrated peaks at 1581, 1051, and 882 cm^{-1} which were attributed to the N-H plane stretching, C-N bond stretching, and $-NH_2$ stretching, respectively. Furthermore, the broad band between 3434 and 3231 cm^{-1}, which was attributed to the −NH stretching, showed an increase in the intensity with an increase in the amount (2, 5, and 10 mmol) of ED grafted.

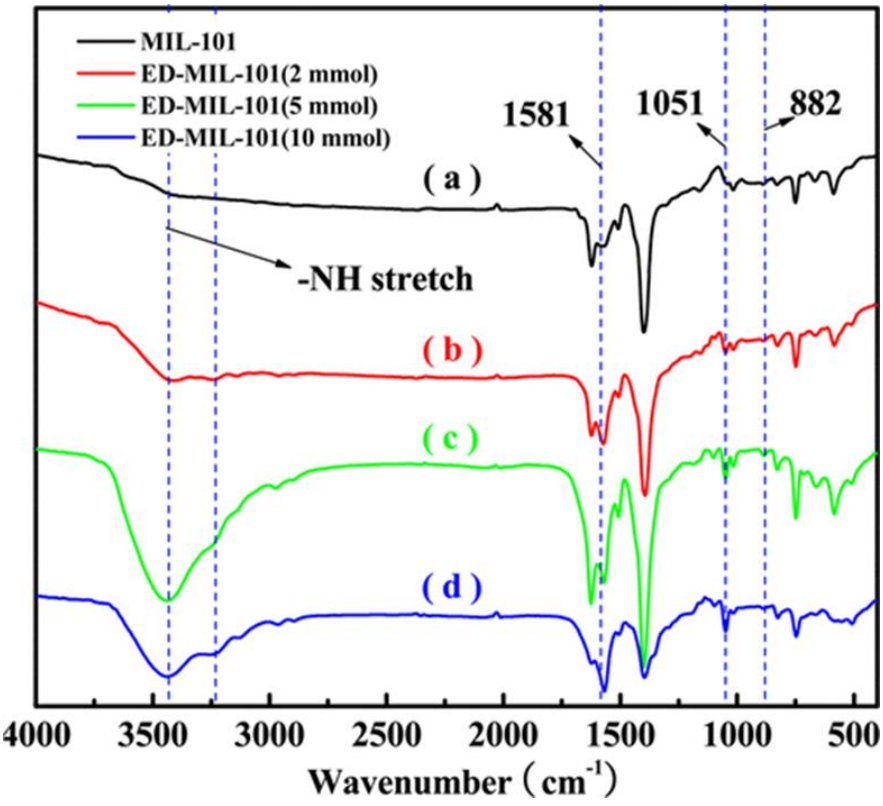

Figure 3.16: FTIR spectra of: (a) MIL-101(Cr); (b) ED-MIL-101(Cr) 2 mmol; (c) ED-MIL-101(Cr) 5 mmol; (d) ED-MIL-101(Cr) 10 mmol [107].

In another study, MIL-101-NH_2 was functionalised with thymine for the adsorption of Hg(II) ions from wastewater [140]. The IR spectrum of the resulting composite after adsorption was also obtained and compared with MIL-101-thymine, as presented in Figure 3.17(a) (i). The authors numbered the carbon atoms on MIL-101-thymine for easy interpretation. The spectrum of MIL-101-NH_2 revealed peaks at 1658 cm^{-1} which were attributed to the stretching vibrations of C_2=O and C_7=O. Moreover, stretching vibration absorption bands of C_3-C_5 and C_6-N were observed at 1124 and 1085 cm^{-1}, respectively. All these distinct peaks were detected on the IR spectrum of MIL−101-thymine (Figure 3.17(a) (ii)). However, after the adsorption of Hg(II) ions, the absorption peaks of C_2=O and C_7=O became broad with a shift to higher wavenumbers (Figure 3.17(a) (iii)). Jalayeri and co-workers reported on the IR spectra of MIL-101(Cr) which was functionalised with amine moieties via the organic linker for the removal of hexavalent chromium from an aqueous solution [141]. The spectrum for the AFMIL, as presented in Figure 3.17(b) (i), showed a peak at 3381 cm^{-1} which was attributed to stretching vibrations of the amino moieties. Furthermore, the N-H bending vibrations and C-N stretching of the aromatic amines were observed at 1621 and 1340 cm^{-1}, respectively. After the adsorption of hexavalent Cr, the IR spectrum (Figure 3.17(b) (ii)) showed some reduction in peak intensity as well as a slight shift to higher wavenumbers, which confirmed the chemical interaction between Cr and amino moieties. In addition, the IR is also one of the characterisation techniques that can be utilised to understand the mechanism of heavy metal adsorption using MOFs. Peng *et al.* [26] showed the IR spectra of MOF−808−EDTA before and after for La(III), Hg(II), and Pb(II) adsorption and revealed the shift of C-N vibration mode from 1214 cm^{-1} to 1220 cm^{-1}, 1242 cm^{-1}, and 1250 cm^{-1}. The shift in bands indicated the strong interaction between heavy metal ions and the grafting of the EDTA functional groups on the framework, which resulted in the chelate complex after adsorption.

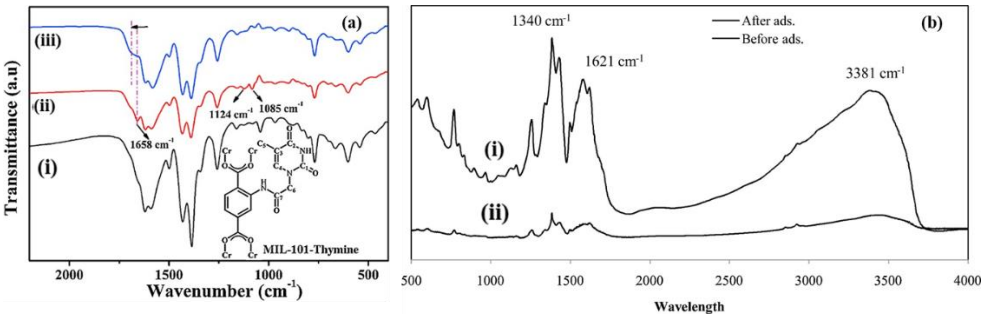

Figure 3.17: (a) FT-IR spectra of (i) MIL-101-NH_2, (ii) MIL-101-thymine, and (iii) Hg-loaded sample of MIL-101-thymine [140]; (b) amino-functionalised MIL-101(Cr) before and after Cr(VI) adsorption [141].

3.3.2. X-Ray Photoelectron Spectroscopy

X-ray photoelectron spectroscopy (XPS) is an analytical technique that uses the photoelectric effect to obtain information about the chemical nature of a material at the atomic and molecular levels [83,115]. This surface-sensitive method involves the irradiation of an X-ray beam onto the surface of a sample. The atoms in the sample absorb the incident light and result in the emission of core electrons of which their kinetic energy (KE) is measured according to Equation (3.10):

$$hv = BE + KE + \Phi_{spec} \quad (3.10)$$

where hv denotes the energy of the X-ray and Φ_{spec} is the spectrometer work function. The rearranged form of Equation (3.11) is used to calculate the binding energy (BE):

$$BE = hv - KE - \Phi_{spec} \quad (3.11)$$

The XPS spectrum is obtained as a function of the number of photoelectrons spotted against the BE. The photoelectron peaks are extracted from the orbital of the elements they were emitted from, and their corresponding BE permit their recognition. The peak intensities generated by the photoelectrons are directly proportional to the concentrations of the elements and can be used for their quantification. The XPS techniques can be used quantitatively to further reveal data regarding the empirical formula, the electronic and chemical states of elements (excluding hydrogen and helium) found within a sample, as well as their interactions with metal centres [83,113,115,142–144]. In the adsorption of heavy metal ions from wastewater by MOF materials, this technique has been widely

used to study and understand the type of interactions taking place as well as to support the deduced adsorption mechanism.

For example, Lim and co-workers studied the interactions of MIL-101(Cr)-NO_2 and MIL-101(Cr)-NH_2 with Pd(II) and Pt(IV) ions in order to understand the mechanism of adsorption [76]. Initially, the XPS N 1s spectra were obtained to confirm the reduction of the NO_2 to NH_2, as represented in Figure 3.18(a). The MIL-101(Cr)-NO_2 spectrum showed a peak at 405.6 eV, which was attributed to the nitro functional group that was attached to the phenyl ring ($PhNO_2$). However, the peak diminished upon the reduction process, as the spectrum for MIL-101(Cr)-NH_2 revealed a new peak at 399.2 eV which was ascribed to the amino group that was attached to the phenyl ring. After the adsorption of Pd and Pt ions, the authors obtained and compared the XPS N 1s spectra for metal-loaded MIL-101(Cr)-NH_2 with the pristine, as shown in Figure 18(b). The spectrum in Figure 3.18(b(1)) revealed two intense peaks at 399.2 and 400.2 eV which were attributed to the N in $PhNH_2$ and $PhNH_3^+$ (interaction with H^+ and Cl^- that remained after the synthesis process). As compared with the Pd-loaded MIL-01(Cr)-NH_2 (Figure 3.18(b) (2)), there was an increase in intensity of the peak at 400.2 eV and a decrease in the intensity of the peak at 399.2 due to the electrostatic interaction of $PhNH_3^+$ with the $[PdCl4]^{2-}$. Similar trends were also observed on the spectrum (Figure 3.18(b(3))) of Pt-loaded MIL-101(Cr)-NH_2, where the electrostatic interaction was between $PhNH_3^+$ and $[PtCl_6]^{2-}$. In addition, the appearance of a new peak at 401.9 eV was also observed, which was due to the partial oxidation of $PhNH_2$ to $PhNO_2$. Furthermore, the Pd 3d spectrum (Figure 3.18(b (5))) revealed a peak at 337.8 eV corresponding to the $[PdCl_4]^{2-}$ adsorbed on the MIL-101(Cr)-NH_2. For the Pt 4f spectrum (Figure 3.18(b(7))), two major peaks of ($4f_{7/2}$) attributed to the $[PtCl_6]^{2-}$ and $[PtCl_4]^{2-}$ were observed at 74.8 and 72.6 eV, respectively. Conversely, the MIL−101(Cr)−NO_2 N 1s spectrum, as shown in Figure 3.18(c (1–3)), showed no significant effects on the adsorption of both the Pd and the Pt, as the peak at 405.6 eV showed no adverse effects which was further supported by the low intensity observed on the Pd 3d and Pt 4f spectra. Moreover, the excellent performance of MOF composites for heavy metal adsorption could be traceable to the electrostatic or strong chelation. The wide-scan XPS spectra indicated that the metal ions were adsorbed in the pores of MOF. In the case of functionalised MOF, the N 1s core level was shifted to higher

binding energy upon metal loading (399.8 eV, 399.5 eV, and 399.9 eV for La(III)@MOF-808-EDTA, Hg(II)@MOF-808-EDTA, and Pb(II)@MOF-808-EDTA, respectively) as compared with the as-synthesised MOF-808-EDTA (399.2 eV) [26]. This showed that the valence of N in EDTA was changed because of the interaction with the guest metal ions.

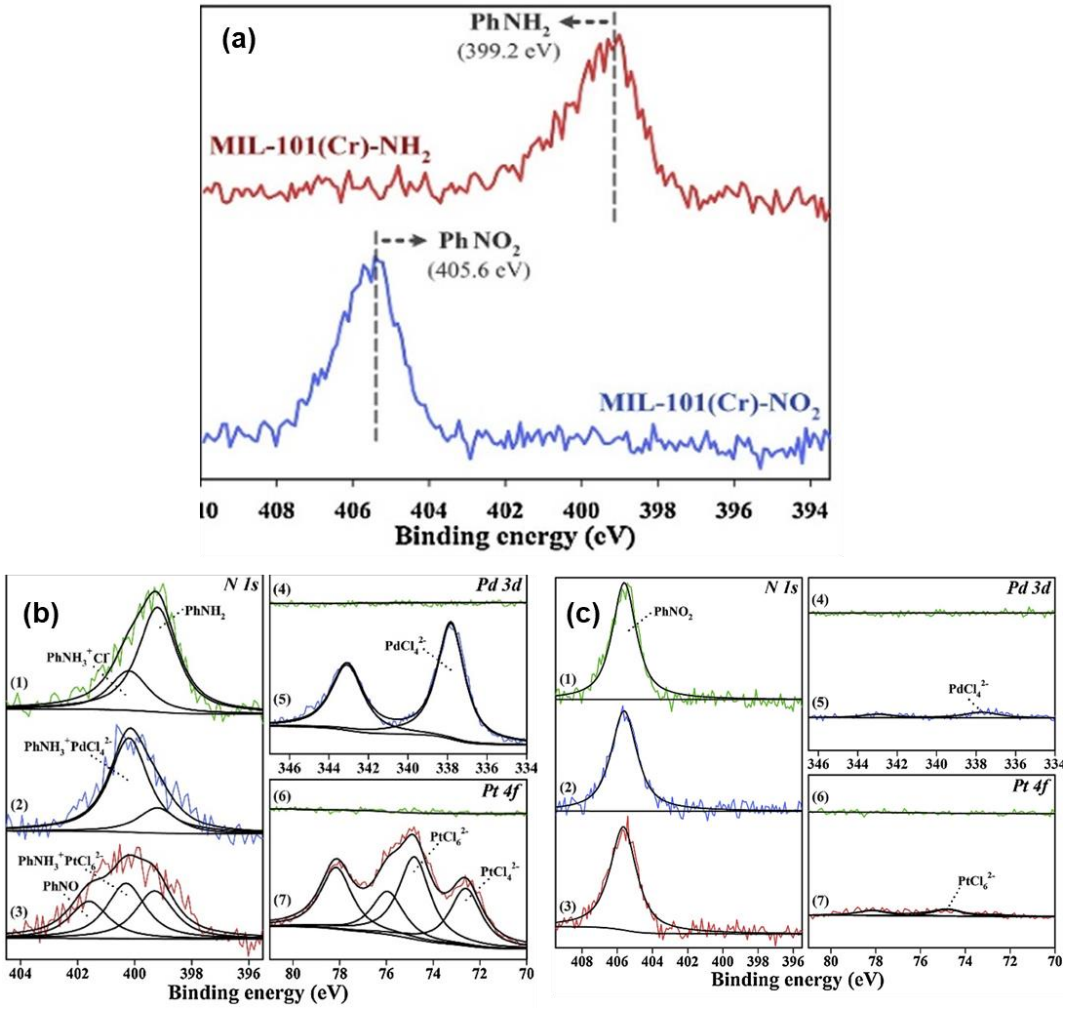

Figure 3.18: (a) XPS for N 1s spectra of MIL-101(Cr)-NH_2 and MIL-101(Cr)-NO_2; (b) MIL-101(Cr)-NH_2 after Pd loading (2) Pd and Pt-loading (3), Pd 3d and Pt 4f of pristine ((4) and (6)), and metal-loaded MIL-101(Cr)-NH_2 ((5) and (7)); (c) XPS for N 1s of MIL-101(Cr)-NO_2 (1) after Pd loading (2), Pt loading (3), XPS for Pd 3d and Pt 4f of MIL-101(Cr)-NO_2 ((4) and (6)), and after metal-loading ((5) and (7)) [76].

3.4. CONCLUSIONS

Some positive aspects of adsorption technology have been demonstrated in the remediation of wastewater containing heavy metal ions. Adsorption technology has been proven to be efficient in removing pollutants from contaminated water owing to its ease of operation and low cost. MOF polymers have shown some potential activity as adsorbents for the adsorption of metal ion pollutants. These materials have very interesting inorganic–organic coordination structures that can be easily tailored to suit a specific application. Furthermore, their surface functionality can be improved by introducing other materials such as metal oxides, nanoparticles, and active functional groups, for the purpose of removing heavy metal ions. MOF composites that have been synthesised and modified for the adsorption of heavy metal ions have been characterized. Hence, in this review, we focussed on various analytical methods that have been employed in the reported studies of heavy metal adsorption. The combination of these techniques has provided a significant amount of data that assist in studying the behaviour of MOF composites and their interactions with metal ions. Microscopic characterisation techniques coupled with EDS/X were able to detect some elements that were adsorbed by MOFs. Further supports were also provided by the FTIR spectroscopy, wherein we observed the vibrational peaks of the introduced functional groups as well as a reduction in the peaks after adsorption. The XPS confirmed the adsorption of heavy metal ions by looking at the orbital of the active elements on MOF composites as well as the orbitals of the targeted metal ion. In conclusion, this review focussed on understanding the role that each analytical technique has in order to determine the efficiency of the adsorption process.

3.5. REFERENCES

1. Burakov, A.E.; Galunina, E.V.; Burakova, I.V.; Kucherova, A.E.; Agarwal, S.; Tkachev, A.G.; Gupta, V.K. Ecotoxicology and Environmental Safety Adsorption of heavy metals on conventional and nanostructured materials for wastewater treatment purposes: A review. *Ecotoxicol. Environ. Saf.* 2018, *148*, 702–712. https://doi.org/10.1016/j.ecoenv.2017.11.034.
2. El-Sayed, M.E. Science of the Total Environment Nanoadsorbents for water and wastewater remediation. *Sci. Total Environ.* 2020, *739*, 139903. https://doi.org/10.1016/j.scitotenv.2020.139903.
3. Dotto, G.L.; Mckay, G.. Current scenario and challenges in adsorption for water treatment. *J. Environ. Chem. Eng.* 2020, *8*, 103988. https://doi.org/10.1016/j.jece.2020.103988.
4. Vardali, S.C.; Manousi, N.; Barczak, M. Novel Approaches Utilising Metal-Organic Framework Composites for the Extraction of Organic Compounds and Metal Traces from Fish and Seafood. *Molecules* 2020, *25*, 515.
5. Jiuhui, Q.U. Research progress of novel adsorption processes in water purification: A review. 2008, *20*, 1–13.
6. Arora, R. Adsorption of heavy metals-a review. *Mater. Today Proc.* 2019, *18*, 4745–4750. https://doi.org/10.1016/j.matpr.2019.07.462.
7. Howarth, A.J.; Peters, A.W.; Vermeulen, N.A.; Wang, T.C.; Hupp, J.T.; Farha, K.O. Best practices for the synthesis, activation, and characterisation of metal–organic frameworks. *Chem. Mat*. 2017, *29*, 26–39.
8. Turanov, A.N.; Karandashev, V.R.; Artyushin, O.I.; Sharova, E.V.; Genkina, G.K. Adsorption of palladium (II) from hydrochloric acid solutions using polymeric resins impregnated with novel N-substituted 2- (diphenylthiophosphoryl) acetamides. *Sep. Purif. Technol.* 2017, *187*, 355–364. https://doi.org/10.1016/j.seppur.2017.06.068.
9. Wang, L.; Wang, K.; Huang, R.; Qin, Z.; Su, Y.; Tong, S. Chemosphere Hierarchically fl ower-like WS_2 microcrystals for capture and recovery of Au (III), Ag (I) and Pd (II). *Chemosphere* 2020, *252*, 126578. https://doi.org/10.1016/j.chemosphere.2020.126578.

10. de Gisi, S.; Lofrano, G.; Grassi, M.; Notarnicola, M. Characteristics and adsorption capacities of low-cost sorbents for wastewater treatment: A review. *Sustain. Mater. Technol.* 2016, *9*, 10–40. https://doi.org/10.1016/j.susmat.2016.06.002.
11. Sims, R.A.; Harmer, S.L.; Quinton, J.S. The role of physisorption and chemisorption in the oscillatory adsorption of organosilanes on aluminium oxide. *Polymers* 2019, *11*, 410. https://doi.org/10.3390/polym11030410.
12. Berger, A.H.; Bhown, A.S. Comparing physisorption and chemisorption solid sorbents for use separating CO_2 from flue gas using temperature swing adsorption. *Energy Procedia* 2011, *4*, 562–567. https://doi.org/10.1016/j.egypro.2011.01.089.
13. Al-Ghouti, M.A.; Da'ana, D.A. Guidelines for the use and interpretation of adsorption isotherm models: A review. *J. Hazard. Mater.* 2020, *393*, 122383. https://doi.org/10.1016/j.jhazmat.2020.122383.
14. Chai, W.S.; Cheun, J.Y.; Kumar, P.S.; Mubashir, M.; Majeed, Z.; Banat, F.; Ho, S.-H.; Show, P.L. A review on conventional and novel materials towards heavy metal adsorption in wastewater treatment application. *J. Clean. Prod.* 2021, *296*, 126589. https://doi.org/10.1016/j.jclepro.2021.126589.
15. Li, W.; Mu, B.; Yang, Y. Bioresource Technology Feasibility of industrial-scale treatment of dye wastewater via bio- adsorption technology. *Bioresour. Technol.* 2019, *277*, 157–170. https://doi.org/10.1016/j.biortech.2019.01.002.
16. Pullumbi, P.; Brandani, F.; Brandani, S. Gas separation by adsorption: Technological drivers and opportunities for improvement. *Curr. Opin. Chem. Eng.* 2019, *24*, 131–142. https://doi.org/10.1016/j.coche.2019.04.008.
17. Lin, R.B.; Xiang, S.; Xing, H.; Zhou, W.; Chen, B. Exploration of porous metal–organic frameworks for gas separation and purification. *Coord. Chem. Rev.* 2019, *378*, 87–103. https://doi.org/10.1016/j.ccr.2017.09.027.
18. Kew, B.; Holmes, M.; Stieger, M.; Sarkar, A. Oral tribology, adsorption and rheology of alternative food proteins. *Food Hydrocoll.* 2021, *116*, 106636. https://doi.org/10.1016/j.foodhyd.2021.106636.
19. Lovskaya, D.; Menshutina, N. Alginate-based aerogel particles as drug delivery systems: Investigation of the supercritical adsorption and in vitro evaluations. *Materials* 2020, *13*, 329. https://doi.org/10.3390/ma13020329.

20. Maponya, T.C.; Ramohlola, K.E.; Kera, N.H.; Modibane, K.D.; Maity, A.; Katata-Seru, L.M.; Hato, M.J. Influence of magnetic nanoparticles on modified polypyrrole/m-phenylediamine for adsorption of Cr(VI) from aqueous solution. *Polymers* 2020, *12*, 679. https://doi.org/10.3390/polym12030679.
21. Ariffin, N.; Abdullah, M.M.; Zainol, M.R.; Murshed, M.F.; Faris, M.A.; Bayuaji, R. Review on Adsorption of Heavy Metal in Wastewater by Using Geopolymer. *MATEC Web Conf.* 2017, *97*, 01023.
22. Qasem, N.A.A.; Mohammed, R.H.; Lawal, D.U. Removal of heavy metal ions from wastewater: A comprehensive and critical review. *Npj Clean Water* 2021, *4*, 36. https://doi.org/10.1038/s41545-021-00127-0.
23. Zhang, L.; Wang, J.; Du, T.; Zhang, W.; Zhu, W.; Yang, C.; Yue, T.; Sun, J.; Li, T.; Wang, J. NH_2-MIL-53 (Al) metal–organic framework as the smart platform for simultaneous high-performance detection and removal of Hg^{2+}. *Inorg. Chem*. 2019, 58, 12573–12581. https://doi.org/10.1021/acs.inorgchem.9b01242.
24. Okoro, H.K.; Ayika, S.O.; Ngila, J.C.; Tella, A.C. Rising profile on the use of metal–organic frameworks (MOFs) for the removal of heavy metals from the environment: An overview. *Appl. Water Sci.* 2018, *8*, 169. https://doi.org/10.1007/s13201-018-0818-3.
25. Rani, L.; Kaushal, J.; Srivastav, A.L.; Mahajan, P. A critical review on recent developments in MOF adsorbents for the elimination of toxic heavy metals from aqueous solutions. *Environ. Sci. Pollut. Res.* 2020, *27*, 44771–44796. https://doi.org/10.1007/s11356-020-10738-8.
26. Peng, Y.; Huang, H.; Zhang, Y.; Kang, C.; Chen, S.; Song, L.; Liu, D.; Zhong, C. A versatile MOF-based trap for heavy metal ion capture and dispersion. *Nat. comm.* 2018, *9*, 187. https://doi.org/10.1038/s41467-017-02600-2.
27. Lin, S.; Zhao, Y.; Bediako, J.K.; Cho, C.; Sarkar, A.K. Structure-controlled recovery of palladium (II) from acidic aqueous solution using metal-organic frameworks of MOF-802, UiO-66 and MOF-808. *Chem. Eng. J.* 2019, *362*, 280–286. https://doi.org/10.1016/j.cej.2019.01.044.
28. Hou, J.X.; Gao, J.P.; Liu, J.; Jing, X.; Li, L.J.; Du, J.L. Highly selective and sensitive detection of Pb^{2+} and UO_2^{2+} ions based on a carboxyl-functionalised Zn(II)-MOF

platform. *Dye. Pigment.* 2019, *160*, 159–164. https://doi.org/10.1016/j.dyepig.2018.08.012.

29. Beauchemin, D. *Inductively Coupled Plasma Mass Spectrometry Methods*, 3rd ed.; Elsevier Ltd.: Amsterdam, The Netherlands, 2016.
30. Meermann, B.; Nischwitz, V. ICP-MS for the analysis at the nanoscale-a tutorial review. *J. Anal. At. Spectrom.* 2018, *33*, 1432–1468. https://doi.org/10.1039/c8ja00037a.
31. Nageswaran, G.; Choudhary, Y.S.; Jagannathan, S. *Inductively Coupled Plasma Mass Spectrometry*; Elsevier Inc.: Amsterdam, The Netherlands, 2017; Volume 2.
32. Novaes, C.G.; Bezerra, M.A.; da Silva, E.G.P.; Santos, A.M.P.d.; Romão, I.L.d.; Neto, J.H.S. A review of multivariate designs applied to the optimization of methods based on inductively coupled plasma optical emission spectrometry (ICP OES). *Microchem. J.* 2016, *128*, 331–346. https://doi.org/10.1016/j.microc.2016.05.015.
33. Sneddon, J.; Vincent, M.D. ICP-OES and ICP-MS for the determination of metals: Application to oysters. *Anal. Lett.* 2008, *41*, 1291–1303. https://doi.org/10.1080/00032710802013991.
34. Eschnauer, H.; Jakob, L.; Meierer, H.; Neeb, R.; Use and Limitations of ICP-OES in Wine Analysis. *Microchim. Acta* 1989, *99*, 291–298. https://doi.org/10.1007/BF01244684.
35. Alqadami, A.A.; Naushad, M.; Alothman, Z.A.; Ghfar, A.A. Novel Metal − Organic Framework (MOF) Based Composite Material for the Sequestration of U (VI) and Th (IV) Metal Ions from Aqueous Environment. *ACS Appl. Mater. Interfaces* 2017, *9*, 36026–36037. https://doi.org/10.1021/acsami.7b10768.
36. Tang, J.; Zhao, J.; Wang, S.; Zhang, L.; Zhao, M.; Huang, Z.; Hu, Y. Pre-modification strategy to prepare a novel Zr-based MOF for selective adsorption of Palladium(II) from solution. *Chem. Eng. J.* 2021, *407*, 127223. https://doi.org/10.1016/j.cej.2020.127223.
37. Walsh, A. The application of atomic absorption spectra to chemical analysis. *Spectrochim. Acta* 1955, *7*, 108–117. https://doi.org/10.1016/0371-1951(55)80013-6.
38. Kokya, T.A.; Farhadi, K. Optimization of dispersive liquid–liquid microextraction for the selective determination of trace amounts of palladium by flame atomic absorption

spectroscopy. *J. Hazard. Mater.* 2009, *169*, 726–733. https://doi.org/10.1016/j.jhazmat.2009.04.005.

39. Shukor, S.A.; Hamzah, M.S.; Rahman, S.A.; Abdullah, N.A.; Elias, S.; Omar, S. Introduction of Flame Atomic Absorption Spectrometry (Faas) for River Water Samples Analysis. *Int. J. Chem. Sci*. 2013, *4*, 1.
40. Ghaedi, M.; Ahmadi, F.; Shokrollahi, A. Simultaneous preconcentration and determination of copper, nickel, cobalt and lead ions content by flame atomic absorption spectrometry. *J. Hazard. Mater.* 2007, *142*, 272–278. https://doi.org/10.1016/j.jhazmat.2006.08.012.
41. Jackson, K.W. Electrothermal atomic absorption spectrometry and related techniques. *Anal. Chem*. 2000, 72, 159-168. https://doi.org/10.1021/a1000008g.
42. Burylin, M.Y.; Pupyshev, A.A. Development of electrothermal atomic absorption spectrometry in 2005–2016. *J. Anal. Chem.* 2017, *72*, 935–946. https://doi.org/10.1134/S1061934817090039.
43. Bader, N.R. Sample preparation for flame atomic absorption spectroscopy: An overview. *Rasayan J. Chem.* 2011, *4*, 49–55.
44. Fuwa, K.; Vallee, B.L. The Physical Basis of Analytical Atomic Absorption Spectrometry: The Pertinence of the Beer-Lambert Law. *Anal. Chem.* 1963, *35*, 942–946. https://doi.org/10.1021/ac60201a006.
45. Matusiewicz, H. Atom trapping and in situ preconcentration techniques for flame atomic absorption spectrometry. *Spectrochim. Acta Part B At. Spectrosc. 1997*, *52*, 1711–1736.
46. Soltani, R.; Pelalak, R.; Pishnamazi, M.; Marjani, A.; Shirazian, S. A water-stable functionalised NiCo-LDH/MOF nanocomposite: Green synthesis, characterisation, and its environmental application for heavy metals adsorption. *Arab. J. Chem.* 2021, *14*, 103052. https://doi.org/10.1016/j.arabjc.2021.103052.
47. Verma, G.; Mishra, M. Development and optimization of UV-Vis spectroscopy—A review. *World J. Pharm. Res.* 2018, *7*, 1170–1180. https://doi.org/10.20959/wjpr201811-12333.

48. Upstone, S.L. Ultraviolet/Visible Light Absorption Spectrophotometry in Clinical Chemistry. In *Encyclopedia of Analytical Chemistry*; John Wiley & Sons Ltd.: Chichester, UK, 2000; pp. 1699–1714.
49. Andruch, V.; Kocúrová, L.; Balogh, I.S.; Škrlíková, J. Recent advances in coupling single-drop and dispersive liquid-liquid microextraction with UV-vis spectrophotometry and related detection techniques. *Microchem. J.* 2012, *102*, 1–10. https://doi.org/10.1016/j.microc.2011.10.006.
50. Mäntele, W.; Deniz, E. Spectrochimica Acta Part A : Molecular and Biomolecular Spectroscopy UV–VIS absorption spectroscopy : Lambert-Beer reloaded. *SAA* 2017, *173*, 965–968. https://doi.org/10.1016/j.saa.2016.09.037.
51. Mäntele, W.; Deniz, E. UV–VIS absorption spectroscopy: Lambert-Beer reloaded. *Spectrochim. Acta A Mol. Biomol. Spectrosc.* 2017, 173, 965-968. https://doi.org/10.1016/j.saa.2016.09.037.
52. Andruch, V.; Kocúrová, L.; Balogh, I.S.; Jana, Š. Recent advances in coupling single-drop and dispersive liquid–liquid microextraction with UV–vis spectrophotometry and related detection techniques. *Microchem. J.* 2012, *102*, 1–10. https://doi.org/10.1016/j.microc.2011.10.006.
53. Britain, G.; Press, P.; Chemistry, A. Derivative ultraviolet-visible region absorption spectrophotometry and its analytical applications. *Talanta* 1988, *35*, 753–761.
54. Ojeda, C.B.; Rojas, F.S. Recent developments in derivative ultraviolet/visible absorption spectrophotometry. *Anal. Chim. Acta* 2004, *518*, 1–24. https://doi.org/10.1016/j.aca.2004.05.036.
55. Limniou, M.; Papadopoulos, N.; Roberts, D. An integrated lecture, virtual instrumentation lab approach to teaching UV-Vis spectroscopy. *Educ. Inf. Technol.* 2007, 229–244. https://doi.org/10.1007/s10639-007-9040-x.
56. Diffey, B.L. Sources and measurement of ultraviolet radiation. *Methods* 2023, *28*, 4–13.
57. Yu, J.; Wang, H.; Zhan, J.; Huang, W. Review of recent UV-Vis and infrared spectroscopy researches on wine detection and discrimination. *Appl. Spectrosc. Rev.* 2018, *53*, 65–86. https://doi.org/10.1080/05704928.2017.1352511.

58. Bosch, S. New calibration method for UV–VIS photothermal deflection spectroscopy set-up. *Appl. Surf. Sci.* 2006, *253*, 158–162. https://doi.org/10.1016/j.apsusc.2006.06.010.
59. Daliran, S.; Ghazagh-Miri, M.; Oveisi, A.R.; Khajeh, M.; Navalón, S.; Âlvaro, M.; Ghaffari-Moghaddam, M.; Delarami, H.S.; García, H. A Pyridyltriazol Functionalised Zirconium Metal-Organic Framework for Selective and Highly Efficient Adsorption of Palladium. *ACS Appl. Mater. Interfaces* 2020, *12*, 25221–25232. https://doi.org/10.1021/acsami.0c06672.
60. Zhang, J.; Zhang, H.; Liu, Q.; Song, D.; Li, R.; Liu, P. Diaminomaleonitrile functionalised double-shelled hollow MIL-101 (Cr) for selective removal of uranium from simulated seawater. *Chem. Eng. J.* 2019, *368*, 951–958. https://doi.org/10.1016/j.cej.2019.02.096.
61. Abdelhameed, R.M.; Ismail, R.A.; El-Naggar, M.; Zarie, E.S.; Abdelaziz, R.; el Sayed, M.T. Post-synthetic modification of MIL-125 with bis-quinoline Mannich bases for removal of heavy metals from wastewater. *Microporous Mesoporous Mater.* 2019, *279*, 26–36. https://doi.org/10.1016/j.micromeso.2018.12.018.
62. Kalantari, H.; Manoochehri, M. A nanocomposite consisting of MIL-101(Cr) and functionalised magnetite nanoparticles for extraction and determination of selenium(IV) and selenium(VI). *Microchim. Acta* 2018, *185*, 196. https://doi.org/10.1007/s00604-018-2731-8.
63. Quan, X.; Sun, Z.; Meng, H.; Han, Y.; Wu, J.; Xu, J.; Xu, Y.; Zhang, X. Surface functionalisation of MIL-101(Cr) by aminated mesoporous silica and improved adsorption selectivity toward special metal ions. *Dalt. Trans.* 2019, *48*, 5384–5396. https://doi.org/10.1039/c9dt00501c.
64. Ryu, S.; Fonseka, C.; Naidu, G.; Loganathan, P.; Moon, H.; Kandasamy, J.; Vigneswaran, S. Recovery of rare earth elements (Lu, Y) by adsorption using functionalised SBA-15 and MIL-101 (Cr). *Chemosphere* 2021, *281*, 130869. https://doi.org/10.1016/j.chemosphere.2021.130869.
65. Zhang, J.Y.; Zhang, N.; Zhang, L.; Fang, Y.; Deng, W.; Yu, M.; Wang, Z.; Li, L.; Liu, X.; Li, J. Adsorption of Uranyl ions on Amine-functionalisation of MIL-101(Cr) Nanoparticles by a Facile Coordination-based Post-synthetic strategy and X-ray

Absorption Spectroscopy Studies. *Sci. Rep.* 2015, *5*, 13514. https://doi.org/10.1038/srep13514.

66. Elaiwi, F.A.; Sirkecioglu, A. Amine-functionalised metal organic frameworks MIL-101 (Cr) adsorbent for copper and cadmium ions in single and binary solution. *Sep. Sci. Technol.* 2020, *55*, 3362–3374. https://doi.org/10.1080/01496395.2019.1706571.
67. Wang, C.; Xiong, C.; He, Y.; Yang, C.; Li, X.; Zheng, J.; Wang, S. Facile preparation of magnetic Zr-MOF for adsorption of Pb (II) and Cr (VI) from water : Adsorption characteristics and mechanisms. *Chem. Eng. J.* 2021, *415*, 128923. https://doi.org/10.1016/j.cej.2021.128923.
68. Xu, W.Q.; He, S.; Liu, S.J.; Liu, X.H.; Qiu, Y.X.; Liu, W.T.; Liu, X.J.; Jiang, L.C.; Jiang, J.J. Post-synthetic modification of a metal-organic framework based on 5-aminoisophthalic acid for mercury sorption. *Inorg. Chem. Commun.* 2019, *108*, 107515. https://doi.org/10.1016/j.inoche.2019.107515.
69. Chauhan, A.; Chauhan, P. Analytical & Bioanalytical Techniques Powder XRD Technique and its Applications in Science and Technology. *J. Anal. Bioanal. Tech.* 2014, *5*, 212. https://doi.org/10.4172/2155-9872.1000212.
70. Fatimah, S.; Ragadhita, R.; Al Husaeni, D.F.; Nandiyanto, A.B.D.ASEAN Journal of Science and Engineering How to Calculate Crystallite Size from X-Ray Diffraction (XRD) using Scherrer Method. *ASEAN J. Sci. Eng.* 2010, *2*, 65–76.
71. Bunaciu, A.A.; gabriela Udriştioiu, E.; Aboul-Enein, H.Y. X-ray diffraction : Instrumentation and Applications. *Crit. Rev. Anal. Chem.* 2015, 45, 289-299,. https://doi.org/10.1080/10408347.2014.949616.
72. Adams, F.C. *X-Ray Absorption and Diffraction—Overview*, 3rd ed.; Elsevier Inc.: Amsterdam, The Netherlands, 2017.
73. Sarrazin, P.; Blake, D.; Feldman, S.; Chipera, S.; Vaniman, D.; Bish, D. Field deployment of a portable X-ray diffraction / X-ray flourescence instrument on Mars analog terrain. *Powder Diffr.* 2005, *20*, 128–133. https://doi.org/10.1154/1.1913719.
74. Dang, Z.; Le Song, X.; Qing Guo, X.; Yun Du, F.; Yang, J.; Yang, J. Applications of powder X-ray diffraction to inclusion complexes of cyclodextrins. Curr. Org. Chem. 2011, 15, 848-861. https://doi.org/10.2174/138527211794518899.

75. Yin, N.; Wang, K.; Xia, Y.; Li, Z. Novel melamine modified metal-organic frameworks for remarkably high removal of heavy metal Pb (II). *Desalination* 2018, *430*, 120–127. https://doi.org/10.1016/j.desal.2017.12.057.
76. Lim, C.R.; Lin, S.; Yun, Y.S. Highly efficient and acid-resistant metal-organic frameworks of MIL-101(Cr)-NH_2 for Pd(II) and Pt(IV) recovery from acidic solutions: Adsorption experiments, spectroscopic analyses, and theoretical computations. *J. Hazard. Mater.* 2020, *387*, 121689. https://doi.org/10.1016/j.jhazmat.2019.121689.
77. Müller, L.; Rubio-Pérez, G.; Bach, A.; Muñoz-Rujas, N.; Aguilar, F.; Worlitschek, J. Consistent DSC and TGA Methodology as Basis for the Measurement and Comparison of Thermo-Physical Properties of Phase Change Materials. *Materials* 2020, *13*, 4486.
78. Saadatkhah, N.; Carillo Garcia, A.; Ackermann, S.; Leclerc, P.; Latifi, M.; Samih, S.; Patience, G.S.; Chaouki, J. Experimental methods in chemical engineering: thermogravimetric analysis—TGA. *Can. J. Chem. Eng*. 2020, 98, 34-43. https://doi.org/10.1002/cjce.23673.
79. Coats, A.W.; Redfern, J.P. Thermogravimetric Analysis, A review. *Analyst* 1963, *88*, 906–924.
80. Loganathan, S.; Valapa, R.B.; Mishra, R.K.; Pugazhenthi, G.; Thomas, S. Thermogravimetric analysis for characterisation of nanomaterials" In *Thermal and Rheological Measurement Techniques for Nanomaterials Characterisation*; Elsevier: Amsterdam, The Netherlands, 2017; pp. 67–108.
81. Bensharada, M.; Telford, R.; Stern, B.; Gaffney, V. Loss on ignition versus thermogravimetric analysis : A comparative study to determine organic matter and carbonate content in sediments. *J. Paleolimnol.* 2022, *67*, 191–197. https://doi.org/10.1007/s10933-021-00209-6.
82. Ng, H.M.; Saidi, N.M.; Omar, F.S.; Ramesh, K.; Ramesh, S.; Bashir, S. Thermogravimetric analysis of polymers. In *Encyclopedia of Polymer Science and Technology*; John Wiley & Sons, Inc.: Hoboken, NJ, USA, 2002; pp. 1–29. https://doi.org/10.1002/0471440264.pst667.
83. Tomoda, B.T.; Yassue-Cordeiro, P.H.; Ernesto, J.V.; Lopes, P.S.; Péres, L.O.; da Silva, C.F.; de Moraes, M.A. Characterisation of biopolymer membranes and films:

Physicochemical, mechanical, barrier, and biological properties. In *Biopolymer Membranes and Films*; Elsevier: Amsterdam, The Netherlands, 2020; pp. 67–95. https://doi.org/10.1016/B978-0-12-818134-8.00003-1.

84. Comesaña, R.; Gómez, M.A.; Álvarez, M.A.; Eguía, P. Thermal lag analysis on a simulated TGA-DSC device. *Thermochim. Acta* 2012, *547*, 13–21. https://doi.org/10.1016/j.tca.2012.08.008.
85. Clausen, P.A.; Kofoed-Sørensen; V.; Nørgaard; A.W.; Sahlgren; N.M.; Jensen; K.A. Thermogravimetry and mass spectrometry of extractable organics from manufactured nanomaterials for identification of potential coating components. *Materials,* 2019, 12, 3657. https://doi.org/10.3390/ma12223657.
86. Karakaya, C.; Ricote, S.; Albin, D.; Sánchez-Cortezón, E.; Linares-Zea, B.; Kee, R.J. Thermogravimetric analysis of InCl3 sublimation at atmospheric pressure. Thermochimica Acta, 2015, 622, 55-63. https://doi.org/10.1016/j.tca.2015.07.018.
87. Wang, N.; Yang, L.Y.; Wang, Y.G.; Ouyang, X.K. Fabrication of composite beads based on calcium alginate and tetraethylenepentamine-functionalised MIL-101 for adsorption of Pb(II) from aqueous solutions. *Polymers* 2018, *10*, 750. https://doi.org/10.3390/polym10070750.
88. Lei, C.; Gao, J.; Ren, W.; Xie, Y.; Abdalkarim, S.Y.; Wang, S.; Ni, Q.; Yao, J. Fabrication of metal-organic frameworks@cellulose aerogels composite materials for removal of heavy metal ions in water. *Carbohydr. Polym.* 2019, *205*, 35–41. https://doi.org/10.1016/j.carbpol.2018.10.029.
89. Danley, R.L. New modulated DSC measurement technique. *Thermochim. Acta* 2003, *402*, 91–98.
90. Russel, M.; Yao, J.; Chen, H.; Wang, F.; Zhou, Y.; Choi, M.M.; Zaray, G.; Trebse, P. Different technique of microcalorimetry and their applications to environmental sciences: a review. *J. Am. Sci*, 2019, 5, 194-208.
91. Boguta, P.; Sokołowska, Z.; Skic, K. Use of thermal analysis coupled with differential scanning calorimetry, quadrupole mass spectrometry and infrared spectroscopy (TG-DSC-QMS-FTIR) to monitor chemical properties and thermal stability of fulvic and humic acids. PLoS One, *2017,* 12, p.e0189653. https://doi.org/10.1371/journal.pone.0189653.

92. Nurazzi, N.M.; Abdullah, N.; Norrrahim, M.N.F.; Kamarudin, S.H.; Ahmad, S.; Shazleen, S.S.; Rayung, M.; Asyraf, M.R.M.; Ilyas, R.A.; Kuzmin, M. Thermogravimetric Analysis (TGA) and Differential Scanning Calorimetry (DSC) of PLA/Cellulose Composites. In Polylactic Acid-Based Nanocellulose and Cellulose Composites, 2022, (pp. 145-164). CRC Press.
93. Nickle, S.K.; Meyers, K.O.; Nash, L.J. September. Shortcomings in the use of TGA/DSC techniques to evaluate in-situ combustion. In SPE Annual Technical Conference and Exhibition. OnePetro. 1987, Dallas, Texas, Paper Number: SPE-16867-MS. https://doi.org/10.2118/16867-MS
94. Mukasyan, A.S. DTA/TGA-based methods. In *Concise Encyclopedia of Self-Propagating High-Temperature Synthesis*; Elsevier: Amsterdam, The Netherlands, 2017; 93–95.
95. Dollimore, D.; Lerdkanchanaporn, S. Thermal Analysis. *Anal. Chem.* 1998, *70*, 17–25. https://doi.org/10.1021/a19800038.
96. Efome, J.E.; Rana, D.; Matsuura, T.; Lan, C.Q. Insight Studies on Metal-Organic Framework Nanofibrous Membrane Adsorption and Activation for Heavy Metal Ions Removal from Aqueous Solution. *ACS Appl. Mater. Interfaces* 2018, *10*, 18619–18629. https://doi.org/10.1021/acsami.8b01454.
97. Naderi, M. Surface Area: Brunauer-Emmett-Teller (BET). In Progress in Filtration and Seperation*;* Elsevier: Amsterdam, The Netherlands 2015, 585–608. https://doi.org/10.1016/B978-0-12-384746-1.00014-8.
98. Ambroz, F.; Macdonald, T.J.; Martis, V.; Parkin, I.P. Evaluation of the BET theory for the characterisation of meso and microporous MOFs. *Small Methods* 2018, *2*, 1800173. https://doi.org/10.1002/smtd.201800173.
99. Fagerlund, G. Determination of specific surface by the BET method. *Matériaux Constr.* 1973, *6*, 239–245. https://doi.org/10.1007/BF02479039.
100. Ladavos, A.K.; Katsoulidis, A.P.; Iosifidis, A.; Triantafyllidis, K.S.; Pinnavaia, T.J.; Pomonis, P.J. The BET equation, the inflection points of N_2 adsorption isotherms and the estimation of specific surface area of porous solids. *Microporous Mesoporous Mater.* 2012, *151*, 126–133. https://doi.org/10.1016/j.micromeso.2011.11.005.

101. Cerofolini, G.F.; Meda, L. A theory of multilayer adsorption on rough surfaces in terms of clustering and melting BET piles. *Surf. Sci.* 1998, *416*, 403–422. https://doi.org/10.1016/S0039-6028(98)00594-9.

102. Scherdel, C.; Reichenauer, G.; Wiener, M. Relationship between pore volumes and surface areas derived from the evaluation of N_2-sorption data by DR-, BET- and t-plot. *Microporous Mesoporous Mater.* 2010, *132*, 572–575. https://doi.org/10.1016/j.micromeso.2010.03.034.

103. Sing, K. The use of nitrogen adsorption for the characterisation of porous materials. *Colloids Surf. A Physicochem. Eng. Asp.* 2001, *187–188*, 3–9. https://doi.org/10.1016/S0927-7757(01)00612-4.

104. Walton, K.S.; Snurr, R.Q. Applicability of the BET method for determining surface areas of microporous metal-organic frameworks. *J. Am. Chem. Soc.* 2007, *129*, 8552–8556. https://doi.org/10.1021/ja071174k.

105. Aguerre, R.J.; Suarez, C.; Viollaz, P.E. New BET type multilayer sorption isotherms. Part II: Modelling water sorption in foods. *LWT-Food Sci. Technol.* 1989, *22*, 192–195.

106. . Mohan, V.B.; Jayaraman, K.; Bhattacharyya, D. Brunauer–Emmett–Teller (BET) specific surface area analysis of different graphene materials: a comparison to their structural regularity and electrical properties. Solid State Commun. 2020, 320,114004. https://doi.org/10.1016/j.ssc.2020.114004.

107. Luo, X.; Ding, L.; Luo, J. Adsorptive removal of Pb(II) ions from aqueous samples with amino-functionalisation of metal-organic frameworks MIL-101(Cr). *J. Chem. Eng. Data* 2015, *60*, 1732–1743. https://doi.org/10.1021/je501115m.

108. Zhou, W.; Apkarian, R.; Wang, Z.L.; Joy, D. Fundamentals of scanning electron microscopy (SEM). In *SCANNING Microscopy for Nanotechnology*; Springer: New York, NY, USA, 2007; pp. 1–40. https://doi.org/10.1007/978-0-387-39620-0_1.

109. Yoshida, A.; Kaburagi, Y.; Hishiyama, Y.; *Chapter 5—Scanning Electron Microscopy*; Tsinghua University Press Limited: 2016.

110. Kirk, T.L. A Review of Scanning Electron Microscopy in Near Field Emission Mode. *Adv. Imaging Electron Phys.* 2017, *204*, 39–109.

111. Newbury, D.E.; Ritchie, N.W. Elemental mapping of microstructures by scanning electron microscopy-energy dispersive X-ray spectrometry (SEM-EDS): extraordinary advances with the silicon drift detector (SDD). *J. Anal. At. Spectrom.* 2013, 28, 973-988. https://doi.org/10.1039/C3JA50026H.

112. Abdullah, A.; Mohammed, A.; Scanning Electron Microscopy (SEM): A Review Scanning Electron Microscopy (SEM): A Review. In Proceedings of the 2018 International Conference on Hydraulics and Pneumatics—HERVEX, Băile Govora, Romania, 7–9 November 2019; pp. 1–9.

113. Baer, D.R.; Thevuthasan, S. Characterisation of thin films and coatings. In *Handbook of Deposition Technologies for Films and Coatings*; William Andrew Publishing: 2010; pp. 749–864.

114. Inkson, B.J. *Scanning Electron Microscopy (SEM) and Transmission Electron Microscopy (TEM) for Materials Characterisation*; Elsevier Ltd.: Amsterdam, The Netherlands, 2016.

115. Neville, A.; Mather, R.R.; Wilson, J.I.B. *Characterisation of Plasma-Treated Textiles*; Woodhead Publishing Limited: 2007.

116. Newbury, D.E.; Ritchie, N.W.M. Is scanning electron microscopy/energy dispersive X-ray spectrometry (SEM/EDS) quantitative? *Scanning* 2013, *35*, 141–168. https://doi.org/10.1002/sca.21041.

117. Akkaş, E.; Akin, L.; Çubukçu, H.E.; Artuner, H. Application of Decision Tree Algorithm for classification and identification of natural minerals using SEM-EDS. *Comput. Geosci.* 2015, *80*, 38–48. https://doi.org/10.1016/j.cageo.2015.03.015.

118. Lovejoy, T.C.; Ramasse, Q.M.; Falke, M.; Kaeppel, A.; Terborg, R.; Zan, R.; Dellby, N.; Krivanek, O.L. Single atom identification by energy dispersive x-ray spectroscopy Single atom identification by energy dispersive x-ray spectroscopy. *Appl. Phys. Lett.* 2012, *154101*, 2–6. https://doi.org/10.1063/1.3701598.

119. Hodoroaba, V.D. Energy-dispersive X-ray spectroscopy (EDS). In *Characterisation of Nanoparticles*; Elsevier: Amsterdam, The Netherlands, 2020; pp. 397–417.

120. Shindo, D.; Tetsuo, O. Energy dispersive x-ray spectroscopy. In *Analytical Electron Microscopy for Materials Science*; Springer: Tokyo, Japan, 2002; pp. 81–102.

121. Bedia, J.; Muelas-ramos, V.; Peñas-garz, M.; Almudena, G.; Rodr, J.J.; Belver, C. A Review on the Synthesis and Characterisation of Metal Organic Frameworks for Photocatalytic Water Purification. *Catalysts* 2019, *9*, 52. https://doi.org/10.3390/catal9010052.

122. Thanh, H.T.M.; Phuong, T.T.; le Hang, P.T.; Toan, T.T.; Tuyen, T.N.; Mau, T.X.; Khieu, D.Q. Comparative study of Pb(II) adsorption onto MIL-101 and Fe-MIL-101 from aqueous solutions. *J. Environ. Chem. Eng.* 2018, *6*, 4093–4102. https://doi.org/10.1016/j.jece.2018.06.021.

123. Wang, Z.L. New developments in transmission electron microscopy for nanotechnology. *Adv. Mater.* 2003, *15*, 1497–1514. https://doi.org/10.1002/adma.200300384.

124. McNeill, A. PLA2G6 Mutations and Other Rare Causes of Neurodegeneration with Brain Iron Accumulation. *Curr. Drug Targets* 2012, *13*, 1204–1206. https://doi.org/10.2174/138945012802002401.

125. Bogner, A.; Jouneau, P.H.; Thollet, G.; Basset, D.; Gauthier, C. A history of scanning electron microscopy developments: Towards 'wet-STEM' imaging. *Micron* 2007, *38*, 390–401. https://doi.org/10.1016/j.micron.2006.06.008.

126. Wang, Z.L. Transmission Electron Microscopy of Shape-Controlled Nanocrystals and Their Assemblies. *J. Phys. Chem.* 2000, 104, 1153–1175. https://doi.org/10.1021/jp993593c.

127. Madsen, J.; Susi, T. The abTEM code : Transmission electron microscopy from first principles. *Open Res. Eur.* 2021, 1, 1-30. https://doi.org/10.12688/openreseurope.13015.2.

128. Denny, M.S.; Parent, L.R.; Patterson, J.P.; Meena, S.K.; Pham, H.; Abellan, P.; Ramasse, Q.M.; Paesani, F.; Gianneschi, N.C.; Cohen, S.M. Transmission Electron Microscopy Reveals Deposition of Metal Oxide Coatings onto Metal−Organic Frameworks. *J. Am. Chem. Soc.* 2018, *140*, 1348–1357. https://doi.org/10.1021/jacs.7b10453.

129. Lv, S.; Liu, J.; Li, C.; Zhao, N.; Wang, Z. A novel and universal metal-organic frameworks sensing platform for selective detection and efficient removal of heavy

metal ions. *Chem. Eng. J.* 2019, *375*, 122111. https://doi.org/10.1016/j.cej.2019.122111.

130. Abedini, H.; Shariati, A.; Khosravi-nikou, M.R. Separation of propane / propylene mixture using MIL-101 (Cr) loaded with cuprous oxide nanoparticles : Adsorption equilibria and kinetics study. *Chem. Eng. J.* 2020, *387*, 124172. https://doi.org/10.1016/j.cej.2020.124172.
131. Liu, L.; Fang, Y.; Meng, Y.; Wang, X.; Ma, F.; Zhang, C. E ffi cient adsorbent for recovering uranium from seawater prepared by grafting amidoxime groups on chloromethylated MIL-101 (Cr) via diaminomaleonitrile intermediate. *Desalination* 2020, *478*, 114300. https://doi.org/10.1016/j.desal.2019.114300.
132. Mohamed, M.A.; Jaafar, J.; Ismail, A.F.; Othman, M.H.D.; Rahman, M.A. *Fourier Transform Infrared (FTIR) Spectroscopy*; Elsevier B.V.: Amsterdam, The Netherlands, 2017.
133. Dutta, A. Fourier transform infrared spectroscopy. In *Spectroscopic Methods for Nanomaterials Characterisation*; Elsevier: Amsterdam, The Netherlands, 2017; pp. 73–93.
134. Blum, M.; John, H. Historical perspective and modern applications of Attenuated Total Reflectance–Fourier Transform Infrared Spectroscopy (ATR-FTIR). *Drug Test. Anal.* 2011, *4*, 298–302. https://doi.org/10.1002/dta.374.
135. Ismail, A.A.; van de Voort, F.R.; Sedman, J. Chapter 4 Fourier Transform Infrared Spectroscopy : Principles and Applications. In *Techniques and Instrumentation in Analytical Chemistry*; Elsevier; Amsterdam, The Netherlands, 1997.
136. Bacsik, Z.; Mink, J.; Keresztury, G. FTIR Spectroscopy of the Atmosphere. I. Principles and Methods. *Appl. Spectrosc. Rev.* 2004, *39*, 295–363. https://doi.org/10.1081/ASR-200030192.
137. Taylor, P.; Bunaciu, A.A.; Aboul-enein, H.Y. Application of Fourier Transform Infrared Spectrophotometry in Pharmaceutical Drugs Analysis Application of Fourier Transform Infrared Spectrophotometry in Pharmaceutical. *Appl. Spectrosc. Rev.* 2010, *45*, 206–219. https://doi.org/10.1080/00387011003601044.
138. Ji, C.; Wu, D.; Lu, J.; Shan, C.; Ren, Y.; Li, T.; Lv, L.; Pan, B.; Zhang, W. Temperature regulated adsorption and desorption of heavy metals to A-MIL-121:

Mechanisms and the role of exchangeable protons. *Water Res.* 2021, *189*, 116599. https://doi.org/10.1016/j.watres.2020.116599.

139. Wang, X.; Manikoff, J.N. Metal-Organic Frameworks for Mercury Sensing and Removal. General Chemistry, 2018, 4, 180003-180003. doi: 10.21127/yaoyigc20180003.

140. Luo, X.; Shen, T.; Ding, L.; Zhong, W.; Luo, J.; Luo, S. Novel thymine-functionalised MIL-101 prepared by post-synthesis and enhanced removal of Hg^{2+} from water. *J. Hazard. Mater.* 2016, *306*, 313–322. https://doi.org/10.1016/j.jhazmat.2015.12.034.

141. Jalayeri, H.; Aprea, P.; Caputo, D.; Peluso, A.; Pepe, F. Synthesis of amino-functionalised MIL-101(Cr) MOF for hexavalent chromium adsorption from aqueous solutions. *Environ. Nanotechnol. Monit. Manag.* 2020, *14*, 100300. https://doi.org/10.1016/j.enmm.2020.100300.

142. Engelhard, M.H.; Droubay, T.C.; Du, Y. X-ray photoelectron spectroscopy applications. In *Related Information: Encyclopedia of Spectroscopy and Spectrometry*, 3rd ed.; Elsevier: Amsterdam, The Netherlands, 2017; pp. 716–724. https://doi.org/10.1016/B978-0-12-409547-2.12102-X.

143. Stevie, F.A.; Donley, C.L. Introduction to x-ray photoelectron spectroscopy. *J. Vac. Sci. Technol. A* 2020, *38*, 063204. https://doi.org/10.1116/6.0000412.

144. Huang, H.; Qiao, Y.; Yuan, Y.; Zhang, J. Surface functionalisation for heterogeneous catalysis. In Encyclopedia of Nanomaterials. Elsevier: Amsterdam, The Netherlands, 2022, pp. 1–13. https://doi.org/10.1016/B978-0-12-822425-0.00073-7.

CHAPTER FOUR

FUNCTIONALISED POLYETHYLENE TEREPHTHALATE-DERIVED METAL-ORGANIC FRAMEWORKS FOR SPECTROSCOPIC DETECTION AND ADSORPTION OF PALLADIUM IONS FROM AQUEOUS SOLUTIONS

4.1. INTRODUCTION

Palladium (Pd) is one of the economically valuable metals belonging to the platinum group metals (PGMs) [1]. Owing to its unique physical and chemical properties, Pd has gained extensive utilisation in modern industrial technologies including catalysis [2], hydrogen production [3] and storage [4] devices, and pharmaceuticals production [5]. With an increase in civilization, there is a need for rapid industrialisation that requires the use of Pd in order to meet the growing demand for its utilisation. However, this leads to the depletion of Pd natural reserves as well as increased discharge of Pd-containing waste into the environment which can be harmful to living organisms [6]. Therefore, the results of these activities trigger the need to develop efficient technologies for the removal and recovery of Pd ions from wastewater. Numerous conventional methods such as precipitation [7], reverse osmosis [8], electrochemical deposition [9], membrane technology [10], solid phase extraction [11], and adsorption [12] have been developed for the removal of Pd ions from wastewater. The adsorption technique has received great attention amongst the mentioned technologies owing to its simplicity in design, high efficiency, and cost-effectiveness [13]. Over the years, different adsorbent materials and their composites have been investigated and they have demonstrated promising activities for recovering and removing Pd ions from simulated wastewater [14][15][16][17]. Amongst the reported materials, a new class of porous coordination polymers such as metal-organic frameworks (MOFs) has gained interest in the field of wastewater treatment due to their fascinating properties [18]–[20]. MOFs are 3D structured polymers consisting of metal ion clusters connected together by organic ligands resulting in a defined micro- or nano-material. The fascinating properties of these materials include high surface area, high pore volume, and chemical tuneability [21][22]. Furthermore, the flexibility and porous nature of MOFs permit guest molecules like metal ions to easily diffuse into the

bulk structure, wherein the shape and size of the pores are able to selectively adsorb the molecules of interest [23]. MOFs may be prepared from polyethylene terephthalate (PET) plastic waste bottle, which serves as the source of organic linker called 1,4-benzenedicarboxylic acid (H_2BDC) [24][25]. The successful development of this method of synthesising MOF materials offers an economically attractive strategy for PET waste management [26][27]. There are several MOFs reported in the literature [28]–[31]. Among these MOFs, chromium-based MOFs which were developed by the Férey group under Material Institut Lavoisier (MIL) have attracted attention owing to their thermal and chemical stability [32][33]. In addition, these MOFs can be modified through the post-synthesis method to enhance their functionality in the selective separation of guest molecules, while maintaining their crystallinity [33]. For example, Hu and his co-workers [34] prepared MIL-101(Cr) functionalised with ethylenediamine (ED) for the capturing of oxytetracycline (OTC). The composite showed the successful incorporation of ED as deduced from FTIR with the appearance of the band 1051 cm^{-1} attributed to the C-N bond stretching of the amino group. They showed that the ED-MIL-101(Cr) adsorbent has the ability to adsorb OTC with the Langmuir maximum adsorption capacity of 454.6 mg/g at 25 ◦C. Furthermore, the composite achieved fast kinetics for the removal of OTC at the equilibrium time of 90 minutes and was reusable for 3 cycles. In a study conducted by Zheng and co-workers [35], MIL-101(Cr) and MIL-101(Cr)/graphene oxide (GO) composites were prepared via the hydrothermal method for the removal of chlorinated volatile organic compounds. MIL-101(Cr) and MIL-101(Cr)/GO composite demonstrated a high BET surface area of 1832 and 2026 m^2 g^{-1}, respectively. They obtained the maximum adsorption capacity of 2044.4 mg/g using MIL-101(Cr) and 2368.1 mg/g using MIL-101(Cr)/GO for the removal of carbon tetrachloride. Zhuo *et a*l. [21] reported on the formation of composite beads between MIL-101(Cr) and natural polymers which are sodium alginate (SA) and chitosan (CS) for the removal of selected pharmaceuticals and personal care products (PPCPs) from wastewater. The XRD results showed that MIL-101(Cr) MOFs maintained their crystallinity even after composites formation and also demonstrated improved BET surface areas. The reported MIL-101(Cr)/SA and MIL-101(Cr)/CS bead composites showed an increase in the uptake of selected PPCPs as compared to their pristine counterparts. Luo and colleagues [36] functionalised MIL-

101(Cr) with thymine for the removal of mercury ions (Hg(II)) from wastewater and obtained a Langmuir maximum adsorption capacity (qm) of 51.27 mg/g. In another study reported by Lim and co-workers [37], MIL-101(Cr)-NH_2 was prepared from the reduction of nitro-functionalised MIL-101(Cr)-NO_2 for recovery of Pd(II) and Pt(IV)from wastewater. The composite showed higher uptake and fast kinetics for the selected PGMs, which was due to the affinity of protonated amino groups in MIL-101(Cr)-NH_2 towards Pd and Pt ions. The maximum adsorption capacities obtained were 277.6 and 140.7 mg/g for Pd(II) and Pt(II), respectively. Hence in this study, we present the functionalisation of MIL-101(Cr) with ED for the removal and recovery of Pd(II) from simulated wastewater. ED is a coordination agent possessing two amine ligands and its incorporation is motivated by the easy protonation of its amino groups ($–NH_3^+$), especially in acidic environments. Thus, the electrostatic attraction between $–NH_3^+$ and Pd anions is highly expected, forming coordination complex at faster rates [38]. The MIL-101(Cr) was prepared from a waste PET bottle as a source of H_2BDC. The prepared MIL-101(Cr)/ED composite was investigated for the adsorption of Pd(II) ions from simulated wastewater, by checking the effects of different parameters such as pH, temperature, contact time, and adsorbent dose. Furthermore, the obtained results were fit to Langmuir and Freundlich models in order to determine the mode of adsorption as well as the qm.

4.2. MATERIALS AND EXPERIMENTS

4.2.1. Materials

Chromium nitrate nanohydrate $Cr(NO_3)_3.9H_2O$, ethylenediamine (ED), palladium chloride ($PdCl_2$), and ethylene glycol (EG) were purchased from Sigma-Aldrich (South Africa). PET waste bottles were collected from the University of Limpopo, Polokwane, South Africa. The bottles' caps, rings, and labels were removed, followed by a thorough cleaning with water and ethanol. After drying at room temperature they were cut into small flakes using a pair of scissors. Other reagents used in this study were of analytical grade and were utilised without any further purification.

4.2.2. Experimental Synthesis and Functionalisation of MIL-101(Cr)

4.2.2.1. Depolymerisation of PET

Preparation of 1,4 benzenedicarboxylic acid (H_2BDC) organic linker was carried out via hydrothermal method in a 100.00 mL autoclave as reported in the literature [24]. Typically, PET flakes (3.00 g) were weighed and put into a reactor together with 6.00 mL of EG and 60.0 mL of deionised (DI) H_2O. The reaction mixture was then heated at 210 °C for 8 hours in an oven. After the reaction, the obtained white precipitates were filtered, followed by washing with ethanol and dried at 100 °C for 24 hours.

4.2.2.2. Synthesis and modification of MIL-101(Cr) and MIL-101(Cr)/ED

Chromium-based MIL was synthesised based on the reported procedure [39]. Briefly, 4.00 g of $Cr(NO_3)_3.9H_2O$ and 1.66 g of H_2BDC were dispersed in DI H_2O, followed by stirring for 15 minutes using a magnetic mixer and then ultra-sonicated for 30 minutes. The acquired suspension was transferred into a Teflon-lined stainless steel autoclave and put in an oven. The reaction was heated and kept at 220 °C for 8 hours. The resulting product was filtered and washed prior to being dried under ambient conditions. For modification, 0.50 g of the prepared MIL-101(Cr) was dispersed in anhydrous toluene (50.0 mL) followed by the addition of 1.00 mL of ED. The reaction mixture was then refluxed for 12 hours. The obtained product was filtered using cellulose filter paper and washed several times with ethanol and finally dried at room temperature.

4.2.3. Spectroscopic and Morphological Characterisation

X-ray diffraction (XRD) patterns for phase identification of the MIL-101(Cr) and MIL-101(Cr)/ED composites were conducted using a Bruker Advance powder diffractometer (Madison, USA; 40 mA, 40 keV, λCu-K = 0.15406 nm. Morphological and elemental analyses were obtained from the field-emission scanning electron microscopy (FE-SEM) (Auriga Cobra focused-ion beam FIB-SEM, Carl Zeiss, Jena, Germany) coupled with energy dispersive x-ray spectroscopy (EDS). The Brunauer–Emmet–Teller (BET) surface area and pore volume measurements of the prepared MIL-101(Cr) and MIL-101(Cr)/ED

composites were deduced using a Tristar micromeritics instrument by using low-pressure nitrogen (77 K) adsorption/desorption technique. The presence of functional groups and composite formation was confirmed by Cary 600 series Fourier transform infrared (FTIR) spectrometer (Spectrum II PerkinElmer). The thermal properties of MIL-101(Cr) and MIL-101(Cr)/ED composites were obtained from a PerkinElmer STA 6000 instrument connected to a PolyScience digital temperature controller under N_2 gas purged at a flow rate of 20 mL/min.

4.2.4. Adsorption Experiments

In order to determine the adsorption behaviour of the prepared MIL-101(Cr)/ED different adsorption parameters were investigated, by using 50.0 mL of Pd(II) solution having a concentration of 100 mg/L. The palladium stock solution was prepared in an acidic medium, by dissolving $PdCl_2$ in 0.100 M hydrochloric acid (HCl) solution. The remaining concentrations of Pd(II), before and after adsorption were determined from the ultraviolet-visible (UV-Vis) spectroscopy (Lambda 365 UV/Vis Spectrophotometer, (PerkinElmer, Johannesburg, South Africa)) operated at a wavelength of 450 nm and the removal efficiency of MIL-101(Cr)/ED towards Pd(II) ions were calculated from the below equations:

$$\% \text{ removal} = \left(\frac{Co-Ce}{Ce}\right) \times 100 \quad (4.1)$$

$$q_e = \left(\frac{Co-Ce}{m}\right)V \quad (4.2)$$

with Co and Ce representing the initial and equilibrium concentrations of Pd(II) in mg/L, respectively. q_e is the amount of Pd(II) ions adsorbed at equilibrium per mass of MIL-101(Cr)/ED measured in mg/g, whereas m (g) signifies the mass of the adsorbent and V (L) the volume of Pd(II) solution utilised.

4.2.4.1. Effect of solution pH and adsorbent dose

The studies on the effect of initial solution pH on the uptake of Pd(II) ions by MIL-101(Cr)/ED were conducted at controlled pH, ranging from 1.0-6.0. This was achieved by

contacting 0.03 g of the prepared adsorbent with 50.0 mL Pd(II) solution at a constant temperature and shaking speed of 298 K and 150 rpm, respectively. The pH of the 100 mg/L Pd(II) solution was adjusted using various concentrations of HCl and sodium hydroxide (NaOH). To understand the effect of adsorbent dosage, the amount of MIL-101(Cr)/ED was varied from 0.01-0.070 g while keeping other parameters such as temperature, initial concentration, contact time, and pH constant.

4.2.4.2. Adsorption isotherms

For the studies on the effect of temperature on the adsorption of Pd(II) ions by MIL-101(Cr)/ED, different initial concentrations (50 − 400 mg/L) were used with the constant adsorbent dose of 0.03 g and a pH of 3.0. The experiments were conducted at three different temperatures of 298, 308, and 318 K in a water bath shaker for 24 hours at a constant speed of 160 rpm. After the completion of the adsorption process, the solution and adsorbent were separated through filtration, followed by the determination of the final concentration. The data was fit to the two isothermal models which are the nonlinear and linear forms of the Langmuir and Freundlich models shown in the below equations.

$$\frac{q_e}{q_m} = \frac{K_L C_e}{1+K_L C_e} \quad (4.3)$$

$$q_e = K_F Ce^{1/n} \quad (4.4)$$

$$\frac{C_e}{q_e} = \frac{1}{qmKL} + \frac{Ce}{q_m} \quad (4.5)$$

$$\ln q_e = \ln K_F + \frac{1}{n} \ln C_e \quad (4.6)$$

where qm (mg/g), K_L (L/mg), K_F (mg/g) and n each represent the Langmuir maximum adsorption capacity, Langmuir constant, Freundlich constant and adsorption intensity, respectively.

4.2.4.3. Adsorption kinetics

For investigating the adsorption kinetics, experiments were conducted using three different Pd(II) initial solution concentrations, which were 25.0, 50.0, and 100 mg/L. The MIL-101(Cr)/ED adsorbent was contacted with the above-mentioned Pd(II) concentration

at varying times to check the effect of contact time on the uptake of Pd(II) ions by the MIL-101(Cr)/ED. In a typical procedure, 0.03 g of MIL-101(Cr)/ED adsorbent was exposed to 500 mL of 100 mg/L Pd(II) solution at a pH of 3.0 in a temperature-controlled water bath. The reaction mixture was mixed using an overhead stirrer set at a speed of 200 rpm at 25 ◦C. Several aliquots were withdrawn from the mixture at specific time intervals and filtered with 0.450 µm cellulose acetate syringe filters, followed by analysis with UV-Vis. The data obtained from kinetics experiments were then used to establish the rate of adsorption and other adsorption kinetics parameters, by fitting it to the nonlinear and linear forms of the pseudo-first-order (PFO) and the pseudo-second-order (PSO) kinetic models determined using the following equations:

$$\frac{dqt}{dt} = k_1 (q_e - q_t) \quad (4.7)$$

$$\frac{dqt}{dt} = k_2 (qe - qt)^2 \quad (4.8)$$

$$\ln (q_e - q_t) = \ln q_e - k_1 t \quad (4.9)$$

$$\frac{t}{qt} = \frac{1}{k_2 q^2 t} + \frac{1}{q_e} t \quad (4.10)$$

where k_1 (1/min) represents PFO rate constant and k_2 (g/mg.min) denotes the PSO rate constant.

4.2.4.4. Competing ions effect

The investigation of the selectivity of the MIL-101(Cr)/ED adsorbent for the uptake of Pd(II) ions was done using various selected cations (Ru^{3+}, Co^{2+}, Ni^{2+}, Ag^{+} Pt^{2+}) and anions (SO_4^{2-}, CO_3^{2-}, Cl^{-}, NO_3^{-}, PO_4^{2-}) at a concentration 100 mg/L in solutions.

4.3. RESULTS AND DISCUSSION

4.3.1. Benzenedicarboxylic acid organic linker

Figure 4.1 shows the FITR spectra for the PET and benzenedicarboxylic acid (BDC) organic linker. The absorption bands of the PET were detected with the major peaks at

1730 cm^{-1} for carbonyl stretching (C=O) of the carboxylic acid group, 1240 and 1124 cm^{-1} for the terephthalate group ($OOCC_6H_4$-COO), 1096 and 1050 cm^{-1} for methylene group and vibrations of the ester C-O bond, whereas the 712 cm^{-1} was for the interaction of polar ester groups and benzene rings [40][41]. The spectrum for BDC revealed numerous peaks in the 2358-3076 cm^{-1} and at 1572, 1510, 1420, and 1280 cm^{-1} which are ascribed to the asymmetric vibrational stretches of the carboxylic functional groups [27], [42]–[44]. The intense peak at 1674 cm^{-1}, as well as the band at 1280 cm^{-1}, are ascribed to the C=O vibrational stretching of the carbonyl groups and the C-O symmetric stretch of the acid sites, respectively. Interestedly, there was a shift and reduction of the terephthalate group of PET polymer in the formation of BDC organic linker. The broadening of the OH peaks at 3432 cm^{-1} for the hydroxyl group was also observed in BDC. Furthermore, the ringing and -out-of-plane bending vibrations of aromatic rings are attributed to the IR bands at 728 and 686 cm^{-1} [27]. All the absorption bands observed are correlating well with those in the literature, signifying the successful conversion of PET to BDC.

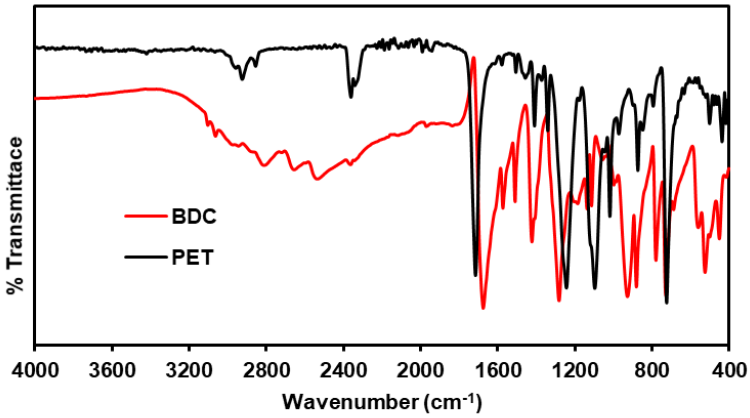

Figure 4.1: FTIR spectra of PET and BDC.

The FTIR spectra of the prepared neat MIL-101(Cr) and the modified MIL-101(Cr)/ED are represented in Figure 4.2(a). These spectra are demonstrated in the wavenumber range of 400–4000 cm^{-1}. The spectrum of MIL-101(Cr) showed bands at 1404 and 1625 cm^{-1} which are assigned to C-O and C=O symmetrical stretching vibration, respectively [45]. The presence of C=C stretching of the benzene ring was observed at 1508 cm^{-1} and C-

H deformation vibrations of the aromatic ring at 750, 884, 1018, and 1160 cm^{-1} respectively [21][46]. Peaks related to stretching vibrations of oxygen with metals are usually observed in the ranges of 400–800 cm^{-1} and in this spectrum, the observed peak at 674 cm^{-1} is associated with Cr-O vibration [21]. Based on the MIL-101(Cr)/ED spectrum, all the characteristic peaks corresponding to the MIL-101(Cr) compound are present [47]. Furthermore, there are broad peaks appearing between 2800-3300 cm^{-1} and a new peak at 1039 cm^{-1} that is attributed to the N-H stretching and C-N stretching, respectively [48][49]. The absorption bands of N-H bend and C-C stretching were observed at 1553 and 1345 cm^{-1} for the amino and the aliphatic CH_2 groups of the ED, respectively. In addition, the N-Cr vibration was observed at 506 cm^{-1}, confirming the successful post-modification process of the MIL-101(Cr) compound with ED.

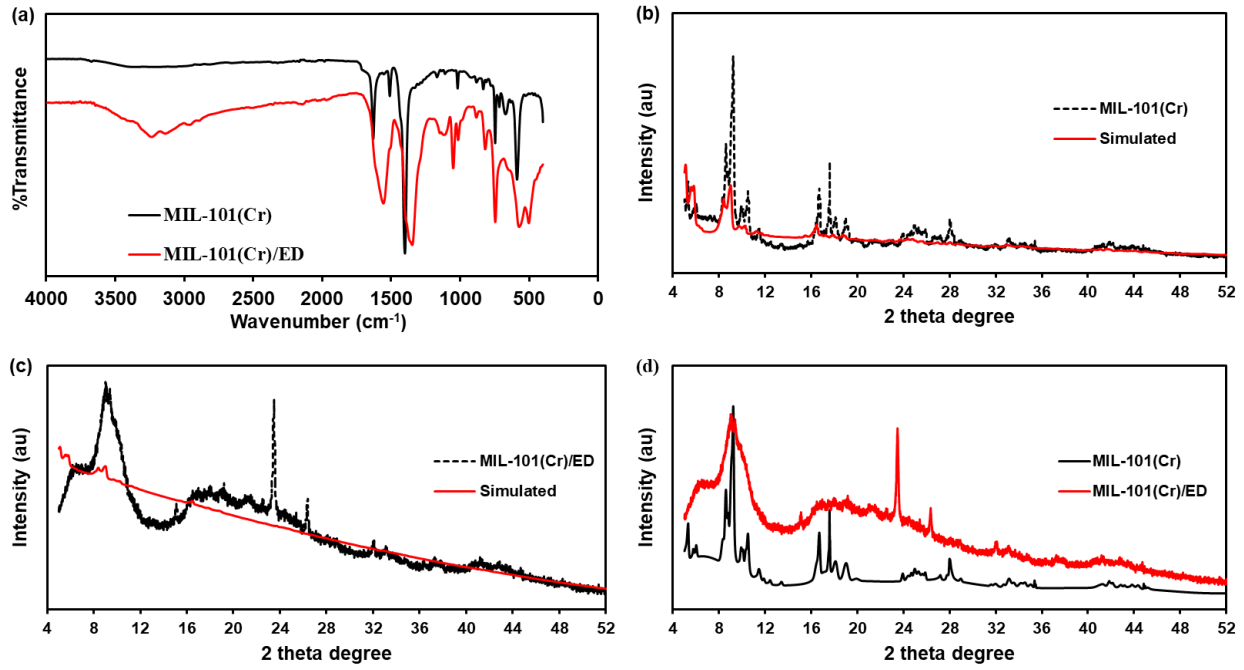

Figure 4.2: (a) FTIR of MIL-101(Cr) and MIL-101(Cr)/ED; (b) XRD patterns and fitted pattern of MIL-101(Cr); (c) XRD patterns and fitted pattern of MIL-101(Cr)/ED and (d) XRD patterns of MIL-101 and MIL-101(Cr)/ED.

To study the crystalline structure and to confirm the successful synthesis of MIL-101(Cr), XRD analysis was performed and the data are shown in Figure 4.2(b). The obtained characteristic peaks at 5.59º, 8.63º, 9.25º, 9.90º, 10.6º, 11.7º, 16.8º, 17.6º, 18.2º, and 19.2º for the MIL-101(Cr) sample correlate well with those reported in the literature [34][45], confirming the successful synthesis of MIL-101(Cr). As shown in Figure 4.2(b), it was observed that the prepared MIL-101(Cr) has a highly crystalline structure. It was reported that the presence of intense peaks at small angles (2θ) as seen here confirms the existence of ample pores in the prepared MIL-101(Cr) structure [50]. In addition, the crystallography information file (CIF) of MIL-101 was used in order to plot the XRD simulated pattern from crystallography information which is available on the crystallography websites [51]. The CIF file was introduced to MAUD software and the powder diffraction analysis was taken. The results of the simulated structure of MIL-101(Cr) are also shown in Figure 2(b), confirming the successful synthesis of MIL-101(Cr) with XRD lattice parameter (a=b=c) of 86.1 Å as compared to 88.9 Å of the simulated one, making the prepared MIL-101(Cr) to have 96.1% of crystallinity.

Upon functionalisation with ED, the peaks were broadened with characteristic peaks still observed on the XRD pattern of MIL-101(Cr)/ED as confirmed by the simulated patterns in Figure 4.2(c) and (d). Moreover, the pattern of MIL-101(Cr)/ED showed a decrease in the peak intensity which is due to the partial filling by the ED molecules. Similar results were also observed by Zhang and co-workers [49]. The amount of MIL-101(Cr) crystallinity in the functionalised material was estimated from its lattice period parameter (a=b=c) of 71.1 Å by applying Vegard's law [52] and found to be 80.1%. Furthermore, the calculated d-spacing $(2d\sin\theta = n\lambda)$ for 333 hkl value was 15.8 and 13.7 Å for MIL-101(Cr) and MIL-101(Cr)/ED (Table 4.1), respectively. The reduction in d-spacing in the functionalised material was due to the broadening and amorphous characteristic of ED [53]. In addition, the crystalline sizes (D) of the materials were determined from the XRD pattern using the Debye-Scherrer equation (Equation 4.11) [50].

$$D = \frac{K\lambda}{\beta\cos\theta} \qquad (4.11)$$

K stands for the Scherrer constant, β is the full width at half maximum (FWHM), λ represents the wavelength of the Cu source and θ is the diffraction angle.

The determined crystallite size was observed to be 756.72 nm for MIL-101(Cr) which was similar to the simulated one whereas the reduction in the crystallite size to 7.81 nm was obtained in the functionalised material. The reduction in the crystallite size was observed by the broadening of the XRD pattern as a result of the lattice strain in the materials. The lattice strain (ε) and dislocation density (ρ) of the MIL-101(Cr) and MIL-101(Cr)/ED were estimated using Equations 4.12 and 4.13 [50], [51], respectively.

$$\varepsilon = \frac{\beta cos\theta}{4} \quad (4.12)$$

$$\rho = \frac{1}{D^2} \quad (4.13)$$

The lattice strain in MIL-101(Cr) was obtained as 4.35 x 10^{-5} which was similar to the simulated one. In the case of MIL-101(Cr)/ED, the strain was increased to 443.81 x 10^{-5} because of the introduction of ED. On the other hand, the dislocation density value (ρ) shows the number of dislocation lines per unit area of crystal defects possessed by a crystal as the size of crystal defects and the degree of the crystalline profile is in relation to the dislocations density value [54]. The ρ values were calculated to be 1.58 x 10^{12} lines/m^2 for MIL-101(Cr) and its corresponding simulated material, whereas MIL-101(Cr)/ED possessed a dislocation density of 1.64 x 10^{16} lines/m^2. The large ρ value of MIL-101(Cr)/ED indicates that the functionalised material has a lower degree of crystallinity as compared to MIL-101(Cr) due to the amorphous nature of ED

Table 4.1: XRD parameters and FTIR vibrations of the as-synthesised materials.

	Characteristics		**Materials**		
			Simulated	**MIL-101(Cr)**	**MIL-101(Cr)/ED**
XRD:	Lattice parameter	a=b=c(Å)	88.9	86.1	71.1
	Crystallinity (%)		100	96.1	80.1
	2Ɵ		9.06	9.25	9.11

	FHWM ($x10^{-3}$ radians)		0.18	0.18	17.81
	D (nm)	Cu	796.56	796.72	7.81
	ε $x10^{-5}$		4.35	4.35	443.81
	ρ $x10^{12}$ (lines/m^2)		1.58	1.58	1.64 x 10^4
FTIR:	Vibrations (cm^{-1})	C-O	-	1404	1378
		C=O		1625	1586
		C=C	-	1508	1508
		C-H	-	A	a
		Cr-O	-	674	674
		-NH	-	-	b
		C-N	-	-	1039

a=750, 884, 1018 and 1160 cm-1

b=2800-3300 cm-1

Figure 4.3(a-c) shows the nitrogen adsorption/desorption isotherms used for determining the BET surface area of the MIL-101(Cr) and MIL-101(Cr)/ED samples. From the results, it was seen that MIL-101(Cr) exhibited characteristics of type I isotherms. These type I isotherms are also known as the Langmuir type. They have a steep slope at the beginning of the nitrogen adsorption process. This slope decreases with an increment in relative pressure. The presence of hysteresis in the given isotherms shows the existence of a mesopore in the MOF materials. This can be used to give vital information related to the geometry of the pores. The observed hysteresis in MIL-101(Cr) is of type A, which indicates the existence of cylindrical pores. In comparison to the MIL-101(Cr) sample, the BET surface area of the prepared MIL-101(Cr)/ED showed a decreased value of 3.4766 m^2/g from the initial value of 308.7265 m^2/g. Furthermore, the pore volume and the average pore size were obtained as 0.026266 cm^3/g and 293.204 Å, respectively. The functionalisation of MIL-101(Cr) with ED molecules affected the adsorption of N_2, as the introduced amine moieties partially occupied the spaces within the pores [55]. Figure 4.3(d) shows the thermogravimetric analysis of TGA curves of the synthesised MIL-101(Cr) and MIL-101(Cr)/ED samples. It was observed in the TGA profile that the first

step, in the range of 25–100 °C, is related to the removal of the guest water and solvent molecules [44]. From the thermograms, it was seen that MIL-101(Cr)/ED displayed improved thermal stability. Approximately, 39.6 and 13.2% weight losses are observed for the MIL-101(Cr) and MIL-101(Cr)/ED, respectively. This was supported by the corresponding DTA curves for MIL-101(Cr) and MIL-101(Cr)/ED (Figure 4.4(a-c)) that showed three degradation steps at 90 ^{o}C which attributes to the weight loss due to solvents. The step from 100 to 390 ^{o}C is attributed to the decomposition of unreacted terephthalic acid and ED [56].

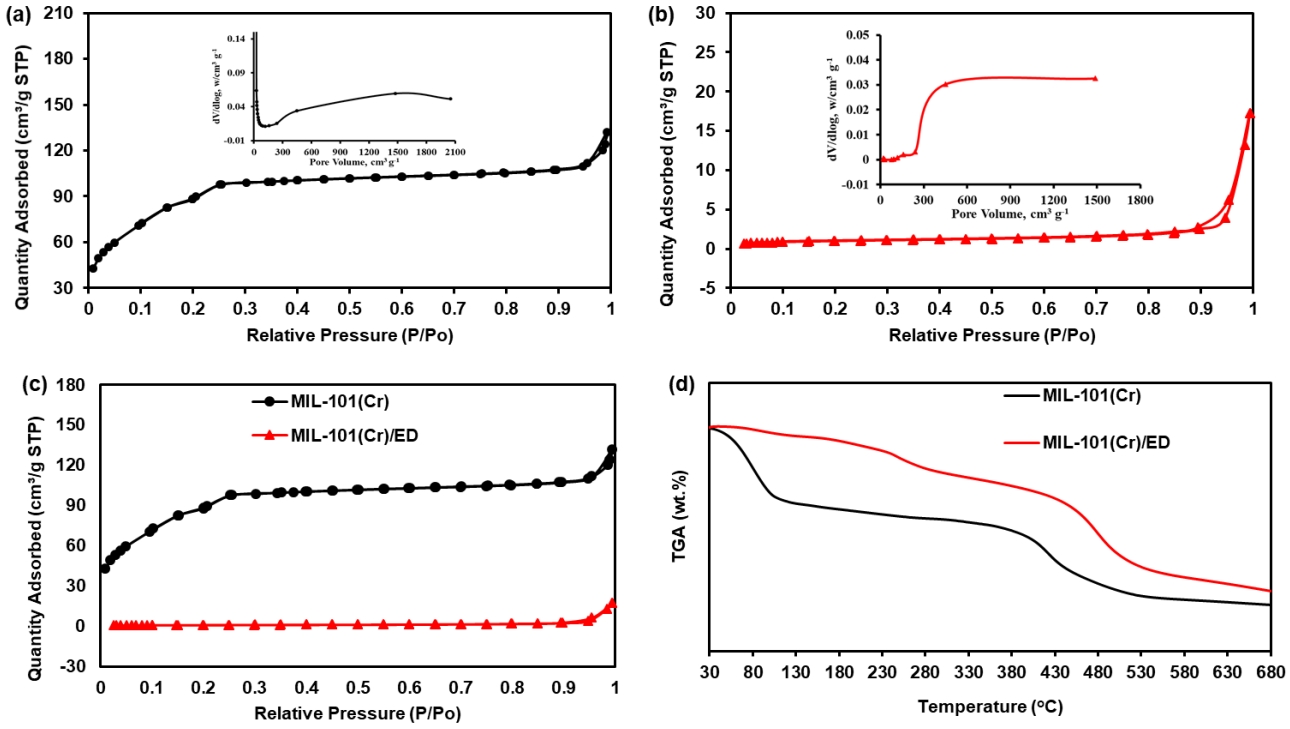

Figure 4.3: BET measurement of (a) MIL-101(Cr) and (b) MIL-101(Cr)/ED (inset: Pore diameter measurement). (c) Comparison BET isotherms and (d) TGA curves of MIL-101(Cr) and MIL-101(Cr)/ED.

The last degradation at 410 ^{o}C is owed to the decomposition of the coordinated organic linker. The MIL-101(Cr)/ED sample demonstrates better thermal stability in comparison

to the pristine MIL-101(Cr) as the framework starts to decompose at a temperature above 480 ^{o}C (Figure 4.4(b and c)). This was supported by the DSC curves of MIL-101(Cr) and MIL-101(Cr)/ED in Figure 4.4(d), showing an intense and small exothermic peak at <100 °C for crystallisation transition. The endothermic peak was observed at 380 °C for MIL-101(Cr) and in the case of MIL-101(Cr)/ED, it was obtained at 280 °C.

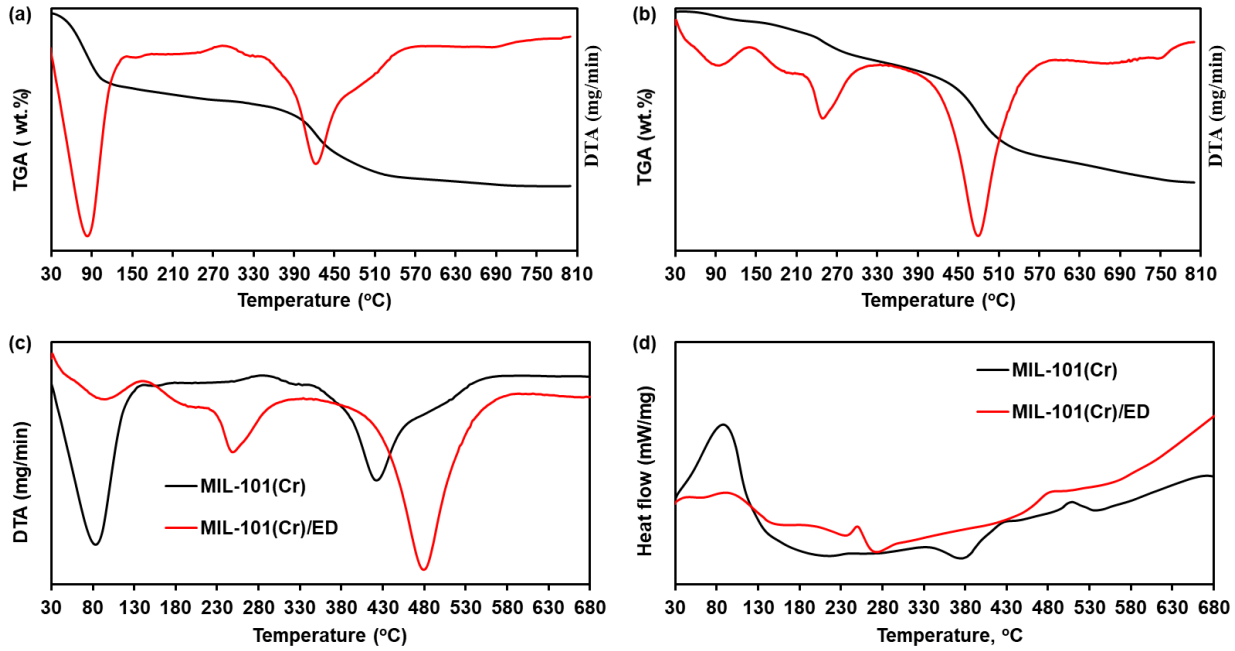

Figure 4.4: TGA/DTA curves of (a) MIL-101(Cr), and (b) MIL-101(Cr)/ED. (c) DTA and (d) DSC of MIL-101(Cr) and MIL-101(Cr)/ED.

The morphological images of MIL-101(Cr) presented in Figure 4.5(a and b) shows highly agglomerated octahedral structures with smooth surface and have an average particle size between 100-200 nm. Moreover, the corresponding EDS analysis (Figure 4.5(c)) revealed that the sample elemental composition consists of C, O, and Cr (the Al element is from the SEM preparation procedure). The composition was further obtained through elemental mapping and confirmed the presence of the desired elements (Figure 4.6). Upon the introduction of ED (Figure 4.5(d)), the octahedral morphologies gradually

disappeared to form irregular-shaped particles and the surface of the MIL-101(Cr)/ED sample tenders to be rougher [34][49]. This effect also resulted in a slight reduction in the particle size as depicted in Figure 4(e). The obtained EDS spectra of prepared MIL-101(Cr)/ED showed a similar elemental composition with the addition of N from ED. The relative contents of N in the MIL-101(Cr)/ED material were determined to be about 4.28 mmol.g^{-1}, which corresponds to an ED/Cr ratio of 3.27 (see Figure 4.5(f)). Furthermore, the elemental mapping in Figure 4.7(c) showed an increased dispersion of the N over the MIL-101(Cr)/ED confirming the presence of ED.

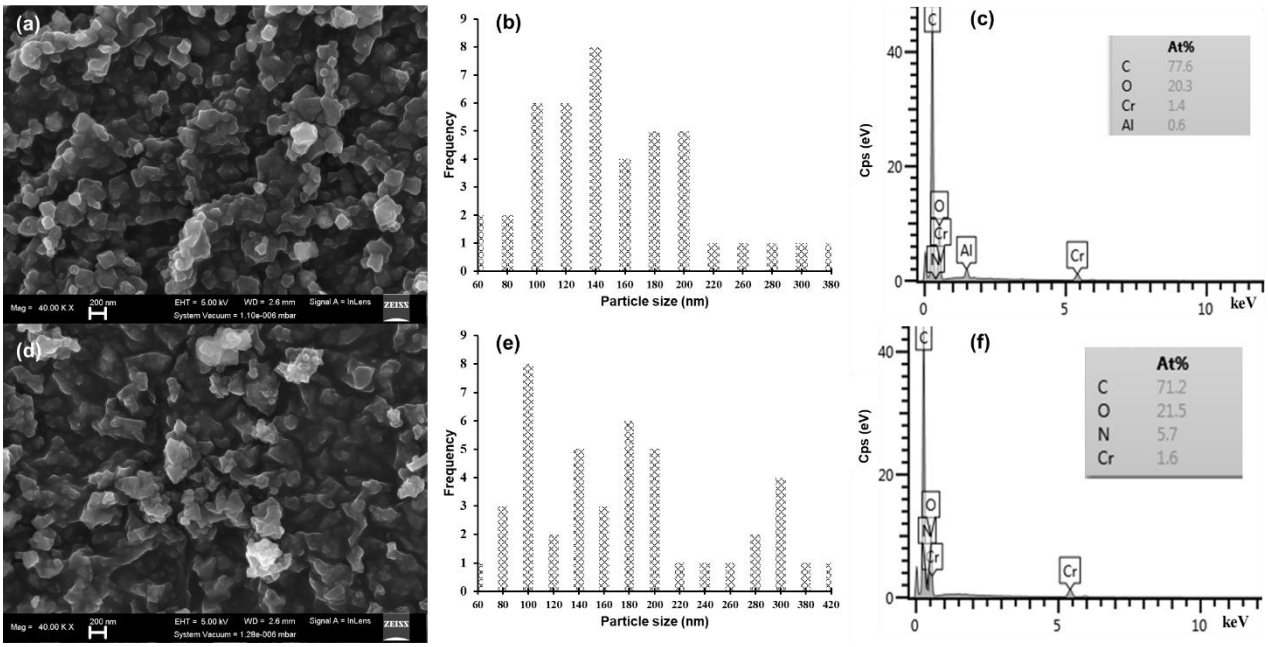

Figure 4.5: SEM image of (a) MIL-101(Cr), and (d) MIL-101(Cr)/ED. Particles distribution of (b) MIL-101(Cr), and (e) MIL-101(Cr)/ED. EDS spectra of (c) MIL-101(Cr), and (f) MIL-101(Cr)/ED (Inset: elemental analysis in atomic percentage).

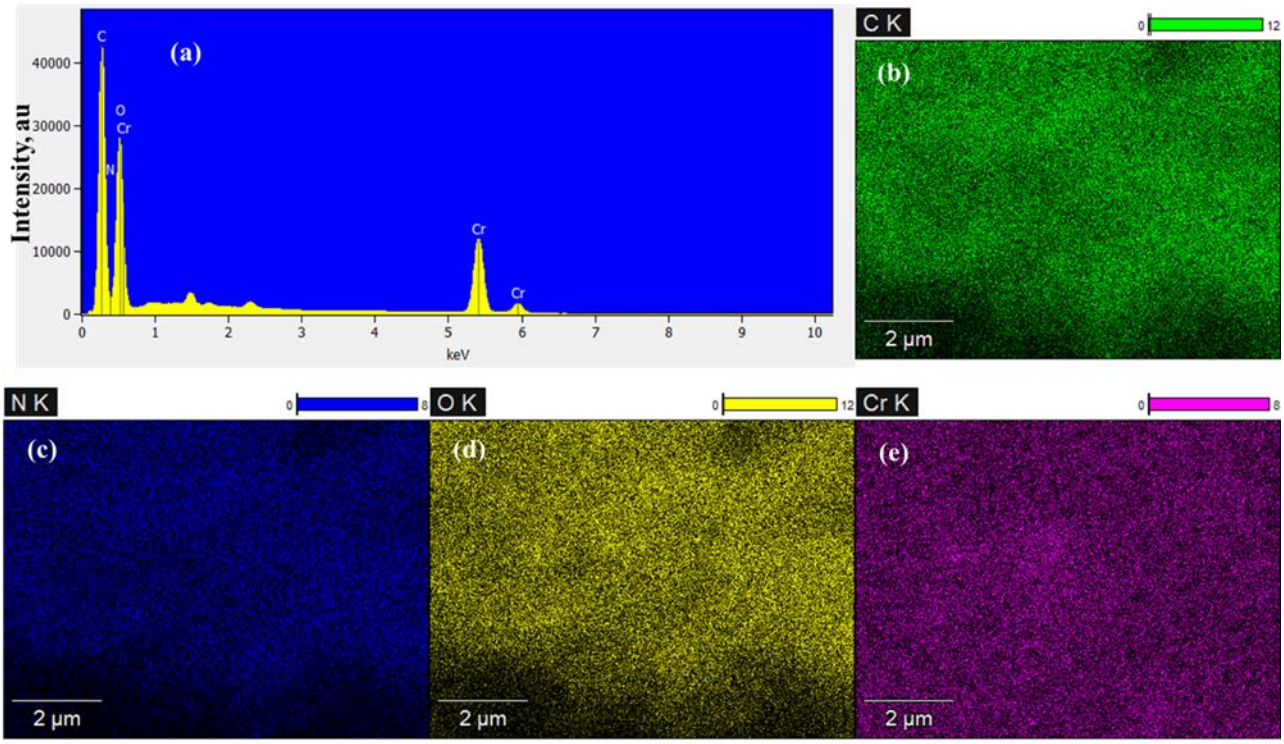

Figure 4.6: Elemental mapping of MIL-101(Cr), (a) EDX spectrum, (b)-(e) mapping image of carbon, nitrogen, oxygen, and chromium elements, respectively.

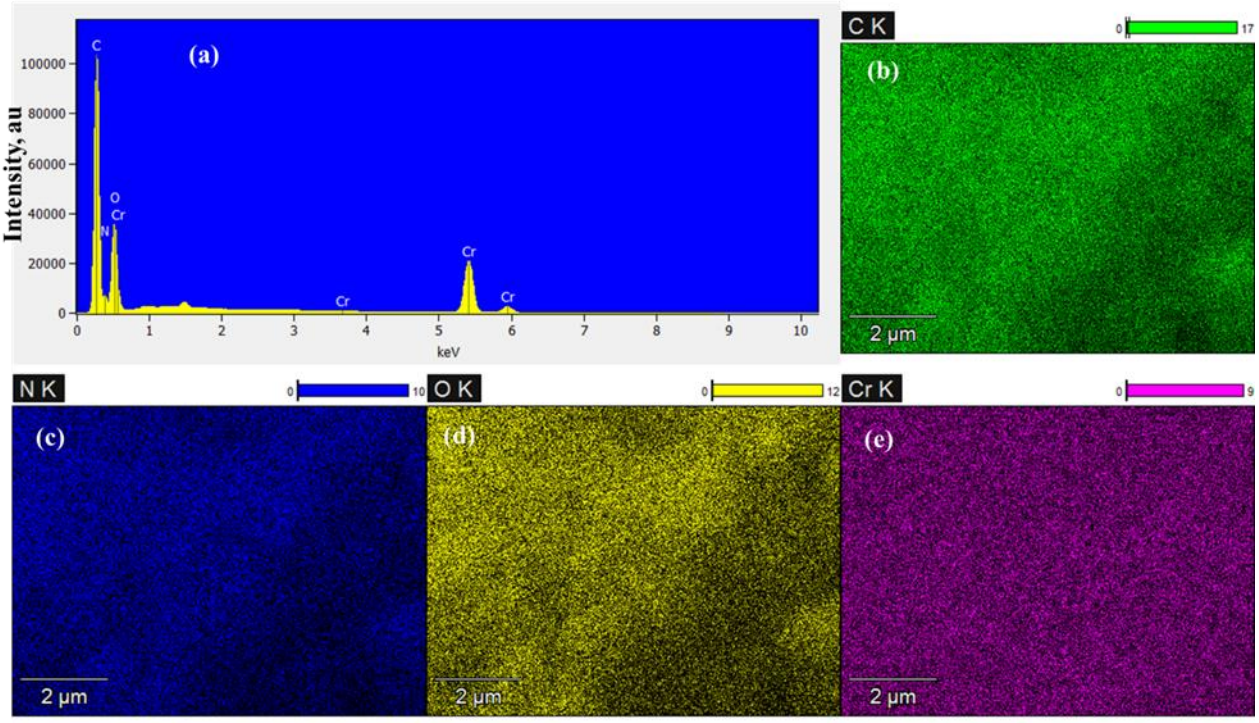

Figure 4.7: Elemental mapping of MIL-101(Cr)/ED, (a) EDX spectrum, (b)-(e) mapping image of carbon, nitrogen, oxygen and chromium elements, respectively.

4.3.2. Adsorption Studies

4.3.2.1. Effect of solution pH and adsorbent dosage

The initial solution pH plays a vital role in the adsorption of Pd(II) ions because it directly contributes to the degree of protonation on polar functional groups found on the surface of the adsorbent and thereby affecting the surface charge of the adsorbent [57]. The adsorptive removal of Pd(II) ions by MIL-101(Cr)/ED was investigated in the pH range 1.0 - 6.0 represented in Figure 4.8(a). The results show that the removal percentage of Pd(II) ions by MIL-101(Cr)/ED was in.0creased with an increase in pH from 1.0 to 3.0. At pH values from 4.0 to 6.0, an increased removal percentage (%R) was also observed with a slight decrease as the pH was moved to higher values. However, due to the hydrolysis of Pd(II) ions, there is a partial formation of the $Pd(OH)_2$ precipitates starting from pH = 4.0 [58]. Moreover, at lower pH ≤1.5, the prevailing species are $[PdCl]^+$ and $PdCl_2$ which are electrostatically repelled by the highly protonated amino groups [59][60]. The increasing %R for pH values between 2.0 -3.5 is attributed to the predominating anion complexes of $[PdCl_3]^-$and $[PdCl_4]^{2-}$ which are able to interact with the positively charged surface of the MIL-101(Cr)/ED [61][62]. Hence, the greatest removal was obtained at the optimum pH of 3.0 as seen in Figure 4.8(a). This was further supported by point of zero charge (PZC) which was obtained to be at 4.0 pH as shown in Figure 4.8(b). In addition, this behaviour was supported by FTIR analysis of MIL-101(Cr)/ED before and after Pd metal ion uptake as shown in Figure 4.8(c). It was seen that the interaction of MIL-101(Cr)/ED with Pd(II) has caused the reduction of peak intensities at 2800-3300, and 1039 cm^{-1} for amino, and amide bands, respectively. The absorption band at 1378 cm^{-1} for C-O vibration shifted to 1394 cm^{-1} upon Pd(II) adsorption. From these observations, the change in absorption intensity, and the shift in wavenumber of functional groups were due to interaction of Pd(II) ion with active sites in MIL-101(Cr)/ED. The Pd(II) ions bound to the active sites of MIL-101(Cr)/ED through either electrostatic attraction or complexation mechanism as seen in pH studies. The electrostatic interaction was between Pd(II) ion and carbonate

group, whereas, the complexation mechanism involved electron pair sharing between electron donor atoms (O and N) [63]. Results from this work indicate that carbonate, carbonyl, amino and amide groups were the main adsorption sites in MIL-101(Cr)/ED.

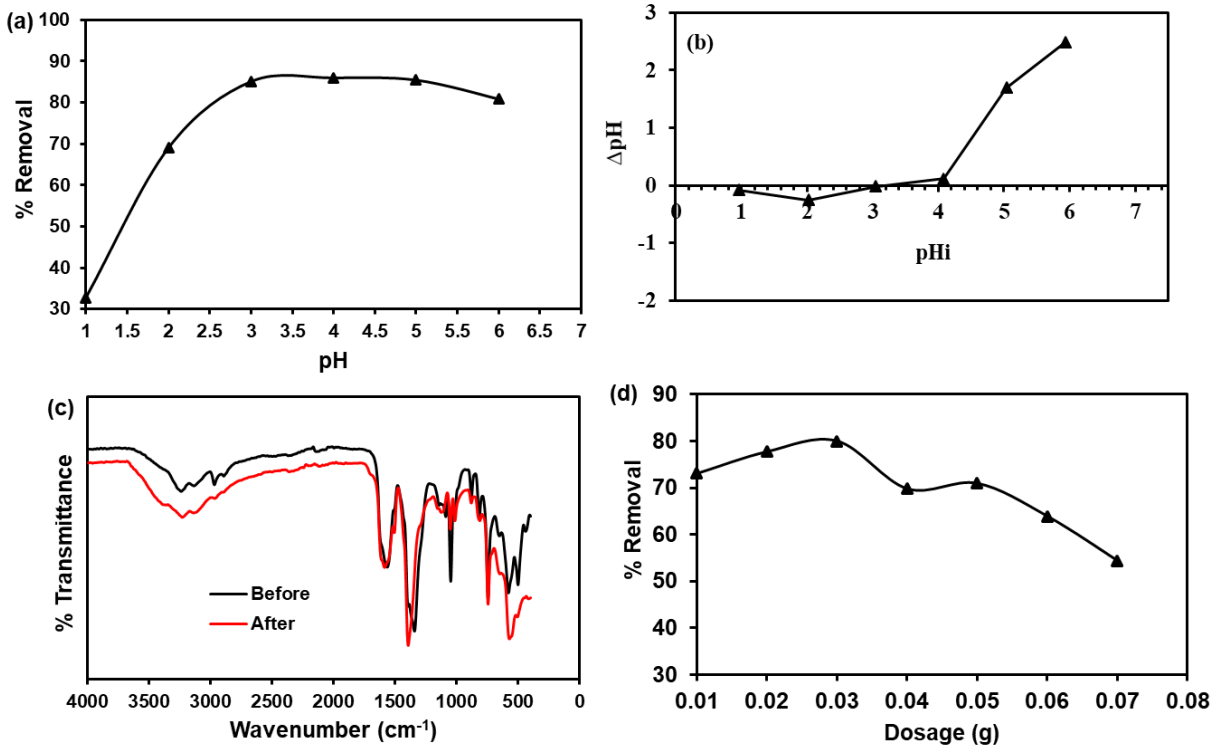

Figure 4.8: (a) Removal percentage of Pd(II) ions by MIL-101(Cr)-ED as a function of pH 1-6. (b) Point of zero charge value for MIL-101(Cr)-ED. (c) FTIR spectra of MIL-101(Cr)-ED before and after Pd (II) removal. (d) Effect of dosage ranging from 0.01-0.07 g.

The effect of the adsorbent dose for MIL-101(Cr)/ED was investigated (0.01 g - 0.07 g) to determine the optimum amount for the adsorption of Pd(II) ions. The obtained results as represented in Figure 4.8(d), show that there is an increase in the uptake of Pd (II) ions with MIL-101(Cr)/ED from 0.01-0.03 g of dosage used. This indicates that functionalisation with ethylenediamine indeed improved the removal efficiency of MIL-101(Cr). The percentage (%) removal increased from 73% to 80% for MIL-101(Cr)/ED at Pd (II) solution conditions of 100 mg/L, pH 3.0 and 0.01-0.03 g MIL-101(Cr)/ED amount

for 24 hours. The optimum dosage was observed to be 0.03 g and used throughout the study.

6.3.2.2. Adsorption isotherms

In order to investigate the effect of initial concentration and temperature, adsorption experiments were conducted at three different temperatures which are 25, 35, and 45 ^{o}C while varying the initial concentration between 50-400 mg/L. The results obtained show that there is an increase in the adsorption of Pd(II) ions by the MIL-101(Cr)/ED with an increase in the concentration and temperature as depicted in Figure 4.9(a) [37][64]. The experimental data were fit to the Langmuir and Freundlich (nonlinear and linear) models in order to deduce the adsorbent-adsorbate interactions and maximum adsorption capacity (qm) as given in Figure 4.9(a-c). From Figures 4.9(a and b), the obtained data fitted more on the Langmuir model than the Freundlich model (Figure 4.9(a and c)), implying monolayer adsorption mechanisms. Moreover, the isothermal parameters were calculated and presented in Table 4.2, wherein the correlation coefficients R^2 values determined from the non-linear and the linear Langmuir models are 0.7727 and 0.9089 for 25 ^{o}C, whereas the ones obtained from the Freundlich model are 0.6271 and 0.6172, for non-linear and linear fittings, respectively. The Langmuir model was further supported by the separation factor (R_L) which is used to determine whether the adsorption process is favourable or unfavourable and was calculated according to the literature [65]. As presented in Table 4.2, the calculated R_L values are in the range of $0<R_L<1$ demonstrating a favourable Langmuir adsorption process [66] between Pd(II) ions and MIL-101(Cr)/ED. The post-functionalisation of MIL-101(Cr) with ED increased the q_m from the value of 454.6 mg/g at 25 ^{o}C to the value of 570.6 mg/g at 45 ^{o}C. The obtained results showed the potential preference of MIL-101(Cr)/ED with higher qm for removal and recovery of Pd(II) ion from wastewater in comparison to those reported in the literature (see Table 4.3). Furthermore, the thermodynamic properties of the synthesised MIL-101(Cr)/ED were determined according to Maponya *et al*. [64]. The ΔG^0 change values obtained at 25, 35 and 45 ^{o}C were found to be -4.69, -5.33, and -5.30 kJ/mol, respectively. The negative values of ΔG^0 suggest that Pd(II) ion adsorption occurs spontaneously at all

of the temperatures under investigation. The van Hoff plot (Figure 4.9(d)) was used to estimate the ΔH^0 value from the slope and ΔS^0 change value from the intercept. The ΔH^0 and ΔS^0 change values were found to be 4.55 kJ/mol and 0.36 kJ/K/mol, respectively. The positive value of ΔH^0 showed that adsorption of Pd(II) onto MIL-101(Cr)/ED was endothermic [64], whereas the positive value of ΔS^0 shows that there is a high affinity between Pd(II) and MIL-101(Cr)/ED [67].

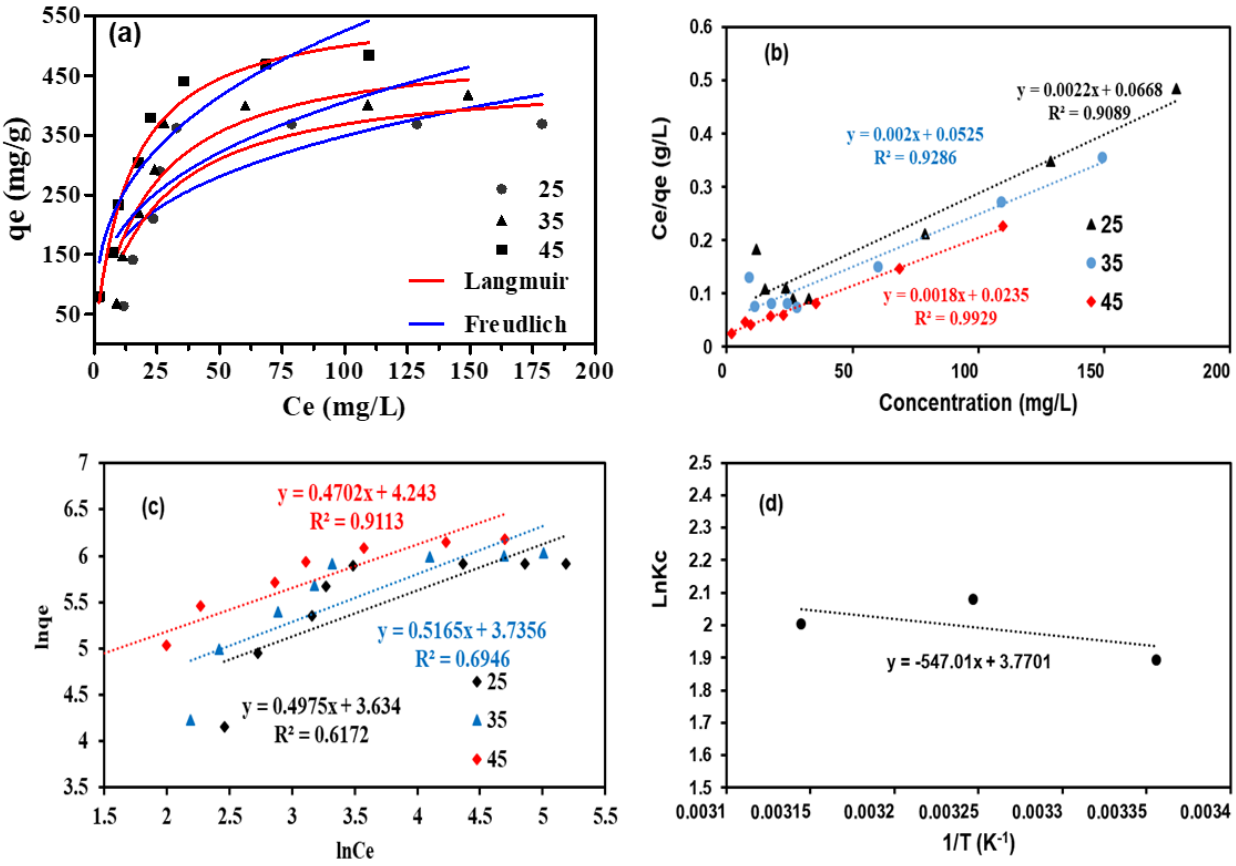

Figure 4.9: Adsorption isotherms of Pd(II) uptakes byMIL-101(Cr)/ED (a) Nonlinear fit of the Langmuir and Freundlich models for Pd(II), (b) Langmuir linear isotherm curve, (c) Freundlich linear curve and (d) Van't Hoff plot.

Table 4.2: Langmuir and Freundlich isotherm parameters for Pd(II) adsorption by MIL-101(Cr)/ED

Isotherm model	**Temperature**		
	25 °C	**35 °C**	**45 °C**
Langmuir			
Linear			
q_m	454.6	500.0	555.6
K_L	0.0329	0.0381	0.0766
R_L	0.108	0.0950	0.0496
R^2	0.9089	0.9286	0.9929
Non-linear			
Best-fit values			
q_m	454.2	506.5	570.2
K_L	0.0431	0.0470	0.0710
Std. Error			
q_m	65.44	58.95	30.36
K_L	0.0189	0.0162	0.0117
95 % Confidence			
q_m	294.1 to 614.3	362.3 to 650.8	495.9 to 644.5
K_L	-0.003 to 0.089	0.007 to 0.087	0.0423 to 0.0996
Goodness of Fit			
Degrees of	6	6	6
R^2	0.7727	0.8610	0.9731
Absolute Sum of	22910	16888	4296
Sy.x	61.79	53.05	26.76
Number of points			
Analysed	8	8	8
Freundlich			
Linear			
K_F	37.864	41.913	69.616
n	2.010	1.936	2.127
R^2	0.6172	0.6946	0.9113
Non-linear			
Best-fit values			
K_F	82.69	85.95	109.6
n	3.199	2.968	2.939
Std. Error			
K_F	38.62	33.92	26.11
n	1.101	0.828	0.5326
95 % Confidence			
K_F	-11.80 to 177.2	2.956 to 168.9	45.70 to 173.5
n	0.505 to 5.892	0.942 to 4.994	1.636 to 4.242
Goodness of Fit			
Degrees of	6	6	6
R^2	0.6271	0.7235	0.876
Absolute Sum of	37584	33602	19861
Sy.x	79.15	74.84	57.53
Number of points			
Analysed	8	8	8

Units: *qm*: mg/g, K_L: L/mg, K_F: mg/g.

Table 4.3: Comparison of MIL-101(Cr)/ED adsorption capacity with other adsorbents used for Pd(II) ion uptake.

Adsorbent	qm (mg/g)	Ph	dosage (mg	Volume (mL)	References
MOF-808	163.9	1	10	20	[68]
MOF-802	25.8	1	10	20	[68]
UiO-66	105.1	1	10	20	[68]
pyromellitic acid modified-UiO-66-NH_2	226.1	2	10	15	[69]
Et-N-Cu(BDC-NH_2)	172.9	7	10	20	[70]
MOR-2-QAS	123.2	7.5	10	20	[71]
UiO-66-L1/L2	147.3	4	10	20	[72]
AHPP-MOF	242.5	4	10	10	[73]
UiO-66-Pyta	294.1	4.5	10	25	[74]
UiO-66-NH_2	197.0	4.5	10	25	[74]
ED-magnetic chitosan nanoparticles	138	2	20	100	[75]
MOF-AFH	191.27	5	10	10	[76]
Amine-Zeolites	0.99	2	10	10	[77]
MIL-101(Cr)-NO_2	119.5	1	10	20	[37]
MIL-101(Cr)-NH_2	277.6	1	10	20	[37]
MIL-101(Cr)/ED	454.6	3	30	50	This work

4.3.2.3. Kinetics experiments

The effect of contact time on the adsorption of Pd(II) ions by MIL-101(Cr)/ED was investigated at initial concentrations of 100 mg/L, pH=3.0, 0.03 g, and a time ranging from 0-120 minutes. As shown in Figure 4.10(a), an increase in the adsorptive removal of Pd(II)

ions by MIL-101(Cr)/ED with increasing time was observed. The equilibrium adsorption capacity value of 126 mg/g was reached within a short period of fewer than 10 minutes. This behaviour is attributed to the large affinity for $[PdCl_4]^{2-}$ ions by the highly protonated amino groups on the surface of the MIL-101(Cr)/ED composite [78]. The obtained data was fit to the linearised and non-linearised forms of the pseudo first-order (PFO) and second-order (PSO) kinetic models in order to determine the rate of the adsorption. The nonlinear (PFO and PSO kinetic models) fit observed in Figure 4.10(a) showed that the data fits both models, however, the PSO model showed to have a higher adsorption capacity than that of the PFO model (Table 4.4). To further validate the observations, the obtained data was fit to the linear forms of the kinetic models as shown in Figures 4.10(b) and (c). The results depict that the data fitted very well for the PSO (Figure 4.10(b) than PFO (Figure 4.10(c)), as supported by the obtained R^2 value of 0.9997 at 100 mg/L concentration and 25 ^oC. In addition, the q_e values predicted by the model are in good agreement with the ones obtained experimentally as well as with nonlinear ones [79].

Table 4.4: Kinetics parameters of Pd(II) ion adsorption by MIL-101(Cr)/ED.

Kinetic Models			
Pseudo-first-		**Pseudo-second-**	
Linear		*Linear*	
q_e *(exp)*	126.002	q_e	133.333
k_1	0.00006	k_2	0.0590
R^2	0.9995	R^2	0.9997
Non-linear		*Non-linear*	
Best-fit values		Best-fit values	
q_e	131.5	q_e	134.3
k_1	0.9875	k_2	0.02065
Std. Error		Std. Error	
q_e	9.976	q_e	12.25
k_1	0.8007	k_2	0.03717
95 % Confidence		95 % Confidence	
q_e	108.5 to 154.5	q_e	106.1 to 162.6
k_1	-0.8589 to	k_2	-0.06505 to 0.1064
Goodness of Fit		Goodness of Fit	
Degrees of	8	Degrees of Freedom	8
Absolute Sum of	6179	Absolute Sum of	6133
Sy.x	27.79	Sy.x	27,69
Number of points		Number of points	
Analysed	10	Analysed	10

Units: q_e: mg/g, k_1: 1/min, k_2: g/mgmin

The adsorption kinetics data were further used to investigate the rate-limiting step of Pd(II) adsorption by the MIL-101(Cr)/ED, by fitting the data to the Weber and Morris intra-particle model [69]. The plot obtained for the intra-particle diffusion model for the Pd(II) adsorption is presented in Figure 4.10(d). It shows that the curve has two different linear regions. The Weber and Morris model predict that the intra-particle diffusion becomes the rate-limiting step once a plot of q_t as a function of $t^{0.5}$ is linear and passes through the origin [80]. From the plot, it can be deduced that the intra-particle diffusion process was not a rate-limiting step, since the plot did not pass through the origin. From the curve, the slope represents the k_i value, it was seen that the rate-limiting step is the second region which is known to be the equilibrium stage [69][80], as it has a smaller slope as compared to the first region.

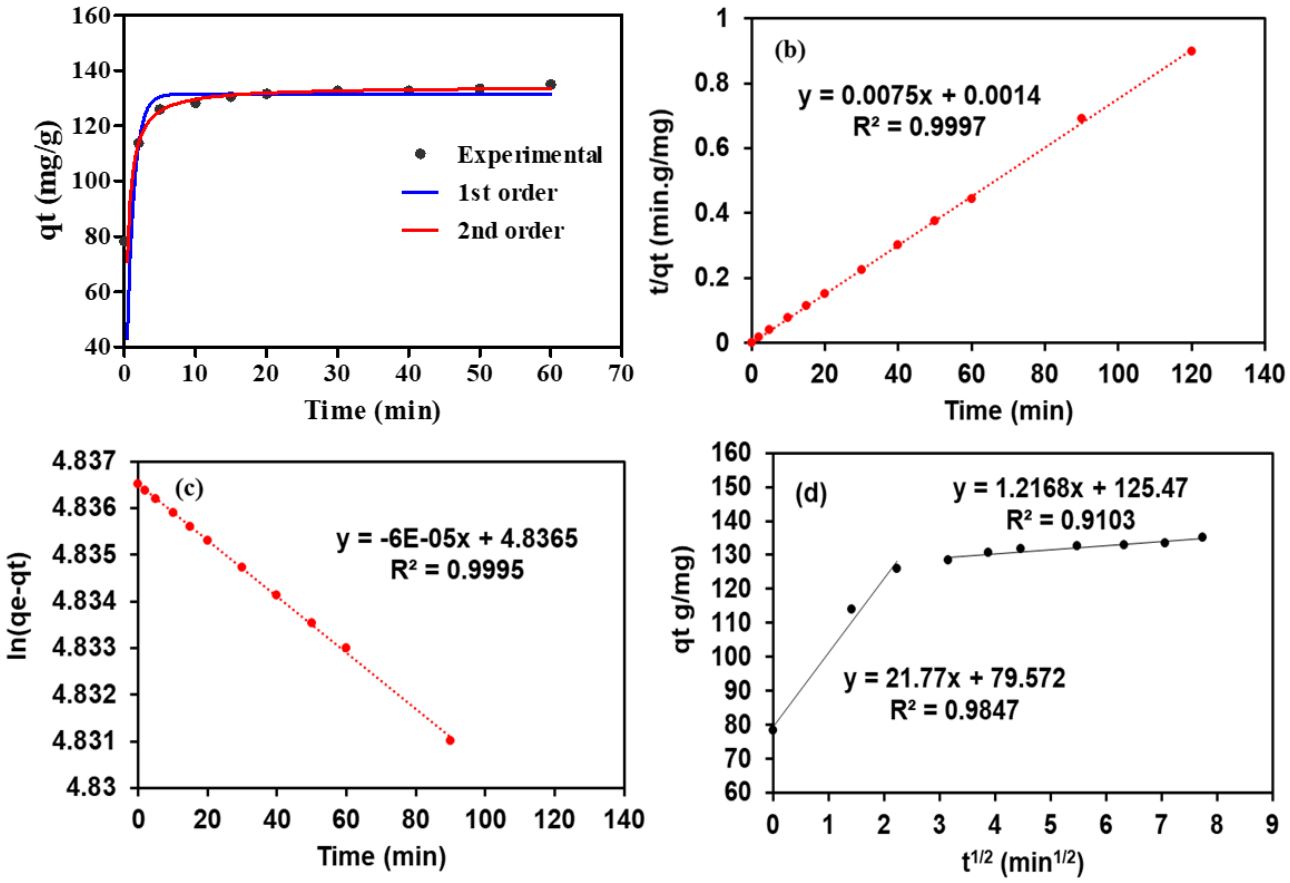

Figure 4.10: (a) Nonlinear fit and experimental; (b) linear fit pseudo-second-order and first order; and (d) intra-particle diffusion model of Pd(II) uptakes by MIL-101(Cr)/ED.

For studying the influence of diverse ions on the adsorptive removal of Pd(II) ions by MIL-101(Cr)/ED composite, various cations (Pt(IV), Ni(II), Co(II), Ag(I), Ru(III)) and anions (SO_4^{2-}, CO_3^{2-}, Cl^-, NO_3^-, PO_4^{2-}) were selected. The initial concentration of the competing ions (10 mg/L) was mixed with Pd (II) solution followed by adjusting the pH to 3.0 before contacting with 0.03 g of MIL-101(Cr)/ED for 24 hours. The obtained results as presented in Figure 4.11, revealed that there was no significant effect on the adsorption of Pd (II) by MIL-101(Cr)/ED as the removal percentage obtained was still above 85% for all the competing ions. This behaviour is due to the electrostatic repulsion of cationic species by the protonated amino groups in acid media between the pH 2.0-3.0 of HCl solution [15][60][81].

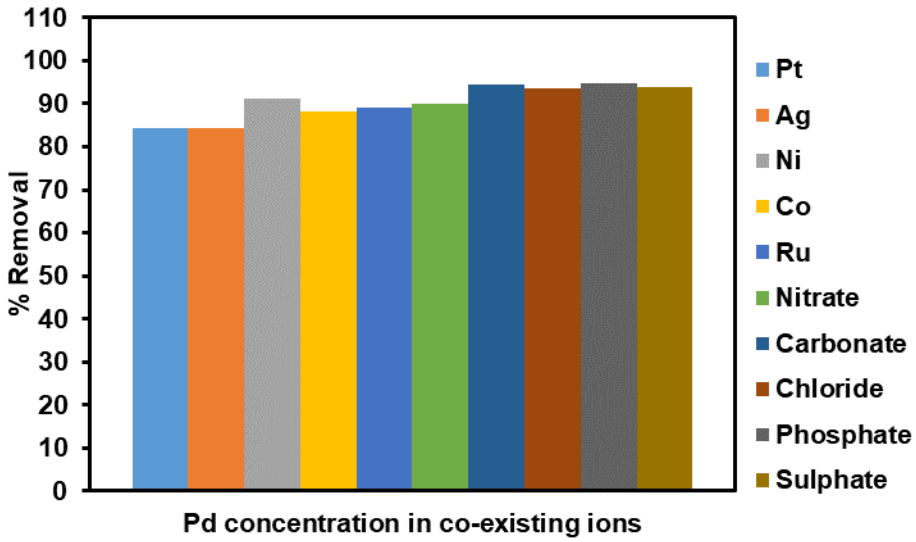

Figure 4.11: Effect of coexisting ions on Pd(II) adsorption by the MIL-101(Cr)/ED**.**

4.4. CONCLUSION

PET waste plastic was successfully recycled into the organic linker which was used for the synthesis of MIL-101. The MIL-101 was grafted with ED in order to study its adsorption towards Pd(II) ions removal from simulated wastewater through batch adsorption studies. The prepared MIL-101(Cr)/ED showed a very high qm of 454.54 mg/g Pd(II) ions when conducting the experiments with initial concentrations ranging between 50-400 mg/L. Furthermore, the most outstanding behaviour of the MIL-101(Cr)/ED is the rapid kinetics which reached equilibrium within 10 minutes of interaction with Pd(II) ions in an acidic solution. Both the adsorption capacity and the reaction rate are very high in comparison to those reported in the literature. Based on the obtained results, it can be concluded that the successful preparation of MIL-101(Cr)/ED from PET waste bottle with an increased number of amine functional groups as a very low cost and super-adsorbent material for heavy metal ions removal was effectively achieved.

4.5. REFERENCES

[1] L. Xu, A. Zhang, N. Pu, C. Xu, and J. Chen, “Development of Two novel silica based symmetric triazine-ring opening N-donor ligands functional adsorbents for highly efficient separation of palladium from HNO_3 solution,” J. Hazard. Mater., vol. 376, pp. 188–199, 2019, doi: 10.1016/j.jhazmat.2019.05.028.

[2] M. D. Makhafola, K. D. Modibane, K. E. Ramohlola, Thabiso. C. Maponya, M. J. Hato, K. Makgopa, and E. I. Iwuoha., “Palladinised graphene oxide-MOF induced coupling of Volmer and Heyrovsky mechanisms, for the amplification of the electrocatalytic efficiency of hydrogen evolution reaction,” *Sci. Rep.*, vol. 11, pp. 1–16, 2021, doi: 10.1038/s41598-021-96536-9.

[3] L. Li, Z. Cai, Q. Wu, W. Lo, N. Zhang, L. X. Chen, and L. Yu “Rational Design of Porous Conjugated Polymers and Roles of Residual Palladium for Photocatalytic Hydrogen Production,” *J. Am. Chem. Soc.*, vol. 138, pp. 7681–7686, 2016, doi: 10.1021/jacs.6b03472.

[4] C. H. Chen, T. Y. Chung, C. C. Shen, M. S. Yu, C. S. Tsao, G. N. Shi, C. C. Huang , M. D. Ger, W. L. Lee, “Hydrogen storage performance in palladium-doped graphene/carbon composites,” *Int. J. Hydrogen Energy*, vol. 38, pp. 3681–3688, 2013, doi: 10.1016/j.ijhydene.2013.01.070.

[5] S. Bhaskaran, M. S. A. Padusha, and A. M. Sajith, “Application of Palladium Based Precatalytic Systems in the Suzuki-Miyaura Cross-Coupling Reactions of Chloro-Heterocycles,” *ChemistrySelect*, vol. 5, pp. 9005–9016, 2020, doi: 10.1002/slct.202002357.

[6] L. Pang, R. Lia, J. Hua, L. Zhanga, M. Zhanga, C. Yanga, G. Wu, “Functionalised polyethylene fibers for the selective capture of palladium ions from aqueous solution,” *Appl. Surf. Sci.*, vol. 433, pp. 116–124, 2018, doi: 10.1016/j.apsusc.2017.10.041.

[7] Q. Xie, G. Liang, T. Lin, F. Chen, D. Wang, and B. Yang, “Selective chelating precipitation of palladium metal from electroplating wastewater using chitosan and its derivative,” *Adsorpt. Sci. Technol.*, vol. 38, pp. 113–126, 2020, doi:

10.1177/0263617420918729.

[8] G. Gwak, D. I. Kim, and S. Hong, “New industrial application of forward osmosis (FO): Precious metal recovery from printed circuit board (PCB) plant wastewater,” *J. Memb. Sci.*, vol. 552, pp. 234–242, 2018, doi: 10.1016/j.memsci.2018.02.022.

[9] J. E. Terrazas-Rodríguez, S. Gutiérrez-Granados, M. A. Alatorre-Ordaz, C. Ponce De León, and F. C. Walsh, “A comparison of the electrochemical recovery of palladium using a parallel flat plate flow-by reactor and a rotating cylinder electrode reactor,” *Electrochim. Acta*, vol. 56, pp. 9357–9363, 2011, doi: 10.1016/j.electacta.2011.08.021.

[10] D. I. Kim, G. Gwak, P. Dorji, D. He, S. Phuntsho, S. Hong, and H. Shon, “Palladium Recovery through Membrane Capacitive Deionisation from Metal Plating Wastewater,” *ACS Sustain. Chem. Eng.*, vol. 6, pp. 1692–1701, 2018, doi: 10.1021/acssuschemeng.7b02923.

[11] M. R. Awual, “Solid phase sensitive palladium(II) ions detection and recovery using ligand based efficient conjugate nanomaterials,” *Chem. Eng. J.*, vol. 300, pp. 264–272, 2016, doi: 10.1016/j.cej.2016.04.071.

[12] W. Lai. K. Zhang, P. Shao, L. Yang, L. Ding, S. G. Pavlostathis, H. Shi, L. Zou, D. Liang, X. Luo, “Optimization of adsorption configuration by DFT calculation for design of adsorbent: A case study of palladium ion-imprinted polymers,” *J. Hazard. Mater.*, vol. 379, p. 120791, 2019, doi: 10.1016/j.jhazmat.2019.120791.

[13] H. Guo, Z. Zheng, Y. Zhang, H. Lin, and Q. Xu, “Highly selective detection of Pb2+ by a nanoscale Ni-based metal–organic framework fabricated through one-pot hydrothermal reaction,” *Sensors Actuators, B Chem.*, vol. 248, pp. 430–436, 2017, doi: 10.1016/j.snb.2017.03.147.

[14] E. Birinci, M. Gülfen, and A. O. Aydin, “Separation and recovery of palladium(II) from base metal ions by melamine-formaldehyde-thiourea (MFT) chelating resin,” *Hydrometallurgy*, vol. 95, pp. 15–21, 2009, doi: 10.1016/j.hydromet.2008.04.002.

[15] F. Liu, S. Wang, and S. Chen, “Adsorption behaviour of Au(III) and Pd(II) on

persimmon tannin functionalised viscose fiber and the mechanism," *Int. J. Biol. Macromol.*, vol. 152, pp. 1242–1251, 2020, doi: 10.1016/j.ijbiomac.2019.10.221.

[16] S. Sharma and N. Rajesh, "Augmenting the adsorption of palladium from spent catalyst using a thiazole ligand tethered on an amine functionalised polymeric resin," *Chem. Eng. J.*, vol. 283, pp. 999–1008, 2016, doi: 10.1016/j.cej.2015.08.061.

[17] M. Sayin, M. Can, M. Imamoɬlu, and M. Arslan, "1,3,5-Triazine-pentaethylenehexamine polymer for the adsorption of palladium (II) from chloride-containing solutions," *React. Funct. Polym.*, vol. 88, pp. 31–38, 2015, doi: 10.1016/j.reactfunctpolym.2015.02.003.

[18] J. Tang, J. Zhao, S. Wang, L. Zhang, M. Zhao, Z. Huang, Y. Hu, "Pre-modification strategy to prepare a novel Zr-based MOF for selective adsorption of Palladium(II) from solution," *Chem. Eng. J.*, vol. 407, p. 127223, 2021, doi: 10.1016/j.cej.2020.127223.

[19] S. Daniel, C. Xiong, Y. He, C. Yang, X. Li, J. Zheng, S. Wang, "Facile preparation of magnetic Zr-MOF for adsorption of Pb(II) and Cr(VI) from water: Adsorption characteristics and mechanisms," *J. Hazard. Mater.*, vol. 18, pp. 1–17, 2020, doi: 10.1016/j.apsusc.2016.02.154.

[20] H. Jalayeri, P. Aprea, D. Caputo, A. Peluso, and F. Pepe, "Synthesis of amino-functionalised MIL-101(Cr) MOF for hexavalent chromium adsorption from aqueous solutions," *Environ. Nanotechnology, Monit. Manag.*, vol. 14, no. February, p. 100300, 2020, doi: 10.1016/j.enmm.2020.100300.

[21] N. Zhuo, Y. Lan, W. Yang, Z. Yang, X. Li, X. Zhou, Y. Liu, J. Shen, X. Zhang, "Adsorption of three selected pharmaceuticals and personal care products (PPCPs) onto MIL-101(Cr)/natural polymer composite beads," *Sep. Purif. Technol.*, vol. 177, pp. 272–280, 2017, doi: 10.1016/j.seppur.2016.12.041.

[22] M. Lu, Y. Deng, Y. Luo, J. Lv, T. Li, J. Xu, S. Chen, and J. Wang, "Graphene Aerogel-Metal-Organic Framework-Based Electrochemical Method for

Simultaneous Detection of Multiple Heavy-Metal Ions," *Anal. Chem.*, vol. 91, pp. 888–895, 2019, doi: 10.1021/acs.analchem.8b03764.

[23] N. A. Khan, Z. Hasan, and S. H. Jhung, "Adsorptive removal of hazardous materials using metal-organic frameworks (MOFs): A review," *J. Hazard. Mater.*, vol. 244–245, pp. 444–456, 2013, doi: 10.1016/j.jhazmat.2012.11.011.

[24] J. Ren, X. Dyosiba, N. M. Musyoka, H. W. Langmi, B. C. North, M. Mathe, and M. S. Onyango, "Green synthesis of chromium-based metal-organic framework (Cr-MOF) from waste polyethylene terephthalate (PET) bottles for hydrogen storage applications," *Int. J. Hydrogen Energy*, vol. 41, pp. 18141–18146, 2016, doi: 10.1016/j.ijhydene.2016.08.040.

[25] D. Senthil Raja, C. C. Pan, C. W. Chen, Y. H. Kang, J. J. Chen, and C. H. Lin, "Synthesis of mixed ligand and pillared paddlewheel MOFs using waste polyethylene terephthalate material as sustainable ligand source," *Microporous Mesoporous Mater.*, vol. 231, pp. 186–191, 2016, doi: 10.1016/j.micromeso.2016.05.035.

[26] X. Dyosiba, J. Ren, N. M. Musyoka, H. W. Langmi, M. Mathe, and M. S. Onyango, "Preparation of value-added metal-organic frameworks (MOFs) using waste PET bottles as source of acid linker," *SUSMAT*, vol. 10, pp. 10–13, 2016, doi: 10.1016/j.susmat.2016.10.001.

[27] K. W. Jung, J. H. Kim, and J. W. Choi, "Synthesis of magnetic porous carbon composite derived from metal-organic framework using recovered terephthalic acid from polyethylene terephthalate (PET) waste bottles as organic ligand and its potential as adsorbent for antibiotic tetracycline hydrochlo," *Compos. Part B Eng.*, vol. 187, p. 107867, 2020, doi: 10.1016/j.compositesb.2020.107867.

[28] A. Jamali, A. A. Tehrani, F. Shemirani, and A. Morsali, "Lanthanide metal – organic frameworks as selective microporous materials for adsorption of heavy," pp. 9193–9200, 2016, doi: 10.1039/c6dt00782a.

[29] L. Esrafili, V. Safarifard, E. Tahmasebi, M. D. Esrafili, and A. Morsali, "metal –

organic frameworks on heavy metal ion," pp. 8864–8873, 2018, doi: 10.1039/c8nj01150h.

[30] A. D. Pournara, A. Margariti, G. D. Tarlas, A. Kourtelaris, V. Petkov, C. Kokkinos, A. Economou, G. S. Papaefstathiou and M. J. Manos, "A Ca^{2+} MOF combining highly efficient sorption and capability for voltammetric determination of heavy metal ions in aqueous media," *J. Mater. Chem. A*, vol. 7, pp. 15432–15443, 2019, doi: 10.1039/c9ta03337h.

[31] M. N. Yazdi, S. Dadfarnia, and A. M. Haji Shabani, "Synthesis of stable S-functionalised metal-organic framework using $MoS_4^{2-}$and its application for selective and efficient removal of toxic heavy metal ions in wastewater treatment," *J. Environ. Chem. Eng.*, vol. 9, p. 104696, 2021, doi: 10.1016/j.jece.2020.104696.

[32] E. Sert, Y. Esra, and F. S. Atalay, "Journal of Solid State Chemistry Preparation and performance of functionalised metal organic framework , MIL-101 , for Knoevenagel reaction," vol. 283, 2020, doi: 10.1016/j.jssc.2019.121138.

[33] H. Yu, J. Xie, Y. Zhong, F. Zhang, and W. Zhu, "One-pot synthesis of nitroalkenes via the Henry reaction over amino-functionalised MIL-101 catalysts," *Catal. Commun.*, vol. 29, pp. 101–104, 2012, doi: 10.1016/j.catcom.2012.09.032.

[34] T. Hu, S. He, S. Shan, H. Su, Y. Zhi, L. He, "Novel functionalised metal-organic framework MIL-101 adsorbent for capturing oxytetracycline," *J. Alloys Compd.*, vol. 727, pp. 114–122, 2017, doi: 10.1016/j.jallcom.2017.08.116.

[35] Y. Zheng, F. Chu, B. Zhang, J. Yan, and Y. Chen, "Ultrahigh adsorption capacities of carbon tetrachloride on MIL-101 and MIL-101/graphene oxide composites," *Microporous Mesoporous Mater.*, vol. 263, pp. 71–76, 2018, doi: 10.1016/j.micromeso.2017.12.007.

[36] X. Luo, T. Shen, L. Ding, W. Zhong, J. Luo, and S. Luo, "Novel thymine-functionalised MIL-101 prepared by post-synthesis and enhanced removal of Hg2+ from water," *J. Hazard. Mater.*, vol. 306, pp. 313–322, 2016, doi: 10.1016/j.jhazmat.2015.12.034.

[37] C. R. Lim, S. Lin, and Y. S. Yun, “Highly efficient and acid-resistant metal-organic frameworks of MIL-101(Cr)-NH_2 for Pd(II) and Pt(IV) recovery from acidic solutions: Adsorption experiments, spectroscopic analyses, and theoretical computations,” *J. Hazard. Mater.*, vol. 387, p. 121689, 2020, doi: 10.1016/j.jhazmat.2019.121689.

[38] F. Ahmadijokani, S. Tajahmadi, A. Bahi, H. Molavi, M. Rezakazemi, F. Ko, T. M. Aminabhavi , M. Arjmand, “Ethylenediamine-functionalised Zr-based MOF for ef fi cient removal of heavy metal ions from water,” *Chemosphere*, vol. 264, p. 128466, 2021, doi: 10.1016/j.chemosphere.2020.128466.

[39] M. Sha, M. Sheikh, A. Rashidi, and A. Samimi, “Synthesis and adsorption performance of a modi fi ed micro-mesoporous MIL- 101(Cr) for VOCs removal at ambient conditions,” vol. 341, pp. 164–174, 2018, doi: 10.1016/j.cej.2018.02.027.

[40] M. Parvinzadeh, S. Moradian, A. Rashidi, and M. E. Yazdanshenas, “Surface characterisation of polyethylene terephthalate/silica nanocomposites,” *Appl. Surf. Sci.*, vol. 256, pp. 2792–2802, 2010, doi: 10.1016/j.apsusc.2009.11.030.

[41] O. Semyonov, S. Chaemchuen, A. Ivanov, F. Verpoort, Z. Kolska, M. Syrtanov, V. Svorcik, M. S. Yusubov, O. Lyutakov, O. Guselnikova a, P. S. Postnikov, “Smart recycling of PET to sorbents for insecticides through in situ MOF growth,” *Appl. Mater. Today*, vol. 22, p. 100910, 2021, doi: 10.1016/j.apmt.2020.100910.

[42] F. Zhang, H. Yang, S. Chen, S. Nie, J. Luo, S. Lin, and Y. Wang, “Waste PET as a reactant for lanthanide MOF synthesis and application in sensing of picric acid,” *Polymers (Basel).*, vol. 11, 2019, doi: 10.3390/polym11122015.

[43] A. M. Al-Enizi, J. Ahmed, M Ubaidullah, S. F. Shaikh, T. Ahamad, M. Naushad, G. Zheng, “Utilisation of waste polyethylene terephthalate bottles to develop metal-organic frameworks for energy applications: A clean and feasible approach,” *J. Clean. Prod.*, vol. 248, p. 119251, 2020, doi: 10.1016/j.jclepro.2019.119251.

[44] X. Dyosiba, J. Ren, N. M. Musyoka, H. W. Langmi, M. Mathe, and M. S. Onyango, “Feasibility of Varied Polyethylene Terephthalate Wastes as a Linker Source in Metal-Organic Framework UiO-66(Zr) Synthesis,” *Ind. Eng. Chem. Res.*, vol. 58,

pp. 17010–17016, 2019, doi: 10.1021/acs.iecr.9b02205.

[45] N. Wang, L. Y. Yang, Y. G. Wang, and X. K. Ouyang, “Fabrication of composite beads based on calcium alginate and tetraethylenepentamine-functionalised MIL-101 for adsorption of Pb(II) from aqueous solutions,” *Polymers (Basel).*, vol. 10, 2018, doi: 10.3390/polym10070750.

[46] S. Lawson, C. Griffin, K. Rapp, A. A. Rownaghi, and F. Rezaei, “Amine-Functionalised MIL-101 Monoliths for CO_2 Removal from Enclosed Environments,” *Energy and Fuels*, vol. 33, pp. 2399–2407, 2019, doi: 10.1021/acs.energyfuels.8b04508.

[47] M. Abroudi, A. Tadjarodi, Z. Rezvani, and A. Mollahosseini, “Microporous and Mesoporous Materials Synthesis and characterisation of Pd nanoparticles anchored on MIL 101(Cr) as a novel and recyclable catalyst for the Suzuki cross-coupling reactions,” vol. 331, 2022.

[48] X. Luo, L. Ding, and J. Luo, “Adsorptive removal of Pb(II) ions from aqueous samples with amino-functionalisation of metal-organic frameworks MIL-101(Cr),” *J. Chem. Eng. Data*, vol. 60, pp. 1732–1743, 2015, doi: 10.1021/je501115m.

[49] J. Y. Zhang, N. Zhang, L. Zhang, Y. Fang, W. Deng, M. Yu, Z. Wang, L. Li, X. Liu & J. Li, “Adsorption of Uranyl ions on Amine-functionalisation of MIL-101(Cr) Nanoparticles by a Facile Coordination-based Post-synthetic strategy and X-ray Absorption Spectroscopy Studies,” *Sci. Rep.*, vol. 5, pp. 1–10, 2015, doi: 10.1038/srep13514.

[50] S. Qiu, Y. Wang, J. Wan, J. Han, Y. Ma, and S. Wang, “Applied Surface Science Enhancing water stability of MIL-101 (Cr) by doping Ni(II),” *Appl. Surf. Sci.*, vol. 525, p. 146511, 2020, doi: 10.1016/j.apsusc.2020.146511.

[51] T. Zhao, L. Yang, P. Feng, I. Gruber, C. Janiak, and Y. Liu, “Inorganica Chimica Acta Facile synthesis of nano-sized MIL-101(Cr) with the addition of acetic acid,” *Inorganica Chim. Acta*, vol. 471, pp. 440–445, 2018, doi: 10.1016/j.ica.2017.11.030.

[52] T. R. Somo, M. W. Davids, M. V Lototskyy, M. J. Hato, and K. D. Modibane, “Improved Hydrogenation Kinetics of TiMn1.52 Alloy Coated with Palladium through Electroless Deposition,” 2021.

[53] L. Yang, T. Zhao, I. Boldog, C. Janiak, X. Yang, Q. Li, Y. Zhou, Y. Xia, D. W. Laia and Y. J. Liu, “Benzoic acid as a selector–modulator in the synthesis of MIL-88B(Cr) and nano-MIL-101(Cr),” vol. 101, pp. 989–996, 2019, doi: 10.1039/c8dt04186e.

[54] A. Demessence, P. Horcajada, C. Serre, and D. Grosso, “Elaboration and properties of hierarchically structured optical thin films of MIL-101(Cr) w,” vol. 101, pp. 7149–7151, 2009, doi: 10.1039/b915011k.

[55] T. K. Vo, W. S. Kim, and J. Kim, “Ethylenediamine-incorporated MIL-101(Cr)-NH_2 metal-organic frameworks for enhanced CO_2 adsorption,” *Korean J. Chem. Eng.*, vol. 37, no. 7, pp. 1206–1211, 2020, doi: 10.1007/s11814-020-0548-8.

[56] L. Liu, X. Tai, and X. Zhou, “Au^{3+}/Au^0 supported on Chromium(III) terephthalate metal organic framework (MIL-101) as an efficient heterogeneous catalystfor three-component coupling synthesis of propargylamines,” *Materials (Basel).*, vol. 10, 2017, doi: 10.3390/ma10020099.

[57] F. Ahmadijokani, S. Tajahmadi, A. Bahi, H. Molavi, M. Rezakazemi, F. Ko, T. M. Aminabhavi, and M. Arjmand, “Ethylenediamine-functionalised Zr-based MOF for efficient removal of heavy metal ions from water,” *Chemosphere*, vol. 264, p. 128466, 2021, doi: 10.1016/j.chemosphere.2020.128466.

[58] G. Chen, Yi. Wang, H. Weng, Z. Wu, K. He, P. Zhang, Z. Guo, and M. Lin, “Selective Separation of Pd(II) on Pyridine- functionalised Graphene Oxide Prepared by Radiation-induced Simultaneous Grafting Polymerisation and Reduction,” no. Ii, 2019, doi: 10.1021/acsami.9b06162.

[59] A. S. K. Kumar, S. Sharma, R. S. Reddy, M. Barathi, and N. Rajesh, “International Journal of Biological Macromolecules Comprehending the interaction between chitosan and ionic liquid for the adsorption of palladium,” *Int. J. Biol. Macromol.*, vol. 72, pp. 633–639, 2015, doi: 10.1016/j.ijbiomac.2014.09.002.

[60] A. K. Mosai, R. H. Johnson, and H. Tutu, “Modelling of palladium(II) adsorption onto amine-functionalised zeolite using a generalised surface complexation approach,” vol. 277, 2021.

[61] Y. Jiang and D. Kim, “Synthesis and selective adsorption behaviour of Pd(II)-imprinted porous polymer particles,” *Chem. Eng. J.*, vol. 232, pp. 503–509, 2013, doi: 10.1016/j.cej.2013.08.008.

[62] S. Lin, W. Wei, X. Wu, T. Zhou, J. Mao, and Y. S. Yun, “Selective recovery of Pd(II) from extremely acidic solution using ion-imprinted chitosan fiber: Adsorption performance and mechanisms,” *J. Hazard. Mater.*, vol. 299, pp. 10–17, 2015, doi: 10.1016/j.jhazmat.2015.05.050.

[63] F. A. Elaiwi and A. Sirkecioglu, “Amine-functionalised metal organic frameworks MIL-101(Cr) adsorbent for copper and cadmium ions in single and binary solution,” *Sep. Sci. Technol.*, vol. 00, pp. 1–13, 2019, doi: 10.1080/01496395.2019.1706571.

[64] T. C. Maponya, K. E. Ramohlola, N. H. Kera, K. D. Modibane, A. Maity, L. M. Katata-Seru and M. J. Hato “Influence of magnetic nanoparticles on modified polypyrrole/m-phenylediamine for adsorption of Cr(VI) from aqueous solution,” *Polymers (Basel).*, vol. 12, pp. 1–17, 2020, doi: 10.3390/polym12030679.

[65] R. Tseng and F. Wu, “Journal of the Taiwan Institute of Chemical Engineers Analyzing concurrent multi-stage adsorption process of activated carbon with a favorable parameter of Langmuir equation,” vol. 40, pp. 197–204, 2009, doi: 10.1016/j.jtice.2008.09.002.

[66] C. Sun, L. Sun, and X. Sun, “Graphical Evaluation of the Favorability of Adsorption Processes by Using Conditional Langmuir Constant,” 2013.

[67] T. Chen, T. Da, and Y. Ma, “Reasonable calculation of the thermodynamic parameters from adsorption equilibrium constant,” *J. Mol. Liq.*, vol. 322, p. 114980, 2021, doi: 10.1016/j.molliq.2020.114980.

[68] S. Lin, Y. Zhao, J. K. Bediako, C. Cho, and A. K. Sarkar, “Structure-controlled recovery of palladium(II) from acidic aqueous solution using metal-organic

frameworks of MOF-802 , UiO-66 and MOF-808," *Chem. Eng. J.*, vol. 362, pp. 280–286, 2019, doi: 10.1016/j.cej.2019.01.044.

[69] Z. Huang, C. Wang, J. Zhao, S. Wang, Y. Zhou, and L. Zhang, "Adsorption behaviour of Pd(II) ions from aqueous solution onto pyromellitic acid modified-UiO-66-," *Arab. J. Chem.*, vol. 13, pp. 7007–7019, 2020, doi: 10.1016/j.arabjc.2020.07.007.

[70] Q. Zhang, M. Chen, L. Zhong, Q. Ye, S. Jiang and Z. Huang, "Highly Effective Removal of Metal Cyanide Complexes and Recovery of Palladium Using," *Molecules,* 2018, doi: 10.3390/molecules23082086.

[71] M. Chen, S. Li, C. Jin, M. Shao, Z. Huang, and X. Xie, "Removal of metal-cyanide complexes and recovery of Pt(IV) and Pd(II) from wastewater using an alkali – tolerant metal-organic resin," *J. Hazard. Mater.*, vol. 406, p. 124315, 2021, doi: 10.1016/j.jhazmat.2020.124315.

[72] Y. Gong, Y. Hou, L. Guo, J. Liu, L. Chen, and Y. Gao, "Compatible with excellent gold / palladium trap and open sites for green Suzuki coupling by an imidazole-modified MOF," *Microporous Mesoporous Mater.*, vol. 337, p. 111877, 2022, doi: 10.1016/j.micromeso.2022.111877.

[73] J. Tang, J. Zhao, S. Wang, L. Zhang, and M. Zhao, "Pre-modification strategy to prepare a novel Zr-based MOF for selective adsorption of Palladium (II) from solution," *Chem. Eng. J.*, p. 127223, 2020, doi: 10.1016/j.cej.2020.127223.

[74] S. Daliran, M. Ghazagh-Miri, A. R. Oveisi, M. Khajeh, S. Navalón, M. Â. Ivaro, M. Ghaffari-Moghaddam, H. S. Delarami, and H. García, "A Pyridyltriazol Functionalised Zirconium Metal-Organic Framework for Selective and Highly Efficient Adsorption of Palladium," *ACS Appl. Mater. Interfaces*, vol. 12, pp. 25221–25232, 2020, doi: 10.1021/acsami.0c06672.

[75] L. Zhou, J. Xu, X. Liang, and Z. Liu, "Adsorption of platinum(IV) and palladium(II) from aqueous solution by magnetic cross-linking chitosan nanoparticles modified with ethylenediamine," *J. Hazard. Mater.*, vol. 182, pp. 518–524, 2010, doi:

10.1016/j.jhazmat.2010.06.062.

[76] J. Tang, Y. Chen, S. Wang, D. Kong, and L. Zhang, “Highly efficient metal-organic frameworks adsorbent for Pd(II) and Au(III) recovery from solutions : Experiment and mechanism,” *Environ. Res.*, vol. 210, p. 112870, 2022, doi: 10.1016/j.envres.2022.112870.

[77] A. K. Mosai, L. Chimuka, E. M. Cukrowska, I. A. Kotzé, and H. Tutu, “The Recovery Of Pd(II), Ir(III) and Rh(III) From Aqueous Solutions With Yeast-functionalised Zeolite,” .

[78] S. Lin, J. K. Bediako, C. Cho, M. Song, Y. Zhao, J. Kim, J. W. Choi, Y. S. Yun “Selective adsorption of Pd(II) over interfering metal ions (Co(II), Ni(II), Pt(IV)) from acidic aqueous phase by metal-organic frameworks,” *Chem. Eng. J.*, vol. 345, pp. 337–344, 2018, doi: 10.1016/j.cej.2018.03.173.

[79] X. Gao, C. Guo, J. Hao, Z. Zhao, H. Long, and M. Li, “Selective adsorption of Pd (II) by ion-imprinted porous alginate beads: Experimental and density functional theory study,” *Int. J. Biol. Macromol.*, vol. 157, pp. 401–413, 2020, doi: 10.1016/j.ijbiomac.2020.04.153.

[80] L. Zhou, J. Liu, and Z. Liu, “Adsorption of platinum(IV) and palladium(II) from aqueous solution by thiourea-modified chitosan microspheres,” *J. Hazard. Mater.*, vol. 172, pp. 439–446, 2009, doi: 10.1016/j.jhazmat.2009.07.030.

[81] A. N. Turanov, V. Karandashev, O. I. Artyushin, E. V. Sharova, and G. K. Genkina, “Adsorption of palladium(II) from hydrochloric acid solutions using polymeric resins impregnated with novel N-substituted 2-(diphenylthiophosphoryl)acetamides,” *Sep. Purif. Technol.*, vol. 187, pp. 355–364, 2017, doi: 10.1016/j.seppur.2017.06.068.

CHAPTER FIVE

HIGHLY ADSORPTIVE REMOVAL OF PALLADIUM AND PLATINUM IONS FROM WASTEWATER USING NOVEL GLUTARALDEHYDE-GRAFTED METAL ORGANIC FRAMEWORK

5.1. INTRODUCTION

Palladium (Pd) and platinum (Pt) are the widely used luxurious members of the platinum group metals (PGMs) due to their exceptional behaviour in catalysis. Consequently, their consumption increases owing to the advancing global economy and technology [1]. In order to meet the intensifying demand, more research is driven toward the recovery and recycling of Pd and Pt from secondary sources such as spent adsorbent electronic scraps, and mining tailings [2]. These efforts are aimed at reducing resource wastage and adverse environmental impacts. Over the years, different technologies such as liquid-liquid extraction [3], cloud point extraction [4], chemical precipitation [5], membrane separation [6], and adsorption [7] have been successfully employed in recovery and separation of these PGMs from wastewater to some extent. However, most of these methods have some drawbacks including generation of secondary contamination, poor removal efficacy, expensive as well as operational complexity [8]. Amongst the explored techniques, adsorption technology has emerged as a better method employed in the removal of metal ion complexes owing to its simple operation, low secondary pollution, and low cost [9][10]. The method needs effective adsorbents such as resins [11], magnetic nanomaterials [12], activated carbon [13], polymer fibres [14], and metal-organic framework (MOFs) materials [15].

MOFs are coordinated polymers made of organic linkers and metal ions connected by coordination bonding. Their unique and outstanding characteristics include easily tuneable structures, adjustable porosity, as well as large specific surface areas [16]. This encouraged their widespread development and applications, including hydrogen storage [17], gas sensing [18] and capturing [19], drug delivery [20] and electrochemical energy storage [21], wastewater treatment [22], and other fields. in case of Pd and Pt removal

and adsorption, MOFs including MIL-101, MOF-802, UiO-66 and MOF-808 have to some extent managed to resolve the current water pollution crisis. For instance, Lin *et al*. [23] studied the Pd adsorptive capabilities of MOF-802, UiO-66, and MOF-808 at ambient temperature. The authors reported that maximum adsorption capacity of MOF-808, UiO-66 and MOF-802 for Pd^{2+} was 164 105 and 26 mg/g, respectively. In a different study, Lin and co-workers [15] studied the binding ability of Pt^{4+} on the surface of UiO-66 in an acidic medium. After contacting 0.01 g of UiO-66 with 100 mg/L of Pt^{4+} solution at a pH of 1.0 for a day, they achieved the maximum adsorption capacity of 144 mg/g. Apart from these types of MOFs, MIL-101(Cr)-type MOFs possess some exceptional properties and are known to be chemically and thermally stable because of the strong Cr-O bonding between metal ions and organic ligands [24], [25]. MIL-101 consists of Cr nodes $[Cr_3(OH)(H_2O)_2O(\text{-}CO_2)_6]$ and 1,4-dicarboxylic acid-type (BDC-type) ligands. An exceptional advantage of using MIL-101 is use of an organic linker, BDC which is easily made using polyethylene terephthalate (PET) waste bottle [26]. The successful usage of PET to synthesise MOFs offers an economically favourable approach for waste management. However, it has been shown that the unmodified MOF material has certain limitations when used in adsorption, including unstable structure, poor selectivity and meagre impact [27].

Therefore, the versatile groups are usually incorporated by post-synthetic functionalisation onto the organic ligand or metal cluster [28]. Luo *et al*. [29] post-modified MIL-101(Cr) with ethylenediamine (ED) for the adsorptive removal of toxic divalent Pb^{2+} from aqueous solutions. The amino functional groups increased the adsorption capacity from 15.7 to 87.64 mg/g. In case of recovering PGMs, Lim *et al*. [30] used amine-functionalised MIL-101(Cr) which was post-synthesised from nitro-functionalised MIL-101(Cr) on the organic linker and tested in Pd^{2+} and Pt^{4+} adsorption from acidic aqueous solutions. They observed MIL-101(Cr)-NH_2 performs much better and possessed higher adsorption capacities for both Pd^{2+} and Pt^{4+} than MIL-101(Cr)-NO_2. However, the observed capacity was still low for recovery of PGMs in real life application. The post-synthetic functionalisation of MIL-101 with glutaraldehyde (GA) was reported by Ragheb *et al*. [31]. The GA has often been used as a crosslink or grafting agent due to its ease of fabrication and effectiveness. Chemical modification of MIL-101 with GA changes its

morphology and structure, which in turn affects the adsorption properties [27]. Therefore, the combination of ED and GA as low molecular weight molecules with a relatively small kinetic diameter containing terminal amino and carbonyl groups have the potential to interact with Pd^{2+} and Pt^{4+}. Their interaction occurs between the aldehyde groups of GA and amine groups of ED on the MIL-101 surface. This results in the formation of an extra amide group to provide further active sites to interact with Pd and Pt metal ions. Hence herein, MIL-101(Cr) was synthesised from a PET waste bottle using the hydrothermal method. The introduction of ED on the Cr node was prepared by post-synthetic functionalisation of MIL-101(Cr) followed by further grafting with GA for additional functional groups. Then the obtained MIL-101(Cr)/ED-GA adsorbent was used for the first time to adsorb Pd^{2+} and Pt^{4+} ions from aqueous environment. The adsorption behaviour and capacity of MIL-101(Cr)/ED-GA was investigated under different factor conditions. Together, the adsorption isotherms and kinetics were studied, followed by the investigation of the potential re-usability of the adsorbent.

5.2. MATERIALS AND METHODS

5.2.1. Reagents and chemicals

Chromium nitrate nanohydrate $Cr(NO_3)_3.9H_2O$, Sigma-Aldrich, 99.5%), ethylene glycol ($HOCH_2CH_2OH$, Sigma-Aldrich, 99.8%), sodium hydroxide (NaOH, Sigma-Aldrich, 99.8%), hydrochloric acid (HCl, Sigma-Aldrich, 99.8%), ethylenediamine ($C_2H_8N_2$, Sigma-Aldrich, 99.8%) and glutaraldehyde ($C_5H_8O_2$, Sigma-Aldrich, 99.8%) were used as received. PET bottles were collected from the University of Limpopo dining Hall, Polokwane, South Africa. Upon removing caps, rings, and labels, the bottles were cut and shaped into smaller chips.

5.2.2. Synthesis of MIL-101(Cr)

The synthetic procedures were conducted in a 100 mL Teflon-lined hydrothermal reactor (Laboratory Supplies, South Africa) [26]. BDC was prepared from a PET waste bottle. Briefly, 3.00 g of PET flakes and 6.00 mL ethylene glycol (EG) were placed into the reactor together with 60.00 mL H_2O. The reaction vessel was heated and kept at 210 ^oC for 8

hours. The resultant white particles were separated by centrifuge, prior to washing with ethanol, then followed by drying at 100 ^{o}C overnight in an oven.

Chromium-based MIL-101 was synthesised based on the reported procedure [32]. Approximately, 4.00 g of $Cr(NO_3)_3.9H_2O$ salt and 1.66 g of H_2BDC were suspended in deionised H_2O. and subsequently stirred for 15 min prior to ultra-sonic mixing for 0.5 hours. The reaction mixture was put into an auto cleavable reactor which and kept in an oven for 8 hours at 220 °C. The resulting product (MIL-101(Cr)) was filtered, washed and dried under 100 °C.

The grafting with ED was done under refluxing by dispersing 0.50 g of the prepared MIL-101(Cr) in anhydrous toluene (50.00 mL), then added ED (1.00 mL). After 12 hours, the obtained brown MIL-101(Cr)/ED precipitates were separated by vacuum filtration, followed by washing with ethanol and finally allowed to dry at 60 ^{0}C overnight.

Preparation of the glutaraldehyde grafted MIL-101(Cr)/ED was performed by suspending 0.50 g of MIL-101(Cr)/ED in 50.00 mL of glutaraldehyde solution. The reaction suspension was kept under stirring for 24 hours at 25 ^{0}C. Then, MIL-101(Cr)/ED-GA particulates were separated by vacuum filtration and dried at 60 ^{o}C for overnight.

5.2.3. Characterisations

Structural studies of MIL-101(Cr)/ED-GA with reference to MIL-101(Cr) were deduced from X-ray diffraction Phillips 1830 instrument of a wavelength (λ) peak positioned at 1.54 angstrom. Functional groups elucidation and Fourier transform infrared (FT-IR) spectroscopic studies were explored from the Agilent Cary 600 Series, Spectrum II PerkinElmer. The Brunauer-Emmett-Teller (BET) isothermal curves were analysed using Micromeritics Tristar 300, where the samples were first degassed at 180 $^{\circ}$C for 4 hours prior to nitrogen gas adsorption-desorption. Perkin-Elmer STA 6000 instrument was used to study the thermal properties of the samples under N_2 gas ejected at 20 mL min^{-1}. The surface morphology, elemental analysis, and mapping were probed by using FE-SEM (Auriga Cobra focused-ion beam scanning electron microscopy fitted with energy dispersive X-ray (EDS), operated at 200 keV.

5.2.4. Sorption experiments

The pH studies were investigated from 1.00-6.00 for Pd^{2+} and Pt^{4+}at 100 mg L^{-1} and 50.0 mL volume using HCl and NaOH for adjustments. The effects of initial concentrations on Pd^{2+} and Pt^{4+} sorption by MIL-101(Cr)/ED-GA were explored from 50-400 mg/L at 25 °C. Kinetics experiments were assessed with an optimum adsorbent amount and pH, of 0.03 g and pH of 3.0 for Pd^{2+}; and 0.02 g and pH of 4.0 for Pt^{4+}. The remaining concentrations of Pd^{2+} and Pt^{4+}, before and after adsorption were determined from the ultraviolet-visible (UV-Vis) spectroscopy (Lambda 365 UV/Vis Spectrophotometer, (PerkinElmer, Johannesburg, South Africa)). The removal efficiency of the composites was deduced from Equation 5.1:

$$\%removal = \left(\frac{Co-Ce}{Co}\right) X \;\; 100 \tag{5.1}$$

C_o and C_e (mg/L) are the original and equilibrium concentrations of metal ions. The adsorption equilibrium adsorption capacity was estimated using the following Equation 5.2:

$$q_e = \;\; \left(\frac{Co-Ce}{m}\right) \;\; V \tag{5.2}$$

q_e (mg/g) is the quantity of metal ion adsorbed per unit mass of MIL-101(Cr)/ED-GA at equilibrium. m (g) and V (L) denote the amount of MIL-101(Cr)/ED-GA, and the volume of metal ion solution. Regeneration and reusability of the MIL-101(Cr)/ED-GA adsorbent were investigated by stirring the prepared adsorbent in a solution containing 6 M HCl solution after the adsorption. This was followed by thorough washing with deionised water prior to the subsequent cycle.

5.3. RESULTS AND DISCUSSION

5.3.1. Structural Characterisations

Figure 5.1(a) represent the FT-IR spectra for the MIL-101(Cr) and MIL-101(Cr)/ED-GA. The IR spectra demonstrated characteristic bands assigned to the benzene-carboxylates vibrations at 1510 and 1414 cm^{-1} for C=O and C-O bonding in the carboxylates [33]. The band at 1631 cm^{-1} is due to the C=C of the benzene ring and the observed peak at 674 cm^{-1} is associated with Cr-O vibration [34]. With the addition of ethylenediamine-

glutaraldehyde, the peak intensities of C=O at around 1510 cm^{-1} decreased. The characteristic bands attributed to the amine and amide group in MIL-101(Cr)/ED-GA were seen at 3221 cm^{-1} for N-H stretch, 2944 $cm^{-1,}$ and 1357 cm^{-1} for C-H and C-C stretching of the aliphatic CH_2 group, 1554 cm^{-1} for N-H bend and 1052 cm^{-1} for C-N stretch of the amide group in ethylenediamine-glutaraldehyde [33][35][36]. In addition, a new peak appeared at 506 cm^{-1} which is assigned to the N-Cr vibrations indicating the successful preparation of MIL-101(Cr)/ED-GA.

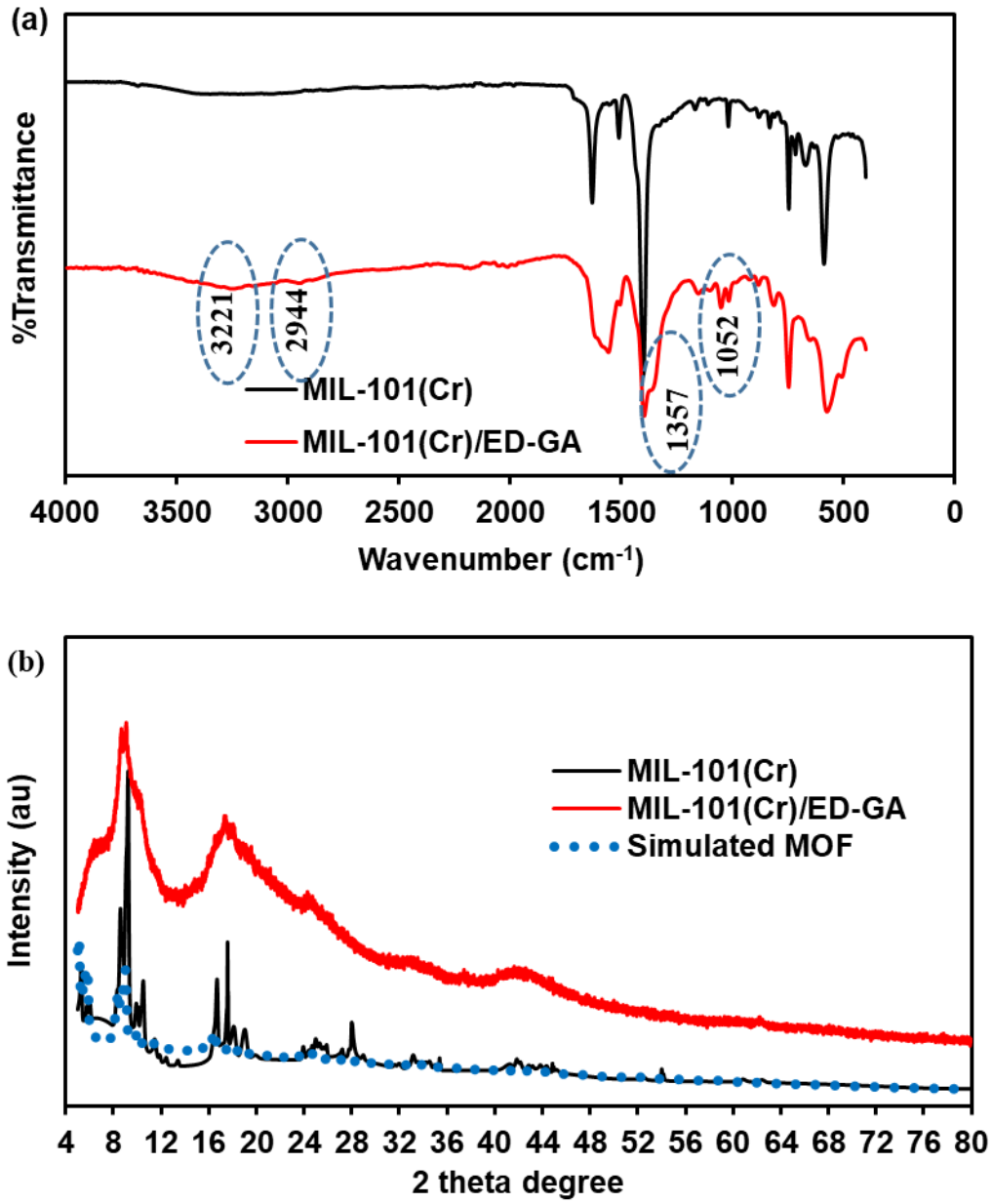

Figure 5.1: (a) FTIR and (b) Diffractograms for MIL-101(Cr) and MIL-101(Cr)/ED-GA.

Figure 5.1(b) shows the XRD patterns of the prepared MOF samples obtained in the range of 5-80 2θ degrees. The diffraction pattern for MIL-101(Cr) revealed characteristic peaks at 5.59º, 8.63º, 9.25º, 9.90º, 10.6º, 11.7º, 16.8º, 17.6º, 18.2º, and 19.2º which correspond with the reported studies [34][37][38]. In comparison to the MIL-101(Cr)/ED-GA patterns, it was seen that post-synthetic functionalisation has some effect on the

symmetry of the crystal as the diffraction peaks broadened. However, the framework of the MIL-101(Cr) was not destroyed as the major characteristic peaks were still observed on the MIL-101(Cr)/ED-GA patterns. This was further supported by determining the amount of MIL-101(Cr) crystallinity in the MIL-101(Cr)/ED-GA using Vegard's law [39]. The calculated value for the lattice period parameters (a=b=c) was 68.0 Å and gave 75.1% crystallinity. The reduced crystallite size in MIL-101(Cr)/ED-GA was also calculated at 2θ degree 10 using the Debye-Scherrer formula [40] shown by Equation 5.3 and found to be 6.1 nm.

$$D = \frac{0.9\lambda}{\beta \mathrm{Cos}\theta} \qquad (5.3)$$

The BET analyses of MIL-101 and MIL-101(Cr)/ED-GA are depicted by Figure 5.2(a)-(c). As illustrated in Figure 5.2(a,b), MIL-101(Cr) and MIL-101(Cr)/ED-GA possessed type I isotherm curves. which suggest the presence of microporous structure of the adsorbents. The steep slope is resulting from the slow adsorption of N_2 by the smaller microporous cavities of MIL-101(Cr) [41][42]. The initial steep slope is then followed by a narrow hysteresis loop in pressures between $0.25 < P/P_0 < 0.95$), signifying mesopores with uniform pore size distribution. Oppositely, Figure 5.2(b) shows that N_2 struggles to penetrate the pores of MIL-101(Cr)/ED-GA at lower P/P_0 values. This can suggest that the material is dominated by very small pores and thus the diffusion is very slow. In both cases, however, an abrupt increase in the N_2 amount is noted when P/P_0 is higher than 0.9. In addition, the surface area of MIL-101(Cr) (Figure 5.2(a)) was measured as 308.73 $m^2\ g^{-1}$ with a pore volume of 0.122 $cm^3\ g^{-1}$. For MIL-101(Cr)/ED-GA, the values decreased to 3.476 $cm^2.g^{-1}$ and 0.026 $cm^3\ g^{-1}$ with the introduction of ethylenediamine-glutaraldehyde on to MIL-101(Cr) surface. This suggests that ethylenediamine-glutaraldehyde took up the pores of the framework and hinder the diffusion and adsorption of N_2 [33].

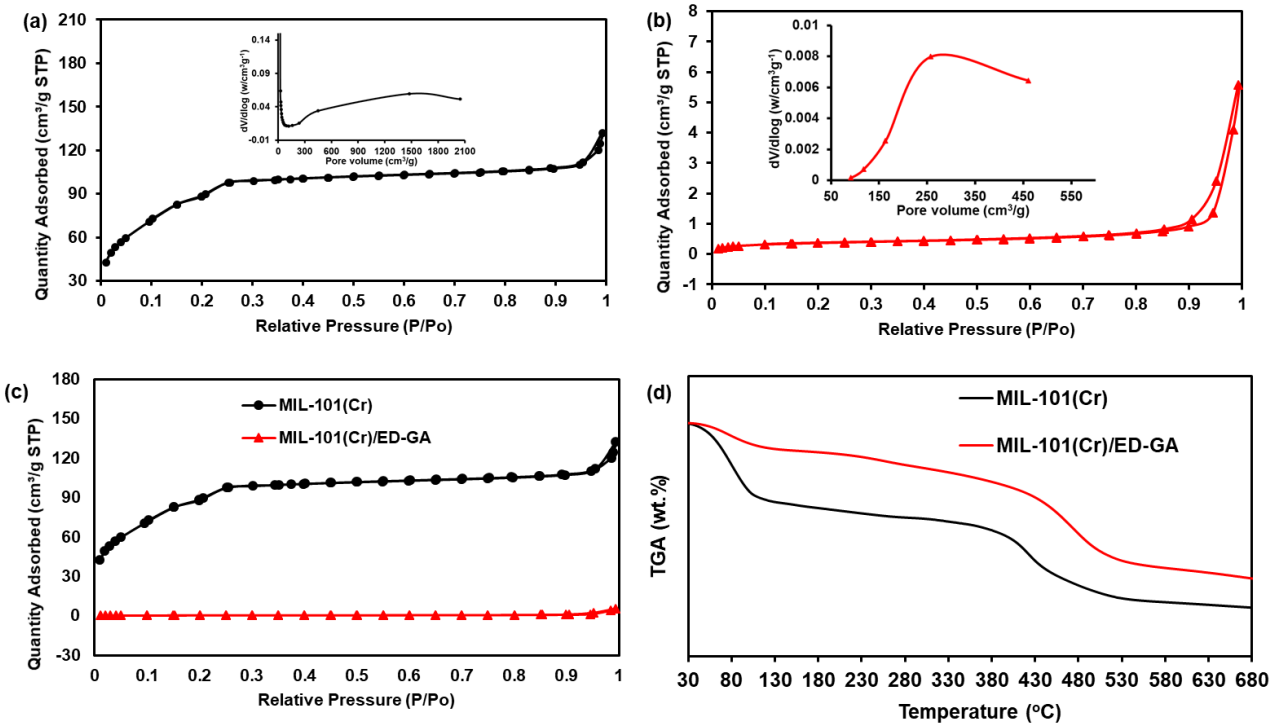

Figure 5.2: BET measurement of (a) MIL-101 and (b) MIL-101(Cr)/ED-GA (inset: Pore diameter measurement). (c) Comparison BET isotherms and (d) TGA curves of MIL-101(Cr) and MIL-101(Cr)/ED-GA.

Thermogravimetric analysis of MIL-101(Cr) and MIL-101(Cr)/EDGA were done to investigate their thermal stability (Figure 5.2(d)). Two degradation steps were observed in both materials as depicted by the TGA plots in Figure 5.2(d). The results were supported by differential thermal analysis (DTA) curves seen in Figure 5.3(a)-(c) for MIL-101(Cr) and MIL-101(Cr)/ED-GA. The TGA in Figure 5.2(d) and DTA (Figure 5.3(c)) comparison thermograms showed an enhancement in the thermal stability of MIL-101(Cr)/ED-GA. The TGA and DTA were supported by DSC curves which displayed endothermic peaks at 100 ^{o}C for water loss and exothermic parks at 400 (MIL-101(Cr)) and 480 ^{o}C (MIL-101(Cr)/ED-GA) for degradation of the framework (Figure 5.3(d)). The curves exhibited an intense exothermic peak at 92 °C for crystallization transition with changes in enthalpy (ΔH) of 2.46 and 2.82 kJ g^{-1} for MIL-101(Cr) and MIL-101(Cr)/ED-GA, respectively. The endothermic peak in MIL-101(Cr)/ED-GA was detected at 272 ^{o}C with ΔH of 0.821 kJ g^{-1} for disintegration of ED and glutaraldehyde on the surface whereas MIL-101(Cr) had an endothermic peak at 382 °C with ΔH 0.782 kJ g^{-1} for degradation of

organic linker [44]. In addition, there were small exothermic peaks at around 500 °C with ΔH 0.789 and 2.00 kJ g^{-1} for MIL-101(Cr) and MIL-101(Cr)/ED-GA, respectively.

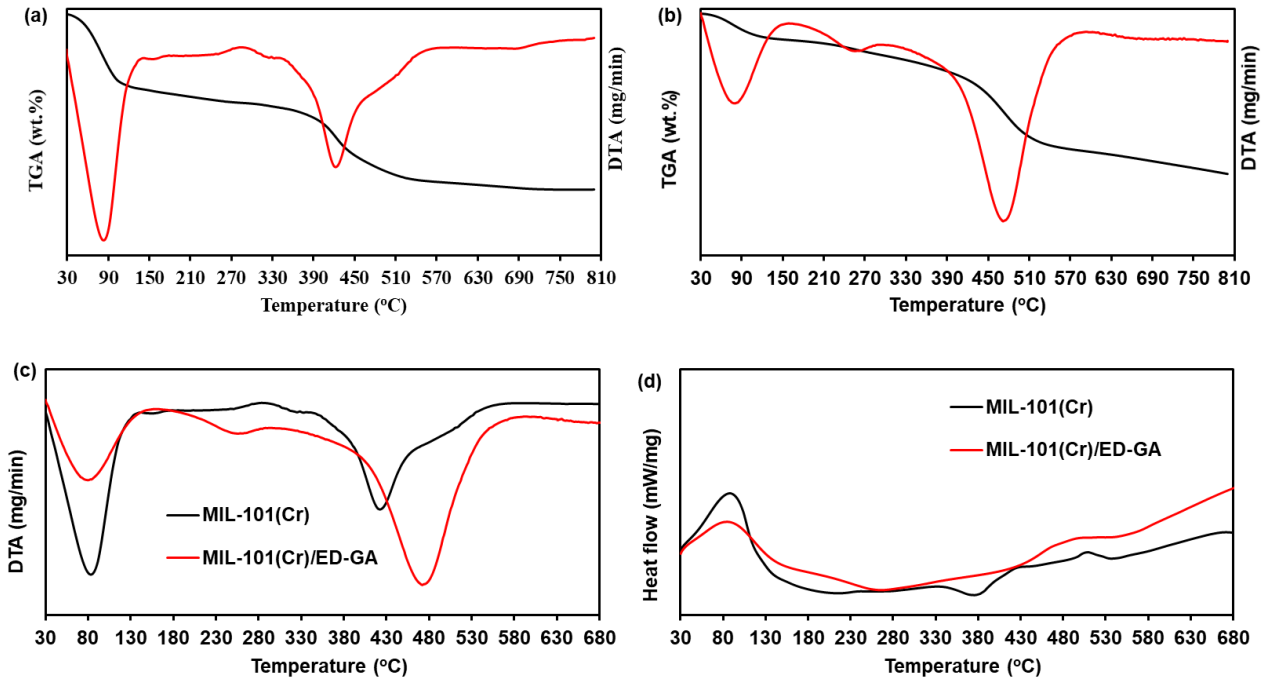

Figure 5.3: TGA/DTA curves of (a) MIL-101(Cr), and (b) MIL-101(Cr)/ED-GA. (c) DTA and (d) DSC of MIL-101 and MIL-101(Cr)/ED-GA.

3.2. Morphological Characterisations

The SEM image of the MIL-101(Cr) in Figure 5.4(a) possessed discrete octahedron shapes with clear edges and corners, consistent with previous reports [29]. Most crystals were made of uniform surface morphologies and some are split or lack angles. The octahedron shapes had a smooth surface with the majority of the particles having a size of 100-40 nm (Figure 5.4(b)). The EDS spectrum of the MIL-101(Cr) presented in Figure 5.4(c) revealed that the sample is composed of C, O, and Cr (the Al element was from the SEM preparation procedure). The inset in Figure 5.4(c) showed the relative contents of C, O, and Cr in the MIL-101(Cr) which were determined to be about 77.6, 20.1, and 1.4%, respectively. The SEM image of the MIL-101(Cr)/ED-GA in Figure 5.4(d) clearly demonstrated that its shape and morphology are similar to those of the MIL-101(Cr) with

some increment in large particle size (Figure 5.4(e)). Endorsing that the crystalline structure of MIL-101(Cr) remains unchanged after incorporating ED and GA as seen in the XRD above. Nonetheless, the structural porosity of MIL-101(Cr) decreased after the incorporation of GA due to the growth of the polymer chain with ED and GA. Figure 5.4(f) and Figure 5.5 show the EDS spectrum and representative images of the MIL-101(Cr)/ED-GA with corresponding elemental mappings. The presence of C, O, Cr, and N elements was observed in the EDS spectrum in Figure 5.4(f). As presented in Figure 5.5(a)-(h), the corresponding elemental mapping distributions also showed the existence of C, O, Cr, and N elements. From the EDS spectra and maps, it was seen that the elements are uniformly distributed over the MIL-101(Cr)/ED-GA, confirming the homogeneity of the samples. The increase in the amount of C and N elements was due to the presence of ED and GA chain, thus confirming the uniform incorporation of ED and GA chain into the porous MIL-101(Cr) framework. The obtained morphological and structural characterisations of the synthesised materials indicated the presence of reactive species in the MIL-101(Cr)/ED-GA. This clearly suggests that the adsorption of Pd^{2+} and Pt^{4+} ions on the MIL-101(Cr)/ED-GA will arise from the electrostatic interaction of these ions with the reactive species on the surface. Hence in this work, the removal of Pd^{2+} and Pt^{4+} ions from contaminated aqueous solutions using MIL-101(Cr)/ED-GA as a novel adsorbent was investigated.

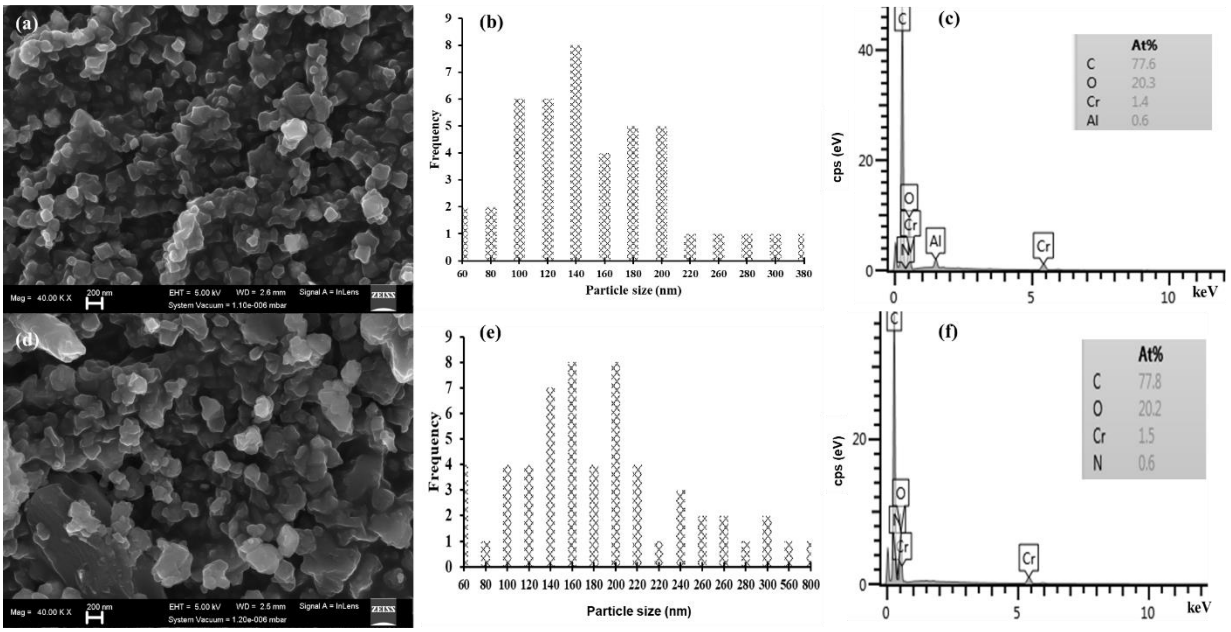

Figure 5.4: (a) SEM image, (b) particle size distribution and (c) EDS spectrum ofMIL-101(Cr) MIL-101(Cr)/ED-GA. (d) SEM image, (e) particle size distribution and (f) EDS spectrum of MIL-101(Cr)/ED-GA (Inset: elemental analysis in atomic percentage).

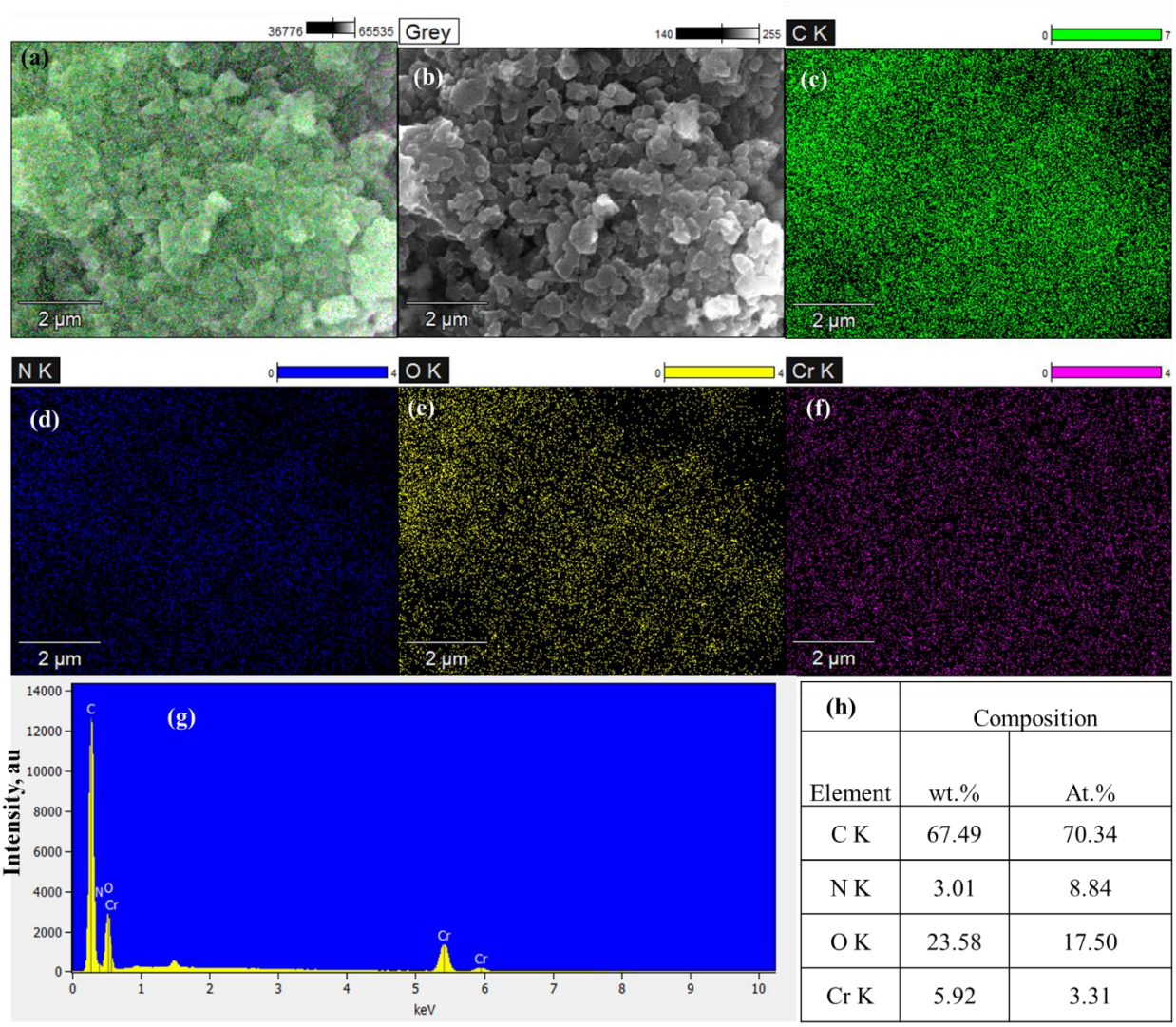

(h)	Composition	
Element	wt.%	At.%
C K	67.49	70.34
N K	3.01	8.84
O K	23.58	17.50
Cr K	5.92	3.31

Figure 5.5: Elemental mapping of MIL-101(Cr)/ED-GA, (a) light, and (b) grey images, (c)-(f) mapping image of carbon, nitrogen, oxygen, and chromium elements, respectively. (g) EDS spectrum and (h) tabulated atomic weight percentages of MIL-101(Cr)/ED-GA.

5.3.3. Adsorption results

5.3.3.1. Influence of pH and adsorbent dosage

The original solution pH directly influences the intake of Pd^{2+} and Pt^{4+} ions by MIL-101(Cr)/ED-GA. Depending on the pH value, the reactive groups can either be protonated or deprotonated to electrostatically interact with metal ions that are present in the solution [45]. Figure 5.6(a) depicts the influence of solution pH on the uptake of Pd^{2+} and Pt^{4+} ions

by MIL-101(Cr)/ED-GA. The results show that the removal percentage for both Pd^{2+} and Pt^{4+} increased with increasing pH from 1.0-4.0 and decreased beyond 4.0. The optimum pH value was obtained as 3.0 for Pd^{2+} and 4.0 for Pt^{4+}. This behaviour is attributed to the higher degree of protonation occurring in acidic media on the N and O of the amide groups on the MIL-101(Cr)-ED-GA surface as shown in Equations 5.4 and 5.5 [11]:

$$O{=}CH{-}NH + H^{+} + Cl^{-} \rightarrow O{=}CH{-}NH_2^{+} + Cl^{-} \quad (5.4)$$

$$HN{-}CH{=}O + H^{+} + Cl^{-} \rightarrow HO{-}CH{=}NH^{+} + Cl^{-} \quad (5.5)$$

Moreover, in lower pH values of HCl the dominating species of the PGMs are anionic chloro-complexes which can interact with the MIL-101(Cr)/ED-GA through electrostatic interaction with the protonated amide groups through the mechanisms shown in Equation 5.6-5.9 [46]:

$$2RNH_2^{+}\ Cl^{-} + PtCl_6^{2-} \leftrightarrow (RNH_2^{+})_2PtCl_6^{2-} + 2Cl^{-} \quad (5.6)$$

$$2RNH^{+}\ Cl^{-} + PtCl_6^{2-} \leftrightarrow (RNH^{+})_2PtCl_6^{2-} + 2Cl^{-} \quad (5.7)$$

$$2RNH_2^{+}\ Cl^{-} + PdCl_4^{2-} \leftrightarrow (RNH_2^{+})_2PdCl_4^{2-} + 2Cl^{-} \quad (5.8)$$

$$2RNH^{+}\ Cl^{-} + PdCl_4^{2-} \leftrightarrow (RNH^{+})_2PdCl_4^{2-} + 2Cl^{-} \quad (5.9)$$

In addition, the pH drift method was employed to assess the point of zero charge (PZC) which was used to further deduce the possible interaction of MIL-101(Cr)/ED-GA with Pd^{2+} and Pt^{4+} ions as presented in Figure 5.6(b). The attained values of PZC for Pd^{2+} and Pt^{4+} are 4.2 and 5.5, respectively. These results suggest that more adsorption is occurring below the PZC values as a result of electrostatic interaction between MIL-101(Cr)/ED-GA and metal ions. The results are in good correlation with the achieved optimum pH. Furthermore, the IR spectra of MIL-101(Cr)/ED-GA after the adsorption of Pd^{2+} and Pt^{4+} were obtained and compared with the spectrum before adsorption and the results are depicted in Figure 5.6(c). From the results, the interaction of Pd^{2+} with MIL-101(Cr)/ED-GA was noted by the reduction in the intensity of the C-N vibration at 1052 cm^{-1} and the disappearance of the N-H peaks at 1554 cm^{-1}. In the case of Pt^{4+}, the adsorption was confirmed by the broadening of the 1554 cm^{-1} peak as well as the enhancement of the

peak at 1288 cm^{-1} which is due to the N-H vibration of the amide group. These results confirm the successful interaction of MIL-101(Cr)/ED-GA with Pd^{2+} and Pt^{4+} ions.

The influence of the amount of MIL-101(Cr)/ED-GA on the removal of Pd^{2+} and Pt^{4+} ions was investigated by varying the amount of adsorbent dose from 0.01-0.0.07 g for Pd^{2+} and 0.005-0.05 g for Pt^{4+} (Figure 5.6(d)). The results for Pd^{2+} showed an increase in the removal percentage (%R) with an increase in the MIL-101(Cr)/ED-GA dose and the equilibrium was reached at 0.03 g. For Pt^{4+}, an increase in the %R was observed from 0.005-0.02 g of MIL-101(Cr)/ED-GA followed by a decrease as the dosage amount was increasing. The trends for Pt^{4+} removal by MIL-101(Cr)/ED-GA suggest that when more material is added there is a limited collision between adsorbate and adsorbent, hence in this work the optimum dose was taken as 0.02 g.

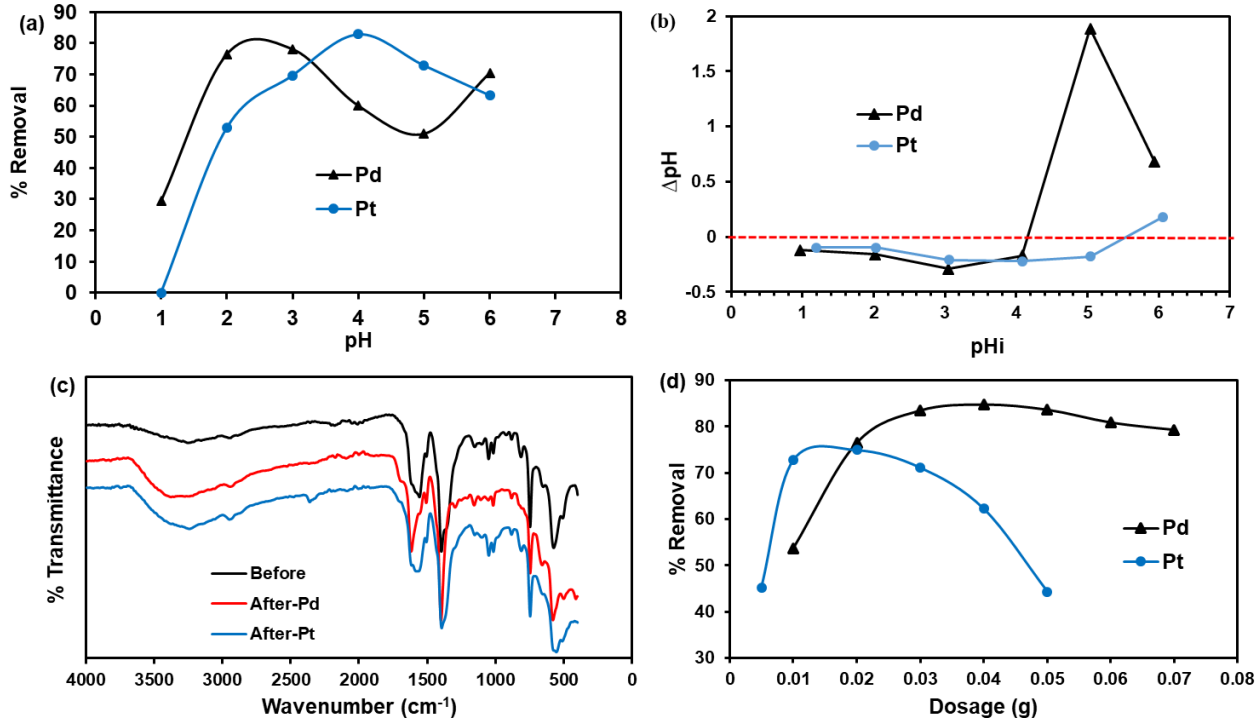

Figure 5.6: (a) pH effect on the removal of Pd^{2+} and Pt^{4+} ions by MIL-101(Cr)/ED-GA (b) PZC of MIL-101(Cr)/ED-GA. (c) FTIR spectra of MIL-101(Cr)/ED-GA before and after Pd^{2+} and Pt^{4+} ions uptake. (d) MIL-101(Cr)/ED-GA dose effect on Pd^{2+} and Pt^{4+} adsorption.

5.3.3.2. Adsorption isotherms

The equilibrium adsorption experiments for Pd^{2+} and Pt^{4+} ions removal by MIL-101(Cr)/ED-GA are shown in Figure 5.7(a). The results revealed that the experimental adsorption capacity of MIL-101(Cr)/ED-GA is increasing with an increase in the initial concentrations from 50-400 mg/L for both Pd^{2+} and Pt^{4+} ions. To deduce the mode of adsorption, the obtained data were fit to the nonlinear Langmuir and Freundlich isotherm models given by the following Equations 5.10 and 5.11, respectively.

$$\frac{qe}{qm} = \frac{K_L C_e}{1+K_L C_e} \quad (5.10)$$

$$qe = KFC_e^{1/n} \quad (5.11)$$

with q_m (mg/g) representing the Langmuir maximum adsorption capacity. The Langmuir and Freundlich constants are denoted by K_L (L mg^{-1}) and KF (mg/g), respectively. The results obtained from the nonlinear fittings revealed that both Pd^{2+} and Pt^{4+}adsorption data fitted well with the Langmuir isotherm model as the correlation coefficients R^2 values were closer to one than those predicted by the Freundlich nonlinear fittings (See Table 5.1). These observations were further supported by the linear fittings of the data to the two isotherm models which are given by Equations 5.12 and 5.13 and the results are shown in Figures 5.7(c) and (d). The R^2 value predicted by the linear Langmuir model was 0.9821 for both Pd^{2+} and Pt^{4+} which was higher than 0.7913 and 0.8526 for Pd^{2+} and Pt^{4+}, respectively, which were depicted by the Freundlich model. This behaviour suggests that the adsorption of Pd^{2+} and Pt^{4+} by MIL-101(Cr)/ED-GA is through a monolayer.

$$\frac{C_e}{q_e} = \frac{1}{qmK_L} + \frac{C_e}{qm} \quad (5.12)$$

$$\ln q_e = \ln K_F + \frac{1}{n} lnC_e \quad (5.13)$$

Furthermore, the maximum adsorption capacity (q_m) of the functionalised MIL-101(Cr)/ED-GA towards Pd^{2+} and Pt^{4+} ions were determined from the linear form of the Langmuir isotherm model and obtained as 322.6 mg/g for Pd^{2+} and 416.7 mg/g for Pt^{4+}. These results show that MIL-101(Cr)/ED-GA has a higher affinity for PGMs as the values are higher than those reported in the literature as shown in Table 5.2. Additionally, the Langmuir isotherm model is associated with a dimensionless parameter called the

separation factor denoted by R_L. This constant assists in deducing the favourability of the adsorption process and is determined by the below Equation 5.14.

$$R_L = \frac{1}{1+K_L\ C_0} \tag{5.14}$$

For the adsorption process to be favourable, the R_L values should be greater than zero but less than one (0< R_L >.1). The calculated values suggest that the adsorption of Pd^{2+} and Pt^{4+} on the surface of MIL-101(Cr)/ED-GA is favourable since R_L = 0.0695 and 0.1546 (see Table 5.1).

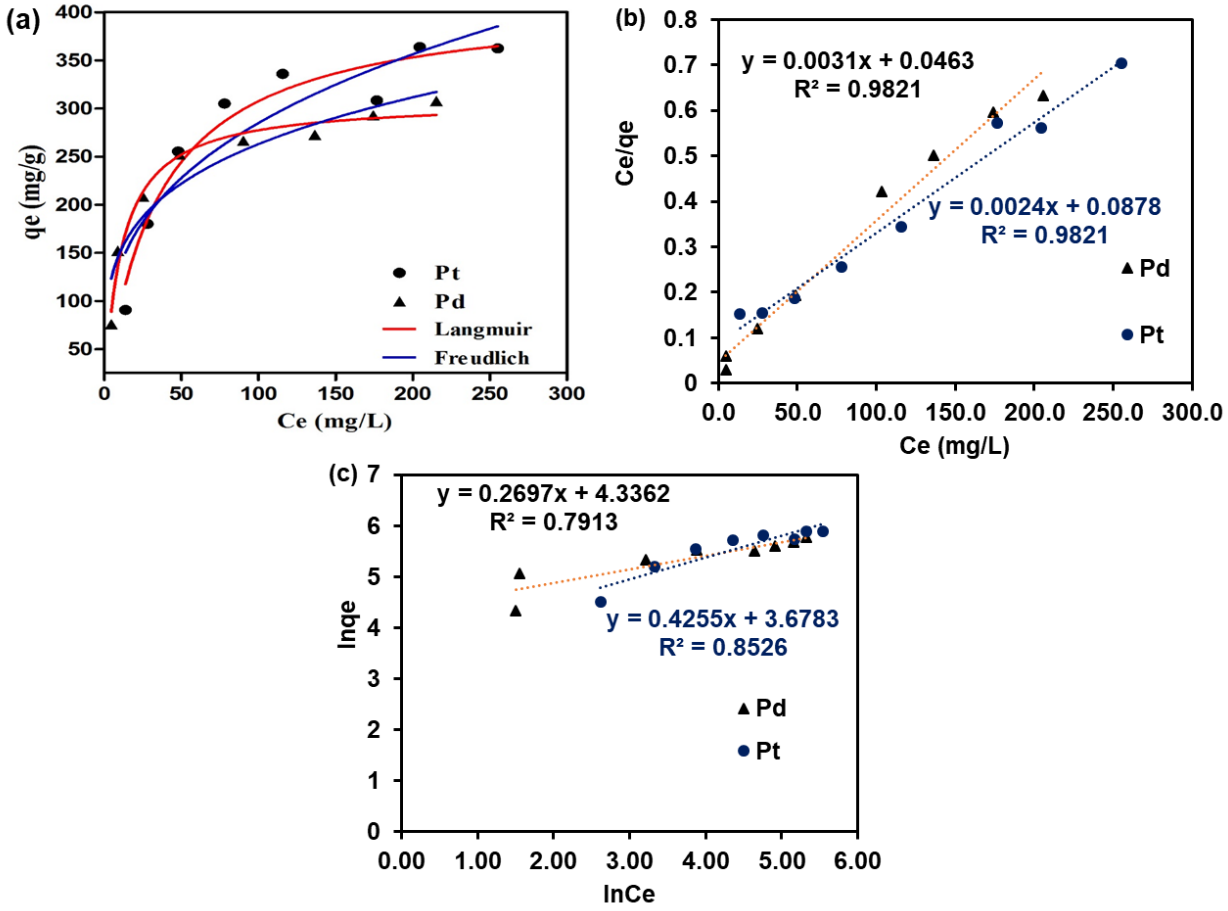

Figure 5.7: (a) Equilibrium adsorption and nonlinear isotherm data for the removal of Pd^{2+} and Pt^{4+} ions by MIL-101(Cr)/ED-GA. (b) Langmuir isotherm linear curve (c) Linear curve of the Freundlich isotherm model.

Table 5.1: Isotherms data of MIL-101(Cr)/ED-GA after the adsorption of Pd^{2+} and Pt^{4+} metal ions.

Isotherm models		
	Pd^{2+}	Pt^{4+}
Langmuir		
Linear		
q_m	322.6	416.17
K_L	0.0670	0.0273
R_L	0.0695	0.1546
R^2	0.9821	0.9821
Non-linear		
Best-fit values		
q_m	308.3	414.4
K_L	0.08948	0.02875
Std. Error		
q_m	7.977	22.97
K_L	0.01165	0.005892
95 % Confidence		
q_m	288.8 to 327.8	358.2 to 470.6
K_L	0.06097 to 0.1180	0.01433 to 0.04316
Goodness of Fit		
Degrees of	6	6
R^2	0.9794	0.9513
Absolute Sum of	906.1	3144
Sy.x	12.29	22.89
Number of points		
Analysed	8	8
Freundlich		
Linear		
K_F	37.864	41.913
n	2.010	1.936
R^2	0.6172	0.6946
Non-linear		
Best-fit values		
K_F	85.29	64.48
n	4.09	3.1
Std. Error		
K_F	15.41	20.6
n	0.6522	0.6246
95 % Confidence		
K_F	47.58 to 123.0	14.08 to 114.9
n	2.495 to 5.686	1.572 to 4.628
Goodness of Fit		
Degrees of	6	6
R^2	0.9052	0.8539
Absolute Sum of	4162	9443
Sy.x	26.34	39.67

Number of points Analysed	8	8

Table 5.2: A comparison of the adsorption capacity of Pd^{2+} and Pt^{4+} metal ions by MIL-101 (Cr)/ED-GA with reported literature.

Adsorbent	**Pt^{4+} q_m (mg/g)**	**Pd^{2+} q_m (mg/g)**	**Experimental conditions**	**Refs**
Calcined aluminum hydroxide gels	23.9	23.4	pH 5.0, 0.02 g, 20 mg/L	[47]
ED/Chitosan NPs	171	138	pH 2.0, 0.05 g, 60	[46]
bayberry tannin collagen fiber	41.7	27.5	pH 3.0 and 4.0, 0.1 g, 50 mg/L	[48]
mGO@SiO2@PPy-PTh	50	45	pH 4.5, 0.019 g, 0.2 mg/L	[49]
GLA-PEI@ algal biomass beads	100	120	pH 2.5, 0.05 g, 50 and 40 mg/L	[45]
L-lysine/Chitosan	129.26	109.47	pH 1.0 and 2.0, 0.1 g, 100 mg/L	[11]
MIL-101(Cr)-NH_2	140.7	277.6	pH 1.0, 0.01 g, 200 "	[30]
MIL-101(Cr)-NO_2	104.5	119.5	pH 1.0, 0.01 g, 200 "	[30]
quaternary ammonium-Zr^{4+}	245.7	123.2	pH 7.5, 200 mg/L, 0.01 g	[50]
Polystyrene nanofiber/EDA	7.4	4.3	pH 1.0, 10 mg/L, 0.15 g	[14]
Glycine/chitosan	122.47	120.39	pH 2.0, 0.33 g, 100	[51]
MIL-101 (Cr)-GA	416.17	322.6	pH 3.0 and 4.0, 200 mg/L, 0.02 g	This work

5.3.3.3. Adsorption kinetics

The influence of contact time on the adsorption of Pd^{2+} and Pt^{4+} metal ions by MIL-101(Cr)/ED-GA was also assessed in order to get an insight into the adsorption process. The experiments were conducted at an initial concentration of 100 mg/L at 25 ^{o}C for both Pd^{2+} and Pt^{4+}. From the results presented in Figure 5.8(a), there is an increase in the

adsorption capacity for both Pd^{2+} and Pt^{4+} ions with an increase in contact time. In addition, the MIL-101(Cr)/ED-GA demonstrated fast kinetics for the adsorption Pd^{2+} which reached equilibrium after 20 minutes as compared to the kinetics for Pt^{4+} which equilibrated after 60 minutes. The data obtained from kinetics experiments were then used to establish the rate of adsorption and other adsorption kinetics parameters, by fitting it to the nonlinear and linear forms of the pseudo-first-order (PFO) and the pseudo-second-order (PSO) kinetic models determined using the following Equations:

$$\frac{dqt}{dt} = k_1 (q_e - q_t) \quad (5.15)$$

$$\frac{dqt}{dt} = k_2 (qe - qt)^2 \quad (5.16)$$

$$\ln (q_e - q_t) = \ln q_e - k_1 t \quad (5.17)$$

$$\frac{t}{qt} = \frac{1}{k_2 q^2 t} + \frac{1}{q_e} t \quad (5.18)$$

where k_1 (min^{-1}) represents the PFO rate constant and k_2 (g mg^{-1} min^{-1}) denotes the PSO rate constant.

The experimental observations were supported by PSO rate constant k_2 values which were obtained as 2.603 x10^{-3} g mg^{-1} min^{-1} for Pd^{2+} and 3.46 x 10^{-4} g mg^{-1} min^{-1} for Pt^{4+} determined from the nonlinear fittings, respectively (see Table 5.3). The data was further fit to the linear pseudo 1st and 2nd order kinetic models (see Figures 5.8(b) and (c)). The results showed a better fit of data to the 2nd order for both Pd^{2+} and Pt^{4+} adsorption by MIL-101(Cr)/ED-GA with the R^2 values of 0.9997 and 0.9918, respectively. This behaviour implies that the rate-limiting step is the chemisorption mechanism wherein, the removal of Pd^{2+} and Pt^{4+} ions from an aqueous solution is through physicochemical interaction with the surface of the MIL-101(Cr)/ED-GA [52][53]. The data was validated by fittings on the Weber and Morris intra-particle diffusion model given by Equation 5.19 [7].

$$q_t = k_i \ t^{0.5} + C \quad (5.19)$$

with k_i (g $mg^{-1}(min^{-1})^{0.5}$) and C (mg g^{-1}) denoting the rate constant measured and intercept associated with the thickness of the boundary layer, respectively. As depicted in Figure

5.8(d), the adsorption of both Pd^{2+} and Pt^{4+} ions by MIL-101(Cr)/ED-GA is controlled by two steps. Step one which is the intra-particle diffusion, it is the rate-limiting and is rapid for Pd^{2+} adsorption with k_i = 28.36 g $mg^{-1}(min^{-1})^{0.5}$than for Pt^{4+} where k_i = 19.04 g $mg^{-1}(min^{-1})^{0.5}$.

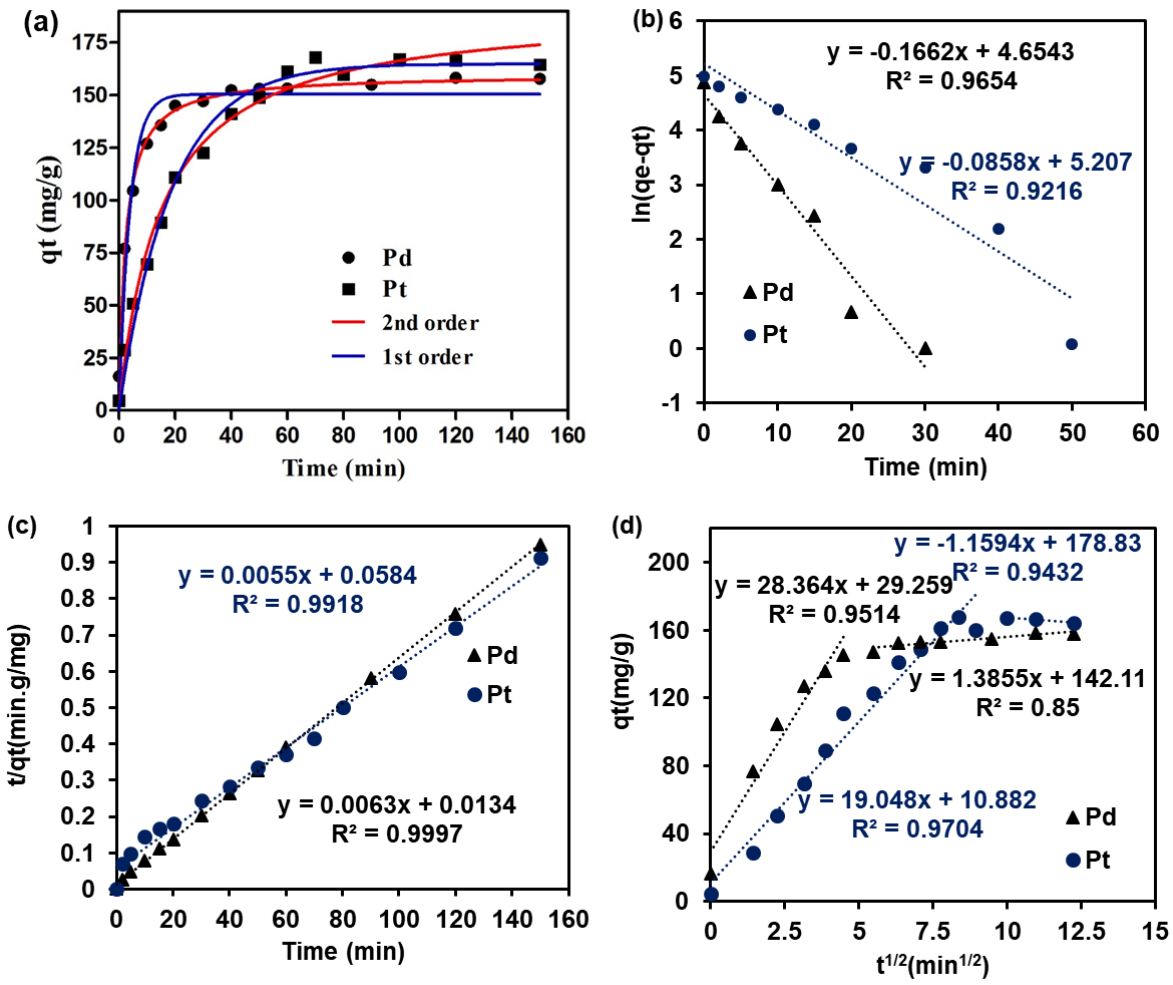

Figure 5.8: (a) Kinetics experimental data and nonlinear fittings. Linear fitting of Pd^{2+} and Pt^{4+} data to the pseudo (b) 1st –order and (c) 2nd order. (d) Intra-particle diffusion model.

Table 5.3: Kinetics data on the adsorption of Pd^{2+} and Pt^{4+} ions by MIL-101 (Cr)/ED-GA.

Kinetic models	**1st -order**		**2nd –order**	
	Pt^{4+}	**Pd^{2+}**	**Pt^{4+}**	**Pd^{2+}**
Linear				
q_e	182.5	105.0	181.8	158.7
k_1 or k_2	0.0858	0.1662	0.001415	0.006168
R^2	0.9216	0.9654	0.9918	0.9997
Non-linear				
Best-fit values				
q_e	165	150.5	191.5	159.9
k_1 or k_2	0.05371	0.2576	0.000346	0.002603
Std. Error				
q_e	2.795	3.247	4.437	2.329
k_1 or k_2	0.003425	0.03484	0.00003838	0.000308
95% Confidence				
q_e	158.9 to 171.0	143.3 to 157.6	181.9 to 201.1	154.8 to 165.0
k_1 or k_2	0.04631 to	0.1809 to	$2.6x10^{-4}$ to	$1.9x10^{-3}$ to
Goodness of fit				
Degrees of	13	11	13	11
R^2	0.9877	0.9509	0.989	0.9847
Absolute Sum of	528.1	1018	474	316.1
Sy.x	6.373	9.619	6.038	5.361
# of points analysed	15	13	15	13

5.3.3.4. Selectivity and Reusability tests

The selectivity of the adsorbent towards the targeted pollutant is a vital parameter in the adsorption process. For assessing the selectivity of the MIL-101(Cr)/ED-GA towards the uptake of Pd^{2+} and Pt^{4+} ions, the different molar ratios of Pd^{2+}/Pt^{4+} (25-100 mg/L) solutions were prepared and contacted with 0.02 g of MIL-101(Cr)/ED-GA at a pH of 3.5 and a temperature of 25 ^oC for 24 h. From the acquired results represented by Figure 5.9(a), MIL-101(Cr)/ED-GA showed the highest affinity towards the adsorption of Pd^{2+} than Pt^{4+}. The removal percentage of Pd^{2+} was still above 95 % after varying the concentration of Pt^{4+}. Conversely, the removal percentage of Pd^{2+} ions demonstrated a significant decrease with an increase in the amount of Pd^{2+}. These results suggest that MIL-101(Cr)/ED-GA is more selective towards the adsorption of Pd^{2+} ions than Pt^{4+} and they are in good correlation with the kinetics data which revealed fast kinetic of Pd^{2+} ions.

In addition to the ideal properties of the adsorbent material, another aspect to consider is the regeneration and the reusability of the adsorbent. The reusability of the MIL-101(Cr)/ED-GA adsorbent was investigated for 5 consecutive cycles and regeneration

was done using 6 M HCl. Figure 5.9(b) revealed that the removal percentage for Pd^{2+} and Pt^{4+} ions by MIL-101(Cr)/ED-GA decreased with an increase in the number of cycles. This may be attributed to the over-oxidation of the ED and glutaraldehyde chain leading to the disruption of the active sites [7]. However, the removal percentage was still above 70% from the 3rd to the 5th cycle on the adsorption of Pt^{4+}. For the adsorption of Pd^{2+} ions, the removal reduced to less than 70% starting from the 4th cycle. In addition to these preliminary results, the desorption procedure can further be investigated and improved to validate the potential utilisation of the prepared MIL-101(Cr)/ED-GA material.

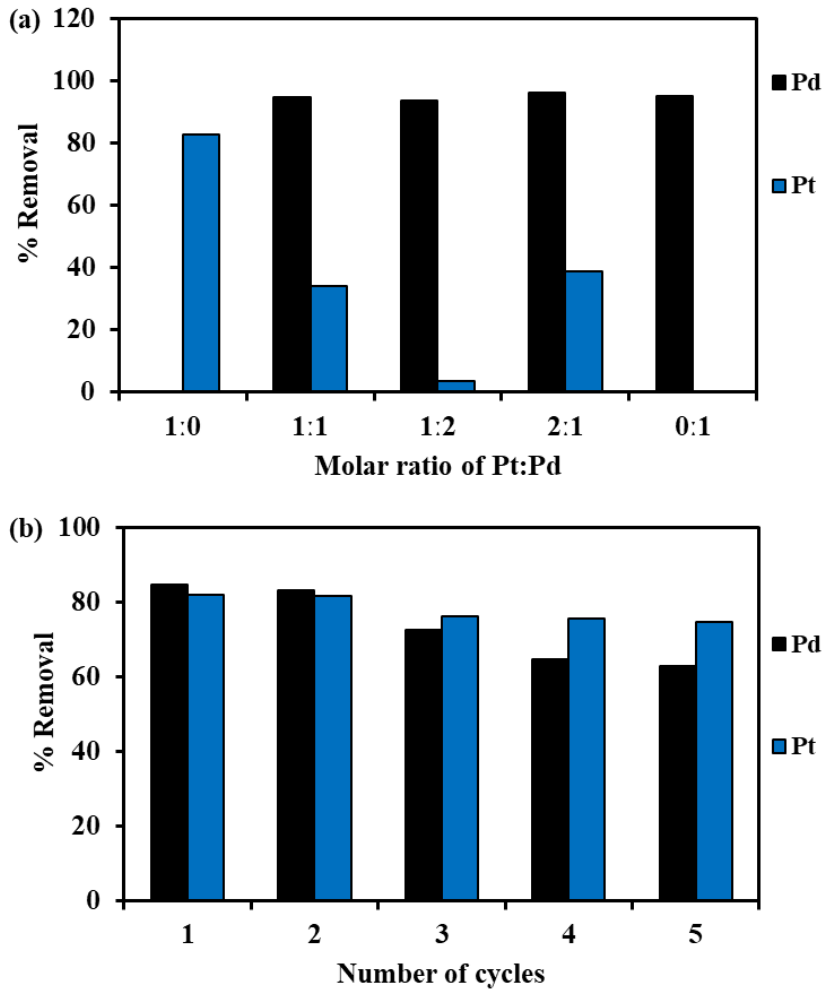

Figure 5.9: (a) Selectivity test of MIL-101(Cr)/ED-GA towards Pd^{2+} and Pt^{4+} adsorption. (b) Reusability of MIL-101(Cr)/ED-GA.

5.4. CONCLUSION

In this work, the focus was on synthesising MIL-101(Cr)/ED-GA to efficiently remove precious metal Pd^{2+} and Pt^{4+} ions from an aqueous solution. The successful synthesis of MIL-101(Cr)/ED-GA was confirmed by the FTIR with the appearance of the amide bond vibrations at 1554 and 1052 cm^{-1} owing to the interaction of ED and GA end. The results showed that more Pd^{2+} and Pt^{4+} ions were removable in acidic media whereby they exist as anion complexes. The isotherm data revealed that MIL-101(Cr)/ED-GA has a higher capacity for Pt^{4+} than Pd^{2+} with values of 416.17 and 322.6 mg/L, respectively. However, MIL-101(Cr)/ED-GA displayed higher affinity for Pd^{2+} since its removal % was more than 95%. Furthermore, the rate of Pd^{2+} adsorption by MIL-101(Cr)/ED-GA was more rapid and resulted in the high selectivity of the ions in the presence of Pt^{4+}. MIL-101(Cr)/ED-GA demonstrated great potential in terms of recovering both Pt^{4+} and Pd^{2+} from industrial wastewater and can serve as good support for Pd and Pt catalysts used for other applications such as hydrogen production.

5.5. REFERENCES

[1] J. M. Wasikiewicz, H. Mitomo, N. Seko, M. Tamada, and F. Yoshii, “Platinum and Palladium Ions Adsorption at the Trace Amounts by Radiation Crosslinked Carboxymethylchitin and Carboxymethylchitosan Hydrogels,” 2006, doi: 10.1002/app.

[2] A. N. Nikoloski, K. Ang, and D. Li, “Hydrometallurgy Recovery of platinum , palladium and rhodium from acidic chloride leach solution using ion exchange resins,” *Hydrometallurgy*, vol. 152, pp. 20–32, 2015, doi: 10.1016/j.hydromet.2014.12.006.

[3] M. Zhang, Y. Lv, Z. Xu, S. Wang, and J. Wang, “The Removal of Platinum Group Metals , Cs, Se, and Te from Nuclear Waste Glass Using Liquid Sb Extraction and Phase Separation Methods,” *Material*s, 13, 5305, 2020; doi:10.3390/ma13225305

[4] L. Yuanpei, Z. Wei, T. A. I. Zhigang, Y. Yaling, S. Jun, and L. I. Zonghao, “Cloud point extraction and flame atomic absorption spectrometry analysis of palladium , platinum , and gold ions from industrial polluted soil,” vol. 31, pp. 512–516, 2012, doi: 10.1007/s12598-012-0549-9.

[5] A. M. Yousif, “Recovery and Then Individual Separation of Platinum, Palladium , and Rhodium from Spent Car Catalytic Converters Using Hydrometallurgical Technique followed by Successive Precipitation Methods,” vol. 2019, 2019.

[6] A. T. N. Fajar, T. Hanada, and M. Goto, “Recovery of platinum group metals from a spent automotive catalyst using polymer inclusion membranes containing an ionic liquid carrier,” *J. Memb. Sci.*, vol. 629, p. 119296, 2021, doi: 10.1016/j.memsci.2021.119296.

[7] T. C. Maponya, K. E. Ramohlola, N. H. Kera, K. D. Modibane, A. Maity, L. M. Katata-Seru and M. J. Hato, “Influence of magnetic nanoparticles on modified polypyrrole/m-phenylediamine for adsorption of Cr(VI) from aqueous solution,” *Polymers (Basel).*, vol. 12, pp. 1–17, 2020, doi: 10.3390/polym12030679.

[8] Y. Göksungur, S. Üren, and U. Güvenç, “Biosorption of cadmium and lead ions by ethanol treated waste baker’s yeast biomass,” *Bioresour. Technol.*, vol. 96, pp.

103–109, 2005, doi: 10.1016/j.biortech.2003.04.002.

[9] R. Arora, “Adsorption of heavy metals-a review,” *Mater. Today Proc.*, vol. 18, pp. 4745–4750, 2019, doi: 10.1016/j.matpr.2019.07.462.

[10] A. Dąbrowski, “Adsorption - From theory to practice,” *Adv. Colloid Interface Sci.*, vol. 93, pp. 135–224, 2001, doi: 10.1016/S0001-8686(00)00082-8.

[11] K. Fujiwara, A. Ramesh, T. Maki, H. Hasegawa, and K. Ueda, “Adsorption of platinum(IV), palladium(II) and gold(III) from aqueous solutions onto L-lysine modified crosslinked chitosan resin,” vol. 146, pp. 39–50, 2007, doi: 10.1016/j.jhazmat.2006.11.049.

[12] A. Uheida, M. Iglesias, C. Fontàs, M. Hidalgo, and V. Salvadó, “Sorption of palladium(II), rhodium(III), and platinum(IV) on Fe_3O_4 nanoparticles,” vol. 301, pp. 402–408, 2006, doi: 10.1016/j.jcis.2006.05.015.

[13] C. A. Snyders, S. M. Bradshaw, G. Akdogan, and J. J. Eksteen, “Hydrometallurgy The effect of temperature , cyanide and base metals on the adsorption of Pt , Pd and Au onto activated carbon,” *Hydrometallurgy*, vol. 149, pp. 132–142, 2014, doi: 10.1016/j.hydromet.2014.07.012.

[14] O. E. Fayemi, A.S. Ogunlaja, P.F. Kempgens, E. Antunes, N. Torto, T. Nyokong, Z.R. Tshentu, “Adsorption and separation of platinum and palladium by polyamine functionalised polystyrene-based beads and nanofibers,” *Miner. Eng.*, vol. 53, pp. 256–265, 2013, doi: 10.1016/j.mineng.2013.06.006.

[15] S. Lin, J. K. Bediako, M. Song, and J. Kim, “ Effective recovery of Pt(IV) from acidic solution by a defective metal-organic frameworks using central,”, *ACS Sustainable Chem. Eng.* 2019, 7, 8, 7510–7518, doi: 10.1021/acssuschemeng.8b04637.

[16] M. D. Makhafola, K. D. Modibane, K. E. Ramohlola, Thabiso. C. Maponya, M. J. Hato, K. Makgopa, and E. I. Iwuoha “Palladinised graphene oxide-MOF induced coupling of Volmer and Heyrovsky mechanisms, for the amplification of the electrocatalytic efficiency of hydrogen evolution reaction,” *Sci. Rep.*, vol. 11, pp. 1–16, 2021, doi: 10.1038/s41598-021-96536-9.

[17] G. R. Monama, M. J. Hato, K. E. Ramohlola, T. C. Maponya, S. B. Mdluli, K. M. Molapo, K. D. Modibane, E. I. Iwuoha, K. Makgopa, M. D. Teffu “Hierarchiral 4-tetranitro copper(II)phthalocyanine based metal organic framework hybrid composite with improved electrocatalytic efficiency towards hydrogen evolution reaction,” *Results Phys.*, vol. 15, p. 102564, 2019, doi: 10.1016/j.rinp.2019.102564.

[18] G. Mashao, K. E. Ramohlola, S. B. Mdluli, G. R. Monama, M. J. Hato, K. Makgopa, K. M. Molapo, M. E. Ramoroka, E. I. Iwuoha, K. D. Modibane, “Zinc-based zeolitic benzimidazolate framework/polyaniline nanocomposite for electrochemical sensing of hydrogen gas,” *Mater. Chem. Phys.*, 2019, doi: 10.1016/j.matchemphys.2019.03.079.

[19] T. E. Mabokela, T. R. Somo, T. C. Maponya, M. J. Hato, E. Makhado, K. Makgopa , K. D. Modibane, “Dynamic carbon dioxide uptake capacity of metal organic framework using thermogravimetrical evaluation at different CO_2 pressure,” *Mater. Lett.*, vol. 317, p. 132086, 2022, doi: 10.1016/j.matlet.2022.132086.

[20] Y. Sun, L. Zheng, Y. Yang, X. Qian, T. Fu, and X. Li, “Metal – Organic Framework Nanocarriers for Drug Delivery in Biomedical Applications,” *Nano-Micro Lett.*, vol. 12, no. 1, pp. 1–29, 2020, doi: 10.1007/s40820-020-00423-3.

[21] D. M. Teffu, M. E. Ramoroka, M. D. Makhafola, K. Makgopa, T. C. Maponya, O. A. Seerane, M. J. Hato, E. I. Iwuoha, K. D. Modibane, “Electrochimica Acta High-performance supercabattery based on reduced graphene oxide / metal organic framework nanocomposite decorated with palladium nanoparticles,” *Electrochim. Acta*, vol. 412, p. 140136, 2022, doi: 10.1016/j.electacta.2022.140136.

[22] J. Tang, Y. Chen, S. Wang, D. Kong, and L. Zhang, “Highly efficient metal-organic frameworks adsorbent for Pd(II) and Au(III) recovery from solutions : Experiment and mechanism,” *Environ. Res.*, vol. 210, p. 112870, 2022, doi: 10.1016/j.envres.2022.112870.

[23] S. Lin, Y. Zhao, J. K. Bediako, C. Cho, and A. K. Sarkar, “Structure-controlled recovery of palladium(II) from acidic aqueous solution using metal-organic frameworks of MOF-802 , UiO-66 and MOF-808,” *Chem. Eng. J.*, vol. 362, pp. 280–

286, 2019, doi: 10.1016/j.cej.2019.01.044.

[24] K. Leng, Y. Sun, X. Li, S. Sun, and W. Xu, “Rapid Synthesis of Metal-Organic Frameworks MIL-101(Cr) Without the Addition of Solvent and Hydro fluoric Acid,” vol. 101, 2016, doi: 10.1021/acs.cgd.5b01696.

[25] A. D. Burrows, D. Jiang, L. L. Keenan, A. D. Burrows, and K. J. Edler, “Synthesis and post-synthetic modification of MIL-101(Cr)-NH_2 via a tandem diazotisation process w,” vol. 48, pp. 99–102, 2012, doi: 10.1039/c2cc36344e.

[26] J. Ren, X. Dyosiba, N. M. Musyoka, H. W. Langmi, B. C. North, M. Mathe, and M. S. Onyango, “Green synthesis of chromium-based metal-organic framework (Cr-MOF) from waste polyethylene terephthalate (PET) bottles for hydrogen storage applications,” *Int. J. Hydrogen Energy*, vol. 41, pp. 18141–18146, 2016, doi: 10.1016/j.ijhydene.2016.08.040.

[27] X. Luo, T. Shen, L. Ding, W. Zhong, and J. Luo, “Novel thymine-functionalised MIL-101 prepared by post-synthesis and enhanced removal of Hg 2 + from water,” *J. Hazard. Mater.*, vol. 306, pp. 313–322, 2016, doi: 10.1016/j.jhazmat.2015.12.034.

[28] L. Wang, X. Zhao, J. Zhang, and Z. Xiong, “Selective adsorption of Pb (II) over the zinc-based MOFs in aqueous solution-kinetics , isotherms , and the ion exchange mechanism,” pp. 14198–14206, 2017, doi: 10.1007/s11356-017-9002-9.

[29] X. Luo, L. Ding, and J. Luo, “Adsorptive removal of Pb(II) ions from aqueous samples with amino-functionalisation of metal-organic frameworks MIL-101(Cr),” *J. Chem. Eng. Data*, vol. 60, pp. 1732–1743, 2015, doi: 10.1021/je501115m.

[30] C. R. Lim, S. Lin, and Y. S. Yun, “Highly efficient and acid-resistant metal-organic frameworks of MIL-101(Cr)-NH_2 for Pd(II) and Pt(IV) recovery from acidic solutions: Adsorption experiments, spectroscopic analyses, and theoretical computations,” *J. Hazard. Mater.*, vol. 387, no. November 2019, p. 121689, 2020, doi: 10.1016/j.jhazmat.2019.121689.

[31] E. Ragheb, M. Shamsipur, F. Jalali, and F. Mousavi, “Modified magnetic-metal organic framework as a green and efficient adsorbent for removal of heavy metals,”

J. Environ. Chem. Eng., vol. 10, p. 107297, 2022, doi: 10.1016/j.jece.2022.107297.

[32] M. Sha, M. Sheikh, A. Rashidi, and A. Samimi, “Synthesis and adsorption performance of a modi fi ed micro-mesoporous MIL-101(Cr) for VOCs removal at ambient conditions,” vol. 341, pp. 164–174, 2018, doi: 10.1016/j.cej.2018.02.027.

[33] M. Abroudi, A. Tadjarodi, Z. Rezvani, and A. Mollahosseini, S. M. S. Ahmadian, “Synthesis and characterisation of Pd nanoparticles anchored on MIL 101(Cr) as a novel and recyclable catalyst for the Suzuki cross-coupling reactions,” Microporous and Mesoporous Materials 331 (2022) 111599.

[34] N. Zhuo, Y. Lan, W. Yang, Z. Yang, X. Li, X. Zhou, Y. Liu, J. Shen, X. Zhang, “Adsorption of three selected pharmaceuticals and personal care products (PPCPs) onto MIL-101(Cr)/natural polymer composite beads,” *Sep. Purif. Technol.*, vol. 177, pp. 272–280, 2017, doi: 10.1016/j.seppur.2016.12.041.

[35] A. Modrow, D. Zargarani, R. Herges, and N. Stock, “Introducing a photo-switchable azo-functionality inside Cr-MIL-101-NH_2 by covalent post-synthetic modification,” *Dalt. Trans.*, vol. 41, pp. 8690–8696, 2012, doi: 10.1039/c2dt30672g.

[36] H. Jalayeri, P. Aprea, D. Caputo, A. Peluso, and F. Pepe, “Synthesis of amino-functionalised MIL-101(Cr) MOF for hexavalent chromium adsorption from aqueous solutions,” *Environ. Nanotechnology, Monit. Manag.*, vol. 14, p. 100300, 2020, doi: 10.1016/j.enmm.2020.100300.

[37] T. K. Vo, W. S. Kim, and J. Kim, “Ethylenediamine-incorporated MIL-101(Cr)-NH_2 metal-organic frameworks for enhanced CO2 adsorption,” *Korean J. Chem. Eng.*, vol. 37, pp. 1206–1211, 2020, doi: 10.1007/s11814-020-0548-8.

[38] E. Sert, Y. Esra, and F. S. Atalay, “Preparation and performance of functionalised metal organic framework , MIL-101 , for Knoevenagel reaction,” *J. Sol State Chemistry,* vol. 283, 2020, doi: 10.1016/j.jssc.2019.121138.

[39] L. R. K. T. Jacob, Shubhra Raj, “Vegard ’ s law : a fundamental relation,” *Int. J. Mater. Res.*, vol. 98, pp. 776–779, 2007.

[40] T. R. Somo, M. W. Davids, M. V Lototskyy, M. J. Hato, and K. D. Modibane,

“Improved Hydrogenation Kinetics of TiMn1.52 Alloy Coated with Palladium through Electroless Deposition,” *Materials* 2021, 14, 1833. https://doi.org/10.3390/ma14081833

[41] Z. Hasan, E. J. Choi, and S. H. Jhung, “Adsorption of naproxen and clofibric acid over a metal–organic framework MIL-101 functionalised with acidic and basic groups,” *Chem. Eng. J.*, vol. 219, pp. 537–544, 2013, doi: 10.1016/j.cej.2013.01.002.

[42] T. Hu. S. He, S. Shan, H. Su, Y. Zhi, L.He “Novel functionalised metal-organic framework MIL-101 adsorbent for capturing oxytetracycline,” *J. Alloys Compd.*, vol. 727, pp. 114–122, 2017, doi: 10.1016/j.jallcom.2017.08.116.

[43] H. Jalayeri, P. Aprea, D. Caputo, A. Peluso, and F. Pepe, “Synthesis of amino-functionalised MIL-101(Cr) MOF for hexavalent chromium adsorption from aqueous solutions,” *Environ. Nanotechnology, Monit. Manag.*, vol. 14, p. 100300, 2020, doi: 10.1016/j.enmm.2020.100300.

[44] C. Lim, S. Lin, and Y. Yun, “Highly efficient and acid-resistant metal-organic frameworks of MIL- 101(Cr)-NH_2 for Pd(II) and Pt(IV) recovery from acidic solutions : Adsorption experiments, spectroscopic analyses, and theoretical computations,” *J. Hazard. Mater.*, vol. 387, p. 121689, 2020, doi: 10.1016/j.jhazmat.2019.121689.

[45] S. Wang, T. Vincent, J. C. Roux, C. Faur, E. Guibal, “Pd(II) and Pt(IV) sorption using alginate and algal-based beads,” *Chem. Eng. J.*, vol. 313, pp. 567–579, 2017, doi: 10.1016/j.cej.2016.12.039.

[46] L. Zhou, J. Xu, X. Liang, and Z. Liu, “Adsorption of platinum (IV) and palladium (II) from aqueous solution by magnetic cross-linking chitosan nanoparticles modified with ethylenediamine,” *J. Hazard. Mater.*, vol. 182, pp. 518–524, 2010, doi: 10.1016/j.jhazmat.2010.06.062.

[47] Q. Fumihiko and N. Kawasaki, “Adsorption of Pt(IV) and Pd(II) by calcined dried aluminum hydroxide gel from aqueous solution system,” *J. Environ. Chem Eng.*,

pp. 1–7, 2013, doi: 10.1016/j.jece.2013.08.011.

[48] H. Ma, X. Liao, X. Liu, and B. Shi, “Recovery of platinum (IV) and palladium(II) by bayberry tannin immobilized collagen fiber membrane from water solution,” vol. 278, pp. 373–380, 2006, doi: 10.1016/j.memsci.2005.11.022.

[49] N. Jalilian, H. Ebrahimzadeh, and A. A. Asgharinezhad, “Extraction and determination of trace amounts of gold (III), palladium (II), platinum (II) and silver (I) with the aid of a magnetic nanosorbent made from Fe_3O_4 -decorated and silica-coated graphene oxide modified with a polypyrrole-polythiophe,” Microchim Acta,pp. 2191–2200, 2017, doi: 10.1007/s00604-017-2170-y.

[50] M. Chen, S. Li, C. Jin, M. Shao, Z. Huang, and X. Xie, “Removal of metal-cyanide complexes and recovery of Pt(II) and Pd(II) from wastewater using an alkali – tolerant metal-organic resin,” *J. Hazard. Mater.*, vol. 406, p. 124315, 2021, doi: 10.1016/j.jhazmat.2020.124315.

[51] A. Ramesh, H. Hasegawa, W. Sugimoto, T. Maki, and K. Ueda, “Adsorption of gold (III), platinum(IV) and palladium(II) onto glycine modified crosslinked chitosan resin,” vol. 99, pp. 3801–3809, 2008, doi: 10.1016/j.biortech.2007.07.008.

[52] L. Zhou, J. Liu, and Z. Liu, “Adsorption of platinum(IV) and palladium(II) from aqueous solution by thiourea-modified chitosan microspheres,” *J. Hazard. Mater.*, vol. 172, pp. 439–446, 2009, doi: 10.1016/j.jhazmat.2009.07.030.

[53] D. Robati, “Pseudo-second-order kinetic equations for modeling adsorption systems for removal of lead ions using multi-walled carbon nanotube,” *J.Of Nanostructure in Chemistry,* 2013, 3:55 pp. 3–8.

CHAPTER SIX

SELECTIVE ADSORPTION OF PALLADIUM IONS FROM WASTEWATER BY ION-IMPRINTED MIL-101(Cr) DERIVED FROM WASTE POLYETHYLENE TEREPTHALATE: ISOTHERMS AND KINETICS

6.1. INTRODUCTION

Over the years, the recovery and removal of palladium ions from wastewater has become very vital due to the economic value and scarcity of this precious metal [1][2]. Furthermore, because palladium (Pd) and its compounds have no biological role, their release into the environment is considered toxic and carcinogenic [3][4]. The consequences of these compounds have led to the development of various methods to recover and remove Pd ions from wastewater. Adsorption technology has been identified as the promising technique for the uptake of Pd^{2+} ions from wastewater as compared to ion exchange, membrane separation, and chemical precipitation [5]. The process occurs when gaseous or liquid solutes (atoms, ions, or molecules) adhere to the surface of a solid or a liquid referred to as the adsorbent resulting in the formation of a molecular or atomic film called the adsorbate [6]. The advantages of this technique lie in its simplicity in design, low operational costs as well as high efficiency even at low pollutant concentrations. A number of studies have been undertaken to develop adsorbents that are highly efficient in removing the Pd ions from wastewater and cost-effective.

Metal-organic frameworks (MOFs) is a subgroup of polymer materials that is made through the self-assembly of metal ions and organic molecule [7]. The resulting 3-D structured MOF nanomaterials possess interesting physical and chemical properties which have led to their wide application in numerous industrial processes such as catalysis, separation, gas adsorption, energy storage, and wastewater treatment [7][8]. These highly porous coordination polymers have inner pore sizes and pore surfaces that can be fine-tuned for a specific application. In addition, they are less dense with large internal surfaces, high thermal stability as well as abundant active function [9]. Owing to their flexible surface functionality and porous structure, MOFs can permit guest molecules for instance metal ions to diffuse through the bulk material leading to the selectivity of the

guest molecule that may be adsorbed [10]. This property is ideal for the intake of Pd^{2+} ions from wastewater. In contrast, MOF based-adsorbents are suffering from instability in water, limited selectivity, and poor regeneration of the adsorbent after the adsorption cycle. Hence, this led to the necessity for further functionalisation of MOFs either via pre-synthesis or post-synthesis modification method. Preceding studies have displayed that modification of MOFs with various functional groups and other materials to form composites offers potential for the removal of heavy metals from wastewater.

Ion-imprinting technology is an attractive technology that offers a great opportunity in terms of improving the selectivity of targeted heavy metal ions from wastewater [11]. This technique allows the synthesis of tailor-made adsorbent materials with specific binding sites (i.e the size, charge, shape, and coordination geometry) for the metal ion of interest, resulting in higher adsorption capacity and fast kinetics as compared to their non-imprinted analogous [11]. Much research work from the literature mainly focuses on the use of a biopolymer named chitosan. For example, Lin *et al*. informed on the preparation of ion-imprinted chitosan fibre for the recovery of Pd^{2+} ions from wastewater. The interactions between the adsorbent and Pd^{2+} ions before and after uptake were established by analytical techniques. The Langmuir maximum adsorption capacity (q_m) was obtained as 326.9 mg/g, and was higher than the non-imprinted polymer (NIP). In another study conducted by Monier and co-workers, the chitosan resin was ion-imprinted using 2-aminobenzaldehyde to form a Schiff's base ligand for the recovery of Pd^{2+} ions. After modelling the equilibrium results, the Langmuir model gave the q_m value of 275 mg/g, whereas its NIP gave 114 mg/g [12]. Di Bello *et al*.[13] also synthesised Pd^{2+} ion-imprinted chitosan-based membrane (Pd-IAzoCsM) using azo-derivative ligand for the efficient removal of Pd^{2+} ions through the copolymerization process in the presence of an excess cross-linker. After fitting their data to different isotherm models, they obtained a q_m value of 101.6 mg/g for Pd-IAzoCsM and 80.0 mg/g for its NIP counterpart. Recently. Moa and co-workers prepared Pd^{2+} imprinted chitosan fibre (ICF) and investigated its selectivity and adsorption behaviour using column studies for the removal of Pd^{2+} ions. When compared to its analogous non-imprinted chitosan fibre, ICF exhibited higher selectivity adsorption for Pd^{2+} with the uptake of 112.4 mg/g and lower Pt^{4+} uptake of 11.9 mg/g in acidic solution [2].

To the greatest of our understanding, there are no literature surveys on IPMIL-101(Cr) for the selective recovery and removal of Pd^{2+} ions from wastewater. Hence, we report on the novel synthesis of Pd^{2+} ion-imprinted MIL-101(Cr) (IPMIL-101(Cr)) modified with ethylenediamine (ED), cross-linked with glutaraldehyde (GA) and imprinted on the glycylglycine chain for selective separation and recovery of Pd^{2+} ions from wastewater. The improved uptake capacity and selectivity test were investigated and compared with the non-imprinted MIL-101(Cr) (NIMIL-101(Cr)) by studying through batch adsorption experiments. The possible interactions of Pd^{2+} ions with the functional groups from the imprinted MIL-101(Cr) that resulted in the higher uptake capacity and selectivity were deduced from Fourier transform infrared (FTIR), with further support from SEM-EDS.

6.2. MATERIALS AND EXPERIMENTS

6.2.1. Materials

Chromium nitrate nanohydrate $Cr(NO_3)_3.9H_2O$, Sigma-Aldrich, 99.5%), ethylene glycol ($HOCH_2CH_2OH$, Sigma-Aldrich, 99.8%), sodium hydroxide (NaOH, Sigma-Aldrich, 99.8%), hydrochloric acid (HCl, Sigma-Aldrich, 99.8%), ethylenediamine ($C_2H_8N_2$, Sigma-Aldrich, 99.8%), glutaraldehyde ($C_5H_8O_2$, Sigma-Aldrich, 99.8%), glycylglycine (Rochelle chemicals, South Africa) and palladium chloride ($PdCl_2$, Rochelle chemicals, South Africa) were acquired and used without further purification. Waste PET water bottles were collected from the University of Limpopo dining Hall, 10 May 2022, Polokwane, South Africa. After the removal of the caps, rings, and labels, the cleaned bottle bodies were cut into small flakes with scissors.

6.2.2. Preparation of IPMIL-101(Cr) polymer and the NIMIL-101(Cr)

6.2.2.1. Synthesis and modification of MIL-101(Cr)

The synthesis of MIL-101(Cr) first involved the recycling of the PET waste to obtain the terephthalic acid (H_2BDC) which was used as the organic linker [14]. Following that, 1.66 g of H_2BDC was dispersed in deionised (DI) water together with $Cr(NO_3)_3.9H_2O$ (4.0 g). The reaction mixture was hydrothermally heated in a Teflon-lined autoclave reactor for 8 hours at 220 °C. The obtained precipitates were centrifuged and dried at 80 °C overnight. Subsequently, 0.5 g of the product was dispersed in a toluene solution containing 1 mL

of ED and refluxed at 90 °C overnight. The product was filtered and washed with an adequate amount of DI and ethanol and dried at ambient conditions for 24 hours. Crosslinking was achieved by using glutaraldehyde, wherein 0.5 g of MIL-101(Cr)/ED was suspended in 50 mL of glutaraldehyde solution and stirred at room temperature overnight. Then the product was filtered and dried at 70 °C for 24 hours.

6.2.2.2. IPMIL-101(Cr) polymer and NIMIL-101(Cr)

The preparation of IPMIL-101(Cr) was done by suspending the 0.33 g of glycylglycine in 50 mL of ethanol and then heated at 60 °C for 1 hour. This was followed by the addition of 10 mL of Pd ion template and the reaction mixture was kept under stirring for 2 hours at 60 °C. The reaction solution was further heated at 80 °C for evaporation until only 20 mL was remaining. Then 0.5 g of the MIL-101(Cr)/ED was introduced into the solution followed by heating at 60 °C under magnetic stirring for 12 hours. The obtained product was filtered and washed with DI prior to drying at 80 °C. Subsequently, the metal template was removed by stirring the IPMIL-101(Cr) in 6M HCl solution for 24 hours. The obtained product was filtered and washed with an adequate amount of DI until no traces of Pd were detected and it was then dried at 80 °C. Similarly, the NIMIL-101(Cr) was prepared with the same procedure without the addition of the metal ion template.

6.2.3. Characterisation

X-ray diffraction (XRD) patterns for phase identification of the MIL-101(Cr), IPMIL-101(Cr), and NIMIL-101(Cr) composites were conducted using a Bruker Advance powder diffractometer (Madison, USA; 40 mA, 40 keV, λCu-K=0.15406 nm. Morphological, elemental analysis and mapping were obtained from the field-emission scanning electron microscopy (FE-SEM) (Auriga Cobra focused-ion beam FIB-SEM, Carl Zeiss, Jena, Germany) coupled with EDS. The Brunauer–Emmet–Teller (BET) surface area and pore volume measurements of the prepared MIL-101(Cr), IPMIL-101(Cr), and NIMIL-101(Cr) composites were deduced using a Tristar micromeritics instrument by using low-pressure nitrogen (77 K) adsorption/desorption technique. The presence of functional groups and composite formation was confirmed by Cary 600 series FTIR spectrometer (Spectrum II PerkinElmer). The thermal properties of MIL-101(Cr), IPMIL-101(Cr), and NIMIL-101(Cr)

were obtained from a PerkinElmer STA 6000 instrument connected to a PolyScience digital temperature controller under N_2 gas purged at a flow rate of 20 mL.min^{-1}.

6.2.4. Adsorption of Pd^{2+} from aqueous solution

The investigations on the adsorption of Pd^{2+} by IPMIL-101(Cr) and NIMIL-101(Cr) materials were conducted in batch mode. To examine the influence of pH, 100 mg/L of Pd^{2+} (50 mL) was adjusted using different concentrations of HCl and NaOH to obtain pH values between 1.0-6.0. The effect of IPMIL-101(Cr) and NIMIL-101(Cr) dosage experiments were conducted by varying the amount from 0.01-0.07 g. Studies on the effects of initial concentrations on the removal of Pd^{2+} by IPMIL-101(Cr) and NIMIL-101(Cr) were done from 50-400 mg/L with a constant dose of 30 mg for both Pd-IMIL-101(Cr) and NIMIL-101(Cr) materials. The effect of contact time was assessed by varying the time between 0-90 minutes at selected time intervals. All the experiments were conducted using a 100 mL plastic bottle which was placed in a temperature-controlled water bath shaker set at 25 °C and 160 rpm. After the systems have reached equilibrium, the IPMIL-101(Cr) and NIMIL-101(Cr) adsorbents were separated from the mother liquor using syringe filters (0.45 µm). The supernatants were analysed using ultraviolet-visible (UV-Vis) spectroscopy (Lambda 365 UV/Vis Spectrophotometer, PerkinElmer, Johannesburg, South Africa) to quantify the remaining Pd^{2+} ions in the solution. The removal efficiencies of the IPMIL-101(Cr) and NIMIL-101(Cr) adsorbents were calculated in percentages from Equation 6.1:

$$\%removal = \left(\frac{Co-Ce}{Co}\right) X \;\; 100 \qquad (6.1)$$

with C_o and C_e representing the initial and equilibrium concentrations of Pd^{2+} in mg/L. The adsorption capacity of the IPMIL-101(Cr) and NIMIL-101(Cr) after reaching equilibrium was determined from the below Equation 6.2:

$$q_e = \left(\frac{Co-Ce}{m}\right) \; V \qquad (6.2)$$

where q_e is the amount of Pd^{2+} adsorbed at equilibrium per unit mass of adsorbent (mg/g), m (g) is the mass of the adsorbent, and V (L) is the volume of the metal ion solution. The influence of co-existing ions on the adsorption of Pd^{2+} by IPMIL-101(Cr) and NIMIL-

101(Cr) was investigated using selected cations including Pt^{4+}, Co^{2+}, Ni^{2+}, Ag^{+} and anions of PO_4^{3-}, SO_4^{2-}, NO_3^{-}, CO_3^{-} and Cl^{-} with the molar ratio of 1:1 on 50 mg/L of Pd^{2+}. The experiments on the reusability of the IPMIL-101(Cr) and NIMIL-101(Cr) adsorbents were conducted by regenerating the prepared adsorbent by stirring in a solution containing 0.01M of thiourea and 1M HCl for 24 hours. This was followed by thorough washing with DI and drying at 60 °C prior to the subsequent cycle.

6.3. RESULTS AND DISCUSSION

6.3.1. Physical Characterisation

The structural chemical properties of the manufactured IPMIL-101(Cr), and NIMIL-101(Cr) with reference to MIL-101(Cr) were identified using FTIR. Figure 6.1 represents the spectrum for the MIL-101(Cr), which correlates well with that reported in the literature by showing the presence of C=O and C-O at 1510 and 1414 cm^{-1} attributing to the bonding in the carboxylates [15]. In addition, the C=C bonding of benzene ring and Cr-O vibration were observed at 1631 and 674 cm^{-1}. These observations suggest the successful preparation of MIL-101(Cr). After surface post-modifications, the spectra of the IPMIL-101(Cr) and NIMIL-101(Cr) revealed new peak at 1553 cm^{-1} which is due to the N-H stretching of the aliphatic groups. Another new peak which is due to the Cr-N vibration was observed at 506 cm^{-1}. The NIMIL-101(Cr) spectrum showed an addition of new peaks at 1370 and 1052 cm^{-1} attributed to the C-N and C-N-C vibrations of the amide bond, whereas the IPMIL-101(Cr) revealed the vibration due to the C=N at 1677 cm^{-1}. Furthermore, the spectrum of Pd-loaded IPMIL-101(Cr) was obtained and compared with the IPMIL-101(Cr) and Pd-IPMIL-101(Cr). The results revealed that all the characteristic peaks were similar to those observed on the NIPMIL-101(Cr). The observations indicate that the removal of the template converted the vibration of C-N-C of amide bond to the vibration of C=N.

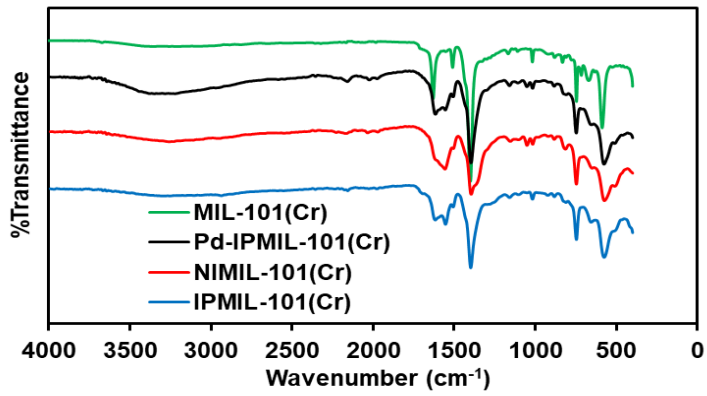

Figure 6.1: FTIR spectra of MIL-101(Cr), Pd-IPMIL-101(Cr), IPMIL-101(Cr), and NIMIL-101(Cr).

The XRD patterns of the prepared MIL-101(Cr), IPMIL-101(Cr), and NIMIL-101(Cr) are presented in Figure 6.2. The diffraction pattern for Pd-IPMIL-101(Cr) was also included in order to compare with the IPMIL-101(Cr) by investigating the effect of removing the template metal from sample structure. All the prepared materials revealed similar peaks between 5.68-12.11^{o} and 16.10-18.23^{o} which correspond to the characteristics diffraction peaks of MIL-101(Cr) [16][17][18]. However, the peaks showed some broadening when compared to those in MIL-101(Cr) confirming the successful synthesis of the Pd-IPMIL-101(Cr), IPMIL-101(Cr), and NIMIL-101(Cr). Furthermore, the lattice parameters and the crystallinity of the prepared samples were calculated and the results are shown in Table 6.1. The obtained values showed a decrease in the crystallinity of MIL-101(Cr) from 96.6% to 70.6 and 73.0% upon formation of the PdIPMIL-101(Cr) and NIMIL-101(Cr). In addition, the IPMIL-101(Cr) showed an increase in crystallinity of 1.4% suggesting that the Pd template has been successfully removed. The crystallite size as determined from the Debye-Scherrer [19] equation revealed that the ordering of the MIL-101(Cr) structure was reduced significantly due to the functionalisation with the amorphous nature of the chelating ligands. However, this change has no adverse effect on the framework of the MIL-101(Cr) as the d-spacing of the prepared Pd-IPMIL-101(Cr), IPMIL-101(Cr) and NIMIL-101(Cr) showed no significant decrease proving that the characteristic planes are still intact within the prepared materials.

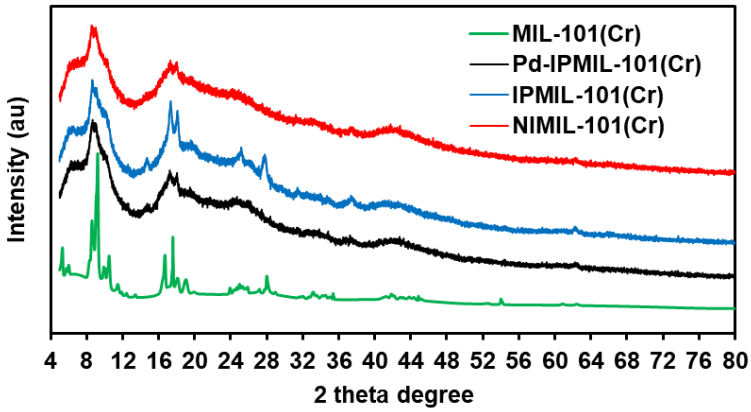

Figure 6.2: XRD patterns of MIL-101(Cr), Pd-IPMIL-101(Cr), IPMIL-101(Cr), and NIMIL-101(Cr).

Table 6.1: XRD data of the MIL-101(Cr), Pd-IPMIL-101(Cr), IPMIL-101(Cr), and NIMIL-101(Cr).

Sample	**Lattice parameters a=b=c (Å)**	**Crystallinity (%)**	***D*** **(nm)**	***d*-spacing (Å)**
MIL-101(Cr)	86.1	96.9	796.72	16.6
Pd-IPMIL-101(Cr)	62.8	70.6	11.38	12.1
IPMIL-101(Cr)	64.0	72.0	8.13	12.3
NIMIL-101(Cr)	64.9	73.0	5.94	12.5

The BET curves of the MIL-101(Cr), Pd-IPMIL-101(Cr), IPMIL-101(Cr), and NIMIL-101(Cr) were obtained in order to study the porosity of the prepared materials. As depicted in Figure 6.3(a-d), the N_2 adsorption-desorption isotherms for the MIL-101(Cr), Pd-IPMIL-101(Cr), IPMIL-101(Cr), and NIMIL-101(Cr) demonstrated a type-IV shape, which indicates the existence of mesoporous structures [20]. The MIL-101(Cr) showed to have a specific BET surface area of 308.73 $m^2.g^{-1}$ and pore volume of 0.1222 $cm^3.g^{-1}$. Whereas the ion imprinted technology indicates a drop in surface area and pore volume.

The IPMIL-101(Cr) showed an increase in specific BET surface area and pore volume of 8.7158 $m^2.g^{-1}$ and 0.026266 $cm^3.g^{-1}$, in comparison to its NIMIL-101(Cr) and Pd-IPMIL-101(Cr) counterparts (see Figure 6.3(d) and Table 6.2). There was an increase in pore size indicating successful ion imprinted and the Pd recognition sites were generated by the removal of the metal template.

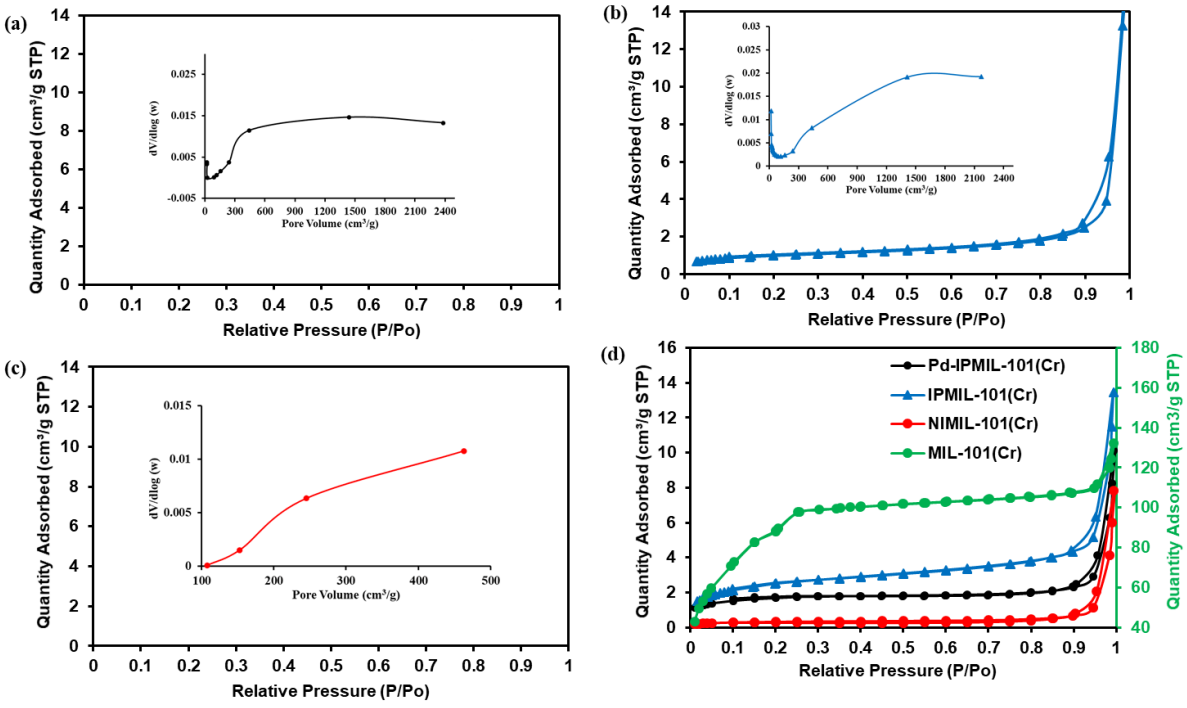

Figure 6.3: BET/Pore volume measurement of a) Pd-IPMIL-101(Cr), (b) IPMIL-101(Cr), and (c) NIMIL-101(Cr). BET comparison curves of Pd-IPMIL-101(Cr), IPMIL-101(Cr), and NIMIL-101(Cr).

Table 6.2: BET and pore volumes for PdIPMIL-101(Cr), IPMIL-101(Cr), and NIMIL-101(Cr).

Material	S_{BET} ($m^2.g^{-1}$)	Pore volume ($cm^3.g^-$	Pore size (Å)
MIL-101(Cr)	308.73	0.1222	35.693
Pd-IPMIL-101(Cr)	6.1702	0.019086	327.878
IPMIL-101(Cr)	8.7158	0.026266	155.079

NIMIL-101(Cr)	1.1344	0.012009	624.852

Figure 6.4(a–c) presents the thermal analysis of the Pd-IPMIL-101(Cr), IPMIL-101(Cr), and NIMIL-101(Cr) material, with a further comparison of their thermal behaviour as shown by Figure 6.4(d–f). The results demonstrated similar degradation behaviour on all the synthesised materials. The initial degradation step at approximately 100 °C is attributed to the weight loss due to water and other solvent moistures that were trapped within the mesoporous structures of the MIL-101(Cr), Pd-IPMIL-101(Cr), IPMIL-101(Cr), and NIMIL-101(Cr). With an increasing temperature, a second degradation step was observed between 120-480 °C and is the weight loss that resulted from the degradation of the polymer chain length [21], of the prepared materials as well as the framework of MIL-101(Cr) (Figure 6.4(d-f)). The DSC provided more information wherein an endothermic peak was observed at 100 °C for the loss of moisture with changes in enthalpy (ΔH) of 1.99, 3.61, 1.75 and 1.64 kJ g^{-1} for MIL-101(Cr), Pd-IPMIL-101(Cr), IPMIL-101(Cr), and NIMIL-101(Cr) material. Furthermore, the Pd-IPMIL-101(Cr), IPMIL-101(Cr), and NIMIL-101(Cr) revealed endothermic peaks at 480, 520, and 570 °C. These peaks correspond to the decomposition of the chelating polymer chain and the collapse of the MIL-101(Cr) structure. These results confirm that the prepared materials have similar structures with an improvement of the thermal stability. In addition, the Pd-IPMIL-101(Cr), IPMIL-101(Cr), and NIMIL-101(Cr) material were further characterized with SEM for morphological analysis.

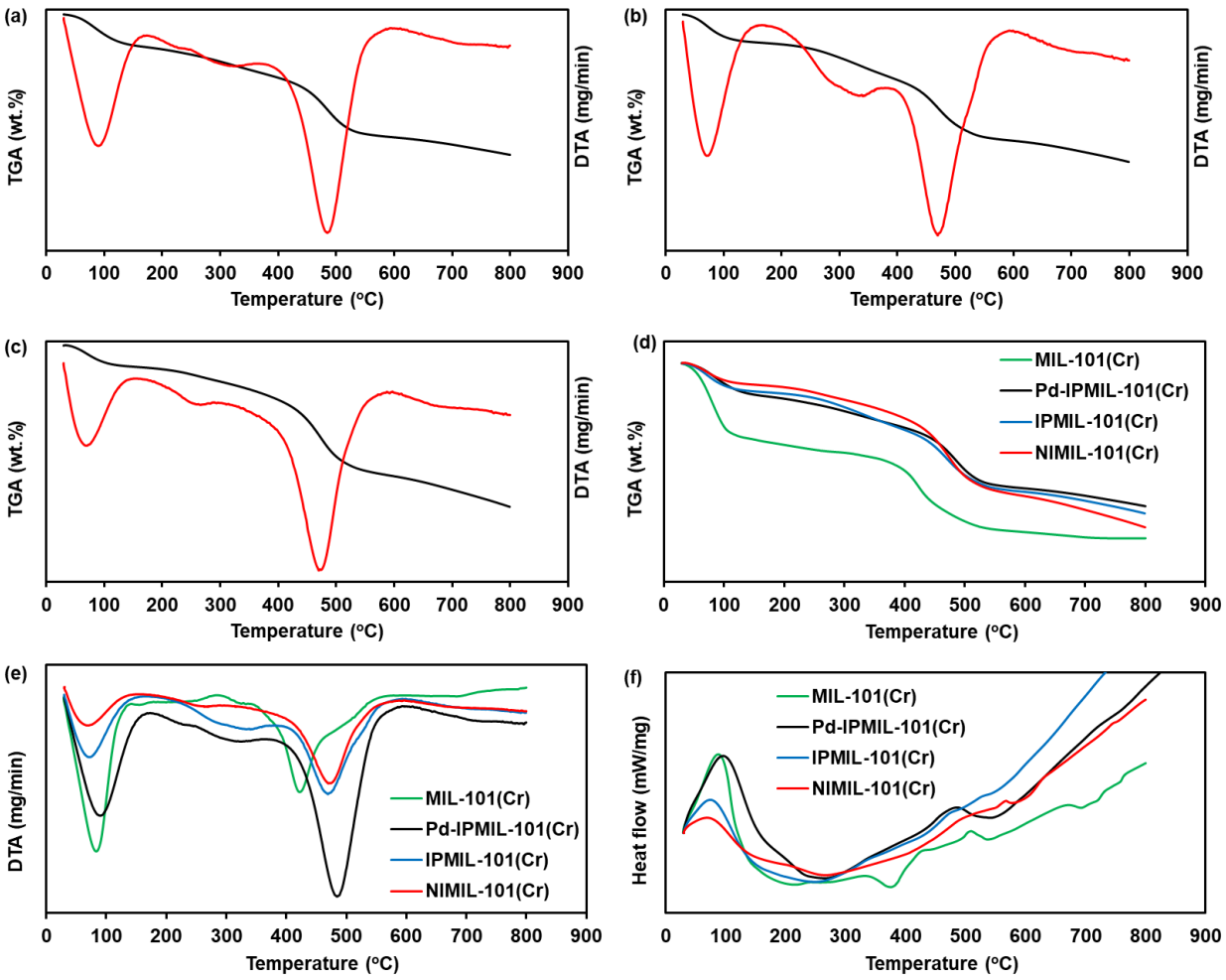

Figure 6.4: TGA/DTA curves of (a) Pd-IPMIL-101(Cr), (b) IPMIL-101(Cr) and (c) NIMIL-101(Cr). (d)TGA, (e) DTA, and (f) DSC of Pd-IPMIL-101(Cr), IPMIL-101(Cr), and NIMIL-101(Cr).

6.3.2. Morphological Analyses

Figure 6.5 presents the morphology, particle size distribution, and EDS data for the Pd-IPMIL-101(Cr), IPMIL-101(Cr), and NIMIL-101(Cr). The SEM image of Pd-IPMIL-101(Cr) in Figure 6.5(a), showed the presence of octahedral structures with rougher surfaces with more particles of 120-200 nm. In addition, the EDS data deduced the composition of the sample showing the presence of C, O, Cr, and Cl as well as the presence of Pd having only 0.1 atomic weight percent (At%) (the Al element was from the SEM preparation

procedure) (see Figures 6.5(a-c)). Upon the removal of the template Pd metal ion, the structure of the IPMIL-101(Cr) in Figure 6.5(b-f), possessed a mixture of highly agglomerated octahedral and rod-like structures having rough surfaces with the majority of the particles being within the 100-120 nm scale. Moreover, the EDS results confirmed the absence of the Pd template by showing no detection indicating that the template was successfully removed (see Figures 6.5(f)). The NIMIL-101(Cr) indicated similar morphology and particle size distribution as that of the Pd-IPMIL-101(Cr). However, the EDS results showed that 0.6 At.% of N was present which is attributed to the bonding nature of the chelating ligand in the NIMIL-101(Cr).

To further validate and support the results obtained from the EDS, the elemental composition mapping of the Pd-IPMIL-101(Cr) represented in Figure 6.6 was compared with the composition mapping of IPMIL-101(Cr) shown in Figure 6.7. The composition mapping images of Pd-IPMIL-101(Cr) show a high density of the C, O, Cr, and Pd which are evenly distributed on the surface of the material. Furthermore, the amount of N was also detected however it appears to be less dense and poorly distributed. This is due to the interaction of the Pd metal ions with the N atoms during chelation. In contrast, Figure 6.7(c) of the IPMIL-101(Cr) shows a highly dense and even distribution of the N after the removal of the template metal ion. These results confirm that Pd ions were successfully printed on the surface of the IPMIL-101(Cr).

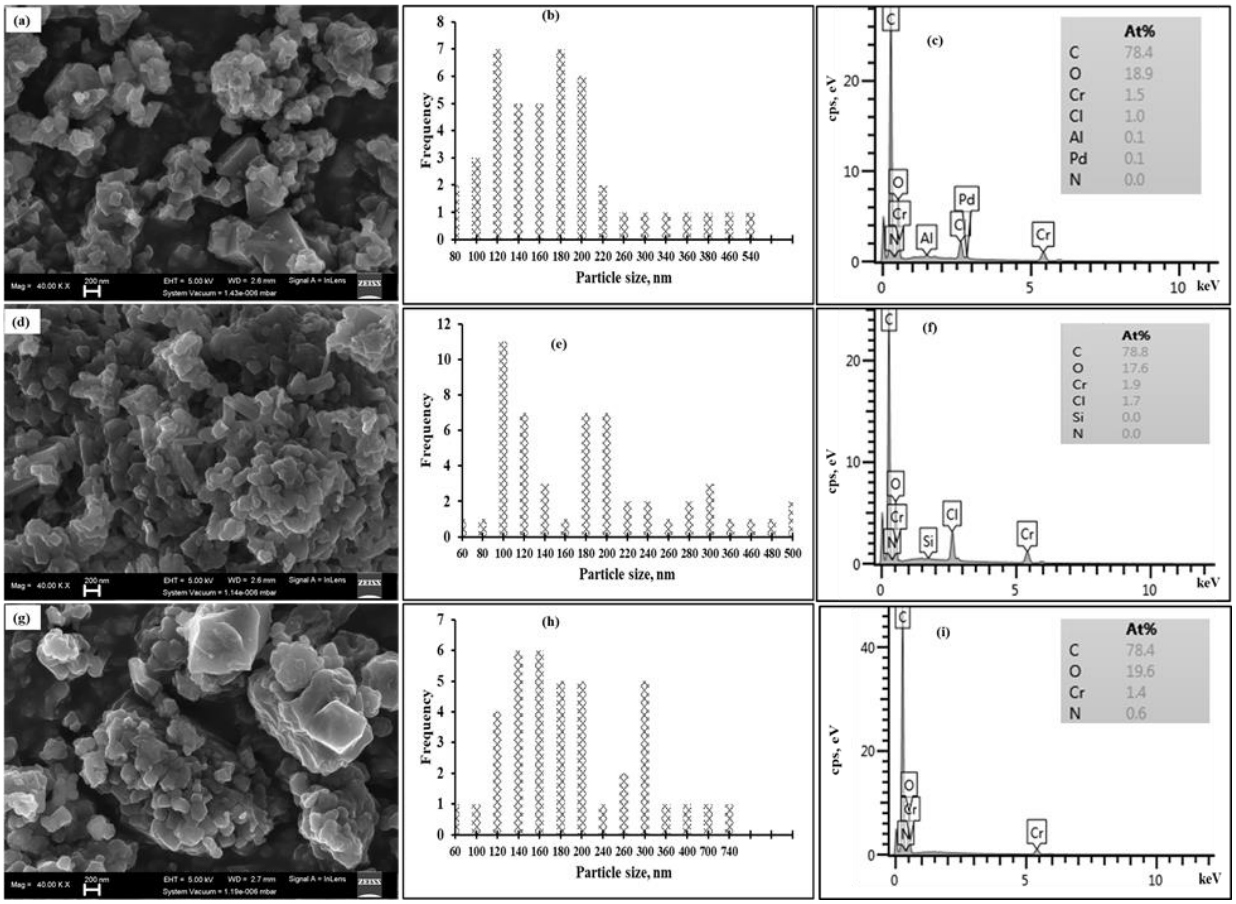

Figure 6.5: SEM image of (a) Pd-IPMIL-101(Cr), (d) IPMIL-101(Cr) and (g) NIMIL-101(Cr). Particles distribution of (b) Pd-IPMIL-101(Cr), (e) IPMIL-101(Cr) and (h) NIMIL-101(Cr). EDS spectra of (c) Pd-IPMIL-101(Cr), (f) IPMIL-101(Cr) and (f) NIMIL-101(Cr) (Inset: elemental analysis in atomic percentage).

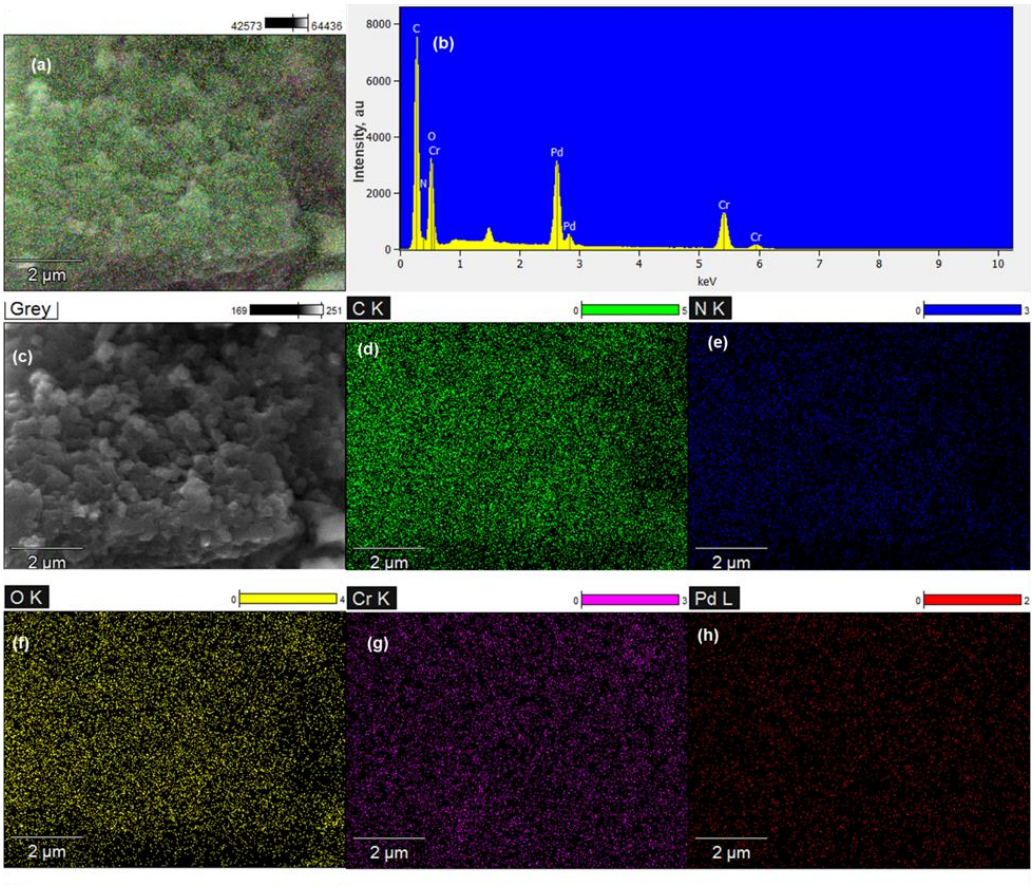

Figure 6.6: Elemental mapping of Pd-IPMIL-101(Cr), (a) light and (c) grey images, (b) EDS spectrum, and (d-h) mapping image of carbon, nitrogen, oxygen, chromium, and palladium elements.

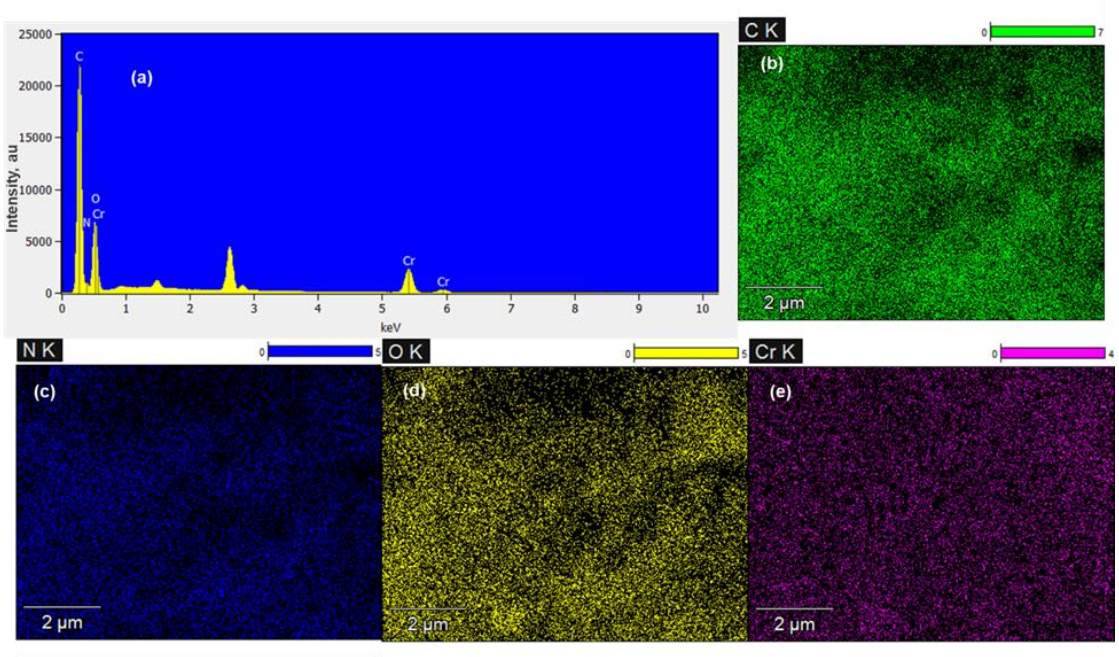

Figure 6.7: Elemental mapping of IPMIL-101(Cr), (a) EDS spectrum, (b-e) mapping image of carbon, nitrogen, oxygen, and chromium elements.

6.3.3. Batch Adsorption experiments

6.3.3.1. pH and dose effect

Figure 6.8(a) represents the investigation of the effect of pH on the removal of Pd^{2+} ions by IPMIL-101(Cr) and NIMIL-101(Cr). The results demonstrated an increase in Pd^{2+} removal percentage (%R) with an increase in pH from 1.0-2.0, followed by a decline from 3.0-6.0. At a pH of 2.0, the IPMIL-101(Cr) showed the highest %R of 95.1% whereas the NIMIL-101(Cr) gave 84.4%. In general, the prevailing species of the Pd^{2+} ions in acidic media are the $[PdCl_3]^-$ and $[PdCl_4]^{2-}$ anions. The increase in pH from 1.0-2.0 causes a high degree of protonation on the nitrogen groups of the amide bond resulting in electrostatic interaction between Pd-chloro complex anions with positively charged surfaces of the as-synthesised adsorbents. At elevated pH, the protonation on the surfaces of the IPMIL-101(Cr) and NIMIL-101(Cr) is reduced and electrostatic repulsion between the anions occurs. However, the generated Pd^{2+} recognition sites on the IPMIL-101(Cr) surface provided the advantage of removing the metal ions even at increased pH. Hence, the IPMIL-101(Cr) adsorbent was still able to adsorb more than 80% of the Pd^{2+} ions. The point-of-zero charge (PZC) was obtained from the pH drift method in order

to determine the surface charge of the prepared IPMIL-101(Cr) and NIMIL-101(Cr) (See Figure 6.8(b)). The results revealed that the IPMIL-101(Cr) has a PZC at 2.0 and NIMIL-101(Cr) is 3.2. Below these values, the surfaces of the prepared adsorbents are positively charged, and hence an increasing %R removal was observed which is in good correlation with the pH. Furthermore, the FTIR spectra of the IPMIL-101(Cr) (Figure 6.8(c)) and NIMIL-101(Cr) (Figure 6.8(d)) were obtained after Pd^{2+} adsorption and compared with the one before adsorption. From both spectra, new peaks attributing to the N-H vibration, C=N stretching, and O-H band were observed at 1288, 1643, and 3500 cm^{-1}. These results confirm the N and O protonation of the amide group which is responsible for the electrostatic interaction with Pd^{2+} ions. Furthermore, the NIMIL-101(Cr) spectrum showed the disappearance of the C-N-C peak at 1052 cm^{-1} after Pd^{2+} adsorption. The effect of IPMIL-101(Cr) and NIMIL-101(Cr) dosage was investigated by varying the amount from 0.01-0.07g. As presented in Figure 6.9(a), the uptake of Pd^{2+} ions increased with an increasing adsorbent dosage and reached the optimum removal at a dosage of 0.04 g for both the IPMIL-101(Cr) and NIMIL-101(Cr). In addition, the IPMIL-101(Cr) showed better efficiency as the %R reached more than 86% in comparison to the NIMIL-101(Cr) which gave 80%. Figure 9(b) shows the adsorption capacity. There was a decrease in adsorption capacity with an increasing dose up to 0.04 g. The adsorption capacity showed to be high for IPMIL-101(Cr) and dropping for NIMIL-101(Cr) after 0.0 4 g of dosage.

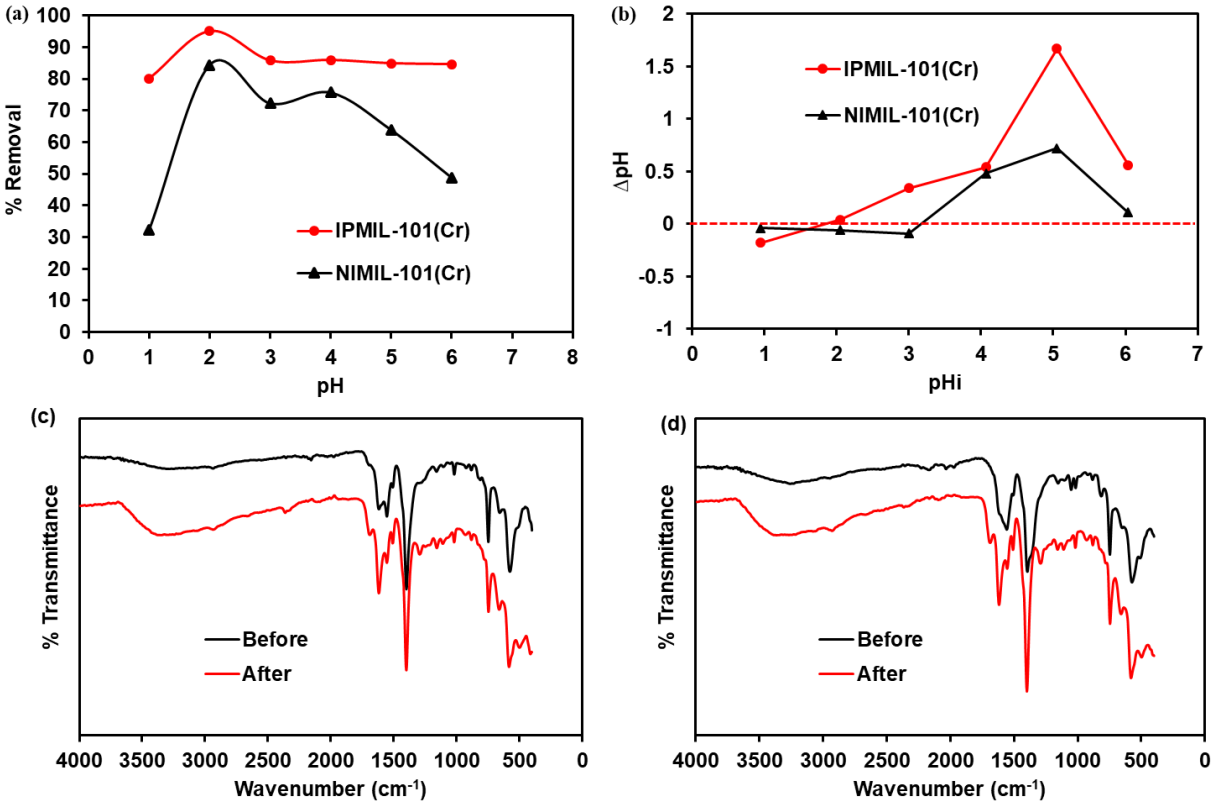

Figure 6.8: (a) Effect of initial solution pH on the removal of Pd^{2+} ions. (b) The point-of-zero charge for IPMIL-101(Cr) and NIMIL-101(Cr) adsorbents. FTIR spectra for (c) IPMIL-101(Cr) and (d) NIMIL-101(Cr) before and after adsorption.

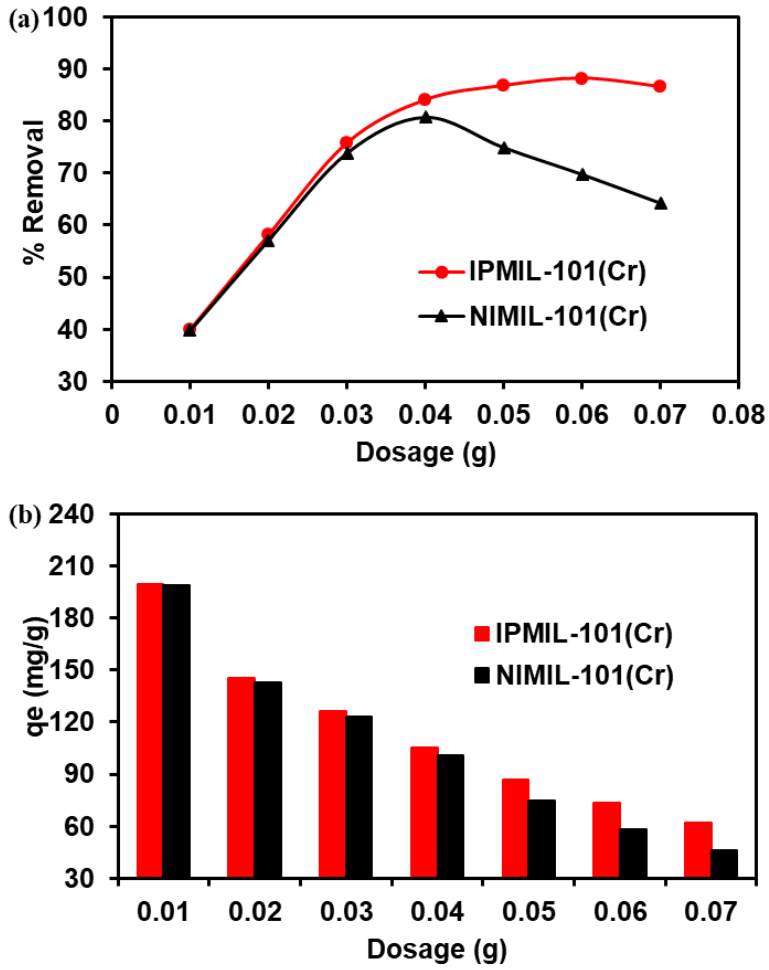

Figure 6.9: Comparison of the (a) Effect of IPMIL-101(Cr) and NIMIL-101(Cr) amount; and the (b) adsorption capacity.

6.3.3.2. Adsorption isotherms

The effects of Pd^{2+} ions concentration on the adsorption behaviour of IPMIL-101(Cr) and NIMIL-101(Cr) were used to obtain the adsorption isotherms as depicted in Figure 10(a). The results showed that the adsorption capacity of both the IPMIL-101(Cr) and NIMIL-101(Cr) increased with an increase in the initial concentration of Pd^{2+} ions solution. The data was fit to the non–linear Langmuir and Freundlich isotherm models in order to determine the mode of adsorption as described by the following Equations 6.3 and 6.4.

$$\frac{qe}{qm} = \frac{K_L C_e}{1+K_L C_e} \qquad (6.3)$$

$$qe = KFC_e^{1/n} \quad (6.4)$$

A better fit to the Langmuir isotherm was observed with the correlation coefficient (R^2) values of 0.9999 and 09998 for both the IPMIL-101(Cr) and NIMIL-101(Cr) in comparison to the Freundlich model which gave a 0.8677 and 0.94222. In addition, the linear isotherm models which are given by Equations 6.5 and 6.6 were also in good correlation with the non-linear isotherm model as shown in Figure 10(b and c) and Table 6.3. The linear Langmuir isotherm was used to calculate the maximum adsorption capacity (qm) of the IPMIL-101(Cr) and NIMIL-101(Cr), which were obtained as 185.2 and 175.4 $mg.g^{-1}$. These observations confirm the improved efficiency of the IPMIL-101(Cr) toward Pd^{2+} ions removal.

$$\frac{C_e}{q_e} = \frac{1}{qmK_L} + \frac{C_e}{qm} \quad (6.5)$$

$$\ln q_e = \ln K_F + \frac{1}{n} lnC_e \quad (6.6)$$

In addition, the q_m values of the IPMIL-101(Cr) and NIML-101(Cr) towards Pd^{2+} ions from the nonlinear form of the Langmuir isotherm model were 193.2 mg/g and 177.7 mg/g. These results show that IPMIL-101(Cr) has a higher affinity for Pd^{2+} uptake as the value is higher than NIMIL-101(Cr) and those reported in the literature as shown in Table 6.4. The dimensionless separation factor R_L, which is another significant parameter relating to the Langmuir isotherm model was determined using Equation 6.7 [22].

$$R_L = \frac{1}{1+K_L C_o} \quad (6.7)$$

The parameter is suggesting the favourability of the adsorption process if the values are between $0<R_L<$. As shown in Table 6.3, the calculated R_L values for both the IPMIL-101(Cr) and NIMIL-101(Cr) suggest that the adsorption of Pd^{2+} ions is favourable.

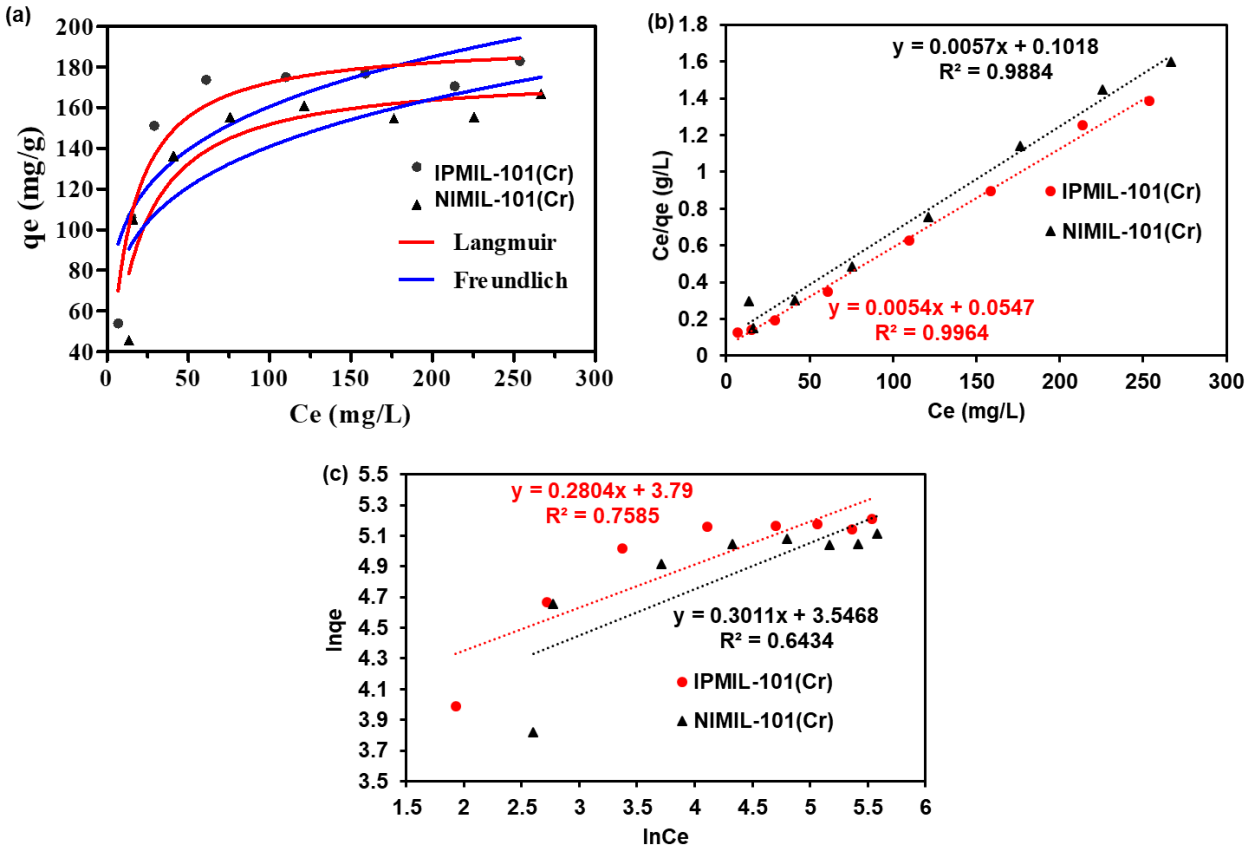

Figure 6.10: (a) Effect of concentration on the adsorption of Pd^{2+} ions by IPMIL-101(Cr) and NIMIL-101(Cr). Linear plots of the (b) Langmuir and (c) Freundlich isotherm models.

Table 6.3: Adsorption isotherm parameters for IPMIL-101(Cr) and NIMIL-101(Cr).

Isotherm models	**Langmuir**		**Freundlich**	
	IPMIL-101(Cr)	**NIMIL-101(Cr)**	**IPMIL-101(Cr)**	**NIMIL-101(Cr)**
Linear				
q_m or K_F	185.2	175.4	42.9	34.7
K_L or N	0.09872	0.055992	3.566334	3.321156
R_L	0.04821	0.08198	–	–
R^2	0.9964	0.9884	0.7585	0.6434
Non-linear				
Best-fit values				
q_m or K_F	193.2	177.7	62.69	51.07
K_L or N	0.08264	0.05848	4.894	4.536
Std. Error				
q_m or K_F	7.31	12.11	16.52	16.72
K_L or N	0.01609	0.0191	1.333	1.393
95% Confidence				

q_m *or* K_F	175.3 to 211.0	148.1 to 207.4	22.27 to 103.1	10.16 to 91.98
K_L or N	0.04327 to	0.01174 to	1.631 to 8.157	1.128 to 7.943
Goodness of fit				
Degrees of Freedom	6	6	6	6
R^2	0.9455	0.8437	0.7538	0.6992
Absolute Sum of	794.7	1842	3590	3545
Sy.x	11.51	17.52	24.46	24.31
# of points analysed	8	8	8	8

Table 6.4: Comparison of the uptake capacity of IPMIL-101(Cr) with other reported ion-imprinted polymer materials used in the adsorption of Pd^{2+} ion.

Adsorbent	**qm (mg/g)**	**pH**	**dosage (g)**	**Concentration (mg/L)**	**Refs**
Polymer-2-hydroxyethyl methacrylate	42.2	4	20	50	[11]
Pd-IAzoCsM	93.48	4	0.003	100	[13]
Pd-IIP-AHTB	60	3	0.05	200	[23]
IPET-CA beads	82.85	3	0.025	0.5	[5]
Pd (II)-imprinted membrane	2.2447	–	–	20	[3]
Pd-ABN-VP complex	39.8	0.5	0.1	50	[1]
Fe_3O_4@SiO_2–Pd(II)-MIIP	67.75	4	0.05	100	[24]
Pd(II)–IP chitosan fiber	87.2	1	0.01	200	[2]
NIMIL-101(Cr)	177.7	2	0.04	100	This work
IPMIL-101(Cr)	193.2	2	0.03	100	This work

6.3.3.3. Kinetics data

Adsorption kinetics provide insight into the reaction pathways that can assist in understanding the possible mechanistic route. Figure 6.11(a) shows the influence of contact time on the uptake of Pd^{2+} ions by IPMIL-101(Cr) and NIMIL-101(Cr). The graph revealed that the adsorption capacity increased with an increase in contact time and it is much higher for the IPMIL-101(Cr) than its non-imprinted counterpart. The experimental data on the removal of Pd^{2+} was studied using the non-linear PFO and the PSOkinetics models which are given by Equations 6.8 and 6.9:

$$\frac{dqt}{dt} = k_1 (q_e - q_t) \quad (6.8)$$

$$\frac{dqt}{dt} = k_2 (q_e - q_t)^2 \quad (6.9)$$

with qe and qt representing the Pd^{2+} capacity at equilibrium and any given time t in (mg/g). k_1 is the PFO rate constant in L/min and k_2 is the PSO rate constant in g/mg.min. The resulting kinetic parameters as presented in Table 6.5, depicts that the rate of Pd^{2+} ions adsorption is faster with the IPMIL-101(Cr) than with the NIMIL-101(Cr). Furthermore, the linear plots of the PSO and PFO kinetic models were obtained from Equations 6.10 and 6.11 in order to determine the rate constants.

$$\frac{t}{qt} = \frac{1}{k_2 q^2 t} + \frac{1}{q_e} t \quad (6.10)$$

$$\ln (q_e - q_t) = \ln q_e - k_1 t \quad (6.11)$$

From the results presented in Figures 6.11(b and c), the adsorption of Pd^{2+} ions onto the IPMIL-101(Cr) surface showed a good fit of the data to the PSO kinetic model with the R^2 values of 0.9993 as compared to the PFO model. However, the NIMIL-101(Cr) fitted both the PSO and PFO. Moreover, the rate constants obtained from both models revealed that the Pd^{2+} adsorbs much faster onto the IPMIL-101(Cr) than the NIMIL-101(Cr) (see Table 6.5). The adsorption kinetics data were further fit to the Weber and Moris intraparticle diffusion model given by Equation 6.12, in order to determine the rate-limiting step [25].

$$q_t = \quad k_i t^{0.5} + C_i \qquad (6.12)$$

where k_i (mg/g.min) and c_i represent the intraparticle rate constants which is the y-intercept. As depicted in Figure 6.11(d), the adsorption mechanism of Pd^{2+} ions onto the as-synthesised adsorbents occur through two steps. The first rapid step is the rate-limiting step which attributes to intraparticle diffusion and the second step represents the equilibrium. The obtained values of k_i shown in Table 6.5 suggest that the adsorption of Pd^{2+} ions is controlled by the diffusion of the adsorbate inside the IPMIL-101(Cr) and NIMIL-101(Cr) adsorbents.

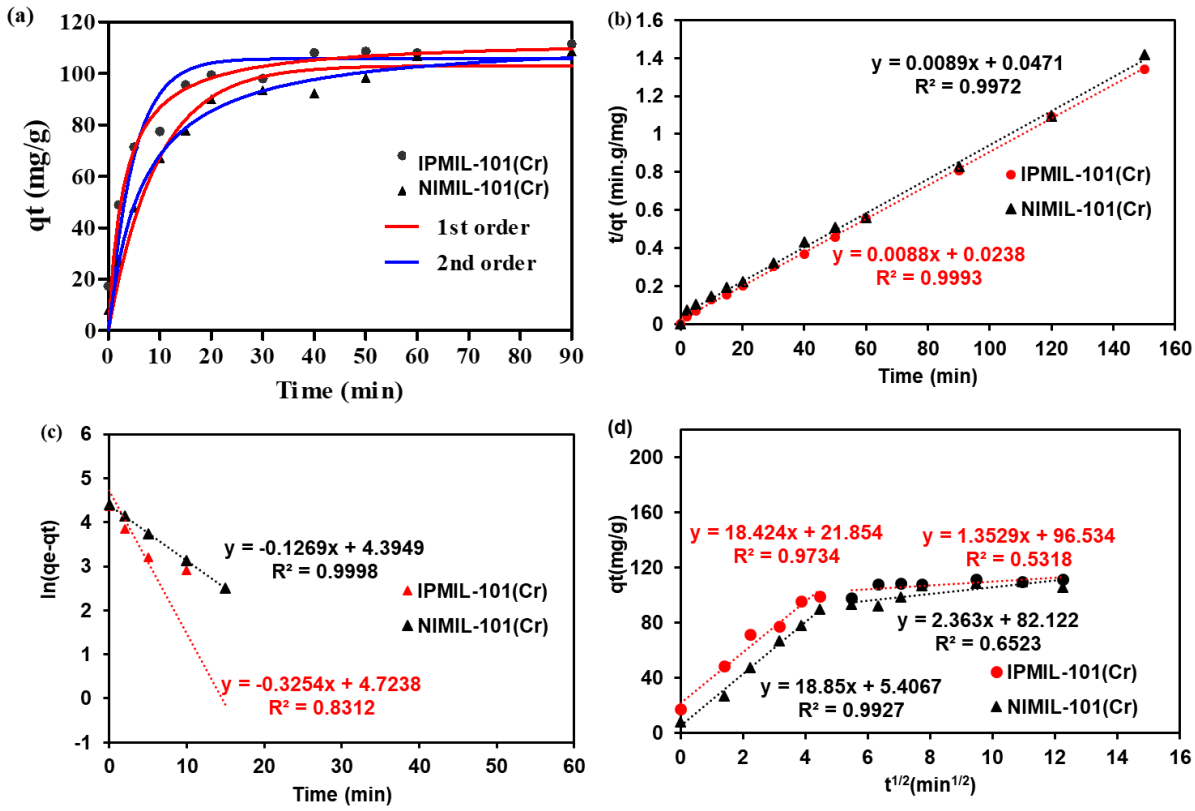

Figure 6.11: (a) Influence of contact time on the adsorption of Pd^{2+} ions by IPMIL-101(Cr) and NIMIL-101(Cr). Linear plots of the (b) PSO and (c) PFO kinetics models. (d) Intra-particle diffusion model.

Table 6.5: Kinetics data on the adsorption of Pd^{2+} ions by IPMIL-101(Cr) and NIMIL-101(Cr).

Kinetic models	**1st -order**		**2nd –order**	
	IPMIL-101(Cr)	**NIMIL-101(Cr)**	**IPMIL-101(Cr)**	**NIMIL-101(Cr)**
Linear				
q_e	112.6	81.0	113.6	112.6
k_1 or k_2	0.354	0.1269	0.003472	0.001755
R^2	0.8312	0.9998	0.9993	0.9972
Non-linear				
Best-fit values				
q_e	105.6	103.1	113.4	114.1.4
k_1 or k_2	0.2041	0.1061	0.00286	0.00130
Std. Error				
q_e	3.191	2.413	2.93	2.216
k_1 or k_2	0.03551	0.01102	0.000551	0.000146
95% Confidence				
q_e	98.83 to 112.9	97.75 to 108.4	106.9 to 119.8	109.2 to 119.0
k_1 or k_2	0.1260 to	0.08186 to	$1.7x10^{-3}$ to	$9.8x10^{-4}$ to
Goodness of fit				
Degrees of Freedom	11	11	11	11
R^2	0.9083	0.9694	0.9551	0.9876
Absolute Sum of	914.4	398	448.2	162.1
Sy.x	9.117	6.015	6.383	3.839
# of points analysed	13	13	13	13

6.3.3.4. Co-existing ions effect and reusability

In the natural water systems, Pd^{2+} ions do not exist alone, hence, the influence of competing ions is a significant factor to be investigated. Figure 6.12 shows the role played by the presence of selected cations and anions on the adsorption of Pd^{2+} ions by IPMIL-101(Cr) and NIMIL-101(Cr). The cations of Pt^{4+}, Co^{2+}, Ni^{2+}, and Ag^{+} showed no effect on the adsorption of Pd^{2+} ions by the IPMIL-101(Cr) as the %R was still above 95 %. Furthermore, Pd^{2+} ions solution was mixed with 50 mg/L of selected anions and the results showed that CO_3^{2-}, SO_4^{2-}, NO_3^{-}, and PO_4^{-} anions had little effect on the adsorption process. The IPMIL-101(Cr) was able to remove more than 80% of Pd^{2+} ions. For the NIMIL-101(Cr), the cations also showed no significant effect on the adsorption of Pd^{2+} ions, whereas in the presence of anions the removal of the Pd^{2+} ions dropped from 80 to

70%. These results suggest that the IPMIL-101(Cr) is more selective towards Pd^{2+} ions in comparison to the NIMIL-101(Cr).

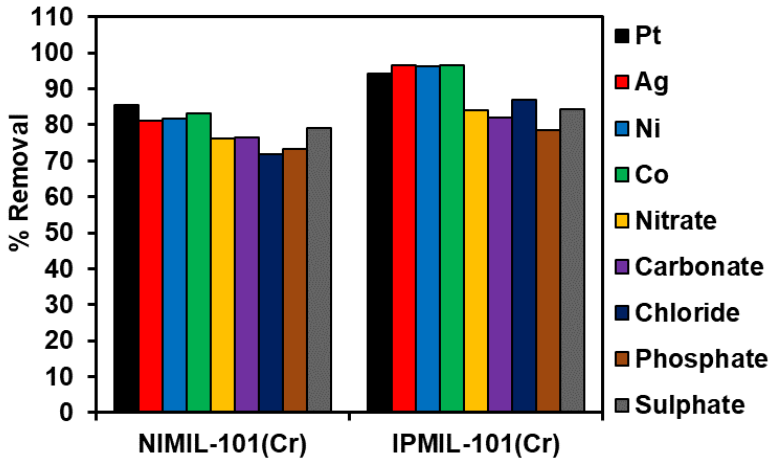

Figure 6.12: Influence of competing ions on the adsorption of Pd^{2+} by the IPMIL-101(Cr) and NIMIL-101(Cr) adsorbents.

The reusability of the IPMIL-101(Cr) and NIMIL-101(Cr) were investigated for the potential sustainability of the adsorption process. Figure 6.13 shows that the IPMIL-101(Cr) can be reused for 5 consecutive cycles without the significant loss of the adsorption capacity as the removal percentage for Pd^{2+} was still above 80% after four-cycle. After the 5^{th} cycle, the %R dropped slightly to 79%, however, this was only 5% in comparison to the first 4 cycles. The NIMIL-101(Cr) demonstrated a reduction in the adsorption capacity due to the decline in the removal percentage from 85% in the initial cycle to 70% in the 2^{nd}, 3^{rd} and 4^{th} cycles. Furthermore, another significant drop to 50 % was observed with the 5^{th} cycle. This indicated that the IPMIL-101(Cr) has the superior advantage of being regenerated and reused over the NIMIL-101(Cr).

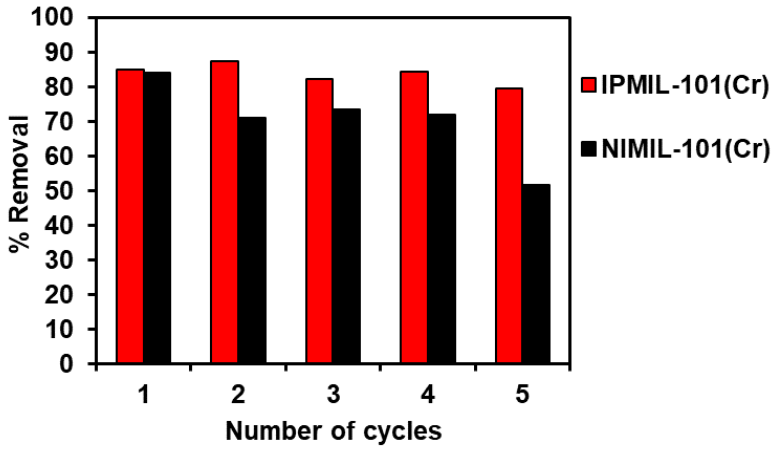

Figure 6.13: Reusability studies of IPMIL-101(Cr) and NIMIL-101(Cr) adsorbents.

6.4. CONCLUSION

The results of this study have demonstrated the potential application of ion-imprinted MOF materials for the removal of Pd^{2+} ions from an aqueous solution. The preparation of the IPMIL-101(Cr) was achieved through post-modification on the MOF surface with a chelating ligand. The adsorption experiments were conducted in the batch mode and numerous parameters were investigated. The equilibrium concentration and contact time studies showed that the %R for Pd^{2+} ions increased with the increase in both parameters. As predicted by the Langmuir isotherm model, the IPMIL-101(Cr) showed an improved adsorption capacity towards the uptake of Pd^{2+} ions with the q_m value of 193.2 mg/g. Kinetics data revealed that the adsorption of Pd^{2+} ions by IPMIL-101(Cr) was rapid and reached equilibrium within 20 minutes with the rate being limited by the intraparticle diffusion step as compared to NIMIL-101(Cr). More importantly, the IPMIL-101(Cr) has shown to be highly selective towards Pd^{2+} ions adsorption and can be regenerated and reused for 5 consecutive cycles without a significant loss in the adsorption capacity. These results show the potential recovery of Pd^{2+} ions from industrial wastewater using the Pd ions imprinted IPMIL-101(Cr).

6.5. REFERENCES

[1] Y. Jiang and D. Kim, “Synthesis and selective adsorption behaviour of Pd(II)-imprinted porous polymer particles,” *Chem. Eng. J.*, vol. 232, pp. 503–509, 2013, doi: 10.1016/j.cej.2013.08.008.

[2] J. Mao, S. Lin, X. J. Lu, X. H. Wu, T. Zhou, and Y. S. Yun, “Ion-imprinted chitosan fiber for recovery of Pd(II): Obtaining high selectivity through selective adsorption and two-step desorption,” *Environ. Res.*, vol. 182, p. 108995, 2020, doi: 10.1016/j.envres.2019.108995.

[3] J. Lu, Y. Qin, C. Yu, X. Lin, M. Meng, Y. Yan, H. Fan, Y. Wu, C. Li, “Stable, regenerable and 3D macroporous Pd(II)-imprinted membranes for efficient treatment of electroplating wastewater,” *Sep. Purif. Technol.*, vol. 235, p. 116220, 2020, doi: 10.1016/j.seppur.2019.116220.

[4] M. R. Awual, “Solid phase sensitive palladium(II) ions detection and recovery using ligand based efficient conjugate nanomaterials,” *Chem. Eng. J.*, vol. 300, pp. 264–272, 2016, doi: 10.1016/j.cej.2016.04.071.

[5] X. Gao, C. Guo, J. Hao, Z. Zhao, H. Long, and M. Li, “Selective adsorption of Pd (II) by ion-imprinted porous alginate beads: Experimental and density functional theory study,” *Int. J. Biol. Macromol.*, vol. 157, pp. 401–413, 2020, doi: 10.1016/j.ijbiomac.2020.04.153.

[6] M. Ince, O. K. Ince, "An Overview of Adsorption Technique for Heavy Metal Removal from Water/Wastewater: A Critical Review" Int. J. Pure Appl. Sci. 3(2): 10-19 (2017).

[7] M. Feng, P. Zhang, H. C. Zhou, and V. K. Sharma, “Water-stable metal-organic frameworks for aqueous removal of heavy metals and radionuclides: A review,” *Chemosphere*, vol. 209, pp. 783–800, 2018, doi: 10.1016/j.chemosphere.2018.06.114.

[8] S. Daliran, S. Ali, S. Ali, H. Xu, R. Wu, Y. Tang, “A Pyridyltriazol Functionalised Zirconium Metal-Organic Framework for Selective and Highly Efficient Adsorption of Palladium,” *ACS Appl. Mater. Interfaces*, vol. 12, pp. 25221–25232, 2020, doi: 10.1021/acsami.0c06672.

[9] F. Ahmadijokani, S. Tajahmadi, A. Bahi, H. Molavi, M. Rezakazemi, F. Ko, T. M. Aminabhavi, M. Arjmand, “Ethylenediamine-functionalised Zr-based MOF for efficient removal of heavy metal ions from water,” *Chemosphere*, vol. 264, p. 128466, 2021, doi: 10.1016/j.chemosphere.2020.128466.

[10] K. W. Jung, J. H. Kim, and J. W. Choi, “Synthesis of magnetic porous carbon composite derived from metal-organic framework using recovered terephthalic acid from polyethylene terephthalate (PET) waste bottles as organic ligand and its potential as adsorbent for antibiotic tetracycline hydrochlo,” *Compos. Part B Eng.*, vol. 187, p. 107867, 2020, doi: 10.1016/j.compositesb.2020.107867.

[11] H. Yu. P. Shao, L. Fang, J. Pei, L. Ding, S. G. Pavlostathis, X. Luo, “Palladium ion-imprinted polymers with PHEMA polymer brushes: Role of grafting polymerization degree in anti-interference,” *Chem. Eng. J.*, vol. 359, pp. 176–185, 2019, doi: 10.1016/j.cej.2018.11.149.

[12] M. Monier, D. A. Abdel-Latif, and Y. G. Abou El-Reash, “Ion-imprinted modified chitosan resin for selective removal of Pd(II) ions,” *J. Colloid Interface Sci.*, vol. 469, pp. 344–354, 2016, doi: 10.1016/j.jcis.2016.01.074.

[13] M. P. Di Bello, M. R. Lazzoi, G. Mele, S. Scorrano, L. Mergola, and R. Del Sole, “A new ion-imprinted chitosan-based membrane with an azo-derivative ligand for the efficient removal of Pd(II),” *Materials (Basel).*, vol. 10, 2017, doi: 10.3390/ma10101133.

[14] J. Ren, X. Dyosiba, N. M. Musyoka, H. W. Langmi, B. C. North, M. Mathe, and M. S. Onyango, “Green synthesis of chromium-based metal-organic framework (Cr-MOF) from waste polyethylene terephthalate (PET) bottles for hydrogen storage applications,” *Int. J. Hydrogen Energy*, vol. 41, pp. 18141–18146, 2016, doi:

10.1016/j.ijhydene.2016.08.040.

[15] M. Abroudi, A. Tadjarodi, Z. Rezvani, and A. Mollahosseini, “Synthesis and characterisation of Pd nanoparticles anchored on MIL101(Cr) as a novel and recyclable catalyst for the Suzuki cross-coupling reactions,” *Microporous and Mesoporous Materials* vol. 331, (2022) 111599.

[16] X. Luo, L. Ding, and J. Luo, “Adsorptive removal of Pb(II) ions from aqueous samples with amino-functionalisation of metal-organic frameworks MIL-101(Cr),” *J. Chem. Eng. Data*, vol. 60, pp. 1732–1743, 2015, doi: 10.1021/je501115m.

[17] J. Y. Zhang, N. Zhang, L. Zhang, Y. Fang, W. Deng, M. Yu, Z. Wang, L. Li, X. Liu & J. Li, “Adsorption of Uranyl ions on Amine-functionalisation of MIL-101(Cr) Nanoparticles by a Facile Coordination-based Post-synthetic strategy and X-ray Absorption Spectroscopy Studies,” *Sci. Rep.*, vol. 5, pp. 1–10, 2015, doi: 10.1038/srep13514.

[18] N. Zhuo, Y. Lan, W. Yang, Z. Yang, X. Li, X. Zhou, Y. Liu, J. Shen, X. Zhang “Adsorption of three selected pharmaceuticals and personal care products (PPCPs) onto MIL-101(Cr)/natural polymer composite beads,” *Sep. Purif. Technol.*, vol. 177, pp. 272–280, 2017, doi: 10.1016/j.seppur.2016.12.041.

[19] T. R. Somo, M. W. Davids, M. V Lototskyy, M. J. Hato, and K. D. Modibane, “Improved Hydrogenation Kinetics of TiMn1.52 Alloy Coated with Palladium through Electroless Deposition,” 2021.

[20] N. Yin, K. Wang, Y. Xia, and Z. Li, “Novel melamine modified metal-organic frameworks for remarkably high removal of heavy metal Pb (II),” *Desalination*, vol. 430, pp. 120–127, 2018, doi: 10.1016/j.desal.2017.12.057.

[21] X. Quan, Z. Sun, H. Meng, Y. Han, J. Xu, Y. Xu and X. Zhang, “Surface functionalisation of MIL-101(Cr) by aminated mesoporous silica and improved adsorption selectivity toward special metal ions,” *Dalt. Trans.*, vol. 48, pp. 5384–5396, 2019, doi: 10.1039/c9dt00501c.

[22] T. C. Maponya, K. E. Ramohlola, N. H. Kera, K. D. Modibane, A. Maity, L. M. Katata-Seru and M. J. Hato “Influence of magnetic nanoparticles on modified polypyrrole/m-phenylediamine for adsorption of Cr(VI) from aqueous solution,” *Polymers (Basel).*, vol. 12, pp. 1–17, 2020, doi: 10.3390/polym12030679.

[23] K. Zhang, Z. Chang, X. Luo, L. Yang, J. Pei, and S. Luo, “Specific spatial transfer PdCl42− to [X-Pd-Y] by strong coordination interaction in a 3D palladium ion-imprinted polymer with footprint cavity,” *Chem. Eng. J.*, vol. 405, p. 126613, 2021, doi: 10.1016/j.cej.2020.126613.

[24] F. Shafizadeh, M. Taghizadeh, and S. Hassanpour, “Preparation of a novel magnetic Pd(II) ion-imprinted polymer for the fast and selective adsorption of palladium ions from aqueous solutions,” *Environ. Sci. Pollut. Res.*, vol. 26, pp. 18493–18508, 2019, doi: 10.1007/s11356-019-05233-8.

[25] H. Jalayeri, P. Aprea, D. Caputo, A. Peluso, and F. Pepe, “Synthesis of amino-functionalised MIL-101(Cr) MOF for hexavalent chromium adsorption from aqueous solutions,” *Environ. Nanotechnology, Monit. Manag.*, vol. 14, p. 100300, 2020, doi: 10.1016/j.enmm.2020.100300.

CHAPTER SEVEN

SYNTHESIS OF NOVEL ION IMPRINTED GLYCYLGLYCINE POLYMER METAL–ORGANIC FRAMEWORK FOR THE SELECTIVE RECOGNITION AND RECOVERY OF PLATINUM IONS FROM WASTEWATER

7.1. INTRODUCTION

Platinum (Pt) is amongst the platinum group elements (PGEs) and has great significance in numerous industrial fields due to its outstanding properties. Pt has good catalytic and electrocatalytic activities, resistance to oxidation and corrosion as well as high melting point that makes it attractive for various applications. Pt and other PGEs, such as iridium, rhodium, ruthenium and palladium, are extensively used as catalysts in the automobile, chemical and petroleum industries. These metals are also used in the electrical and electronics industries as conductors, and in medicine and jewellery [1]. However, the development and application of these technologies are accompanied by the discharge of Pt into the environment during normal exploitation of cars, as well as in its production and processing. Therefore, the constant rise in the contamination of water by Pt metals can be observed [1][2][3]. Hence, the effective adsorption and recovery of Pt from wastewater may have potential importance, both economically and in environmental protection.

In general, Pt metals are difficult to be separated and recovered from wastewater [4]. As a result, a number of methods have been employed to remove and recover Pt metals, such as co-precipitation, fire-assay, biosorption, solid-phase extraction, reverse osmosis, membrane separation, and evaporation [5]–[8]. Amongst these methods, the solid phase extraction has been identified as a promising method because it has several mechanism of sorption including adsorption, ion-exchange, ion-pairing or chelation [9]–[12]. These mechanisms have been utilised in analysis of wide range of samples due to easy operation, cost effectiveness, low energy consumption, treatment superiority in minimizing the adverse impacts on the environment or human health [13], [14]. For example, in adsorption technology, Fujiwara *et al*. [15] prepared a cross–linked chitosan resin chemically modified with l-lysine as an adsorbent for adsorption of Pt(IV) from aqueous solutions. They observed the maximum adsorption capacity of 129.26 mg/g. But,

these materials suffer from several setbacks, including low adsorption capacity and poor stability. Therefore, continuous efforts are still required to tackle the challenge of Pt recovery.

Metal-organic frameworks (MOFs) are class of materials consisting of inorganic blocks that form a textured structure with each other by organic linkers [12]. MOFs have been recognised as alternative adsorbents to overcome the technical limitations of conventional porous materials [15]. These porous polymers have been used as solid-phase sorbents to adsorb and remove environmentally toxic metal ions from aqueous solutions, but there are few studies on the Pt ions separation. MIL-101 has drawn a great attention due to its high water stability. In addition, it can be synthesised from waste polyethylene terephlalate (PET) plastic that provides the benzenedicarboxylic acid (BDC) organic linker. This method of synthesising MIL-101 makes it to be part of recycling waste managements. MIL-101 possesses high surface area, accessible coordinatively unsaturated sites and high chemical stability [16]. Lim *et al*. [17] showed the adsorption and recovery of Pt(IV) from acidic aqueous solutions using a nitro- and an amine-functionalised MIL-101(Cr) which were prepared from the BDC organic linker. Their adsorption kinetics and isotherms revealed that the Pt(IV) uptake was obtained as 140.7 mg g^{-1} by MIL-101(Cr)-NH_2 which was higher than the uptake of 104.5 mg/g by MIL-101(Cr)-NO_2. In another study, Lin *et al*. [18] investigated the removal of Pt metals ions using zirconium (Zr) based BDC MOF (UiO-66) and UiO-66-NH_2. The maximum adsorption capacity of UiO-66 for Pt(IV) was observed to be 166 mg/g, whereas UiO-66-NH_2 possessed a higher adsorption capacity of 193 mg/g. However, the adsorbents have common disadvantages of the poor recognition and selectivity, hence; new competent adsorbents must be established.

Ion imprinting polymer (IIP) is similar to molecular imprinting polymer in which ion-specific recognition is achieved because of its stereochemistry and morphology. In the process of IIP, a metal ion interacts with an imprinted molecule, and then it is fixed with a cross-linking ligand into a polymeric network. The extraction of metal ion leaves a predetermined arrangement of imprinted metal ions [19]. The obtained IIP offers high

recognition and selectivity towards imprinted metal ions, which makes it possible to bind the target ion in the presence of other metal ions [19]. Currently, IIPs have been extensively used as new adsorbents for the adsorption of Pb(II) [20], Au(III) [21], Cu(II) [22], Ni(II) [23], Pd(II) [24], etc. from wastewater. Even though there are studies on the Pt(IV) uptake, setbacks such as the low adsorption capacity [25] and poor selectivity [26] have been observed. For example, Jiang *et al*. [27] obtained the maximum adsorption capacity of 38.89 mg/g for Pt(IV) uptake using an IIP prepared from divinylbenzene and styrene in the presence of self-assembled chelates of 4-vinylpyridine and dimethylglyoxime functional monomers. Leśniewska *et al*. [28] prepared IIP by copolymerization of ethylene glycol dimethacrylate and methacrylic acid in the presence of numerous chelating agents for Pt(II) ions recognition using 2,2′-azo-bis-isobutyronitrile initiator. They demonstrated the effect of Pt ion imprinting into a polymeric matrix using a quantitative retention of Pt(II) and Pt(VI) ions to be 92-97% and 87-92%, respectively.

Here, we report the preparation of a novel ion-imprinted glycylglycine polymer based on metal-organic frameworks (IIGlyMIL-101(Cr)) from waste PET bottle. The synthesised IIGlyMIL-101(Cr) was applied to adsorb and remove Pt(IV) from simulated wastewater. The influence of the initial Pt(IV) solution pH and concentrations, competing ions and contact time on the adsorption behaviour IIGlyMIL-101(Cr) towards of Pt(IV) uptake were interrogated, and the regeneration of the prepared adsorbent was evaluated. In addition, the adsorption kinetics and isotherm data were fit to the models in order to determine the adsorption mechanism and maximum capacity. To the best of our knowledge, it is the first time that the MIL-101(Cr) prepared from waste PET plastic is coupled with IIP and applied for recognition and recovery of Pt ions. This work will open a new path for PET waste management and precious metal removal and recovery.

7.2. MATERIALS AND EXPERIMENTS

7.2.1. Materials

All the reagents of analytical grade were used as received without any modification. Hydrochloric (HCl), sodium hydroxide (NaOH), ethylenediamine (ED) and chromium nitrate nanohydrate $Cr(NO_3)_3.9H_2O$ were obtained from Rochelle Chemicals (South Africa). Chloroplatinic acid hydrate ($H_2PtCl_6.6H_2O$), ethylene glycol (EG), toluene

(anhydrous 99.8%) and glutaraldehyde (GA) solution (50 wt% in H_2O) were procured from Sigma-Aldrich (South Africa). Waste PET bottles were collected from the University of Limpopo, Polokwane, South Africa.

7.2.2. Synthesis of the ion-imprinted polymer

7.2.2.1. Preparation and functionalisation of MIL-101(Cr)

An organic linker, 1,4 benzenedicarboxylic acid (H_2BDC), was prepared using hydrothermal method in a 100 mL autoclave as reported in the literature [29]. Initially, 3.00 g of PET plastic chips were suspended in a solution of EG and distilled water. The mixture was allowed to heat for 8 hours in an oven set at 210 °C. The resulting precipitates were collected by filtration and washed with ethanol followed by drying at 110 °C for overnight.

MIL-101(Cr) was prepared using a method reported in literature [30]. In this procedure, $Cr(NO_3)_3.9H_2O$ salt (4.00 g) and H_2BDC (1.66 g) were mixed with distilled water through magnetic stirring for 30 minutes. The reaction suspension was then heated at 220 °C for 8 hours in a Teflon-lined autoclevable reaction vessel that was put in the oven. The formed particulates were filtered and washed with ethanol prior to be dried at 120 °C. For grafting with ethylenediamine (ED), a suspension of MIL-101(Cr) (0.050 g) and ED (1.00 mL) in anhydrous toluene was refluxed at 90 °C for 12 hours. The resulting solid particles of MIL-101(Cr)/ED were collected by vacuum filtration, followed by washing with toluene and ethanol before drying at 70 °C overnight.

7.2.2.2. Preparation of IIGlyMIL-101(Cr)

The materials were synthesised according to the method similar to that available in literature with some modification [31]. Initially, the MIL-101(Cr)/ED was modified with a cross-linking agent prior to ion imprinting. Approximately, 0.50 g MIL-101(Cr)/ED was added into an aqueous solution (50 mL) that contained 5% (w/w) glutaraldehyde (GA) and stirred for 12 hours. Then, excess deionised water was used to wash–off the aldehyde-decorated MIL-101(Cr)/ED-GA to remove the residual GA. Finally, the product was dried at 80 °C for 10 h.

The synthesis of the IIGlyMIL-101(Cr) was achieved by dispersing 10.0 mmol L^{-1} glycylglycine in ethanol, followed by stirring under heat at 60 °C for 1 hour. Then 10 mL of $H_2PtCl_6.6H_2O$ solution for the metal ion template was added and continuously heated for another 2 hours before evaporation of the solvent at 90 °C. MIL-101(Cr)/ED-GA (1.00 g) was added into the reaction mixture and stirred for 12 hours at 60 °C. The resulting brown precipitates of Pt@IIGlyMIL-101(Cr) were collected by filtration and washed with abundant deionised water to remove the residual glycylglycine and Pt ions. Chelated Pt(IV) ions were removed from Pt@IIGlyMIL-101(Cr) by eluting with a solution mixture of HCl (6M) and thiourea (1M) for 24 hours under rapid stirring, followed by filtration and washing with deionised water several times to form IIGlyMIL-101(Cr). The procedure was repeated three times and the eluent was analysed with ultraviolet visible spectroscopy (UV-Vis) to ensure that no Pt(IV) remained in the IIGlyMIL-101(Cr) polymer. Finally, the product was dried at 80 °C for 24 hours. The same process was used to synthesis the non-imprinted polymer (NIGlyMIL-101(Cr)) with the exclusion of the $H_2PtCl_6.6H_2O$ metal template.

7.2.3. Spectroscopic and Morphological Characterisation

Morphological and elemental analyses were obtained from the field-emission scanning electron microscopy (FE-SEM) (Auriga Cobra focused-ion beam FIB-SEM, Carl Zeiss, Jena, Germany) coupled with energy dispersive x-ray spectroscopy (EDS). The presence of functional groups and composite formation was confirmed by Cary 600 series Fourier transform infrared (FTIR) spectrometer (Spectrum II PerkinElmer). The thermal properties of Pt@IIGlyMIL-101(Cr), IIGlyMIL-101(Cr) and NIGlyMIL-101(Cr) as well as MIL-101(Cr) were obtained from a PerkinElmer STA 6000 instrument connected to a PolyScience digital temperature controller under N_2 gas purged at a flow rate of 20 mL/min.

7.2.4. Adsorption Experiments

The adsorption studies for the synthesised IIGlyMIL-101(Cr) and NIGlyMIL-101(Cr) were conducted following the batch mode of adsorption. The platinum stock solution was prepared in an acidic medium, by dissolving $H_2PtCl_6.6H_2O$ in 0.100 M hydrochloric acid (HCl) solution. All the equilibrium experiments were performed in a temperature controlled

water bath shaker set at 25 °C and a speed of 160 rpm. After the optimization of pH and adsorbent dosage, the studies were done using 20 mg of the prepared adsorbents with the Pt(IV) solution pH and volume being kept at 3.0 and 50 mL, respectively. The adsorption efficiency of the IIGlyMIL-101(Cr)and NIGlyMIL-101(Cr) was determined by analyzing the Pt(IV) solution samples before and after adsorption using ultraviolet-visible (UV-Vis) spectroscopy (Lambda 365 UV/Vis Spectrophotometer, (PerkinElmer, Johannesburg, South Africa)) operating at 370 nm, followed by calculations in Equation 7.1 and 7.2:

$$\% \text{ removal} = \left(\frac{Co-Ce}{Ce}\right) \times 100 \quad (7.1)$$

$$q_e = \left(\frac{Co-Ce}{m}\right)V \quad (7.2)$$

The symbol Co and Ce represent the initial and equilibrium concentrations of Pt(IV) in mg/L, respectively. The symbol qe is the amount of Pt(IV) ions adsorbed at equilibrium per mass of IIGlyMIL-101(Cr) and NIGlyMIL-101(Cr) adsorbent measured in mg/g, whereas m (g) signifies the mass of the adsorbent and V (L) the volume of Pt(IV) solution utilised.

7.2.4.1. Effect of solution pH and adsorbent dose

The studies on the influence of initial solution pH on the uptake of Pt(IV) ions by IIGlyMIL-101(Cr) and NIGlyMIL-101(Cr) were conducted at controlled pH, ranging from 1.0-8.0. This was achieved by contacting 0.03 g of the prepared adsorbents with 50.0 mL Pt(IV) solution at a constant temperature and shaking speed of 298 K and 160 rpm, respectively. The pH of the 100 mg/L Pt(IV) solution was adjusted using various concentrations of HCl and sodium NaOH. To understand the effect of adsorbent dosage, the amount of IIGlyMIL-101(Cr) or NIGlyMIL-101(Cr) was varied from 0.005-0.050 g while keeping other parameters such as temperature, initial concentration, contact time, and pH constant.

7.2.4.2. Adsorption isotherms

The influence of concentration on the removal of Pt(IV) ions by IIGlyMIL-101(Cr) and NIGlyMIL-101(Cr), different initial concentrations (50-400 mg/L) were used with the

constant adsorbent dose of 0.02 g and a pH of 3.0 at 298 K in a water bath shaker for 24 hours at a constant speed of 160 rpm. After the completion of the adsorption process, the solution and adsorbent were separated through filtration, followed by the determination of the final concentration. The data was fit to the two isothermal models which are the nonlinear and linear forms of the Langmuir and Freundlich models shown in the below equations.

$$\frac{q_e}{q_m} = \frac{K_L C_e}{1+K_L C_e} \quad (7.3)$$

$$q_e = K_F Ce^{1/n} \quad (7.4)$$

$$\frac{C_e}{q_e} = \frac{1}{qmKL} + \frac{Ce}{q_m} \quad (7.5)$$

$$\ln q_e = \ln K_F + \frac{1}{n} \ln C_e \quad (7.6)$$

where qm (mg/g), K_L (L/mg), K_F (mg/g) and n each represent the Langmuir maximum adsorption capacity, Langmuir constant, Freundlich constant and adsorption intensity, respectively.

7.2.4.3. Adsorption kinetics

Adsorption kinetics experiments were conducted using Pt(IV) initial solution concentration of 100 mg/L. The contact time between Pt(IV) ions and the IIGlyMIL-101(Cr) or NIGlyMIL-101(Cr) adsorbents was varied from 0-120 minutes. Approximately 0.2 g of IIGlyMIL-101(Cr) or NIGlyMIL-101(Cr) were exposed to 500 mL of 100 mg/L Pt(IV) solution at a pH of 3.0. The reaction mixture was mixed using an overhead stirrer set at a speed of 200 rpm at 25 ◦C. Several aliquots were withdrawn from the mixture at specific time intervals and filtered with 0.450 µm syringe filters. The experimental data was fit to the nonlinear and linear forms of the pseudo-first-order (PFO) and the pseudo-second-order (PSO) kinetic models given by the following equations:

$$\frac{dqt}{dt} = k_1 (q_e - q_t) \quad (7.7)$$

$$\frac{dqt}{dt} = k_2 (qe - qt)^2 \quad (7.8)$$

$$\ln (q_e - q_t) = \ln q_e - k_1 t \quad (7.9)$$

$$\frac{t}{qt} = \frac{1}{k_2 q^2 t} + \frac{1}{q_e} \text{ t} \quad (7.10)$$

where k_1 (1/min) represents PFO rate constant and k_2 (g/mg.min) denotes the PSO rate constant.

7.2.4.4. Competing ions effect

The investigation on the selectivity of the IIGlyMIL-101(Cr) or NIGlyMIL-101(Cr) adsorbents towards the uptake of Pt(IV) ions was done using various selected cations (Co^{2+}, Ni^{2+}, Ag^{+} Pd^{2+}) and anions (SO_4^{2-}, CO_3^{2-}, NO_3^{-}, PO_4^{2-}). For each ion, 25 mL having a concentration 50 mg/L was mixed with 25 mL of 50 mg/L Pt(IV).

7.3. RESULTS AND DISCUSSION

7.3.1. Structural characterisation

The FT-IR spectra of the Pt@IIGlyMIL-101(Cr), IIGlyMIL-101(Cr) and NIGlyMIL-101(Cr) are shown in Figure 7.1. In all samples, the characteristic bands accredited to the C-O and C=O symmetrical stretching of MIL-101(Cr) [33] were observed at 1394 and 1625 cm^{-1}, respectively. The existence of C=C stretching of the benzene ring in MIL-101(Cr) [40] was observed at 1508 cm^{-1}. The vibration due to the C-H deformation of the aromatic ring appeared at 750, 884 and 1160 cm^{-1}. The peak associated with the stretching vibrations of chromium metal to oxygen of organic linker was noticed at 658 cm^{-1} in all three samples [21]. The IR spectra for all the post-modified samples revealed bands at 1370 and 505 cm^{-1} due to the C-N (amide bond) and Cr-N vibrations. The vibrational bond assigned to the N-H and C-N-C stretching of the aliphatic groups were observed at 1560 and 1042 cm^{-1} in the spectra for Pt@IIGlyMIL-101(Cr) and NIGlyMIL-101(Cr). The spectrum for IIGlyMIL-101(Cr) showed a reduction of a peak at 1042 cm^{-1} showing the involvement of the -N group of the polymer chain in the binding with Pt(IV) ions. In addition, the appearance of a peak at 1587 cm^{-1} ascribed to the C=N was observed on the spectra for IIGlyMIL-101(Cr). The results confirm the successful preparation of the IIGlyMIL-101(Cr) with the Pt(IV) ions recognition sides.

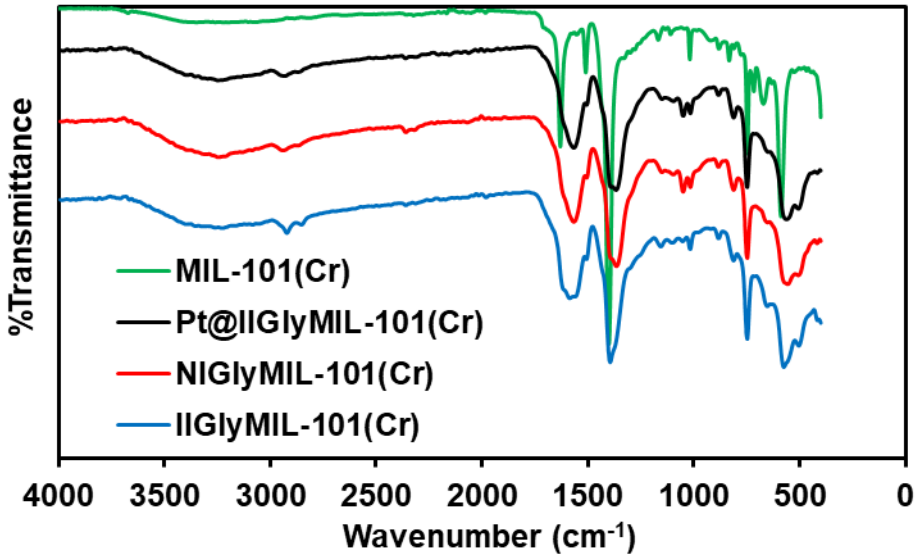

Figure 7.1: FTIR spectra of MIL-101(Cr), Pt@IIGlyMIL-101(Cr), IIGlyMIL-101(Cr) and NIGlyMIL-101(Cr).

Figure 7.2(a-d) shows the TGA curves of the synthesised MIL-101(Cr), Pt@IIGlyMIL-101(Cr), IIGlyMIL-101(Cr) and NIGlyMIL-101(Cr) samples. The initial degradation step observed between 25-100 °C on thermogram of MIL-101(Cr) in Figure 7.2(a), is related to the evaporation of the water and solvent guest molecules [41]. The TGA profiles for the Pt@IIGlyMIL-101(Cr), IIGlyMIL-101(Cr) and NIGlyMIL-101(Cr) showed an improvement in the thermal stability. Less than 10% weight losses were observed in all the three composites as compared to 39.6% in MIL-101(Cr). The degradation steps at 300 ^{o}C and 400-480 ^{o}C were ascribed to the decomposition of polymer chain and terephthalic acid [42], respectively. The Pt@IIGlyMIL-101(Cr), IIGlyMIL-101(Cr) and NIGlyMIL-101(Cr) samples demonstrate a better thermal stability in comparison to the pristine MIL-101(Cr) as the framework started to decompose at a temperature above 400 ^{o}C (Figure 7.2(b-d)). This was also supported by the corresponding DSC curves for MIL-101(Cr), Pt@IIGlyMIL-101(Cr), IIGlyMIL-101(Cr) and NIGlyMIL-101(Cr) samples (Figure 7.2(a-d)) which showed degradation steps at 90 ^{o}C attributing to the weight loss due to solvents. The DSC curves of the prepared materials showed an intense and small exothermic peak at <100 °C for crystallization transition with ΔH values of 2.45, 3.61, 3.61, and 1.64 kJ.g^{-1} for

MIL-101(Cr), and NIGlyMIL-101(Cr) respectively. The Pt@IIGlyMIL-101(Cr) showed two endothermic peaks at 235 and 395 °C with ΔH values of -0.536 and -9.63 kJ.g^{-1}, respectively. Whereas the IIGlyMIL-101 (Cr) possessed an endothermic peak at 373 with ΔH value of -14.5 kJ.g^{-1}.

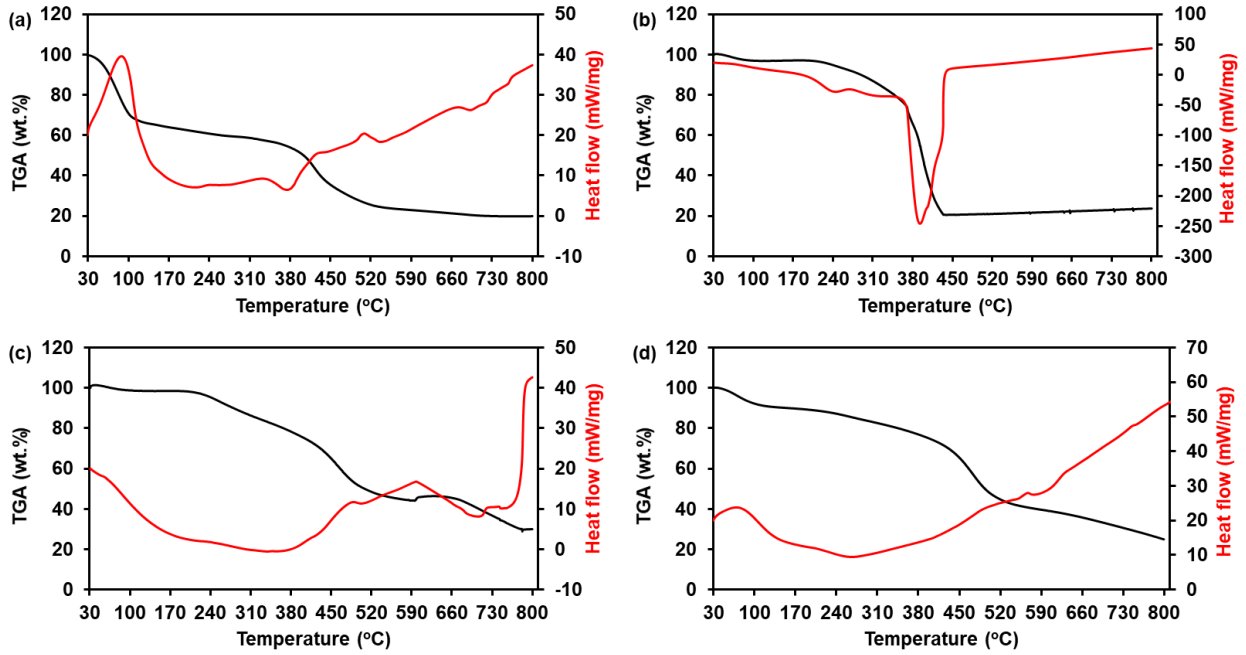

Figure 7.2: TGA/DSC curves of (a) MIL-101(Cr), (b) Pt@IIGlyMIL-101(Cr), (c) IIGlyMIL-101(Cr) and (d) NIGlyMIL-101(Cr).

7.3.2. Morphological characterisation

The morphological image of MIL-101(Cr) presented in Figure 7.3(a) showed highly agglomerated octahedral structures with smooth surface and have an average particle size between 100-200 nm. Moreover, its corresponding EDS analysis (Figure 7.3(b)) revealed that the sample elemental composition consists of C, O, and Cr (the Al element is from the SEM preparation procedure). Upon post-functionalisation the images for the Pt@IIGlyMIL-101(Cr), IIGlyMIL-101(Cr) and NIGlyMIL-101(Cr) composites (Figure 7.3(c, e and g)), indicated that the octahedral morphologies were maintained with reduction in particle size for IIGlyMIL-101(Cr). The analogous EDS spectra of the prepared

composites (Figure 7.3(d, f and h)) showed similar elemental composition to that of the parent material, however, with the addition of N, Pt and increment of oxygen content. The presence of Pt(IV) in Pt@IIGlyMIL-101(Cr) was clearly shown in the EDS spectrum with 0.04 at % (See Figure 7.4(d)). Complete removal of Pt(IV) ions in the preparation of IIGlyMIL-101(Cr) was confirmed in the comparison between the spectra of the two polymer samples before and after the washing process.

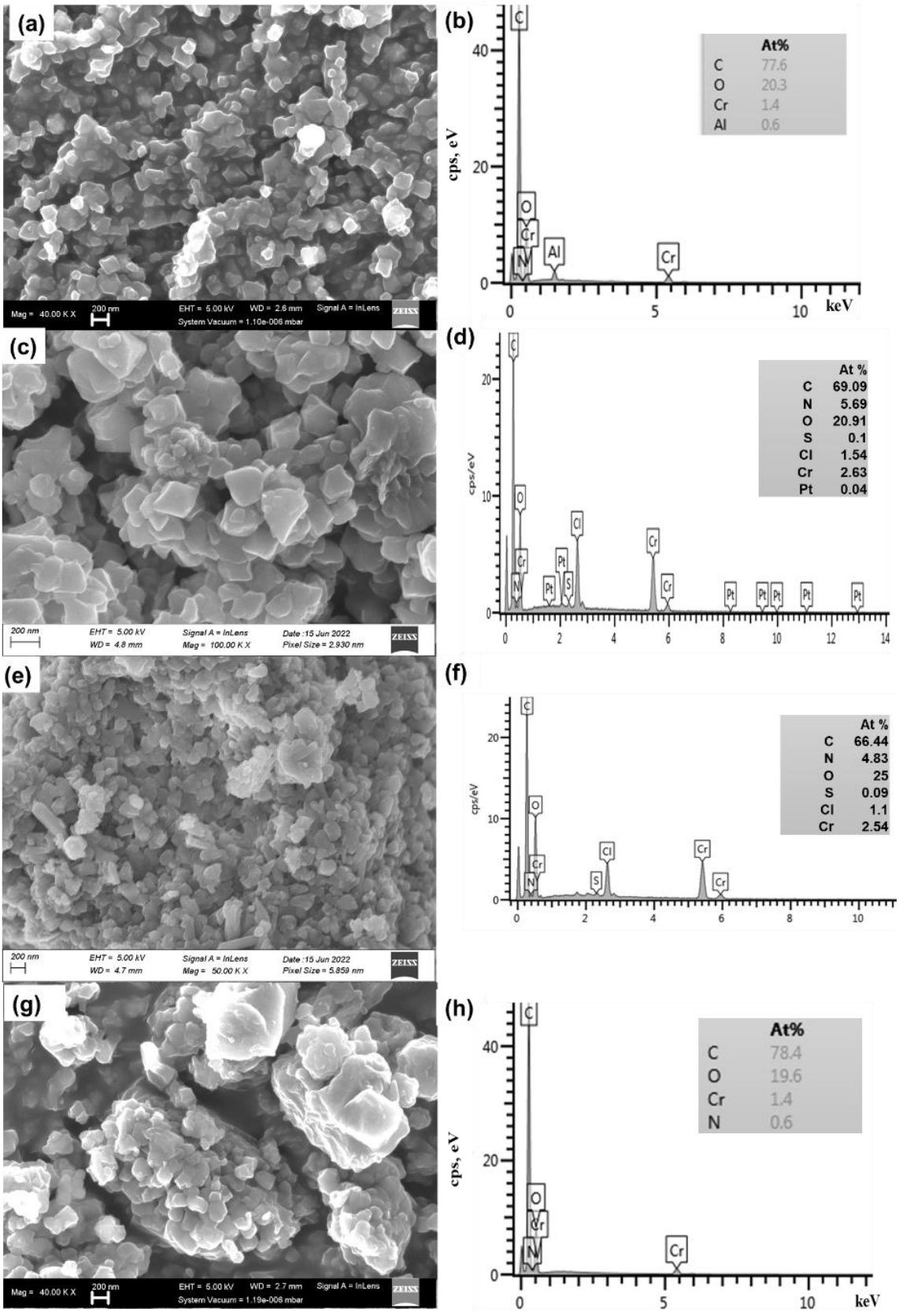
(a)
Mag = 40.00 K X
200 nm
EHT = 5.00 kV
WD = 2.6 mm
Signal A = InLens
System Vacuum = 1.10e-006 mbar
(b)
At%
C 77.6
O 20.3
Cr 1.4
Al 0.6
cps, eV
keV
(c)
200 nm
EHT = 5.00 kV
WD = 4.8 mm
Signal A = InLens
Mag = 100.00 K X
Date :15 Jun 2022
Pixel Size = 2.930 nm
(d)
At %
C 69.09
N 5.69
O 20.91
S 0.1
Cl 1.54
Cr 2.63
Pt 0.04
cps/eV
(e)
200 nm
EHT = 5.00 kV
WD = 4.7 mm
Signal A = InLens
Mag = 50.00 K X
Date :15 Jun 2022
Pixel Size = 5.859 nm
(f)
At %
C 66.44
N 4.83
O 25
S 0.09
Cl 1.1
Cr 2.54
cps/eV
(g)
Mag = 40.00 K X
200 nm
EHT = 5.00 kV
WD = 2.7 mm
Signal A = InLens
System Vacuum = 1.19e-006 mbar
(h)
At%
C 78.4
O 19.6
Cr 1.4
N 0.6
cps, eV
keV

Figure 7.3: SEM-EDS images of (a and b) MIL-101(Cr), (c and d) Pt@IIGlyMIL-101(Cr), (e and f) IIGlyMIL-101(Cr) and (g and h) NIGlyMIL-101(Cr) materials.

7.3.3. Adsorption Studies

7.3.3.1. Effect of solution pH and adsorbent dosage

The optimum removal percentages (%R) of Pt(IV) ions by the IIGlyMIL-101(Cr) and NIGlyMIL-101(Cr) samples were investigated and compared in the pH between 1.0-8.0 (See Figure 4(a)). The obtained results revealed that the IIGlyMIL-101(Cr) had superior performances over a wide range of pH with the highest removal of 85% achieved at pH = 3.0 in comparison its non-imprinted counterpart. For the NIGlyMIL-101(Cr) composite, the highest removal was obtained to be 70%. The increasing %R for pH values between 2.0 -4.0 is accredited to the predominating anion complexes of $[PtCl_6]^{2-}$ which were able to interact with the protonated nitrogen atoms of the IIGlyMIL-101(Cr) and NIGlyMIL-101(Cr) composites [10][43]. However, at lower pH < 2.0, the chloride ions are dominating and compete with the $[PtCl_6]^{2-}$ hence the observed lower %R of Pt(IV) by the NIGlyMIL-101(Cr) [25][44]. The dropping %R with elevating pH values for both composites is due to the hydrolysis of Pt(II) ions, which leads to the partial formation of the $Pt(OH)_2$ starting from pH = 5.0 and above [25]. The point of zero charge (PZC) data as shown in Figure 7.4(b) further supported the protonated surfaces of the IIGlyMIL-101 (Cr) and NIGlyMIL-101 (Cr). According to the obtained results, the surface charge of the prepared composites is positively charged between 1.0-3.0 pH values. This indicates that the IIGlyMIL-101(Cr) and NIGlyMIL-101(Cr) can electrostatically interact with the $[PtCl_6]^{2-}$ complexes. Furthermore, this behaviour was reinforced by FTIR analysis of the IIGlyMIL-101(Cr) and NIGlyMIL-101(Cr) before and after Pt metal ion adsorption as depicted in Figure 7.4(c) and (d), respectively. It was observed in both samples that the adsorption of Pt(IV) by the IIGlyMIL-101(Cr) has caused the reduction of peak intensities at 1652, 1288 and 1039 cm^{-1} for amino, and amide bands, respectively. The absorption band at 1378 cm^{-1} for C-O vibration shifted to 1394 cm^{-1} upon Pt(IV) adsorption. From these observations, the change in absorption intensity, and the shift in wavenumber of functional groups were due to interaction of Pt(IV) ion with active sites in IIGlyMIL-101(Cr)

and NIGlyMIL-101(Cr). The Pt(IV) ions bound to the active sites of IIGlyMIL-101(Cr) and NIGlyMIL-101(Cr) through either electrostatic attraction or complexation mechanism as seen in pH studies. The electrostatic interaction was between Pt(IV) ion and carbonate group, whereas, the complexation mechanism involved electron pair sharing between electron donor atoms (O and N) [45]. In addition, it was seen that IIGlyMIL-101(Cr) has higher adsorption capacity than NIGlyMIL-101(Cr) as a resulting of interaction of Pt(IV) with the IIGlyMIL-101(Cr) using chelating effect.

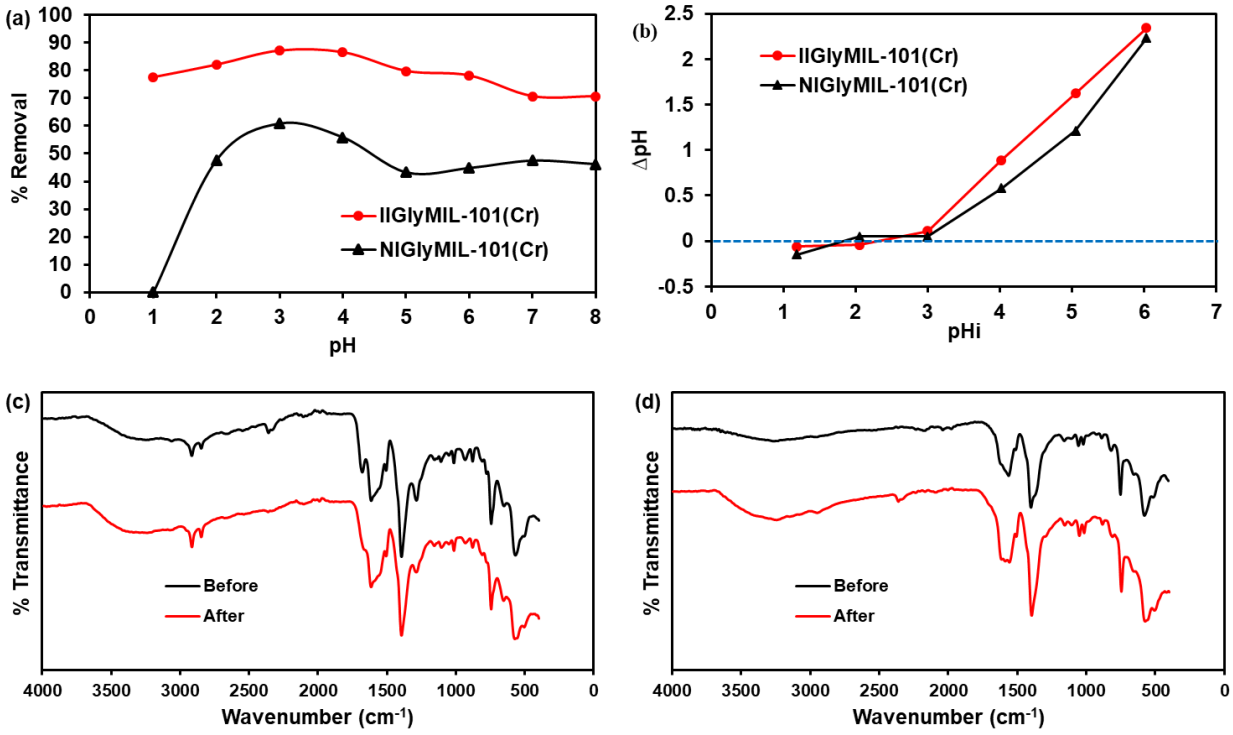

Figure 7.4: (a) Removal percentage of Pt(IV) ions by the IIGlyMIL-101(Cr) and NIGlyMIL-101(Cr) sample as a function of pH 1.0-8.0. (b) PZC values for the IIGlyMIL-101(Cr) and NIGlyMIL-101(Cr) sample. FTIR spectra of the (c) IIGlyMIL-101(Cr) and (d) NIGlyMIL-101(Cr) sample before and after Pt(IV) removal.

The effect of the IIGlyMIL-101(Cr) and NIGlyMIL-101(Cr) dosage was investigated (0.005-0.05 g) to determine the optimum amount for the adsorption of Pt(IV) ions. As depicted in Figure 7.5(a) and (b), the adsorption of Pt (IV) ions was raised as the amount

of the IIGlyMIL-101(Cr) and NIGlyMIL-101(Cr) increased from 0.005-0.03 g. The IIGlyMIL-101(Cr) demonstrated to have higher %R and adsorption capacity over the NIGlyMIL-101(Cr) composite. This indicates that ion imprinted technology indeed improved the removal efficiency of MIL-101(Cr). The %R increased from 58% to 88% for IIGlyMIL-101(Cr) at Pt(IV) solution conditions of 100 mg/L, pH 3.0 and 0.05-0.03 g IIGlyMIL-101(Cr) amount for 24 hours. The optimum dosage was acquired to be 0.02 g in both composites and used throughout the study.

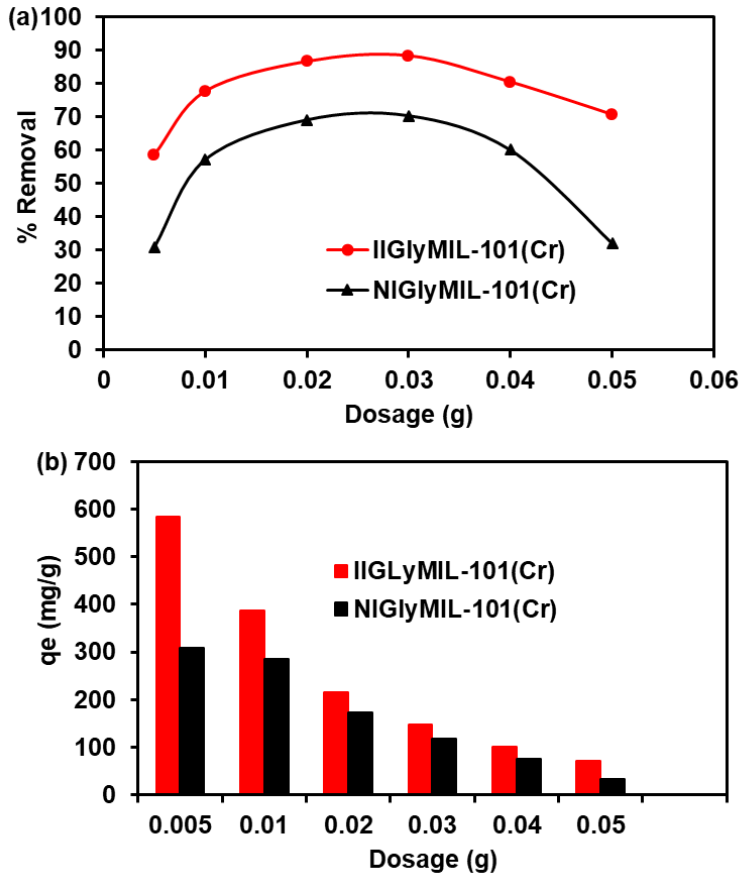

Figure 7.5: Effect of the IIGlyMIL-101(Cr) and NIGlyMIL-101(Cr) dosage on the (a) % R and (b) capacity towards Pt(IV) ions uptake.

7.3.3.2. Adsorption isotherms

Figure 7.6(a) depicts the influence of original concentration on the intake of Pt(IV) ions by the IIGlyMIL-101(Cr) and NIGlyMIL-101(Cr) composites. The obtained data displayed

that there was an increment in the adsorption of Pt(IV) ions by the IIGlyMIL-101(Cr) and NIGlyMIL-101(Cr) sample with an increase in the original concentration of Pt(IV). The experimental data were subjected to the Langmuir and Freundlich non-linear (Figure 7.6(a)) and linear (Figure 7.6(b and c)) models in order to comprehend the adsorbent-adsorbate interactions and maximum adsorption capacity (q_m). The modelled data showed that the Langmuir model was more favoured as compared to the Freundlich model owing to the correlation coefficients (R^2) values which were close to the unity, suggesting monolayer adsorption mechanisms [46]. The estimated isothermal parameters are presented in Table 7.1. The R^2 values determined from the linear Langmuir models were 0.989 and 0.873 for the IIGlyMIL-101(Cr) and NIGlyMIL-101(Cr), which are higher than the those of the Freundlich model (See Figure 7.6(b and c)). In addition, the separation factor (R_L) values were determined according to the literature to evaluate if the Langmuir adsorption process is favourable or unfavourable [47]. As given in Table 7.1, the estimated R_L values were in the range of $0<R_L<1$ indicating a favourable Langmuir adsorption process [48] between Pt(IV) ions and the IIGlyMIL-101(Cr) and NIGlyMIL-101(Cr) composites. The ion imprinted mechanism increased the q_m from the value of 296.4 mg/g for the NIGlyMIL-101(Cr) to the value of 531.3 mg/g for the IIGlyMIL-101(Cr) composite. The obtained results displayed the potential preference of IIGlyMIL-101(Cr) composite with high q_m for removal and recovery of Pt(IV) ion from wastewater in comparison to those reported in the literature (see Table 7.2).

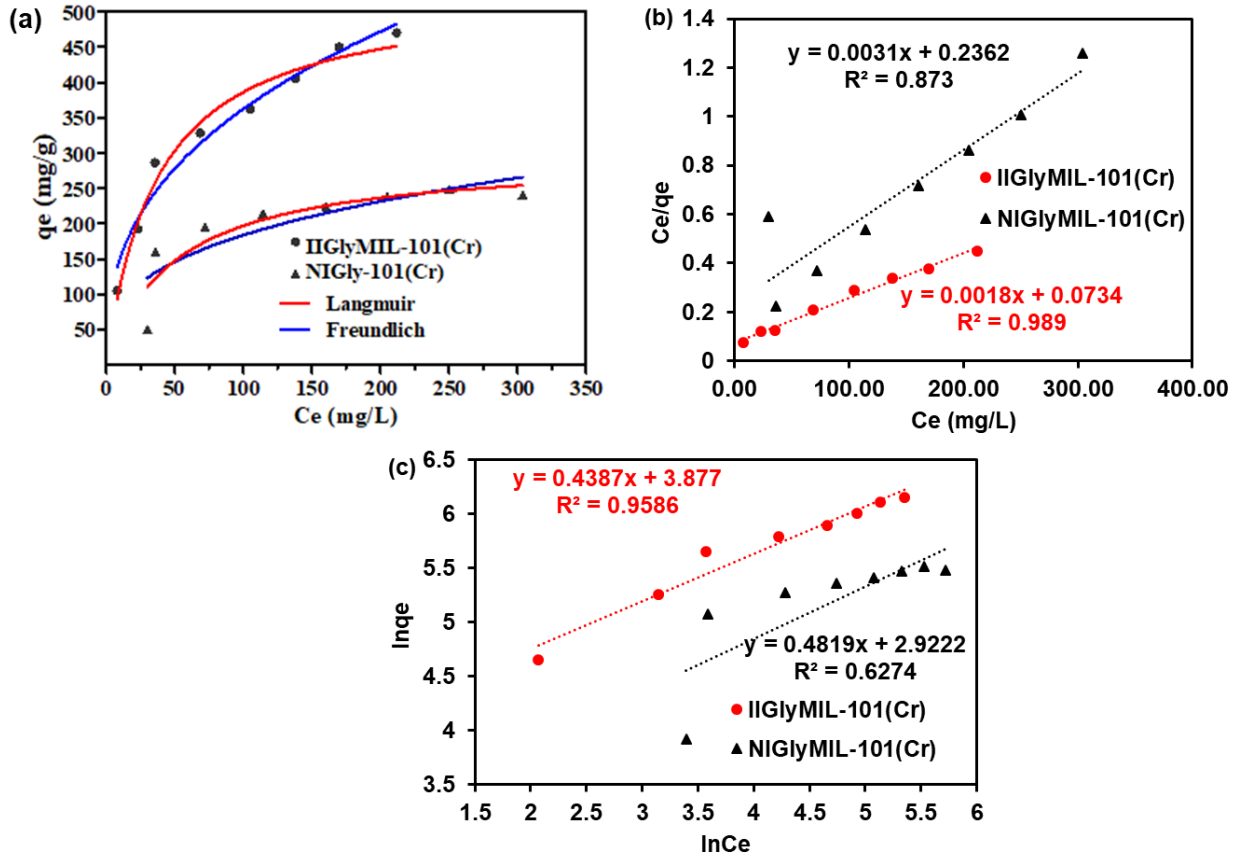

Figure 7.6: Adsorption isotherms of Pt(IV) uptakes by IIGlyMIL-101(Cr) and NIGlyMIL-101(Cr) composites (a) Nonlinear fit of the Langmuir and Freundlich models, (b) Langmuir linear curve, and (c) Freundlich linear curve.

Table 7.1: Langmuir and Freundlich isotherm parameters for Pt(IV) ions adsorption by IIGlyMIL-101(Cr) and NIGlyMIL-101(Cr) composites.

Isotherm model	**Material**	
	IIGlyMIL-101(Cr)	**NIGlyMIL-101(Cr)**
Langmuir		
Linear		
q_m	555.6	322.6
K_L	0.0245	0.0131
R_L	0.169	0.276
R^2	0.989	0.873
Non-linear		
Best-fit values		
q_m	531.3	296.4
K_L	0,02664	0,0198
Std. Error		
q_m	26,11	34,28
K_L	0.00443	0.008006
95 % Confidence Intervals		
q_m	467.4 to 595.2	212.5 to 380.3
K_L	0.01580 to 0.03748	0.0002139 to 0.03939
Goodness of Fit		
Degrees of Freedom	6	6
R^2	0.9743	0.8157
Absolute Sum of Squares	2880	5561
Sy.x	21.91	30.44
Number of points Analysed	8	8
Freundlich		
Linear		
K_F	48.28	18.58
n	2.280	2.075
R^2	0.9586	0.6274
Non-linear		
Best-fit values		
K_F	62.54	39.81
n	2,621	3,009
Std. Error		
K_F	10.57	19.64
n	0,2421	0,8721
95 % Confidence Intervals		
K_F	36.68 to 88.39	-8.257 to 87.87
n	2.028 to 3.213	0.8754 to 5.143
Goodness of Fit		
Degrees of Freedom	6	6
R^2	0.9682	0.7287
Absolute Sum of Squares	3568	8185
Sy.x	24.39	36.93
Number of points Analysed	8	8

Units: *qm*: mg/g, K_L: L/mg, K_F: mg/g.

Table 7.2: Comparison of IIGlyMIL-101(Cr) and NIGlyMIL-101(Cr) sample adsorption capacity with other adsorbents used for Pt(IV) ion uptake.

Adsorbent	qm (mg/g)	pH	dosage (g)	Co (mg/L)	References
IIP-membrane (PMMA-b-P4VP)	79.68	0.5	0.1	100	[1]
Pt(II)TCTES/S2	65.8	2.5	0.005	100	[25]
Pt(II)TCTES/S1	78.7	2.5	0.005	100	[25]
Pt-DMG-VP	40.5	0.5	0.1	50	[27]
MIIP-poly(EGDMA)	172.9	1.0	0.01	50	[49]
UiO-66(A)	144.5	1.0	0.01	100	[50]
MIL-101(Cr)-NO_2	104.5	1.0	0.01	100	[17]
MIL-101(Cr)-NH_2	140.7	1.0	0.01	100	[17]
NIP	296.4	3.0	0.02	100	This work
IIP	531.3	3.0	0.02	100	This work

7.3.3.3. Kinetics experiments

The kinetics of Pt(IV) adsorption onto the IIGlyMIL-101(Cr) and NIGlyMIL-101(Cr) composites are represented by Figure 7.7(a). The plots demonstrated a rise in the intake capacity of the IIGlyMIL-101(Cr) and NIGlyMIL-101(Cr) with increasing time. The IIGlyMIL-101(Cr) demonstrated superior performance and reached equilibrium within 30 minutes as compared to the NIGlyMIL-101(Cr) which equilibrated after 60 minutes. This behaviour was attributed to the higher affinity for $[PtCl_6]^{2-}$ ions by the ion imprinted composite [51]. The obtained data was subjected to the non-linearized and linearized forms of the pseudo first-order (PFO) and second-order (PSO) kinetic models for the elucidation of the adsorption mechanism. As seen in Figure 7.7(a, b and c), the data correlated more with the PSO linear and nonlinear model as supported by the obtained

R^2 value of 0.9975 and 0.8972 for the IIGlyMIL-101(Cr); and 0.9461 and 0.9898 for the NIGlyMIL-101(Cr) at 100 mg/L concentration and 25 ^oC (Table 7.3). Moreover, the PSO linear model showed to have a higher adsorption capacity than that of the PFO model and the q_e values estimated by the model are in good agreement with the ones obtained experimentally as well as with nonlinear ones [28]. Furthermore, the rate-limiting step of Pt(IV) adsorption by the IIGlyMIL-101(Cr) and NIGlyMIL-101(Cr) composites was investigated by fitting the kinetics data to the Weber and Morris intra-particle model [52]. Figure 7.7(d) illustrated that the intake of Pt(IV) ions by both composites proceeds through two steps. The initial rapid region is attributed to the film diffusion and the second region is the intra-particle diffusion. From the results shown by the inset equation, the rate limiting step is associated with the film diffusion since the intra-particle step deviates from linearity and the plots does not pass through the origin [53][54]. In addition, the greater y-intercept which is associated with the boundary layer effect or surface adsorption showed to have a contribution in the rate-limiting step [55].

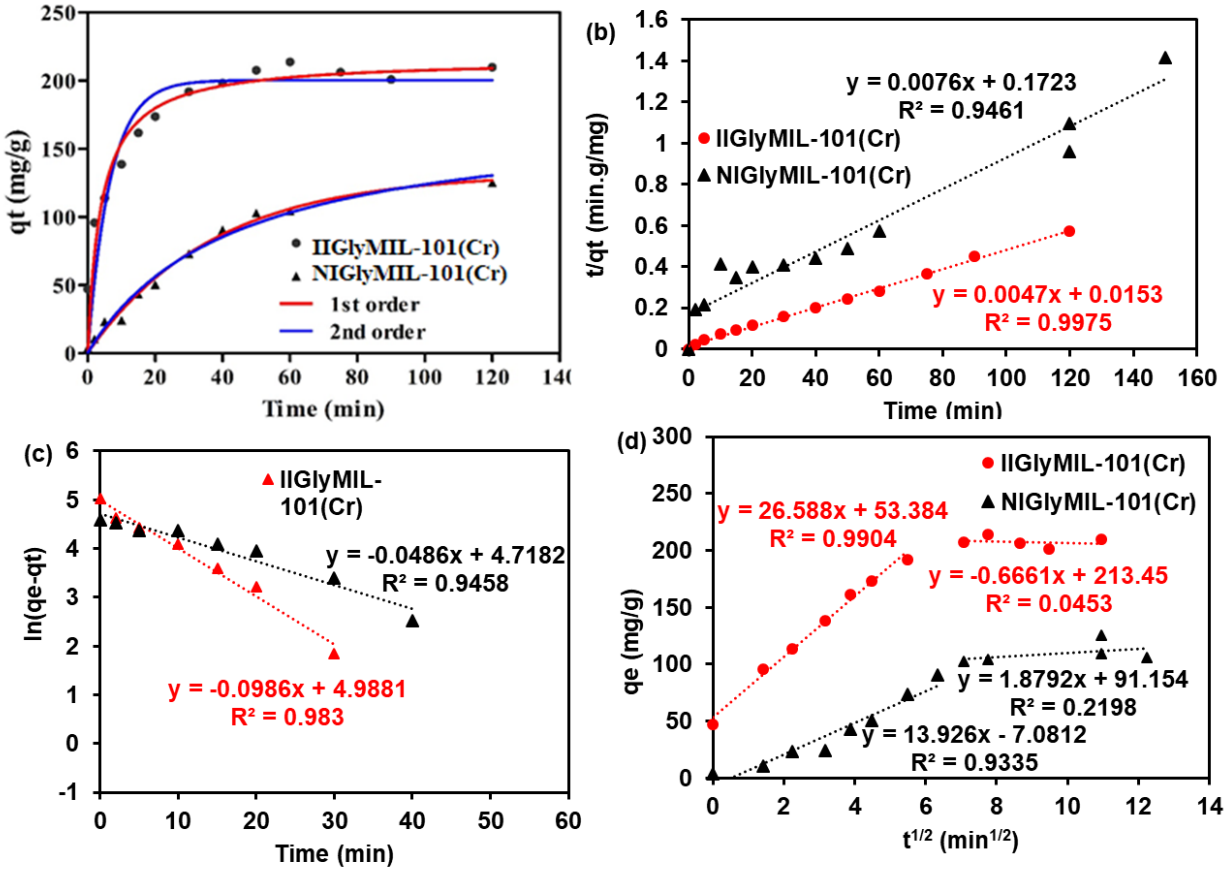

Figure 7.7: (a) Nonlinear fit and experimental; (b) linear fit pseudo-second-order and (c) first order; and (d) intra-particle diffusion model of Pt(IV) uptake by IIGlyMIL-101(Cr) and NIGlyMIL-101(Cr) composites.

Table 7.3: Pseudo-first- and pseudo-second-order parameters of Pt(IV) ion adsorption by IIGlyMIL-101(Cr) and NIGlyMIL-101(Cr) materials.

Pseudo-first-order	**Material**		**Pseudo-second-order**	**Material**	
	IIGlyMIL-	NIGlyMIL-		IIGlyMIL-	NIGlyMIL-101(Cr)
Linear			*Linear*		
q_e *(exp)*	146.658	111.966	q_e	212.766	131.5789
k_1	0.0986	0.0486	k_2	0.005402	0.00048
R^2	0.9830	0.9458	R^2	0.9975	0.9461
Non-linear			*Non-linear*		
Best-fit values			Best-fit values		
q_e	200.3	103.1	q_e	215.9	132
k_1	0.15	0.1061	k_2	0.001146	0,02699
Std. Error			Std. Error		
q_e	8.263	2.413	q_e	8.87	5,446
k_1	0,03165	0.01102	k_2	0,0003186	0,002328
95 % Confidence			95 % Confidence		
q_e	182.1 to 218.5	97.75 to 108.4	q_e	196.4 to 235.5	119.7 to 144.3
k_1	0.08037 to 0.2197	0.08186 to 0.1304	k_2	0.0004451 to 0.001848	0.02173 to 0.03226
Goodness of Fit			Goodness of Fit		
Degrees of	11	11	Degrees of Freedom	11	
R^2	0.8347	0.9694	R^2	0.8972	0.9898
Absolute Sum of	5471	398	Absolute Sum of	3401	181,1
Sy.x	22,3	6.015	Sy.x	17.58	4,485
Number of points			Number of points		
Analysed	13	13	Analysed	13	11

Units: q_e: mg/g, k_1: 1/min, k_2: g/mgmin

7.3.3.4. Competitive ions

The selectivity test of the IIGlyMIL-101(Cr) and NIGlyMIL-101(Cr) towards Pt(IV) ions intake was studied in the presence of selected cations (Pd^{2+}, Ni^{2+}, Co^{2+}, Ag^{+},) and anions (SO_4^{2-}, CO_3^{2-}, NO_3^{-}, PO_4^{2-}). In each case the original concentration of 1:1 ratio was adjusted to a pH of 3.0 before contacting it with 0.03 g of IIGlyMIL-101(Cr) and NIGlyMIL-101(Cr). The results shown in Figure 7.8 revealed that the IIGlyMIL-101(Cr) was able to achieve a %R of more than 75% for Pt(IV) ions intake in the presence of various ions. However, Pd^{2+} ions demonstrated to have an influence on the uptake of Pt(IV) ions as the %R was reduced to 50%. This observation suggests that there is more than one mechanism of adsorption occurring and Pd is more reactive in comparison to the Pt. For the uptake of Pt(IV) ions by the NIGlyMIL-101(Cr) composite, there was a significant effect by all of the selected anions with %R ranging between 55-40 %, as well as the Pd ions which led to the removal of 20% of the Pt(IV) ions. These results confirm the advantages offered by the ion imprinting technique in selecting the targeted metal ions in the presence of diverse ions. Hence, the prepared IIGlyMIL-101(Cr) showed superior performance in comparison to the NIGlyMIL-101(Cr).

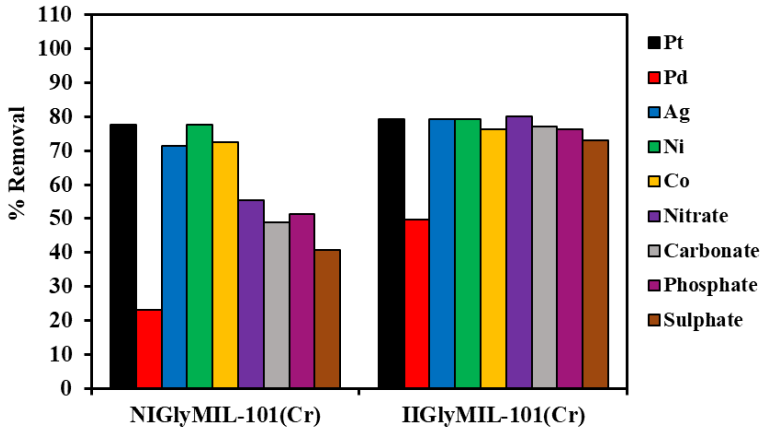

Figure 7.8: Influence of competing ions on the uptake of Pt(IV) ions by the IIGlyMIL-101(Cr) and NIGlyMIL-101(Cr) composites.

7.3.3.5. Reusability experiments

The potential economical sustainability and efficiency of the IIGlyMIL-101(Cr) and NIGlyMIL-101(Cr) composites were investigated by assessing the regeneration and reusability of the prepared materials. The experiments were conducted for 5 successive cycles in which the IIGlyMIL-101(Cr) and NIGlyMIL-101(Cr) composites were regenerated using 6 M HCL prior to the subsequent cycle. As illustrated by Figure 7.9, the results showed that the IIGlyMIL-101(Cr) can be utilised for 5 consecutive cycles without the significant loss of Pt(IV) intake capacity. This was observed by the removal of 88.2% obtained in the first cycles that was slightly reduced 87.4% after the 5th cycles. The removal efficiency of the NIGlyMIL-101(Cr) composite showed a decrease with the increasing number of cycles from 78.36% of the initial cycle being reduced to 68.77% after the 5th cycle. These observations signify the advantageous adsorption performance of the IIGlyMIL-101(Cr) over its non-imprinted counterpart.

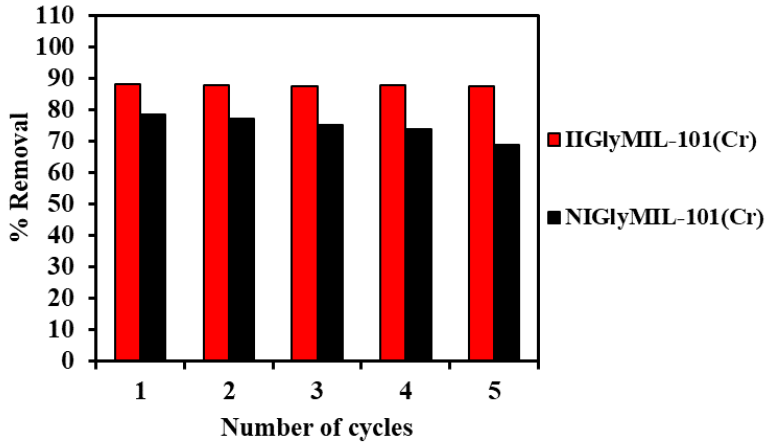

Figure 7.9: Experimental regeneration and reusability of the IIGlyMIL-101(Cr) and NIGlyMIL-101(Cr) composites.

7.4. CONCLUSION

This work was aimed at developing a highly efficient IIGlyMIL-101(Cr) adsorbent for the recovery of Pt(IV) ions from industrial wastewater. The synthesis of IIGlyMIL-101(Cr) was

achieved by using a PET- derived organic linker in the preparation of MIL-101(Cr) followed by post-modification with cross-linking agents and a functional monomer to produce an ion imprinted composite. The adsorption behaviour of the IIGlyMIL-101(Cr) towards Pt(IV) ions removal and recovery was investigated in batch mode and its efficiency was compared with its non-imprinted counterpart. The adsorption of Pt(IV) ions by the IIGlyMIL-101(Cr) was optimum in acidic media of pH = 3.0 due to the electrostatic interaction between the protonated N and O atoms with the Pt(IV) ions. The IIGlyMIL-101(Cr) demonstrated a high adsorption capacity of 531.4 mg/g, which was higher than 296.4 mg/g of the NIGlyMIL-101(Cr) as predicted from the Langmuir linear equation. Furthermore, the IIGlyMIL-101(Cr) revealed an improved adsorption rate, which reached equilibrium in less than 30 minutes and fitted well with the PSO. The selectivity of the composite for Pt(IV) ions was also enhanced in comparison to the NIGlyMIL-101(Cr) as its %R was maintained above 75% in the presence of various ions. The IIGlyMIL-101(Cr) was regenerated and reused for 5 successive cycles without significant loss in the removal efficiency.

7.5. REFERENCES

[1] J. Zeng, C. Lv, G. Liu, Z. Zhang, Z. Dong, J. Y. Liu, Y. Wang “A novel ion-imprinted membrane induced by amphiphilic block copolymer for selective separation of Pt(IV) from aqueous solutions,” *J. Memb. Sci.*, vol. 572, pp. 428–441, 2019, doi: 10.1016/j.memsci.2018.11.016.

[2] B. Leśniewska, M. Kosińska, B. Godlewska-Zyłkiewicz, E. Zambrzycka, and A. Z. Wilczewska, “Selective solid phase extraction of platinum on an ion imprinted polymers for its electrothermal atomic absorption spectrometric determination in environmental samples,” *Microchim. Acta*, vol. 175, pp. 273–282, 2011, doi: 10.1007/s00604-011-0685-1.

[3] J. Mao, S. Kim, X. H. Wu, I. S. Kwak, T. Zhou, and Y. S. Yun, “A sustainable cationic chitosan/E. coli fiber biosorbent for Pt(IV) removal and recovery in batch and column systems,” *Sep. Purif. Technol.*, vol. 143, pp. 32–39, 2015, doi: 10.1016/j.seppur.2015.01.023.

[4] J. K. Bediako, S. W. Park, J. Choi, M. Song, and Y. Yun, “Journal of Environmental Chemical Engineering chloride fibers : fabrication and application for recovery of platinum from acidic wastewaters,” *J. Environ. Chem. Eng.*, vol. 7, p. 102839, 2019, doi: 10.1016/j.jece.2018.102839.

[5] M. Chen, S. Li, C. Jin, M. Shao, Z. Huang, and X. Xie, “Removal of metal-cyanide complexes and recovery of Pt(II) and Pd(II) from wastewater using an alkali–tolerant metal-organic resin,” *J. Hazard. Mater.*, vol. 406, p. 124315, 2021, doi: 10.1016/j.jhazmat.2020.124315.

[6] T. H. Nguyen, C. H. Sonu, and M. S. Lee, “Separation of platinum(IV) and palladium(II) from concentrated hydrochloric acid solutions by mixtures of amines with neutral extractants,” *J. Ind. Eng. Chem.*, vol. 32, pp. 238–245, 2015, doi: 10.1016/j.jiec.2015.08.022.

[7] W. Wei, S. Lin, D. H. K. Reddy, J. K. Bediako, and Y. S. Yun, “Poly(styrenesulfonic acid)-impregnated alginate capsule for the selective sorption of Pd(II) from a Pt(IV)-Pd(II) binary solution,” *J. Hazard. Mater.*, vol. 318, pp. 79–89, 2016, doi: 10.1016/j.jhazmat.2016.06.050.

[8] Y. S. Petrova, A. V. Pestov, M. K. Usoltseva, E. I. Kapitanova & L. K. Neudachina “Methods for correction of selectivity of N-(2-sulfoethyl) chitosan-based materials towards platinum (IV) and palladium (II) ions,” *Sep. Sci. Technol.*, vol. 00, pp. 1–9, 2018, doi: 10.1080/01496395.2018.1505912.

[9] L. Zhou, J. Xu, X. Liang, and Z. Liu, “Adsorption of platinum (IV) and palladium (II) from aqueous solution by magnetic cross-linking chitosan nanoparticles modified with ethylenediamine,” *J. Hazard. Mater.*, vol. 182, pp. 518–524, 2010, doi: 10.1016/j.jhazmat.2010.06.062.

[10] O. Buriac, M. Ciopec, N. Duţeanu, A. Negrea, P. Negrea, and I. Grozav, “Platinum (IV) recovery from waste solutions by adsorption onto Dibenzo-30-crown-10 ether immobilized on amberlite XAD7 resin-factorial design analysis,” *Molecules*, vol. 25, 2020, doi: 10.3390/molecules25163692.

[11] A. Ramesh, H. Hasegawa, W. Sugimoto, T. Maki, and K. Ueda, “Adsorption of gold (III), platinum (IV) and palladium (II) onto glycine modified crosslinked chitosan resin,” vol. 99, pp. 3801–3809, 2008, doi: 10.1016/j.biortech.2007.07.008.

[12] L. Tan *et al.*, “Selective adsorption of palladium and platinum from secondary wastewater using Escherichia coli BL21 and Providencia vermicola,” *Bioprocess Biosyst. Eng.*, vol. 43, pp. 1885–1897, 2020, doi: 10.1007/s00449-020-02378-6.

[13] H. Zheng, Y. Ding, Q. Wen, B. Liu, and S. Zhang, “Separation and purification of platinum group metals from aqueous solution: Recent developments and industrial applications,” *Resour. Conserv. Recycl.*, vol. 167, p. 105417, 2021, doi: 10.1016/j.resconrec.2021.105417.

[14] O. E. Fayemi, A.S. Ogunlaja, P.F. Kempgens, E. Antunes, N. Torto, T. Nyokong, Z.R. Tshentu, “Adsorption and separation of platinum and palladium by polyamine functionalised polystyrene-based beads and nanofibers,” *Miner. Eng.*, vol. 53, pp. 256–265, 2013, doi: 10.1016/j.mineng.2013.06.006.

[15] K. Fujiwara, A. Ramesh, T. Maki, H. Hasegawa, and K. Ueda, “Adsorption of platinum (IV), palladium (II) and gold (III) from aqueous solutions onto l -lysine modified crosslinked chitosan resin,” vol. 146, pp. 39–50, 2007, doi: 10.1016/j.jhazmat.2006.11.049.

[16] J. De Decker, K. Folens, J. Clercq, M. Meledina, G. Van Tendeloo, G. Du Laing, P. Van Der Voort, “Ship-in-a-bottle CMPO in MIL-101(Cr) for selective uranium recovery from aqueous streams through adsorption,” *J. Hazard. Mater.*, vol. 335, no. 2017, pp. 1–9, 2017, doi: 10.1016/j.jhazmat.2017.04.029.

[17] C. Lim, S. Lin, and Y. Yun, “Highly efficient and acid-resistant metal-organic frameworks of MIL- 101(Cr)-NH_2 for Pd(II) and Pt(IV) recovery from acidic solutions : Adsorption experiments , spectroscopic analyses, and theoretical computations,” *J. Hazard. Mater.*, vol. 387, p. 121689, 2020, doi: 10.1016/j.jhazmat.2019.121689.

[18] S. Lin, J. K. Bediako, C. Cho, M. Song, Yu. Zhao, J. Kim, J. C. Yun “Selective adsorption of Pd(II) over interfering metal ions (Co(II), Ni(II), Pt(IV)) from acidic aqueous phase by metal-organic frameworks,” *Chem. Eng. J.*, vol. 345, pp. 337–344, 2018, doi: 10.1016/j.cej.2018.03.173.

[19] T. P. Rao, R. Kala, and S. Daniel, “Metal ion-imprinted polymers-Novel materials for selective recognition of inorganics,” *Anal. Chim. Acta*, vol. 578, pp. 105–116, 2006, doi: 10.1016/j.aca.2006.06.065.

[20] H. Wang, H. Shang, X. Sun, L. Hou, M. Wen, and Y. Qiao, “Preparation of thermo-sensitive surface ion-imprinted polymers based on multi-walled carbon nanotube composites for selective adsorption of lead (II) ion,” *Colloids Surfaces A*, vol. 585, p. 124139, 2020, doi: 10.1016/j.colsurfa.2019.124139.

[21] B. Zhao, M. He, B. Chen, H. Xu, and B. Hu, “Spectrochimica Acta Part B Poly (1-vinylimidazole) functionalised magnetic ion imprinted polymer for fast and selective extraction of trace gold in geological , environmental and biological samples followed by graphite furnace atomic absorption spectrom,” *Spectrochim. Acta Part B At. Spectrosc.*, vol. 143, pp. 32–41, 2018, doi: 10.1016/j.sab.2018.02.011.

[22] P. Fang, W. Xia , Y. Zhou, Z. Ai , Weiyan Yin, M. Xia, J. Yu , R. Chic , Q. Yue, “Ion-imprinted mesoporous silica/magnetic graphene oxide composites functionalised with Schiff-base for selective Cu(II) capture and simultaneously being transformed as a robust heterogeneous catalyst,” *Chem. Eng. J.*, vol. 385, p. 123847, 2020, doi: 10.1016/j.cej.2019.123847.

[23] N. H. Elsayed, A. Alatawi, and M. Monier, “Diacetylmonoxine modified chitosan derived ion-imprinted polymer for selective solid-phase extraction of nickel(II) ions,” *React. Funct. Polym.*, vol. 151, p. 104570, 2020, doi: 10.1016/j.reactfunctpolym.2020.104570.

[24] J. Mao, S. Lin, X. J. Lu, X. H. Wu, T. Zhou, and Y. S. Yun, “Ion-imprinted chitosan fiber for recovery of Pd(II): Obtaining high selectivity through selective adsorption and two-step desorption,” *Environ. Res.*, vol. 182, no. November 2019, p. 108995, 2020, doi: 10.1016/j.envres.2019.108995.

[25] J. Dobrzynska, M. Dabrowska, R. Olchowski, E. Zieba, and R. Dobrowolski, “Development of a method for removal of platinum from hospital wastewater by novel ion-imprinted mesoporous organosilica,” *J. Environ. Chem. Eng.*, vol. 9, no. 4, 2021, doi: 10.1016/j.jece.2021.105302.

[26] L. Carvalho, M. Costa, M. P. Torres, C. Vale, and E. Pereira, “Journal of Environmental Chemical Engineering Platinum-group elements sorption by living macroalgae under different contamination scenarios,” vol. 9, no. December 2020, 2021, doi: 10.1016/j.jece.2021.105100.

[27] Y. Jiang and D. Kim, “Synthesis and Selective Sorption Behaviour of Pt (IV) Ion-Imprinted Polymer Particles,” no. Iv, 2014.

[28] X. Gao, C. Guo, J. Hao, Z. Zhao, H. Long, and M. Li, “Selective adsorption of Pd (II) by ion-imprinted porous alginate beads: Experimental and density functional theory study,” *Int. J. Biol. Macromol.*, vol. 157, pp. 401–413, 2020, doi: 10.1016/j.ijbiomac.2020.04.153.

[29] J. Ren, X. Dyosiba, N. M. Musyoka, H. W. Langmi, B. C. North, M. Mathe, and M. S. Onyango, “Green synthesis of chromium-based metal-organic framework (Cr-MOF) from waste polyethylene terephthalate (PET) bottles for hydrogen storage applications,” *Int. J. Hydrogen Energy*, vol. 41, pp. 18141–18146, 2016, doi: 10.1016/j.ijhydene.2016.08.040.

[30] M. Sha, M. Sheikh, A. Rashidi, and A. Samimi, “Synthesis and adsorption performance of a modified micro-mesoporous MIL-101(Cr) for VOCs removal at ambient conditions,” vol. 341, pp. 164–174, 2018, doi: 10.1016/j.cej.2018.02.027.

[31] G. Yuan, H. Tu, M. Li, J. Liu, C. Zhao, J. Liao, Jiali, Y. Yang, J. Yang, Jijun, N. Liu, Ning, “A novel ion-imprinted polymer induced by the glycylglycine modified metal-organic framework for the selective removal of Co(II) from aqueous solutions,” *Chem. Eng. J.*, vol. 333, pp. 280–288, 2018, doi: 10.1016/j.cej.2017.09.123.

[32] J. Zhang, H. Zhang, Q. Liu, D. Song, R. Li, and P. Liu, “Diaminomaleonitrile functionalised double-shelled hollow MIL-101(Cr) for selective removal of uranium from simulated seawater,” *Chem. Eng. J.*, vol. 368, pp. 951–958, 2019, doi: 10.1016/j.cej.2019.02.096.

[33] X. Luo, L. Ding, and J. Luo, “Adsorptive removal of Pb(II) ions from aqueous samples with amino-functionalisation of metal-organic frameworks MIL-101(Cr),” *J. Chem. Eng. Data*, vol. 60, pp. 1732–1743, 2015, doi: 10.1021/je501115m.

[34] J. Y. Zhang, N. Zhang, L. Zhang, Y. Fang, W. Deng, M. Yu, Z. Wang, L. Li, X. Liu & J. Li, “Adsorption of Uranyl ions on Amine-functionalisation of MIL-101(Cr) Nanoparticles by a Facile Coordination-based Post-synthetic strategy and X-ray Absorption Spectroscopy Studies,” *Sci. Rep.*, vol. 5, pp. 1–10, 2015, doi: 10.1038/srep13514.

[35] T. R. Somo, M. W. Davids, M. V Lototskyy, M. J. Hato, and K. D. Modibane, “Improved Hydrogenation Kinetics of TiMn1.52 Alloy Coated with Palladium through Electroless Deposition,” 2021.

[36] M. Cr, “Benzoic acid as a selector–modulator in the synthesis of MIL-88B(Cr) and nano-MIL-101(Cr),” vol. 101, pp. 989–996, 2019, doi: 10.1039/c8dt04186e.

[37] S. Qiu, Y. Wang, J. Wan, J. Han, Y. Ma, and S. Wang, “Applied Surface Science Enhancing water stability of MIL-101(Cr) by doping Ni(II),” *Appl. Surf. Sci.*, vol. 525, no. December 2019, p. 146511, 2020, doi: 10.1016/j.apsusc.2020.146511.

[38] T. Zhao, L. Yang, P. Feng, I. Gruber, C. Janiak, and Y. Liu, “Inorganica Chimica Acta Facile synthesis of nano-sized MIL-101 (Cr) with the addition of acetic acid,” *Inorganica Chim. Acta*, vol. 471, pp. 440–445, 2018, doi: 10.1016/j.ica.2017.11.030.

[39] A. Demessence, P. Horcajada, C. Serre, and D. Grosso, “Elaboration and properties of hierarchically structured optical thin films of MIL-101(Cr),” vol. 101, pp.

7149–7151, 2009, doi: 10.1039/b915011k.

[40] H. Thi, T. Phuong, P. Hang, T. Toan, T. Tuyen, T. Mau, D. Q. Khieu, “Journal of Environmental Chemical Engineering Comparative study of Pb(II) adsorption onto MIL-101 and Fe-MIL-101 from aqueous solutions,” *J. Environ. Chem. Eng.*, vol. 6, pp. 4093–4102, 2018, doi: 10.1016/j.jece.2018.06.021.

[41] N. Wang, L. Y. Yang, Y. G. Wang, and X. K. Ouyang, “Fabrication of composite beads based on calcium alginate and tetraethylenepentamine-functionalised MIL-101 for adsorption of Pb(II) from aqueous solutions,” *Polymers (Basel).*, vol. 10, no. 7, 2018, doi: 10.3390/polym10070750.

[42] X. Huang, J. Lu, W. Wang, X. Wei, and J. Ding, “Experimental and computational investigation of CO_2 capture on amine grafted metal-organic framework NH2-MIL-101,” *Appl. Surf. Sci.*, vol. 371, pp. 307–313, 2016, doi: 10.1016/j.apsusc.2016.02.154.

[43] Y. Jiang and D. Kim, “Synthesis and selective adsorption behaviour of Pd(II)-imprinted porous polymer particles,” *Chem. Eng. J.*, vol. 232, pp. 503–509, 2013, doi: 10.1016/j.cej.2013.08.008.

[44] H. Sharififard, M. Soleimani, and F. Z. Ashtiani, “Evaluation of activated carbon and bio-polymer modified activated carbon performance for palladium and platinum removal,” *J. Taiwan Inst. Chem. Eng.*, vol. 43, no. 5, pp. 696–703, 2012, doi: 10.1016/j.jtice.2012.04.007.

[45] F. A. Elaiwi and A. Sirkecioglu, “Amine-functionalised metal organic frameworks MIL-101 (Cr) adsorbent for copper and cadmium ions in single and binary solution,” *Sep. Sci. Technol.*, vol. 00, no. 00, pp. 1–13, 2019, doi: 10.1080/01496395.2019.1706571.

[46] H. T. Minh Thanh *et al.*, “Comparative study of Pb(II) adsorption onto MIL-101 and Fe-MIL-101 from aqueous solutions,” *J. Environ. Chem. Eng.*, vol. 6, no. 4, pp. 4093–4102, 2018, doi: 10.1016/j.jece.2018.06.021.

[47] R. Tseng and F. Wu, “Journal of the Taiwan Institute of Chemical Engineers Analyzing concurrent multi-stage adsorption process of activated carbon with a favorable parameter of Langmuir equation,” vol. 40, pp. 197–204, 2009, doi:

10.1016/j.jtice.2008.09.002.

[48] C. Sun, L. Sun, and X. Sun, “Graphical Evaluation of the Favorability of Adsorption Processes by Using Conditional Langmuir Constant,” 2013.

[49] L. A. Limjuco and F. K. Burnea, “Evaluation of dithiadiamide - based molecular ion imprinted polymer (MIIP) for selective recovery of platinum from acid - digested spent automobile catalytic converter (ACC) solution,” *MRS Commun.*, vol. 12, no. 2, pp. 175–182, 2022, doi: 10.1557/s43579-022-00158-9.

[50] S. Lin, J. K. Bediako, M. Song, and J. Kim, “organic frameworks using central composite design for synthesis Effective recovery of Pt (IV) from acidic solution by a defective metal-organic frameworks using central,” no. Iv, 2019, doi: 10.1021/acssuschemeng.8b04637.

[51] S. Lin *et al.*, “Selective adsorption of Pd (II) over interfering metal ions (Co (II), Ni (II), Pt (IV)) from acidic aqueous phase by metal-organic frameworks,” *Chem. Eng. J.*, vol. 345, no. February, pp. 337–344, 2018, doi: 10.1016/j.cej.2018.03.173.

[52] Z. Huang, C. Wang, J. Zhao, S. Wang, Y. Zhou, and L. Zhang, “Adsorption behaviour of Pd (II) ions from aqueous solution onto pyromellitic acid modified-UiO-66-,” *Arab. J. Chem.*, vol. 13, no. 9, pp. 7007–7019, 2020, doi: 10.1016/j.arabjc.2020.07.007.

[53] Z. Khademi, B. Ramavandi, and M. Taghi, “Journal of Environmental Chemical Engineering Journal of Environmental Chemical Engineering The behaviours and characteristics of a mesoporous activated carbon prepared from Tamarix hispida for Zn (II) adsorption from wastewater,” *Biochem. Pharmacol.*, vol. 3, no. 3, pp. 2057–2067, 2015, doi: 10.1016/j.jece.2015.07.012.

[54] S. Mortazavian, A. Saber, J. Hong, J. Bae , D. Chun,“Synthesis, characterisation and kinetic study of activated carbon modified by polysulfide rubber coating for aqueous hexavalent chromium removal,” *J. Ind. Eng. Chem.*, no. October, 2018, doi: 10.1016/j.jiec.2018.09.028.

[55] L. Zhou, J. Liu, and Z. Liu, “Adsorption of platinum(IV) and palladium(II) from aqueous solution by thiourea-modified chitosan microspheres,” *J. Hazard. Mater.*, vol. 172, pp. 439–446, 2009, doi: 10.1016/j.jhazmat.2009.07.030.

CHAPTER 8

GENERAL DISCUSSION, CONCLUSION AND RECOMMENDATIONS

8.1 DISCUSSION AND CONCLUSION

In this chapter, a brief discussion on the results presented in this work is provided. Furthermore, a conclusion based on the comprehensive study and future recommendations is made in relation to the findings. The overall purpose of this study was to develop highly efficient and selective MOF-based adsorbents through the ion imprinting technique in order to increase their scope in the application for the removal and recovery of PGMs metal ions from aqueous solution. The MOF adsorbent materials were chosen based on their interesting properties such as high chemical and thermal stabilities in harsh conditions, tuneable pore size and surface functionality, high porosity and surface area, availability of various functional groups for reactivity, and their ability to be synthesised from waste PET as the organic linker. Based on their previous application in the recovery of Pd and Pt metals ions, the prepared MOFs were post-modified through ion imprinting by incorporating amino and carboxyl group rich components including ethylenediamine, glutaraldehyde, and glycylglycine to improve their performances and reusability in the removal and recovery of selected PGMs. The overview of this work is encompassed of seven chapters.

Chapter one mainly focussed on the introduction of this work where the background on the utilisation of PGMs was briefly provided. Furthermore, these uses have contributed to the increased global demand resulting in the need to produce more PGMs. However, the excessive mining activities posed challenges relating to mineral resource scarcity as well as water pollution. Different technologies have developed, with more consideration being given to the adsorption technology as it has demonstrated some promising effects in terms of ease of operation and capital cost. Hence, the motivation of this study has identified the MOF composites as potential adsorbents to recover PGMs from aqueous

solutions. In addition, the selectivity towards targeted precious metal ions has been set to be improved through the modification of the synthesised MOFs with ion-imprinted polymers and thereby leading to the aim and objectives of the study.

In chapter two, a literature survey on the synthesis of MOFs and their application in various fields was covered, with more attention given to their application in the removal of heavy metal ions from industrial wastewater. The chapter initially introduced a background on PGMs in relation to their wide range of applications in numerous fields, their increasing demand and limited availability due to their non-renewable nature, potential pollution, and impact associated with their improper disposal, and finally, the efforts implemented through adsorption to recover and remove them from aqueous solution by ion-imprinted MOF adsorbents. Detailed background on the existing different structures of MOFs and how they can be prepared using various methods were also discussed. The post-modification process has been identified to offer advantages in terms of forming MOF composites and was the common method employed in the applications discussed in this chapter. A further deliberation of the utilisation of MOF composites in the adsorption of pollutants has been made and it was noted that even though there are some reports on the removal of heavy metal ions, there is a lack of information with regards to ion-specific modified MOF composites for the removal and recovery of precious metal such as PGMs.

Chapter three described the analytical techniques used in this study to characterize the prepared MOF composites and analyse the concentrations of the targeted metal ions before and after adsorption. In the introduction, water pollution emanating from various sources, its impact on the environment, and different technologies implemented in order to curb their effect were briefly discussed. MOF-based composites were chosen as the adsorbent materials of choice during the adsorption process to be reviewed in terms of their structural characterisation and interaction with heavy metal ions such as PGMs. The chapter further provided a detailed literature review on different analytical instruments such as ICP-MS, FAAS and ICP-OES used in the determination of the remaining concentration of heavy metal ions before and after adsorption by MOFs and compared it with the UV-Vis spectroscopy analysis used in this study. This was achieved by

comparison of some of the adsorption parameters results from various reported studies in which these analytical instruments were utilised. Moreover, a comprehensive discussion on a variety of techniques employed in the structural characterisation of MOF composites before and after their interaction with heavy metals has been outlined. The highlighted techniques include physical, morphological, and spectroscopic characterisation methods that have been used in this work such as XRD, BET, TGA, SEM-EDS, FTIR, and those that have been used in other literature including TEM-EDX and XPS to understand the mechanism of interaction between MOF composites and heavy metal ions (PGMs included).

In this work, the first approach to the application of MOFs composites for the adsorption of PGMs was presented in chapter four. This chapter focused on the synthesis and functionalised polyethylene terephthalate-derived metal-organic frameworks with ethylenediamine (MIL-101(Cr)-ED) for spectroscopic detection and adsorption of Pd(II) ions from aqueous solutions. The MIL-101(Cr)-ED composite was prepared from the waste PET organic linker using the hydrothermal method, prior to functionalisation with ED. The grafted ED moieties were noted from FTIR with vibration 2800-3300 cm^{-1}, the appearance of N content on the EDS, and the reduction in the crystallinity of MIL-101(Cr) from 96.1 to 80.1 % as seen from XRD data. Batch adsorption experiments revealed that the MIL-101(Cr)-ED was more efficient towards Pd(II) ions intake in acidic media of pH 3.0 and acquired a 95% removal efficiency at 25 ^{o}C with the initial concentration of 100 mg/L. The adsorption isotherm data collected at three different temperatures (25, 35, and 45 ^{o}C) fitted well with the Langmuir model which estimated the q_m values of 454.2, 506.5, and 570.2 mg/g for 25, 35, and 45 °C, respectively. The rate of interaction between the MIL-101(Cr)-ED and Pd(II) was very rapid as the kinetics experiments reached equilibrium within three minutes. Though showed some potential in the removal of Pd(II), adsorbent regeneration still posed some challenges due to the over-oxidation of the ED amino groups.

Chapter five presented the second approach of this study which was focused on synthesising a highly adsorptive MIL-101(Cr)/ED-GA composite for the removal of Pd(II) and Pt(IV) ions from wastewater. The successfully incorporated GA formed an amide bond with the ED end in MIL-101(Cr)-ED which was seen by the 1554 cm^{-1} for the N-H bend and 1052 cm^{-1} for the C-N stretch of the amide group. In addition, the crystallinity of MIL-101(Cr) was further reduced to 75.1% as observed on the XRD. In this chapter, the removal efficiencies towards Pd(II) and Pt(IV) by the MIL-101(Cr)/ED-GA composite were compared. The adsorption data also correlated well with the Langmuir isotherm model which gave the q_m of 416.17 and 322.6 mg/g for Pt(IV) and Pd(II) ions, respectively. The kinetics data showed that the MIL-101(Cr)/ED-GA composite had a higher affinity for the uptake of Pd(II) ions than Pt(IV) ions which suggested that selectivity was still a challenge. Furthermore, the adsorbents demonstrated potential regeneration which was limited to two cycles in terms of maintaining the initially acquired removal efficiencies for both Pd(II) and Pt(IV) ions.

Chapter six presented the initial approach based on the main aim of this study which was on improving the selectivity towards Pd(II) ions for the purpose of recovering the majority of them from industrial wastewater. The IPMIL-101(Cr) was prepared through chelation of Pd(II) ions onto the glycylglycine functional monomer on the MIL-101(Cr)/ED-GA surface, wherein the FTIR revealed the formation of C=N at 1677 cm^{-1} upon removal of the metal template to form IIP. The results were also supported by the XRD and BET data, which showed the increased crystallinity (72.0%) and surface area (8.7158 m^2/g) of the IPMIL-101(Cr) from the 70.6% crystallinity and 6.1702 m^2/g surface area in the Pd-loaded composite. The conducted batch adsorption experiments showed that the IPMIL-101(Cr) was able to recover more than 95% of Pd(II) ions in acidic media with pH = 2.0 using 0.04 g of the adsorbent. The kinetics data were rapid and fitted well with the PSO model. The fitted Langmuir isotherm model estimated the q_m values of 195.3 mg/g for the adsorption of Pd(II) ions which was higher than the NIMIL-101(Cr) capacity of 177.7 mg/g and those that are reported in the literature. Furthermore, the IPMIL-101(Cr) showed some improved selectivity with more than 80% Pd(II) ions removal still achieved in the presence of various cations and anions. The ion-imprinted MIL-101(Cr) adsorbent was

reusable for five consecutive cycles without any loss in the removal efficiency and adsorption capacity.

Chapter 7 focus on the second approach used to achieve the main aim of this research in which a IIGlyMIL-101(Cr) composite was synthesised to selectively recover Pt(IV) ions from aqueous solutions. The same chelating functional monomer in chapter 6 was used to prepare the IIGlyMIL-101(Cr) composite, however with the utilisation of the Pt metal template. The FTIR spectrum for the IIGlyMIL-101(Cr) composite showed the appearance of a characteristic peak at 1587 cm^{-1} attributed to the C=N vibration of the amide bond upon leaching out of the metal template. The adsorption experiments of the IIGlyMIL-101(Cr) composite toward Pt(IV) recovery were also compared to those of the NIP@MIL-101(Cr) adsorbent. At an initial solution pH of 4.0, 0.020 g of IIGlyMIL-101(Cr) and NIP@MIL-101(Cr) were able to remove 85% and 65% of Pt(IV) ions, respectively. The isotherm data fitted the Langmuir model and the calculated q_m reached higher values of 531.3 and 296.4 mg/g for the IIGlyMIL-101(Cr) and NIP@MIL-101(Cr), respectively. These values are much higher than those reported in the literature. The adsorption of Pt(IV) onto the Pt(IV)-IIP@MIL-101(Cr) adsorbent equilibrated within 30 minutes and the data fitted the PSO kinetics model. Competing ions studies revealed that the IIGlyMIL-101(Cr) was selective towards Pt(IV) ions removal in the presence of other ions. However, Pd(II) ions had an influence due to their higher affinity and reactivity with protonated N groups in comparison to the Pt(IV) ions. Furthermore, the IIGlyMIL-101(Cr) was regenerated and reused for five successive cycles and still maintained the efficiency of 89% removal.

The results obtained and presented in this thesis have demonstrated successful functionalisation of the MIL-101(Cr) which was prepared from waste PET plastic as an organic linker. The synthesised adsorbents have shown some activity in the removal and recovery of Pd(II) and Pt(IV). It can be concluded that the composite form of MIL-101(Cr)/ED-GA with ion-imprinted polymer has shown to be very effective in recognising the targeted metal ions which in turn contributed to the high intake capacity of Pd(II)-IIP@MIL-101(Cr) and IIGlyMIL-101(Cr) towards Pd(II) and Pt(IV) metal ions, respectively.

Furthermore, the reusability data also proved that the ion-recognition active sites can be regenerated.

8.2 RECOMMENDATIONS

The application of both the IPMIL-101(Cr) and IIGlyMIL-101(Cr) in the recovery of Pd(II) and Pt(IV) metal ions has shown some promising activity. However, some improvements need to be made in terms of the adsorption of Pd(II) ions due to the limited solubility of $PdCl_2$ which might affect the ion-imprinting process. Furthermore, the influence of temperature should also be investigated in order to understand and determine the thermodynamic properties associated with the adsorption process. The reusability experiments can be extended to more cycles in order to draw an overall conclusion on the stability of the IPMIL-101(Cr) and IIGlyMIL-101(Cr) in the recovery of Pd(II) and Pt(IV) metal ions. The use of other functional monomers can also be considered in order to enhance the selectivity of the prepared composites and to further minimize the influence of competing ions, especially the effect of Pd(II) ions on the intake of Pt(IV) ions. The adsorption experiments were performed in batch mode using simulated wastewater, in this regard real-world application is recommended in order to validate the efficiencies of the IPMIL-101(Cr) and IIGlyMIL-101(Cr). In addition, the experiments need to be conducted in column studies for the purpose of potential industrialisation. The obtained results should also be confirmed by employing other detection techniques such as ICP-MS and FAAS which are more specific to elemental analysis.